The chemistry of low dosage clathrate hydrate inhibitors

ANDREA PERRIN

The chemistry of low dosage clathrate hydrate inhibitors

A thesis submitted for the degree of

Doctor of Philosophy

In the Department of Chemistry at Durham University

By

Andrea Perrin

2015

Abstract

Clathrate hydrate formation remains a significant problem in the oil and gas industry, often resulting in pipeline blockage and field-site shutdown. To this end, a series of low dosage hydrate inhibitors are utilised in industry to circumvent potentially catastrophic effects. While a plethora of inhibitors are in application, to date there has been no conclusive determination of the mechanism of action of these important compounds. In order to drive the optimisation of inhibitor design, there remains a need to understand their complex behaviour and the role of key functional groups.

This thesis begins with a systematic study of the hydration behaviour of a series of commercially available poly(lactam) hydrate inhibitors. Solution IR spectroscopic titrations are reported for these polymers, providing insight into water binding at the polar amide carbonyl moiety. In an attempt to overcome the complexities associated with gaining quantitative insight into the behaviour of polymers, this thesis reports the development and analysis of model compounds. The model compounds are, in general, small dimeric analogues containing the key functionalities from the parent polymer appended on an aliphatic backbone. Finally, the solution and solid-state behaviours of these small model compounds are examined through a combination of analytical techniques.

Neutron scattering studies can provide unique insight into the structures of disordered systems. This thesis examines the liquid structures of aqueous THF, aqueous 2-butoxyethanol and aqueous lactam systems. By combining experimental neutron data with computational modelling it was possible to elucidate some insight into these systems of interest in solution as a function of temperature.

The final chapters report a series of lactam-metal coordination complexes, wherein the high polarity of the amide carbonyl moiety is exploited in the formation of interesting carbonyl-bound metal complexes. The X-ray single crystal structures are included for complexes containing sodium, potassium, zinc and calcium cation centres, with short carbonyl-metal bond distances observed in all instances. The versatility of ligand binding is encouraging, and may be of industrial importance.

Declaration

The work described in this thesis was carried out in the Department of Chemistry at Durham University (UK) between October 2011 and December 2014, under the supervision of Professor Jonathan W. Steed. In addition, neutron experiments were carried out at the Rutherford Appleton Laboratory in Oxfordshire. Two of the coordination complexes in Chapter 5 were synthesised by Dominic Myers, a summer student, as acknowledged in the relevant experimental section. The material contained in this thesis has not been previously submitted for a degree at this or any other university.

Statement of copyright

Financial Support

I gratefully acknowledge Ashland Inc. and the Engineering and Physical Sciences Research Council for their funding of this research. Open data statement: the work in this thesis was jointly funded by EPSRC and Ashland Inc. Because of the commercial sensitivity of the underlying research data it is not being made available in open format at the present time.

Acknowledgments

I would like to thank the following people, without their support this work would not have been possible:

- My supervisor, Professor Jonathan Steed, for his unwavering patience and support. I have been lucky to learn so much over the past few years, and working on this project has been a real joy. Thank you!
- Dr Osama Musa for his boundless energy and enthusiasm, and truly caring about every detail. The industrial insight gained from this collaboration has been extremely valuable, and I am immensely grateful for this opportunity. In addition, thank you to Ashland Inc. for the support.
- The Science & Technology Facilities Council (ISIS) for funding the neutron experiments. Thank you to experimental scientists Dr Samantha Callear and Dr Tristan Young. In addition, many thanks go to Professor Alan Soper for helping me with EPSR.
- I would like to thank the Durham Chemistry Analytical Staff. In particular, huge thanks to Dr Dmitry Yufit and Dr Horsch Puschmann for support with X-ray crystallography. Thanks to Dr Alan Kenwright and Dr Juan Aguilar-Malavia for help with NMR experiments. Thanks to Doug Carswell for TGA and DSC measurements, and to Gary Oswald for PXRD analysis. Thank you to Dr Aileen Congreve for help with chromatography. Thanks to Dr Mark Fox for performing Gaussian calculations.
- Thank you to the members of the Steed Group, past and present, for all of the support and the many laughs. Huge thanks to Dr Katharina Fucke for helping me to settle in at the very start. In particular, many thanks to the group members during my final year for keeping me sane and for the many meals out; Rachael, Chris, Yuexian, Melissa, Stuart and all other members of CG50. Thank you to summer student Dominic Myers.
- Outside of work, I have many people to thank for their continued support, encouragement and for ensuring that I find time to relax. In particular I must thank previous housemates and close friends, namely Net, Jessica, Jennifer, Sarah and Amy.
- Being part of Girlguiding has been fundamental in keeping me sane (and busy) outside of work, and I am very grateful for the many friends I have made through this. Thank you to the fantastic leadership team and Brownies.
- I am indebted to my family and friends for everything they have done over the years. I genuinely could not have done this without you. My parents have been my rock, and I could not have asked for more support or encouragement; thank you from the bottom of my heart.

Publication list

A. Perrin, O.M. Musa and J.W. Steed, The chemistry of low dosage clathrate hydrate inhibitors, *Chem. Soc. Rev.*, 2013, **42**, 1996 – 2015.

A. Perrin, D. Myers, K. Fucke, O.M. Musa and J.W. Steed, *N*-alkyl pyrrolidone ether podands as versatile alkali metal ion chelants, *Dalton Trans.*, 2014, **43**, 3153 – 3161.

S.J. James, A. Perrin, C.D. Jones, D.S. Yufit and J.W. Steed, Highly interlocked anion-bridged supramolecular networks from interrupted imidazole-urea gels, *Chem. Commun*., 2014, **50**, 12851 – 12854.

List of Abbreviations

AA – Anti Agglomerants

AFP – Antifreeze Proteins

br – broad

CCD – charge coupled device

CD_3CN (d_3 – MeCN) – deuterated acetonitrile

$CDCl_3$ – deuterated Chloroform

CSD – Cambridge Structural Database

d (NMR) – doublet

D_2O – deuterium oxide

DCM – dichloromethane

Dd (NMR) – doublet of doublets

Ddd (NMR) – doublet of doublets of doublets

DFT – Density Functional Theory

DMF – dimethylformamide

DSC – Differential Scanning Calorimetry

EPSR – Empirical Potential Structure Refinement

ES – Electrospray

EtOH – ethanol

Equiv – equivalents

GPa – Gigapascal

HPLC – High Performance Liquid Chromatography

Hz – Hertz

H_2SO_4 – sulphuric acid

IR – Infrared

J (NMR) – Coupling constant

K – Kelvin

K_{11} – Association constant

KHI – kinetic hydrate inhibitor

LDHI – low dosage hydrate inhibitor

m (NMR) – multiplet

MD – Molecular Dynamics

MeCN – Acetonitrile

MeOH – Methanol

M_n – Number average molecular weight

MPa – Megapascal

MW – Molecular weight

NMR – Nuclear Magnetic Resonance

ppm – parts per million

PXRD – Powder X-ray diffraction

SANS – Small Angle Neutron Scattering

t (NMR) – triplet

T_{cl} – Cloud point

TFA – Trifluoroacetic acid

TGA – Thermogravimetric Analysis

THF – Tetrahydrofuran

THI – Thermodynamic Inhibitor

TLC – Thin Layer Chromatography

UV – Ultraviolet

VCap – *n*-vinyl caprolactam

VP – *n*-vinyl pyrrolidone

wt% - weight%

β – Stepwise binding constant

δ – Chemical shift

λ – Wavelength

ΔT_{sub} – Subcooling temperature

Table of Contents

1 Introduction

Work detailed in this chapter is an updated and amended version of that published by the author in 2013.[1]

1.1 Clathrate Hydrates

1.1.1 Clathrate hydrate introduction

Clathrate hydrates are crystalline, non-stoichiometric host-guest compounds comprising a hydrogen bonded water framework entrapping small molecular guest species such as methane. The lack of strong directional interactions between the guest and host allows guests to vibrate and rotate whilst restricting translational motion.[2] Typically, common clathrate hydrates comprise 85 mol% water and 15 mol% guest(s) when all of the cavities are occupied.[3] Formation of clathrate hydrates is exacerbated by environments of ambient temperature (generally less than 300 K) and moderate pressure (> 0.6 MPa); conditions prevalent in oil and gas pipelines.[4]

The initial reporting of gas hydrates is accredited to Sir Humphrey Davy in 1811, who focussed upon the crystallisation of a cold aqueous solution of chlorine (known as oxymuriatic gas at the time).[5] Villard and de Forcrand were prevalent early gas hydrate researchers; with Villard the first to determine the existence of methane, ethane and propane hydrates.[6-8] Hammerschmidt, in 1934, highlighted that clathrate hydrates are responsible for the plugging of oil and gas pipelines and therein catalysed research investment in this area.[9]

Today, clathrate hydrates pose a major problem for the petrochemical industry with plug formation causing many safety concerns, in addition to causing pipeline shutdown. The shutdown period results in reduced field site performance and may have significant financial repercussions. The destructive nature of clathrate hydrates was highlighted during BP's efforts to contain the oil spillage following the Deepwater Horizon blowout.[10] Consequently, research into methods of preventing formation of such icy masses is of huge importance to the industry. Avoidance of pipeline shutdown is a priority to many oil and gas companies, and as such considerable investment is being made into research into clathrate hydrate inhibition to circumvent such potentially catastrophic effects.

1.1.2 Fuel reserves

While much of the petrochemical industry is working towards chemistries to circumvent the formation of clathrate hydrates, additional research is underway to exploit methane hydrate as a potential fuel reserve.[3, 11] It is believed that a vast quantity of methane (amongst other gases) resides in the Earth's permafrost and deep sea regions, and may provide the solution to natural gas shortages.[12] However, the purification process remains a drawback at present; therefore the reserves remain largely unexploited to date.[12] Furthermore, there is significant concern as to the potential global warming effect of methane clathrate hydrate dissociation as climate temperatures continue to rise.[13, 14] The dissociation of such gas hydrate may have run-away consequences to global climate change.[13, 14]

1.1.3 Clathrate hydrate structures

Three common clathrate hydrate structures exist: structure I (cubic); structure II (cubic) and structure H (hexagonal); with the structure adopted being dependent predominantly on the size of the guest(s).[15] Typically each cavity will accommodate one guest molecule, although when exposed to higher pressures (500 bar) multiple occupancy can be reached.[16] The vast majority of clathrate hydrate species take the form of structure I, structure II or structure H.[8] However there are some exceptions, such as the structure T (trigonal) species which forms in the presence of dimethyl ether.[17] In addition, an unusual complex structure is known comprising alternating stacks of structure H and structure II.[18] However, only structure I and structure II will be discussed herein, as these are the two most frequently observed in pipelines and hence are of importance in the context of inhibition chemistries.

The formalism A^B is frequently used to describe the cage structure of each water host cavity within a clathrate hydrate structure, where A represents the number of OH···O hydrogen-bonded edges of the face (*i.e.* the face shape) and B represents the number of faces with A sides.[19] The faces are made from hydrogen bonded rings of water molecules, with arrangements such as those in Figure 1.1.[16]

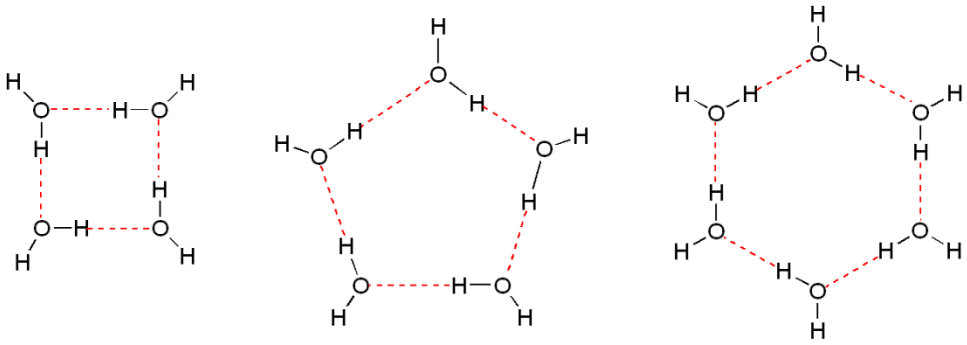

Figure 1.1: Hydrogen bonded water motifs comprising the faces in clathrate hydrate cages.[16]

The structure I and structure II crystal structures were first elucidated by von Stackelberg and coworkers following the interpretation of several earlier hydrate crystal diffraction experiments.[20-23] This was later followed by Mak, McMullan and Jeffrey who completed additional diffraction studies to provide more conclusive evidence for these structures.[24, 25] Later work by Ripmeester *et al.* (in 1987) resulted in the discovery and characterisation of structure H through use of solid state NMR spectroscopy and diffraction experiments.[26]

Figure 1.2 shows a simplistic representation of the cavity composition found in structures I, II and H, with the 5^{12} cavity common to each.[16] The pentagonal dodecahedral 5^{12} results from the combination of 12 pentagons to form the basic building block cavity. When these 5^{12} cavities are linked by their vertices the result is structure I hydrate, whilst those with face-sharing 5^{12} cavities result in structure II.[8] The difference in linkages allows for the formation of the larger voids within the structure I and structure II cavities ($5^{12}6^2$ and $5^{12}6^4$ respectively).[8]

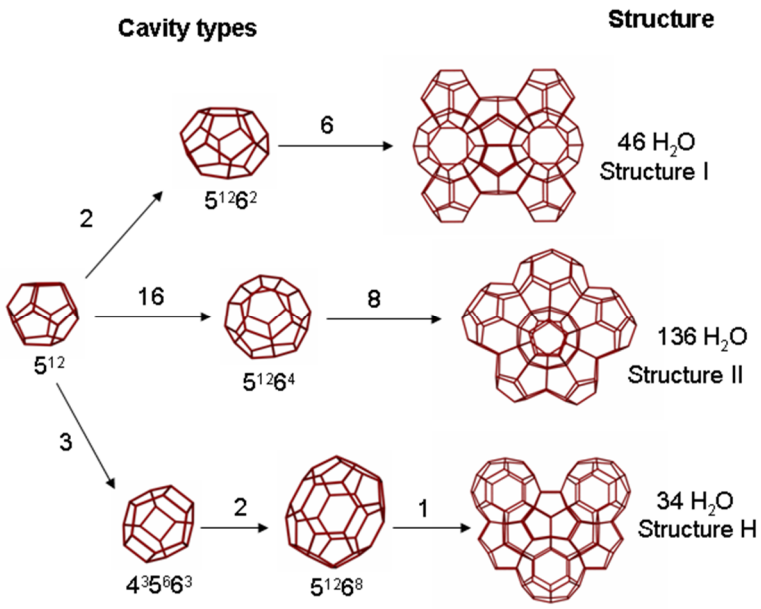

Figure 1.2: Common clathrate hydrate structures[16]

Structure I hydrate comprises two 5^{12} cavities and six $5^{12}6^2$ cavities (tetrakaidecahedron), with the unit cell containing 46 water molecules.[27] The tetrakaidecahedral cavity ($5^{12}6^2$) is 14-sided with 12 pentagonal and 2 hexagonal faces, and has an average radius of 4.33 Å which can include molecules with a diameter of up to about 6.0 Å.[8] In contrast, the unit cell of structure II hydrate contains sixteen 5^{12} and eight $5^{12}6^4$ cages. The $5^{12}6^4$ (hexakaidecahedron) cages have 12 pentagonal faces and four hexagonal faces, to form the 16-hedron cavity.[8] This larger cage can accommodate molecules with a diameter of up to 6.6 Å.[8] Therefore, small hydrocarbon guests such as methane and ethane occupy structure I cavities, while the larger hydrocarbons, such as propane and iso-butane occupy the larger structure II cavities. Methane hydrate, for example, is a structure I compound with average composition $CH_4 \cdot 5.75\ H_2O$. Methane hydrate undergoes a phase transition to structure H when exposed to high pressures (0.9 – 1.0 GPa).[28] Structure H, which has significantly larger cavities, forms in the presence of larger guest molecules such as some of the heavier components of crude oil in conjunction with a light gas (*e.g.* methane).[8, 29]

The cavities present within clathrate hydrates are supported by the repulsion forces imparted on the water molecules by the guest species.[30] Rodger has argued that such repulsive forces prevent the collapse of the expanded cavities (relative to ice, I_h), and that the attractive dispersion forces are unimportant in this context.[30]

Many inhibition studies involve THF hydrate as a means to test the performance of new compounds. Use of this model hydrate system is due to the low solubility of natural gas within water, in addition to the ease of synthesis. Whilst THF hydrate is known to form a structure II hydrate, further testing may be necessary to ensure the relevance of THF hydrate based model studies and appropriate performance in the field.

1.1.4 Importance to the oil industry

Water is frequently present during the extraction of oil and gas, and due to the close proximity of an abundance of hydrocarbon species it comes as no real surprise that clathrate hydrate species can form within pipelines particularly under the high pressure, low temperature environments such as the sea bed. Figure 1.3shows an example of a pipeline plug,[31] illustrating the true immensity of disruption that may result by the formation of an icy mass in this context. Moreover, pressure build-up behind the pipeline plug is a significant safety concern.

Figure 1.3: Clathrate hydrate plug.[31]

For these reasons, the petrochemical industry continues to research species to prevent, or delay, this kind of large scale clathrate hydrate formation. Broadly, clathrate hydrate inhibitors can be split into two categories; thermodynamic inhibitors (THI) and low-dosage hydrate inhibitors (LDHI).

Traditionally, inhibition has been performed through the addition of methanol or ethylene glycol, thermodynamic inhibitors, which shift the phase boundary for the formation of clathrate hydrates to lower temperatures and higher pressures, preventing hydrate formation in the prevailing conditions in the pipeline.[19] However, while the addition of

thermodynamic inhibitors is successful, large quantities (20 – 50 wt%) of these inhibitors are required for effect.[32] This brings with it significant financial implications, exacerbated by the difficulty in recovering or recycling the inhibitor post-addition. In addition to the treatment costs, transportation costs associated with supplying considerable volumes of THIs to an oilfield site are highly significant. Therefore, industry has shifted the focus to the implementation of LDHIs, which can be added in much smaller quantity (0.01 – 5 wt%) and hence have markedly reduced transportation costs.[33] It is these LDHIs that form the focus of this work.

1.2 Low-dosage hydrate inhibition

LDHIs can be split into two categories; kinetic hydrate inhibitors (KHI) and anti-agglomerants (AA). Broadly, KHIs inhibit the rate of nucleation and growth of clathrate hydrate crystals, while AAs prevent the aggregation of small hydrate crystals into large, pipeline-blocking masses.[32] Within the context of gas pipelines, the application of AAs is not possible since they require a liquid hydrocarbon phase, therefore KHIs are essential in this field context.[32]

KHIs and AAs offer slightly different properties in terms of the degree of subcooling and cloud point, thereby dictating a preference for a particular type of species at a given field site. The subcooling (ΔT_{sub}, Figure 1.4) is an important property for comparing the performance of different inhibitor species, and can be defined as the difference between the hydrate equilibrium temperature and the operating temperature at a given pressure.[32] It is advantageous for a LDHI to have a high subcooling, since this in principle allows lower operating temperatures (as is necessary for extraction in some locations). The cloud point is the temperature at which the inhibitor becomes cloudy in solution due to aggregation, and can often be visually monitored. The clouding out of some polymers is an established phenomenon, with early research studying the cloud-point curves for a series of polymer-solvent systems.[34] Of interest to this work is the cloud point behaviour of aqueous-polyvinylcaprolactam, which undergoes a reversible transition from coil to globular state upon heating.[35] Wu *et al.* used IR spectroscopy to probe changes in the aqueous-poly(lactam) system upon heating above the lower critical solution temperature (LCST).[35] By combining IR spectroscopic data with molecular dynamics simulations, they concluded that above the LCST polyvinylcaprolactam forms a "sponge-like" mesoglobule structure with a hydrophobic core.[35] This globular structure would result in aggregation of the polymer, and expulsion of water, which could be observed as solution clouding.

Of great importance to oilfield considerations is the deposition temperature, this is the temperature at which the inhibitor polymer precipitates out of solution, thereby becoming ineffective. Deposition temperature is typically 5-15 ^{o}C above the cloud point, but can be much higher depending on conditions.[36]

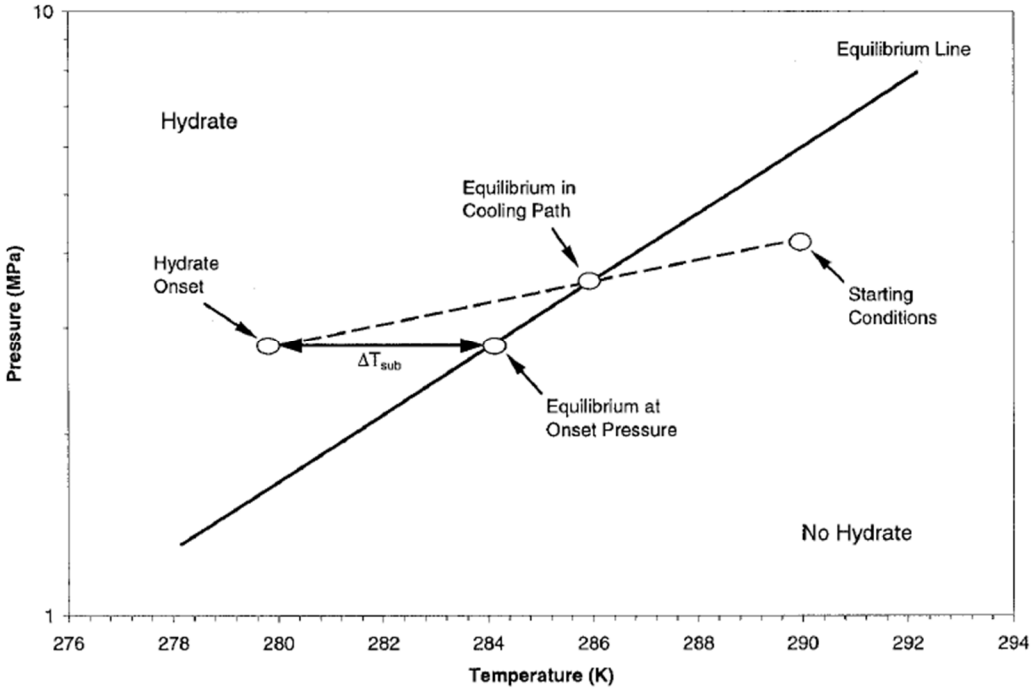

Figure 1.4: The subcooling (ΔT_{sub}) is the temperature difference between the hydrate equilibrium temperature and the operating temperature.[37]

1.3 Kinetic Hydrate Inhibitors

KHIs are water-soluble polymers that can either effectively delay the onset of hydrate nucleation or can delay the growth of hydrate crystals for periods long enough to ensure transport of the fluid without pipeline blockage.[32] This chapter will consider the variety of different KHIs that have been reported, looking at their synthesis, their practical application and proposals for the inhibitors' mode of action. In the oilfield business KHIs are often used in conjunction with synergists, such as 2-butoxyethanol, which are generally added at the same time as the polymer and effectively enhance the performance of the inhibitors. Such synergists will be introduced where their presence is important to the KHI mode of action, however they do not form a primary focus.

1.3.1 Development of KHIs

Nature provides some clues into the kinds of structures that might inhibit the crystallisation of ice and ice-like materials in the form of natural antifreeze proteins. Fish such as Winter Flounder which live in or near to the polar regions possess an interesting mixture of proteins to prevent them from freezing in the often extreme cold temperatures. These proteins fall into two categories (i) antifreeze glycoproteins (AFGP) and (ii) antifreeze proteins (AFP).[38] The proteins exhibit structural features such as a regular array of hydrophilic amino acid residues that are thought to interact with the growing surface of an ice crystal.[39] The ability of antifreeze proteins to prevent the freezing of arctic fish by inhibiting ice crystallisation provokes the question as to whether it is possible to artificially synthesise analogues of such proteins and whether these would exhibit similar antifreeze properties with gas hydrates.[32] The synthesis of glycoproteins has been undertaken and proven to be successful at interfering with hydrate crystal growth, however it did not prove to be an economically viable inhibition methodology.[40] Several studies have been reported which compare the efficacy of AFPs with synthetic KHIs such as poly(*N*-vinyl pyrrolidone) (PVP, **1.1**), indicating that AFPs may hold advantages in prolonging induction periods by having a more pronounced effect upon nucleation.[41] There has been considerable work probing the mechanism of action of AFPs at inhibiting ice growth, reporting a surface adsorption mechanism.[42, 43] The mechanism of action for type-I antifreeze proteins is believed to occur through hydrogen bond formation between four threonine residues with oxygen atoms from the ice lattice.[44] While ice and hydrocarbon hydrates are structurally related, the interactions of AFPs with these species is known to differ.[41] AFPs are known to adsorb to the ice surface and therein prevent ice growth, while the proteins are believed to inhibit the nucleation of gas hydrates.[41, 45] The use of antifreeze proteins for hydrate inhibition is an interesting area, and may offer an exciting alternative, as highlighted by Kelland, Ripmeester and Walker.[41, 45-47]

It was these concepts which led Shell to investigate alternative water-soluble amides in connection with clathrate hydrate inhibition, and the discovery of hydrate inhibition by PVP (**1.1**), independently to the Colorado School of Mines (CSM).[32] PVP was first synthesised in 1939, and has found application as a flocculant and sorbent amongst many others.[48] The clathrate hydrate inhibition activity of PVP was first reported by the CSM in the early 1990s.[49]

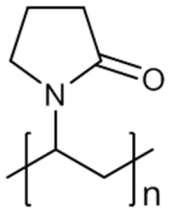

1.1

This polymeric species is particularly appealing due to its low toxicity, thereby reducing any associated risks if accidental pipeline leakage were to occur. Testing of the inhibition properties was completed by CSM through use of a ball-stop rig in which PVP successfully prevented formation of THF hydrate for a period in excess of 24 hours.[49] Ball-stop rig testing is a popular methodology for analysing the inhibition performance of LDHIs; this technique measures the time taken for a metal ball to cease movement when located within a cooled cell containing a hydrate-forming liquid (frequently THF and water in a 1:17 ratio) and inhibitor species.[32] The cessation of ball movement is indicative of hydrate plug formation. Obviously the longer time period over which ball movement is possible, the more efficient the inhibitor is at preventing the plug appearance.

CSM explored the effect of PVP molecular weight upon inhibitor performance, again utilising ball-stop rig testing, and comparing the ball-stop time and induction times for an array of different molecular weight polymers.[50] With a molecular weight of 360,000 the ball did not stop moving throughout the testing period (6 hours).[50] Higher molecular weight polymers are believed to adsorb more strongly to the hydrate surface and hence act as effective crystal growth inhibitors.[51] However, it has also been shown that low molecular weight PVP has a more pronounced effect on perturbing the water structure, and hence has a greater effect upon gas hydrate nucleation.[51] So it seems that regardless of the molecular weight chosen, PVP is able to function to some extent as a KHI. As a result of its efficacy, PVP is now commercially available and is sold in large quantities by Ashland Inc. and BASF, amongst others.[52]

As discussed in Section 1.1.3, the cavities of clathrate hydrates possess some pentagonal faces (5^{12}) and it has been speculated that a 5-membered ring upon a polymer backbone might enable optimum interaction with clathrate hydrate pentagonal faces and hence prevent these faces from participating in the formation of a larger clathrate hydrate mass.[53] However, it is difficult to see the logic in such an idea since it does not explain the efficacy of seven-membered caprolactam KHIs and even pyrrolidone derivatives do not

possess five-fold symmetry because of the presence of the carbonyl group and polymer backbone.

Whilst this first generation inhibitor species (PVP) is effective at a temperature of 285.6 K, upon reducing the temperature to 277 K the inhibition performance is exceeded by the use of second generation inhibitors such as polyvinylcaprolactam (PVCap, **1.2**), and a terpolymer of vinyl pyrrolidone (VP), vinyl caprolactam (VCap) and dimethylaminoethyl methacrylate (**1.3**, marketed commercially as Gaffix VC-713).[54] Inhibition performance can be monitored and compared through use of high pressure apparatus in which gas consumption indicates hydrate formation (an increased gas consumption is indicative of hydrate formation and therefore an ineffective inhibitor).[54] Inhibitors **1.2** and **1.3** are found to have significantly reduced gas consumption relative to **1.1** (when analysed at 277.2 K), and are therefore promising for industrial application.[54]

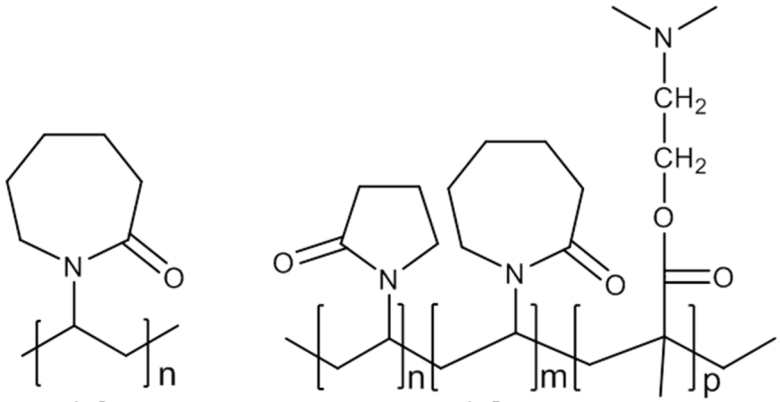

As a continuation of their work in this field, CSM investigated the inhibition properties of **1.3** which at the time was being synthesised for alternative application within the hair-care industry.[32, 55] The optimal composition for polymer **1.3** is reported as: VCap (65-80 wt%), VP (17-32 wt%) and dimethylaminoethyl methacrylate (3-6 wt%).[56] Ball stop testing of the inhibition performance using an aqueous solution containing sodium chloride (3.5 wt%), THF (20 wt%) and polymer **1.3** (0.5 wt%) at 0 ^{o}C showed no hydrate formation during the 8 hours of monitoring.[53] Inhibitor **1.3** is reported as having a subcooling of 8-9 ^{o}C.[8]

It has been suggested that the inclusion of a small non-cyclic organic group such as dimethylaminoethyl methacrylate may further enhance the inhibition properties by providing an additional group to which “free” water molecules may cluster.[55] If the water molecules are

clustered around the inhibitor pendant arm, this would reduce the likelihood of their being incorporated into a hydrate mass, thereby enhancing the inhibitor performance.

The improvement in inhibitor performance on including the vinyl caprolactam component led to the exploration of the performance of the homopolymeric species, PVCap, which has since become an industry leading inhibitor.[32] PVCap can be prepared by the addition of a monomer premix of vinyl caprolactam with di-*t*-butyl peroxide initiator to pre-heated 2-butoxyethanol at 150 ^{o}C, with the later addition of further di-*t*-butyl peroxide.[57] This synthetic methodology is used for the production of low molecular weight polymers (MW 500 – 2000). Carrying out the polymerisation in a mixture of 2-butoxyethanol and water (80 : 20), at a pH of 8-12, enables the formation of PVCap with molecular weight 500 to 4000.[58] Alternatively, a significantly higher average molecular weight (2.1×10^4) can be achieved through use of azobisisobutyronitryl (AIBN) as the radical polymerisation initiator, with reaction proceeding in isopropanol.[59] Dependent upon the field application there may be preference for a specific molecular weight; with low molecular weight PVCap exhibiting a markedly higher cloud point than the higher molecular weight analogue.[60] In warmer waters, such as the Gulf of Mexico, the inhibitor cloud point can be a significant concern, and as such high cloud point inhibitors are an active area of research (*vide infra*). PVCap is a thermoresponsive polymer undergoing a phase transition to globules at its lower critical solution temperature of 31 – 38 ^{o}C.[61] At lower temperature, however, it is a very efficient and effective hydrate inhibitor, and is now the industry standard to which new KHIs are compared.

Within PVCap the oxygen atom of the lactam group possesses a significant negative partial charge of approximately -0.4[59] making this functional group a good hydrogen-bond acceptor. As a result, the polymer is expected to interact strongly with water and this interaction has been implicated in the mechanism of hydrate inhibition by this species. Hydrogen bond formation, between the C=O of PVCap and water, was confirmed by IR spectroscopy and results in a considerable shift in the frequency of the carbonyl stretching mode (*vide infra*).[59] Comparison of the carbonyl stretching band for PVP *versus* PVCap (1685 *vs.* 1640 cm^{-1})[59] suggests that PVP has more carbonyl double bond character whilst PVCap shows greater enolate character. The greater carbonyl double bond character in PVP results from the increased strain within the 5-membered ring. The carbonyl oxygen atom within PVCap is a particularly good hydrogen-bond acceptor due to the greater contribution to the enolate resonance form as a result of the less strained 7-membered ring.[62]

Lederhos *et al.* carried out comparative KHI testing on PVP, PVCap and **1.3** in an attempt to evaluate KHI performance.[54] Their work initially used a ball-stop rig and subsequently a high pressure autoclave with gas consumption an indicator of hydrate formation using a typical Gulf of Mexico natural gas mixture.[54] Their research found that performance was affected by high pressure, low temperature and inhibitor concentration.[54] Whilst terpolymer **1.3** and PVCap were found to perform well at moderate pressures (6.89 MPa) performance at higher pressures (10.3 MPa) was significantly reduced.[54] Copolymers of VP/VCap were also studied, showing that when the ratio of VP/VCap is equal to or less than 1:3, copolymer inhibitor performance is equal to that of PVCap or **1.3**. This suggests that it is reasonable to speculate that the caprolactam ring is crucial for inhibition properties.[54]

Within the literature there is report of a potential problem with dissolving in water a polymer containing an organic ring functionality in that the presence of this hydrophobic residue enhances the probability of polymer self-association as opposed to effective interaction of the polymer with liquid water or the growing clathrate hydrate crystal surface (as would be desirable for inhibition).[55] If the polymer molecules self-associate then this will likely reduce their efficiency as inhibitors by restricting the dispersion of the polymer within solution. Moreover, some polymers may adopt a compacted form in water. In order to prevent transition to this compacted conformation, it has been proposed that modifications to the polymer to provide steric hindrance may ensure that the extended conformation is maintained.[55] Alternatively, there is report of the inclusion of ionic groups, which, through enhancing charge repulsions, may also prevent the transition to the compacted form.[63]

The efficacy of PVCap is further enhanced through the use of synergists, which are believed to work in conjunction with the polymer. There are several reports as to the use of quaternary ammonium or phosphonium salts such as tetrabutylammonium bromide (TBAB) and tetrapentylammonium bromide (TPAB) as crystal growth inhibitors for structure II hydrates when used in conjunction with PVCap.[32, 64, 65] Inhibition enhancement is believed to result from the differing geometries of PVCap and TPAB (or TBAB) enabling attachment at different hydrate crystal sites.[32, 64, 65] Kelland and co-workers postulated that the pentyl group of TPAB is perfectly sized to embed within a cavity on the hydrate surface and hence hinder hydrate growth, with reduced synergistic performance found for analogues containing *n*-hexyl or *n*-propyl pendant arms.[64, 65] In addition to acting as KHI synergists, quaternary salts can function as anti-agglomerants upon transformation into surfactants, *vide infra* (Section 1.7).[64] Recently, there has been report of the use of tetra(iso-hexyl) ammonium bromide

(TiHexAB, **1.4**), which shows improvement in slowing THF hydrate growth rate in comparison to TBAB and TPAB, and is believed to be the most powerful synergist and crystal growth inhibitor studied to date.[64] Combining TiHexAB with PVCap results in an average hydrate onset temperature of 4.3 °C, as measured through use of a rocker rig (at a concentration of 2500 ppm of PVCap and 2500 ppm TiHexAB) which is an improvement of 9.2 °C and 5.6 °C for PVCap plus TBAB and TPAB, respectively.[64]

The use of PVP (5-membered lactam ring) and PVCap (7-membered lactam ring), provokes the question as to the performance of polyvinyl piperidone (PVPip, **1.5**) which contains a 6-membered ring. Unfortunately, the vinyl piperidone monomer is not currently readily available commercially which limits studies on PVPip. However, recently O'Reilly *et al.* have compared the relative performance of all three poly vinyl lactam species at inhibiting structure II hydrate formation.[51] It was concluded that PVPip functions as a clathrate hydrate inhibitor with efficacy intermediate between PVP and PVCap, with PVCap being the most effective of the three. As a result further research into PVPip seems to be of low priority.[51]

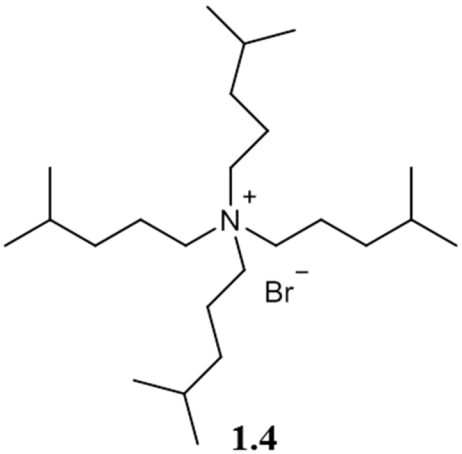

1.4

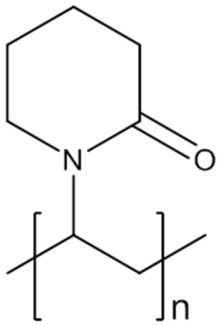

1.5

As established earlier, the inclusion of small organic functionalities upon the polymer backbone, alongside lactam groups, may further enhance inhibition performance. To this end, the inhibition behaviour of the copolymer of *N*-methyl-*N*-vinylacetamide (VIMA) and VCap (or VP), labelled **1.6** and **1.7** respectively, was explored.[66] Synthesis of the VIMA/VCap copolymer can be achieved by heating a reaction mixture comprising VIMA, VCap and AIBN in ethanol, at 78 °C for 8 hours.[66] Inhibition testing (using a mini-loop system) of copolymer **1.7** showed an improvement in subcooling relative to PVCap, whereby PVCap has a subcooling of 12.4 °C and P(VIMA/VCap) (3:1) has a subcooling of 14.7 °C.[66] This confirms the synergistic effect of VIMA upon VCap.

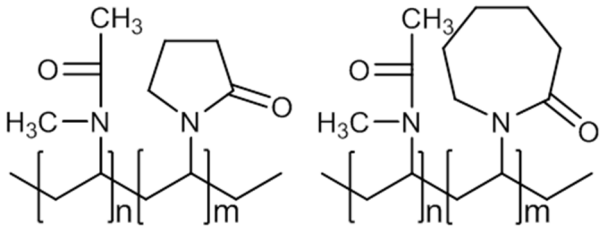

1.6 **1.7**

Copolymeric inhibitor **1.7** was found to successfully prevent hydrate formation in the oil flowlines of the West Pembina Field, Canada.[67] This field application nicely highlights the significant economic advantage upon switching from THIs to KHIs. Originally, 130 – 260 gallons of methanol were used at this site per week in order to prevent hydrate plugging.[67] In contrast, only 0.5 gallons of KHI are required each day for inhibition. This significant reduction in the quantity of inhibitor required will impart a reduction in costs, and should make this the economically advantageous choice. A comparison of the approximate cost of different inhibitors at the West Pembina Field is detailed in Table 1.1.[67]

Inhibitor	Dose rate (gal per day)	Chemical cost (C$ per day)
Methanol (130 litre batch treatment every 3 days)	43	68.50
Methanol (calc. requirement for continuous injection)	34.6	53.67
KHI **1.7**	0.5	< 20

Table 1.1: Economic comparison for costing of different inhibitors at the West Pembina Field.[67]

Prior to industrial use, copolymer **1.7** is mixed with a carrier solvent to ease with application. This premix carrier solvent is generally water or methanol, dependent upon the likely operation temperatures. There is a preference for the use of water as this reduces the safety implications for the handling and storage of the inhibitor species.[68] Whilst **1.7** may appear to be the ideal KHI, unfortunately, due to difficulties in obtaining the VIMA monomer, this copolymer is no longer commercially available.[32]

On a similar theme, Exxon postulated that the presence of amide functionality attached to a hydrophobic group is integral for KHI performance.[32] This led to the investigation of several polyalkylacrylamides and polydialkylacrylamides.[32] Good inhibition performance was found using polyacryloylpyrrolidine (polyAP, **1.8**), polydiethylacrylamide (polyDA, **1.9**) and polyisopropylacrylamide (polyIP, **1.10**).[32] Since then, a broad range of polyalkylacrylamides of type **1.11** have been explored and patented.[69]

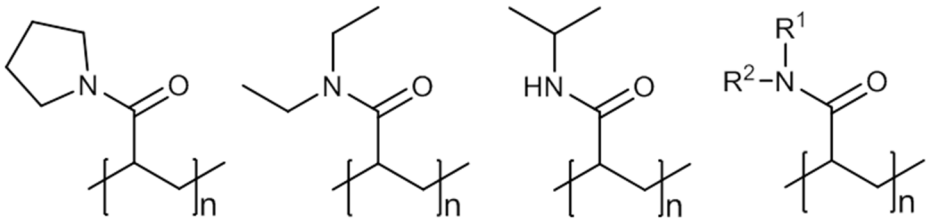

1.8 **1.9** **1.10** **1.11**

Kelland proposed the mode of action of the polyalkylacrylamides to be similar to that of PVCap or PVP, whereby there is interaction between the hydrate surface and the pendant groups on the inhibitor.[36] The alkyl groups are believed to fit within available cavities on the hydrate surface while the carbonyl group hydrogen bonds to the surface.[36] The cloud point (T_{cl}) of a KHI is a significant consideration prior to selection; it is advantageous for an inhibitor to have an increased cloud point as this will enable application of such species in field sites such as the Gulf of Mexico wherein the high temperatures may otherwise circumvent the use of low T_{cl} inhibitors. Copolymer **1.8** was found to have an appreciably higher T_{cl} than PVCap, as shown in Table 1.2.[36]

Inhibitor	M_n	T_{cl}/°C in DI H_2O	T_{cl}/°C in 3.6wt% SSW
1.2	1300	33	30
1.3	4500	33	30
VP/VCap	4000	70	60
1.7	2000	74	62
1.8	1200	60	53

Table 1.2: Cloud points for an array of different inhibitor species. SSW is the acronym for Synthetic Sea Water.[36]

The results from sapphire cell testing indicate that polyAP and polyIP are particularly promising KHIs, with some showing performance to equal or exceed that of the PVCap tested.[36] However, it is worth noting that inhibitor performance was found to be largely dependent on the polymer molecular weight.[36] Additionally, blending a large amount of low MW alkylacrylamide polymer with small amounts of PVCap was found to significantly improve hydrate induction times.[36] More recently, Mady *et al.* have developed copolymers of dimethylhydrazidoacrylamide and polyIP, and found these to have pleasing KHI performance, and excellent cloud points.[70]

Analysis of inhibitor performance is commonly conducted using sapphire cell testing or the use of mini-loop systems. Sapphire cell testing requires an arrangement comprising

sapphire cells (manufactured using sapphire crystals), a cooling bath and a data centre, and simulates a North Sea well stream through use of synthetic natural gas, condensate and synthetic sea water.[71] Figure 1.5 shows the general arrangement for sapphire cell testing.[36] In contrast, the mini-loop system comprises stainless steel tubing through which fluid (often synthetic sea water with hydrocarbon condensate) is circulated.[66] Inhibitor species are injected as an aqueous solution into the fluid.[66] The loop is placed in a water bath, wherein the temperature is reduced at a constant rate to test for hydrate formation.[66] The system is carefully monitored for any changes in temperature or pressure, as indicators for hydrate formation.

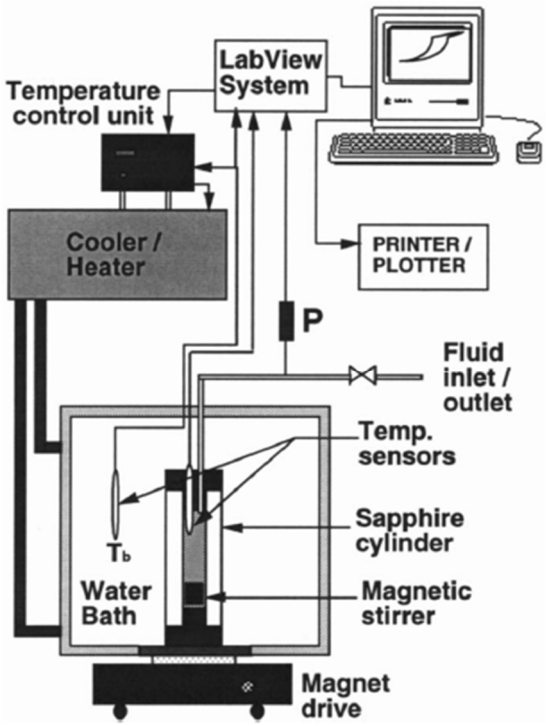

Figure 1.5: Sapphire cell testing equipment as illustrated by Kelland *et al.*[36]

As a further development for the synthesis and testing of vinyl(lactam) copolymers, a copolymer comprising 80-95 wt% VCap and 5-20 wt% *N,N*-diethylaminoethyl(meth)acrylate (DEAEMA) (**1.12**) was examined.[72] Most notably, the copolymer comprising 13 wt% DEAMA was found to inhibit hydrate formation for a period in excess of 24 hours.[72] This copolymer is synthesised through the addition of di-*t*-butyl peroxide (initiator) into a mixture of VCap and DEAMA in 2-butoxyethanol. The reaction mixture is purged with nitrogen throughout and heated to 150 ^{o}C, with the addition of further boosts of initiator to yield the desired

product.[72] Alongside a maximum subcooling of 10.5 °C, copolymer **1.12** also has corrosion inhibition properties and is commercially available.[72]

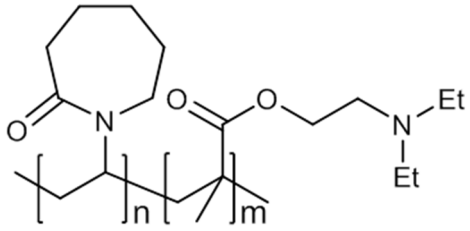

1.12

The employment of synergists has allowed further optimisation of KHI performance. The use of glycol ethers is common, in particular 2-butoxyethanol (butyl glycol ether), although an array of glycol ethers comprising at least three carbon atoms in the alkoxy group result in a significant improvement in performance with respect to terpolymer **1.3**.[73, 74] The effect that altering the solvent may have upon inhibition was clearly shown by Young and coworkers who conducted a study using gas consumption as the indicator of the extent of inhibition (reduced gas consumption implies good inhibitor performance as less hydrate has formed).[74] Their research used synthetic sea water and Green Canyon gas to assess the performance of PVCap in ethanol *versus* 2-butoxyethanol.[73, 74] A significant reduction in gas consumption resulted when using only 0.3 wt% 2-butoxyethanol in comparison to 0.75 wt% ethanol, as shown in Figure 1.6.[73, 74]

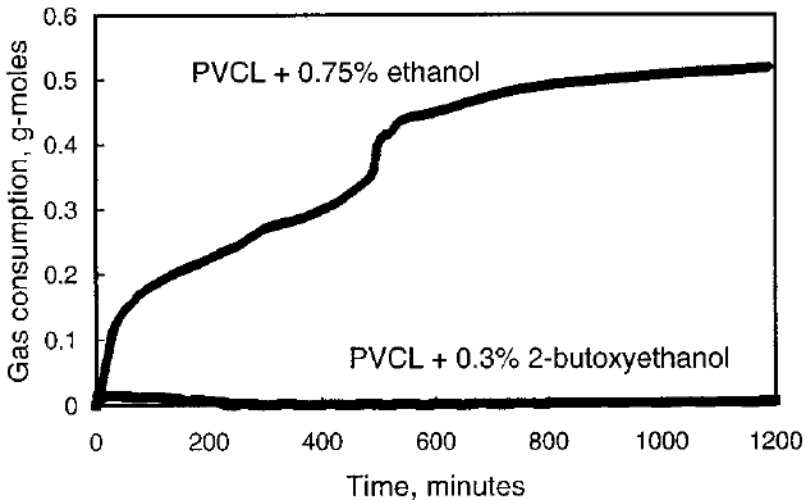

Figure 1.6: Gas consumption comparison for PVCap plus ethanol (0.75 wt%) *versus* 2-butoxyethanol (0.3 wt%) measured at 4 °C, 1000 psig in 3.5 wt% sea saltwater.[73]

As alternative KHIs (and also AAs) Shell has patented the use of an array of hyperbranched poly(esteramide)s, such as **1.13**, which are trademarked and commercially available under the name of HYBRANES.[75, 76] These species possess a common functionality, in that they each have at least one hydroxyalkylamine end group. Species of this type can typically be synthesised through the self-condensation of a cyclic anhydride with a dialklanolamine.[76, 77] Similarly to the application of vinyl lactam inhibitors, it is generally only necessary to use between 0.5 and 3.5 wt%, with the application of such species being either as a dry powder, or more commonly as a concentrated solution.[77] The amide groups are expected to form hydrogen bonds with the hydrate crystal (as suggested for vinyl lactam polymers) whilst the hydrophobic functionality will form van der Waals interactions with the surface.[32] Overall, the cumulative effect of the hydrogen bond and the van der Waals interactions offers a qualitative explanation for the mode of action of these species as KHIs and results in the retardation of the crystal growth rate. Studies on THF hydrate indicate that inhibition is not an inherent property of these compounds, and that inhibitor performance is dependent upon the size of the hydrophobic groups.[77] When considering the size of the structure II cavities in THF hydrate, the efficiency of an inhibitor may depend in part upon the ability of such a polymer to fit within the hydrate cavity.[77] Optimal inhibition results are obtained from a hyperbranched polymer comprising isobutyl groups attached to the 2-carbon of the succinyl units.[77] Test results for the inhibition of THF hydrate show that whilst the investigated poly(esteramide)s do function as KHIs (efficiency being size dependent), complete inhibition is not achieved, even when used in high concentration.[77]

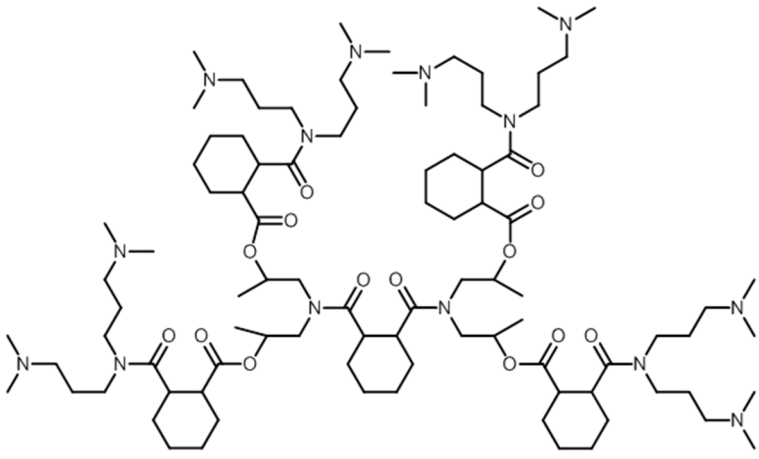

1.13

1.4 Most recent developments in KHIs

Whilst the use of PVCap is industry leading due in part to the long hydrate induction time and economic benefits in comparison to thermodynamic inhibitors, there is still room for further development in improving the biodegradability and performance under extremes of salinity and temperature. Issues such as the salt and temperature tolerance become significant on application of KHIs in challenging environments such as high salt conditions, or in the warm waters as found in the Gulf of Mexico. The deposition temperature and cloud point may be crucial considerations as the clouding out of the inhibitor will result in reduced performance and may leave the system vulnerable to plugging. As a result of these additional considerations, recent research has resulted in a number of next generation lactam type KHIs that address these industry drivers.

In recent years strict regulations have been imposed with regard to the biodegradability required prior to large-scale application of an inhibitor. The restrictions posed for application in the North Sea can be split into three categories:[78]

1. Green: >60% degradability in 28 days
2. Yellow: 20-60% degradability in 28 days
3. Red: <20% degradability in 28 days

Clearly, it is desirable to produce an inhibitor possessing green category biodegradability (>60%), but there is a fine balance with altering the properties to achieve green status without compromising on KHI performance. Recent work at Ashland Inc. has resulted in the development of new polymeric inhibitors offering performance similar to that of PVCap whilst also possessing improved biodegradability. One such species is a copolymer of PVCap with polyvinyl alcohol (VOH) (**1.14**), as developed by Musa and co-workers.[79] This copolymer exhibits an induction time in excess of two days and has a subcooling of 10.5 ^{o}C, as tested using an autoclave with Green Canyon gas.[79] Synthesis of **1.14** proceeds *via* a two-step reaction process; involving firstly the synthesis of a copolymer of VCap and vinyl acetate, and subsequently the hydrolysis of this intermediate to yield inhibitor **1.14**, as shown in Scheme 1.1.[79] A variety of solvent systems have been trialled for the copolymer synthesis, including methanol/water, 2-butoxyethanol/water, 2-butoxyethanol and IPA/water, all yielding a copolymer comprising 82% VCap and 18% VOH.[79] In all cases an induction time in excess of 2800 minutes resulted at a low inhibitor dosage (0.3-0.6%).[79] In addition to this high performance, the inclusion of the alcohol functionality enables improved biodegradability

relative to the PVCap homopolymer. Biodegradability testing of inhibitor **1.14** as supplied to site (within 2-butoxyethanol) reports an impressive 76% in 28 days.[79]

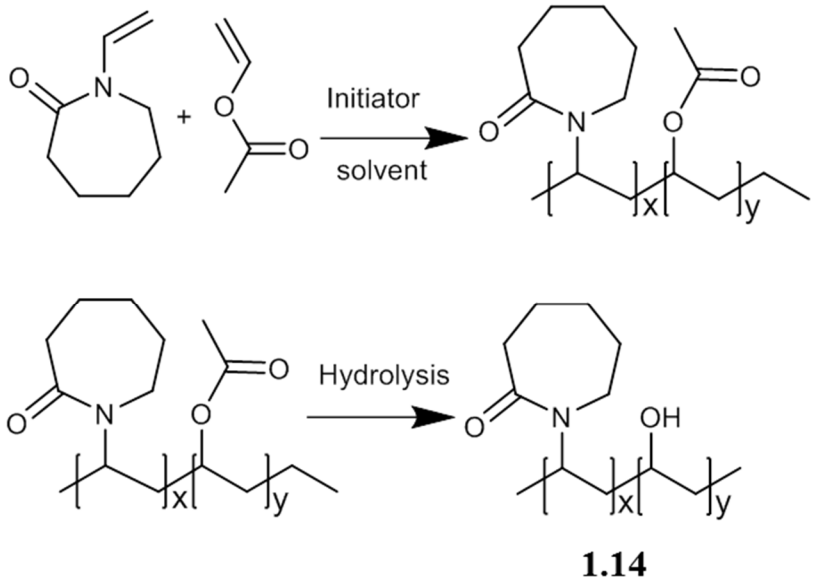

Scheme 1.1: Synthesis of PVCap/VOH copolymer (**1.14**)

Incorporation of a hydrolysable ester linkage was found to further enhance the biodegradability of the polymer, as seen with the copolymer of VCap and hydroxyethylmethacrylate (VCap-HEMA) (**1.15**).[79] A composition of 95% VCap and 5% HEMA results in a high subcooling (9.5 – 10.5 ^{o}C) with induction times in excess of 48 hours.[79] The inclusion of the alcohol functionality in compound **1.15** allows for post-modification of the compound in order to meet specific demands, for example with the grafting of poly(lactide) onto **1.15** to formulate an inhibitor with an extended pendant arm (**1.16**).[80]

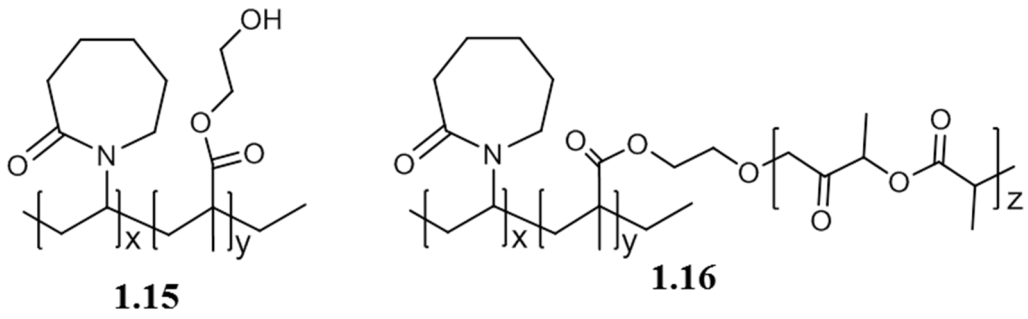

Polyaspartamides are an alternative polymeric inhibitor believed to possess improved biodegradability, high cloud point and good inhibition performance.[81] Such inhibitors can be synthesised by the ring opening of polysuccinimides using alkylamines, an example of such is shown in Scheme 1.2.[82] More specifically, polyaspartamides comprising 75 – 80% isobutyl

groups and 20 – 25% methyl groups were found to have good inhibition performance and exhibit good average hydrate induction times.[82] However, while this species does have some desirable biodegradability (>20% in 28 days) the inhibition performance is exceeded by vinyl lactam KHIs.[82] More recently, it has been noted that incorporation of a high percentage of isopentyl groups is advantageous to the inhibition performance, although this does also require the inclusion of minor amounts of very hydrophilic alkylamines to circumvent water-insolubility issues.[81] While there is still room for further improvement in the inhibition performance to exceed that of currently used lactam KHIs, these results seem very encouraging.

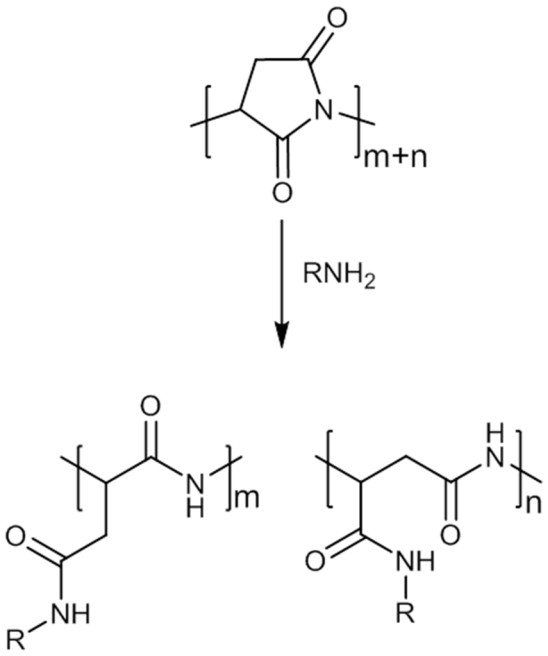

Scheme 1.2: Synthesis of polyaspartamides from polysuccinimide.

Within the oil and gas industry, scale inhibitors (SI) and corrosion inhibitors (CI) are frequently added to pipelines in addition to KHIs. Some polyaspartamides/polyaspartates will act as inhibitors for both carbonate and sulphate scale in addition to functioning as a KHI, therefore use of inhibitors such as **1.16** may circumvent the need for the addition of two inhibitor species with differing functionalities to the pipeline.[81] Such dual functionality may increase the benefits with use of such as polymer, although this area is still awaiting further clarification of performance.[81] In addition, there has been report of the potential problems with the addition of both a KHI and a CI, in that the combination may reduce the KHI performance due to an incompatibility of some CIs in conjunction with a KHI.[83]

Combining corrosion inhibition with KHI performance has been achieved in copolymers comprising both vinylcaprolactam and phosphoric acid functionality, as in inhibitor **1.17**.[84] This copolymer exhibits a high subcooling (10.5 °C at a temperature of 7 °C) with a hydrate induction time of >48h. Synthesis of **1.17** occurs *via* a two-step reaction in 2-butoxyethanol/water according to Scheme 1.3.[84]

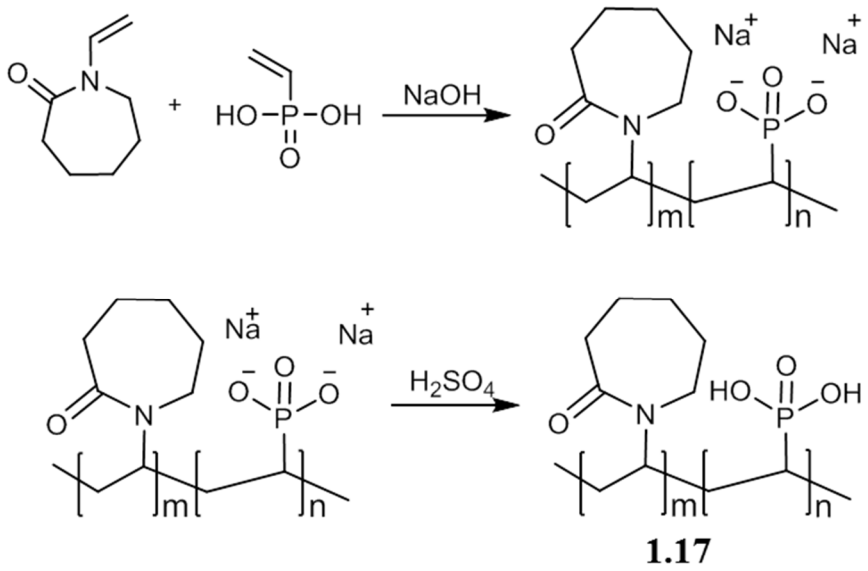

Scheme 1.3: Synthesis of vinylcaprolactam phosphoric acid copolymer (**1.17**).[84]

As gas and oil extraction moves deeper and further afield, industry has seen an increased demand for KHIs with improved salt tolerance and improved tolerance when subjected to a high injection temperature. If a polymer has little temperature tolerance it may precipitate out of the solution upon injection, thereby reducing performance. PVCap has a cloud point of 40 °C, but a cloud point in excess of 70 °C is required for some field applications. Musa and coworkers have reported a terpolymer (**1.18**) of PVCap/PVP and 2-acrylamide-2-methyl-1-propane sulfonate (AMPS) which possesses an increased salt and temperature tolerance.[85] Inhibitor **1.18** contains vinyl lactam functionalities to provide KHI performance, whilst the incorporation of the AMPS groups increases the water affinity of the polymer and enables high salt tolerance to be achieved. At a polymer dosage of 0.5 % this terpolymer was found to prevent gas hydrate formation for in excess of 48 hours at a subcooling of 10.3 °C, representing excellent performance for a low dosage.[85] Testing of the salt and temperature tolerance conclude that a maximum injection temperature of 85 °C can be reached without polymer precipitation whilst using a 15 wt% brine solution.[85] In addition to high performance in seawater, this terpolymer possesses a cloud point of 89 °C for fresh water sites.[85]

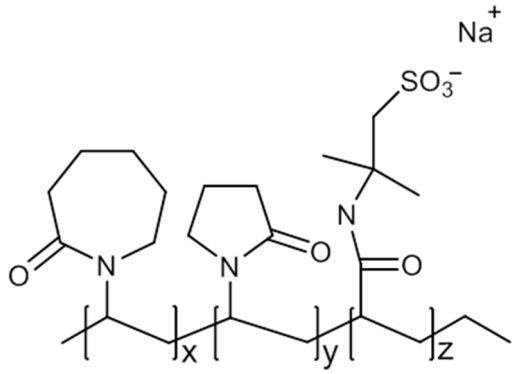

1.18

The high cloud point criterion is also achieved by a terpolymer comprising *N*-vinyl formamide (20%), VCap (50%) and VP (30%) (**1.19**).[86] Synthesis within ethylene glycol yields an alternating or block copolymer having a molecular weight between 500 and 5 000 000 amu. Inhibitor **1.19** has a high cloud point of 89 °C in addition to good KHI performance (induction time >48h at a subcooling of 10.3 °C).[86]

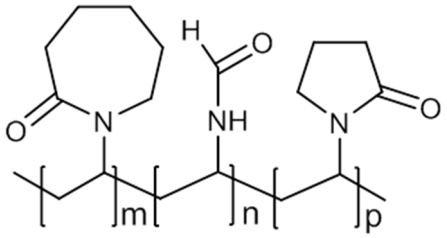

1.19

In the knowledge that PVP successfully functions as a KHI, Kelland and coworkers examined the inhibition performance following inclusion of alkyl functionalities on the pyrrolidone ring, for species as shown in the general structure **1.20**.[87] Of the polymers examined in their work the best KHI performance was found for the 1:1 *n*Propyl-VP/VIMA copolymer.[87] However, due to complexities associated with the large-scale synthesis of alkylated PVPs such copolymers are not currently commercially available.

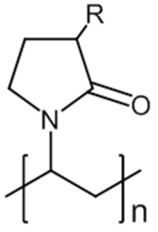

1.20

Kelland and co-workers noted that the KHI performance of *N*-vinyl lactam polymers increased as lactam ring size increased, with PVCap showing better performance than PVP and PVPip (as discussed in Section 1.3.1).[88] In order to examine this trend further, the group have recently studied the behaviour of the 8-membered lactam ring polymer, poly(*n*-vinyl azacyclooctanone) (PVACO) (**1.21**).[88] High pressure rocking cell experiments indicated that the 8-membered analogue exhibited better KHI performance than the smaller ring species, when comparing the inhibition behaviours of similar molecular weight polymers.[88] However, the cloud point of PVACO is low, ranging from 15-24 ^{o}C dependent on polymerisation methodology, which may limit the viability of industrial application.[88] In an attempt to overcome the low cloud point issue, work is reported into the behaviours of VIMA/VACO copolymers, on the basis that incorporation of the hydrophilic VIMA monomer may increase the cloud point.[89] It was found that the 1:1 VIMA/VACO copolymer exhibited better KHI performance than homopolymer **1.21**, while also having a higher cloud point.[89] While the initial studies of these species are encouraging, unfortunately the lack of commercial availability of the VACO monomer is currently limiting further work in this area.

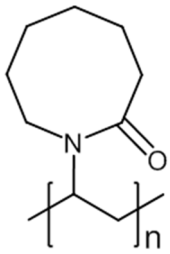

1.21

Finally, recently a variety of work has been reported regarding the development and inhibition analysis of several novel non-lactam based polymers including poly(β-peptoid)s[90], poly(fluoroalkylacrylamide)s[91], poly(*n*-alkylglycine)s[92] and pol(vinylphosphonate) diesters[93]. Such research generally compares the inhibition performance to that of the traditional lactam KHIs, showing reasonable inhibition performance, in addition to some specific high performing examples. Work reported to date appears to be only the very start of the exploitation and development of novel non-lactam based KHIs, however the performance analysis is encouraging.

While there are several polymeric species showing great promise as the KHIs of the future, in many instances the commercial availability and complexities associated with synthesis are limiting progress in this area. With the industrial focus on the development and optimisation

of KHIs it is anticipated that a multitude of inhibitors will continue to be developed, particularly to meet the increasingly demanding conditions and regulatory requirements.

1.5 Formation mechanism of clathrate hydrates

Clathrate hydrate nucleation and growth has received considerable attention in recent years, both from a thermodynamic and kinetic perspective. A full understanding of the formation process will enable insight into the inhibition mechanisms. In order to introduce fundamental concepts first a brief description of crystal nucleation and growth will be provided, this will be followed by an overview of current mechanistic understanding of gas hydrate formation.

1.5.1 Crystal nucleation and growth

Crystallisation can be defined as the phase change from solution, melt or vapour to the solid phase, and for a solution is achieved through supersaturation. Classically, the formation of a crystal mass (and in this context a clathrate hydrate mass) proceeds *via* nucleation followed by crystal growth.[94] As the solute concentration increases (towards supersaturation) dissolved molecules begin to aggregate, enabling the formation of a critical nucleus; an essential precursor for further growth.[94]

The process of nucleation can be artificially induced (*i.e.* through introduction of crystal seeds, a process termed secondary nucleation) or can occur spontaneously (primary nucleation).[94] In order for nucleation to occur, it is necessary to overcome the interfacial energy barrier, which is the difference between the free energy of the molecule within the bulk ΔG_v and the surface ΔG_s; it has a positive value and in effect represents the instability of the growing, sub-critical nucleus in comparison to liquid or solution phase species.[94] Once the critical size is achieved, the interfacial energy becomes small relative to the bulk crystal energy and hence provides less hindrance to further growth. As a result dissipation of supercritical nuclei is disfavoured and crystal growth continues until the supersaturation is depleted to the solubility limit. The time taken for the formation of a critical size nucleus is known as the induction time. The free energies associated with this process are plotted in Figure 1.7, which shows the free energy associated with achieving a nucleus of critical size, and the energetic favourability of growth once the critical radius has been met.[95] It is worth noting that despite nucleation being a vital process, in reality it is an extremely rare event due to the diminishingly small critical nucleus concentration.

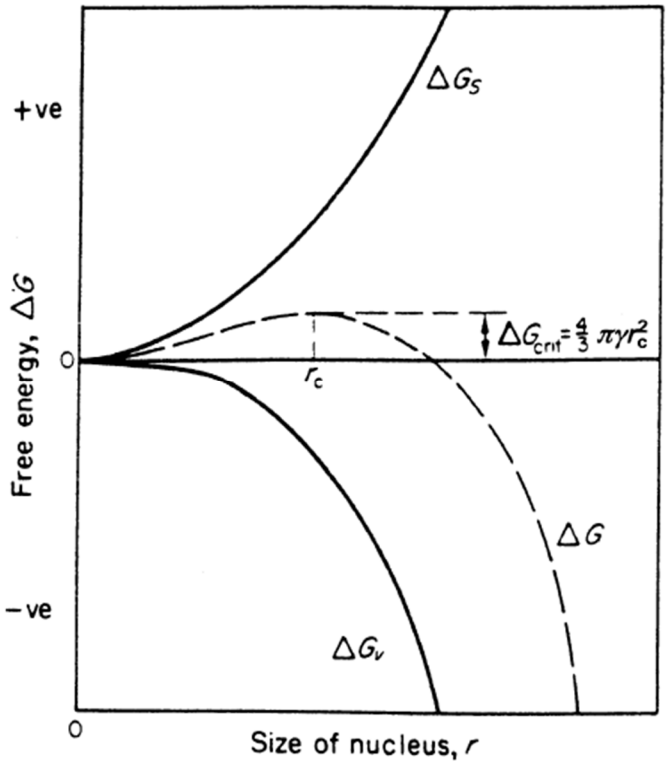

Figure 1.7: Gibbs free energy of a crystal nucleus as a function of particle radius.[95]

While homogeneous nucleation can occur in ultrapure systems, there have been reports as to the difficulties in achieving such a pure system.[8] In fact, heterogeneous nucleation is far more commonly encountered, on substrates such as a surface (*e.g.* pipe wall) or foreign body (*e.g.* a dust particle).[95] Kashchiev and Firoozabadi examined the kinetics of gas hydrate nucleation (both heterogeneous and homogeneous nucleation), and the effects of inhibition additives upon nucleation pathways.[96]

Following nucleation, crystal growth can occur by the diffusion and incorporation of growth units or "building blocks" onto the critical nucleus surface.[94] There are two proposals for the site of crystal growth, these being the Terrace-Ledge Kink theory or growth at screw dislocation sites.[94] The Terrace-Ledge Kink theory (also known as the Kossel-Stranski model) assumes the pre-existence of steps on a crystal surface, whereby it is preferable for maximisation of contact sites. The kink site is most preferable for the growth of the crystal, as this provides the site with the highest degree of coordination to an incoming growth unit and therefore imparts the greatest stability.[94] A plausible source of steps and kinks is through the formation of dislocations (many dislocations may pre-exist on crystal surfaces due to their imperfect nature).[94] Screw dislocations result in a spiral growth pattern and are the consequence of atom displacement along the dislocation line.[95]

1.5.2 Gas hydrate nucleation and growth

Clathrate hydrate formation is known to be stochastic (randomly determined), which makes the conclusive determination of a mechanism very challenging. Hydrate nucleation is believed to occur at the water-hydrocarbon interface, as this is the site of the necessarily high concentrations of both guest and host species, thereby making the attainment of a critically sized nucleus more likely.[32, 97] The site of hydrate nucleation was investigated by Long and Sloan in 1996, studying mixtures of deionised water and Green Canyon gas in a sapphire tube.[98] They observed that upon dissolving gas molecules in liquid water, small needles of hydrate crystals formed at the interface (at 277 K and 6.9 MPa); whilst the induction time was not reproducible between experimental runs, the investigation seems conclusive that hydrate nucleation originates at the interface.[98]

Recently, Ohmura and coworkers used videographs to study the growth of crystals at the liquid-gas interfaces for systems containing gaseous methane, ethane or propane.[99] A water droplet was held on a Teflon stage placed within a test cell, wherein the temperature and pressure could be monitored and maintained.[99] The air environment within the test cell was replaced with hydrocarbon gas (*e.g.* methane) and the temperature reduced to promote hydrate formation.[99] By examining the sequential videograph images it was concluded that nucleation occurred at a random point upon the water droplet, and was followed by growth to cover the surface with a polycrystalline layer (Figure 1.8).[99] Additionally, a relationship between subcooling and crystal morphology was observed, with high subcooling resulting in small sword-like crystals, and low subcooling leading to larger polygon crystals.[99]

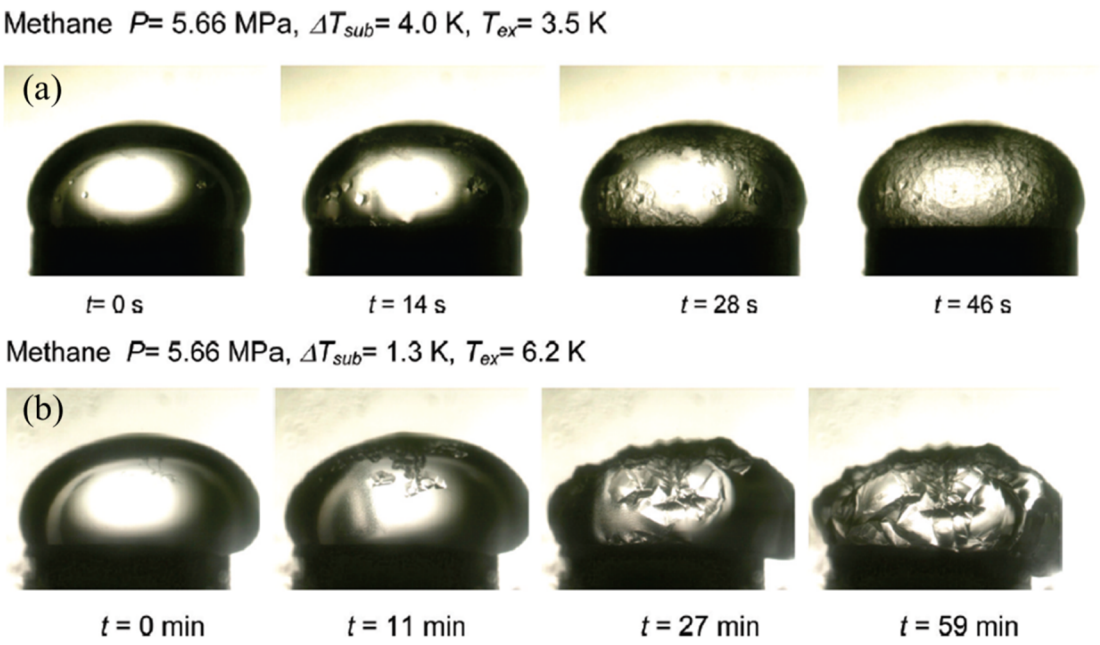

Figure 1.8: Videographs showing the growth of methane hydrate on the surface of a water droplet (a) high subcooling and (b) low subcooling.[99]

There exist several suggestions as to the hydrate nucleation mechanism, including the "labile cluster" hypothesis, interfacial nucleation and local structuring nucleation; these will be addressed in more detail below.

(1) The "labile cluster" hypothesis was proposed by Sloan and Christiansen in 1994, as shown in Figure 1.9.[100] This hypothesis suggests that labile clusters will form immediately upon dissolution of gas molecules (guests) in water at the appropriate temperature and pressure conditions.[100] Such labile clusters are metastable species of below critical size which can either dissipate or agglomerate. Upon agglomeration, and attainment of a critical size, growth of the hydrate may then begin.[100]

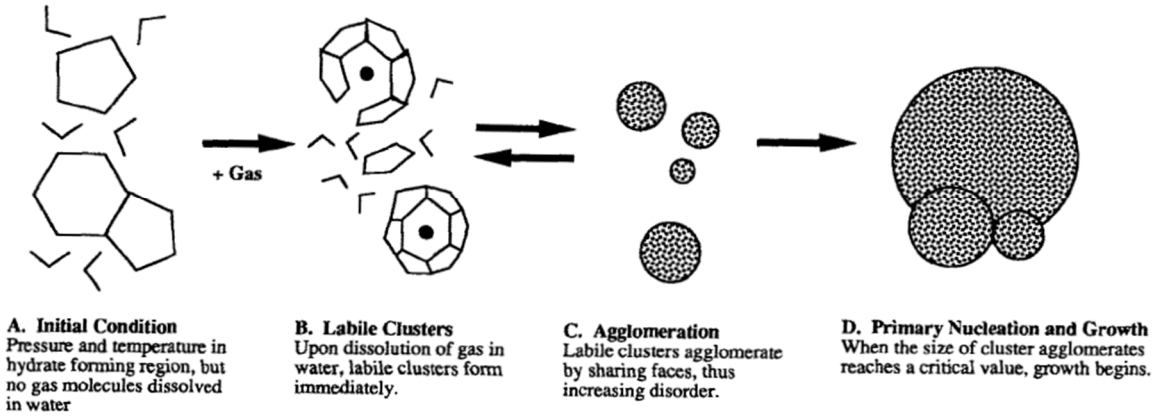

Figure 1.9: Labile cluster hypothesis (reproduced from Sloan and Christiansen)[100]

(2) The interfacial nucleation mechanism hypothesis was proposed by Long and Kvamme, wherein gas molecules are transported to the interface.[8] Surface diffusion allows the migration of molecules to the desired site where cage formation of water molecules can occur.[8]

(3) There are a few reports into the local structuring nucleation postulate, obtained through molecular simulation studies. Baez and Clancy used Molecular Dynamics (MD) to obtain snapshots of the molecular configurations within the bulk phase both during the dissolution of a hydrate crystal and during the growth of a hydrate crystal.[101] More recently, Radhakrishnan and Trout have used Monte Carlo simulations in order to provide further simulated evidence for the local structuring hypothesis, and also to disprove the labile clustering hypothesis.[102] CO_2 hydrate was chosen for study in their work, as this is known to nucleate at the liquid-liquid interface.[102] They found that guest molecules arrange themselves in a configuration similar to the clathrate hydrate, as a result of thermal fluctuation.[102] Consequently, water molecule structuring is perturbed relative to the bulk phase and providing the number of guest molecules is high enough a critical nucleus may be attained, and growth of a hydrate cluster may then result.[102] As a further exploration of this postulate, Moon *et al.* reported MD simulations of methane hydrate nucleation, studying nucleation at the water-gas interface.[103] They observed that at moderate subcooling rapid ordering occurs within 10 ns, with clusters of 280 water molecules.[103]

In further MD studies, Walsh *et al.* examined the nucleation and growth of methane hydrate.[104] They found that following nucleation and growth, the hydrate crystal is believed

to be a combination of structure I and structure II, linked by $5^{12}6^3$ cages.[104] In this simulation, small face-sharing cages (structure II) form initially, but sterics and thermodynamics favours the later formation of the structure I cages.[104]

In situ neutron diffraction has provided insight into hydrate formation, for carbon dioxide hydrate (from deuterated ice),[105] propane hydrate[106] and methane hydrate.[107] Henning *et al.* used neutron powder diffraction between 230-290 K to study the formation of CO_2 hydrate from deuterated ice crystals.[105] Whilst initially fast conversion of ice to hydrate is observed, this is followed by a diffusion-limited stage.[105] H/D isotopic substitution was used in the methane hydrate study in order to probe the environment of dissolved methane molecules, concluding that even within the liquid phase water clusters are formed around methane.[19, 107]

There is a plethora of work investigating whether nucleation of hydrates occurs directly to yield the thermodynamic species or whether it goes *via* a metastable intermediate.[108] Several MD studies have suggested that nucleation proceeds *via* an amorphous intermediate, which then undergoes a solid-solid rearrangement to yield the familiar crystalline clathrate species.[109-111] In contrast, recent work examining multiple MD simulations for methane clathrate hydrate nucleation indicates that nucleation occurs predominantly *via* a set of seven Eulerian cages which can interconvert and form solids with long-range order.[108] The results imply that templates for the exclusive growth of the thermodynamically preferred crystalline phase can form almost immediately upon nucleation.[108]

Once a critically sized nucleus is formed, growth of the clathrate hydrate crystal may proceed. To enable nucleus growth a continuous supply of both water and hydrocarbon gas must reach the growing crystal surface.[97] There have been many attempts to model post-nucleation growth of clathrate hydrates, and several detailed growth models have been developed.[8] In one such model, Englezos *et al.* proposed that clathrate hydrate crystal growth occurs *via* a two-step process: (1) dissolved gas diffuses from the solution bulk to the crystal-liquid interface; (2) gas molecules are adsorbed into the water network therein stabilising the hydrate lattice.[112] Whilst these studies go some way to understanding the nucleation and crystal growth of clathrate hydrates, there is still the need for experimental verification of such results, but due to the stochastic nature of hydrate formation this remains a challenge.[19] A detailed discussion of post-nucleation growth is beyond the present scope and the

interested reader is directed to excellent discussions by Ribeiro and Lage[97] and Sloan and Koh[8] for more information.

1.5.3 Thermodynamics of hydrate formation

Van der Waals and Platteeuw developed the first thermodynamic model for the formation of gas hydrates in 1958, through the use of statistical thermodynamics.[113] Several assumptions were made in the development of their model, including: (1) the gas molecule moves within a spherical cavity; (2) each cavity can only hold one guest molecule; (3) no interactions exist between the guest molecules; (4) guests are small enough so as no distortion to the hydrate lattice results; (5) guest-host interactions are limited to weak van der Waals forces and extend only to the first shell of water molecules surrounding each guest.[113]

Further developments have been made to this thermodynamic model due to slight inaccuracies upon moving away from the ice point of water, however, this model provided the fundamental concepts for further study. Since 1958, there has been a great deal of work into extensions of the van der Waals and Platteeuw model, for example to incorporate multi-component mixtures as in the work of Parrish and Prausnitz in 1972.[114] Also, there has been argument that in order to calculate guest-host interactions, the effects of the second and third shells should be taken into account, along with changes in the cell parameters upon guest binding; both of these concepts were not considered in the original model.[115] The more recent model by Klauda and Sandler removed the assumption of a constant lattice, and uses published Kihara cell parameters to improve the accuracy of predictions.[115]

1.6 KHI mode of action

The mode of action of KHIs is a subject of much debate and current research and presumably depends to a considerable extent on the particular KHI in question. While the mode of action of kinetic inhibitors is not currently fully understood, there are a number of interesting reports concerning the solvation of KHIs, and their mode of interaction with a growing clathrate hydrate crystal surface that shed some light into plausible inhibition mechanisms. Broadly speaking there are three proposed mechanisms for the inhibition of clathrate hydrates, namely:

(1) Adsorption of the inhibitor onto the growing crystal surface
(2) Binding to a pre-critical nucleus preventing it from reaching critical size
(3) Structuring of water molecules in order to prevent nucleation.

A plethora of techniques are used in order to gain insight into gas hydrate nucleation and growth, and also as to the potential mode of action of KHIs on the macroscopic and microscopic scale.[31, 116, 117] There have been several recent developments in this area, with the introduction of high-pressure powder X-ray diffraction (PXRD),[118] NMR and high-pressure calorimetry[119] to probe inhibition using chemical KHIs or anti-freeze proteins by enabling characterisation of resulting gas hydrate phases.[117] To enable the close simulation of pipeline conditions, Englezos and coworkers have recently reported the development of a small-scale stirred reactor, which allows for the study of nucleation and decomposition of mixed gas hydrates when using KHIs or AFPs, whilst providing a more "real-world" environment.[120]

1.6.1 Macroscopic studies of KHIs

One theory, favoured by many, is that pendant functionalities upon KHIs enable the adsorption of the inhibitor to the growing crystal surface, generally through hydrogen bonding. Following adsorption, the hydrophobic backbone of the polymer will effectively restrict further hydrate growth, thereby reducing the likelihood of large scale hydrate formation and hence pipeline plugging. In the case of the vinyl lactam homologues (PVP, PVCap *etc.*) it is postulated that hydrogen bonding between the amide functionality (through the carbonyl) and the hydrate surface allows for the adsorption of the KHI.[121]

The adsorption hypothesis has been tested through a consideration of the crystal growth and morphology of uninhibited and inhibited systems of THF hydrate, which crystallises as structure II, and ethylene oxide, a structure I complex.[121] When the THF hydrate is allowed to form in an uninhibited melt, the crystal adopts a regular octahedral morphology with predominantly {111} crystallographic faces.[121] In the same uninhibited melt conditions ethylene oxide hydrate crystals are dodecahedral with rhombic {110} faces.[121] When applied in low concentration (<0.1 wt%) inhibitors **1.1**, **1.2** and **1.3** result in the alteration in the growth of the crystal from the regular octahedral shape to a 2-dimensional hexagonal morphology (Figure 1.10).[121] Upon use of a higher concentration of inhibitors **1.2** or **1.3** the crystal growth is completely inhibited.[121] It is believed that the hydrate is unable to grow between the polymer strands at these high concentrations and hence crystal growth halts.[121] As a true test for this hypothesis, a hydrate crystal from an inhibited solution was transferred to an uninhibited mixture; crystal growth did not recommence, thereby indicating that inhibition is irreversible in practical terms, and lending support to the theory that the inhibitor is bound to the hydrate surface.[121] When considering the adsorption of the polymer to the hydrate, there will be many pendant groups along the length of the polymer, so it may

not be too surprising that the adsorption is irreversible because in order to fully desorb this would require the many pendant groups to all simultaneously desorb from the surface.[121] This concept is an example of the principle of multivalency in supramolecular chemistry.[122]

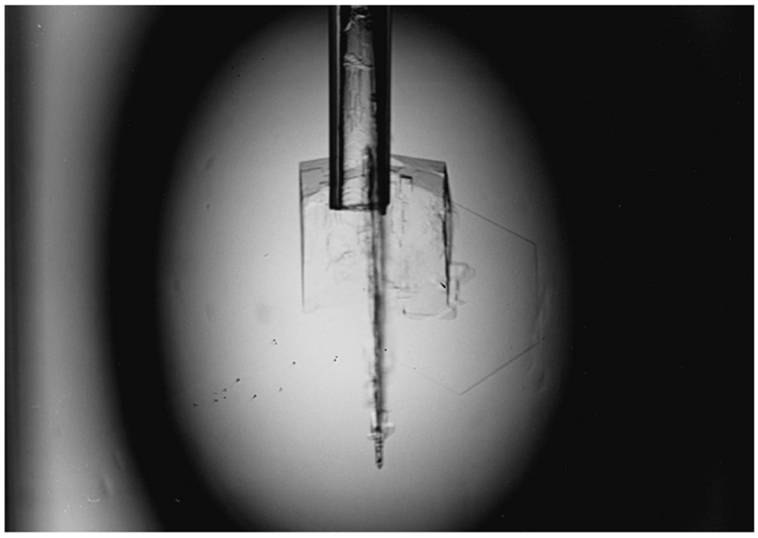

Figure 1.10: Plate morphology THF hydrate crystal following transfer to solution containing 0.025 wt% PVCap.[121]

Lee and coworkers studied the adsorption of PVCap and PVP on cyclopentane hydrates.[123] Calculation of the adsorption isotherms for both vinyl lactam polymers concluded that PVP follows the Langmuir isotherm whilst PVCap follows the BET-type; the combination of the increased molecular size and multilayer adsorption as seen for PVCap results in inhibition performance exceeding that for PVP.[123]

Small-angle neutron scattering studies for poly(ethylene oxide) (PEO), PVP, PVCap and a copolymer of VIMA/VCap on a model THF hydrate surface suggests that as the polymer adsorption to the surface increases, more growth sites are blocked.[124] By studying the THF hydrate system containing inhibitor polymer both above and below the hydrate forming temperature, King *et al.* were able to observe conformational changes in the inhibitor polymers believed to be associated with the adsorption of the inhibitor to the hydrate surface.[124] By making the assumption that majority of the low-q scattering is the result of adsorbed polymer, comparisons between the different KHIs are possible, confirming the increased efficiency of PVCap and P(VIMA/VCap) over the PEO species.[124]

1.6.2 Microscopic studies of KHIs

Raman spectroscopy can provide insight into the degree to which gas molecules are enclathrated within the hydrate lattice.[125] In addition, the v_1 band acts as a signature to

enable identification of the crystal structure attained.[125] The peak position of the v_1 band is different in each of the hydrate structures and for "free" methane (in the gas phase), as shown in Table 1.3.[125]

Condition	Structure		
	I	II	H
Small cavity	5^{12}	5^{12}	5^{12}
Position (cm^{-1})	2915.04±0.58	2913.73±0.76	2912.76±0.30
Large cavity	$5^{12}6^2$	$5^{12}6^4$	$4^35^66^3$
Position (cm^{-1})	2904.85±0.33	2903.72±0.28	2905

Table 1.3: Raman peak positions (cm^{-1}) corresponding to methane in different hydrate crystal structures.[125]

The ability to calculate the relative occupancy of the hydrate cages, when coupled with information on the hydration number, can allow for the determination of the absolute occupancies.[125] The overlaid Raman spectra in Figure 1.11shows the difference between free and enclathrated methane.[125] Furthermore, the spectrum for methane within the hydrate phase comprises a split band, indicating the partitioning between the small and large cavities of the structure I hydrate.[125]

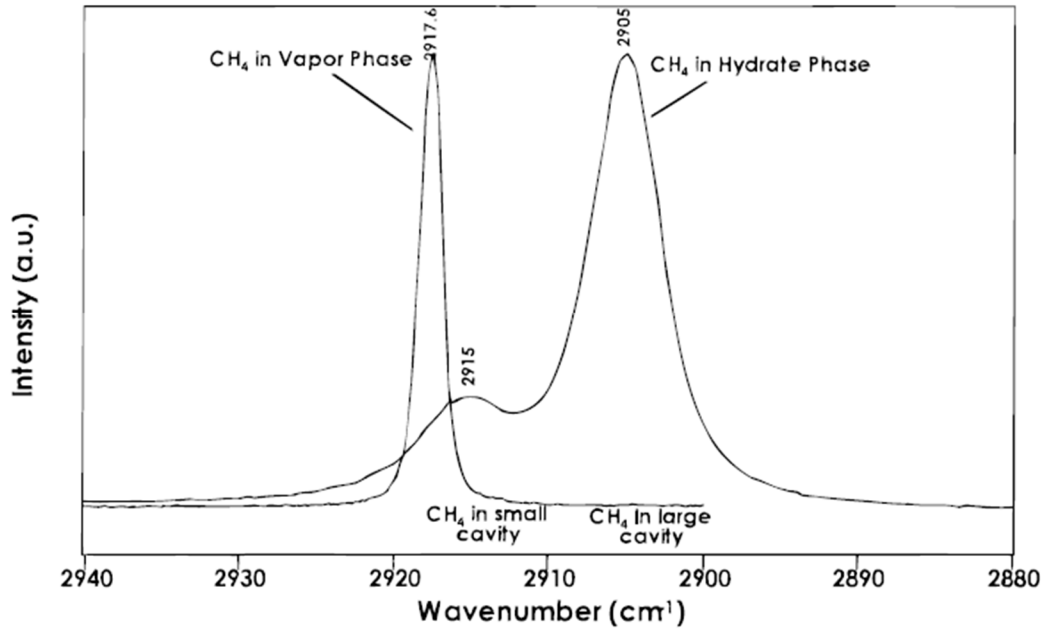

Figure 1.11: Raman spectra for v_1 of methane vapour incorporated in the structure I hydrate. Two peaks are seen for the hydrate phase, showing that CH_4 is incorporated into both cavities of the structure I hydrate.[125]

Raman spectroscopy has been utilised to monitor methane hydrate formation (from dissolved methane) in both uninhibited and inhibited solution systems.[37] As seen in Figure 1.12, as time progresses the band shifting indicates the formation of methane hydrate.[37] Whilst methane hydrate forms in both (a) the uninhibited system and (b) the inhibited system, the temperature in the latter case is 4 °C lower than the former.[37] The ratio between the large and small cage occupancy differs between the two systems.

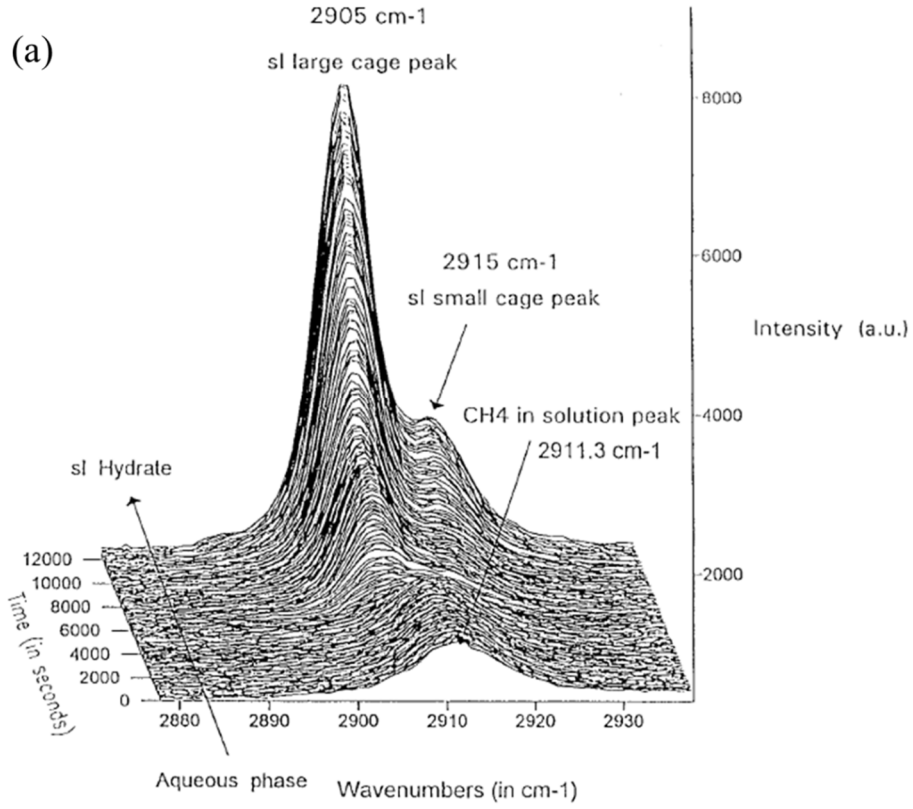

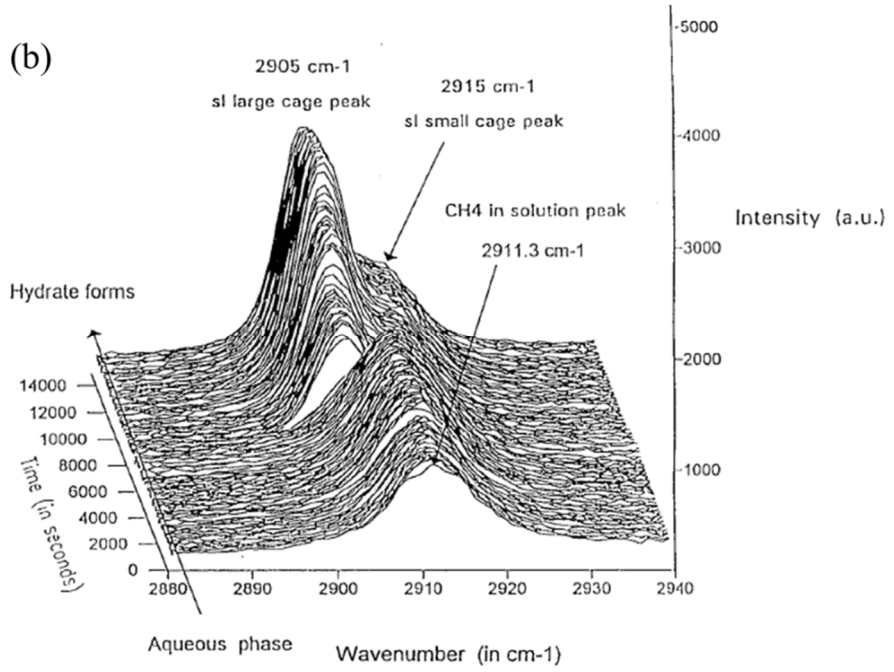

Figure 1.12: Raman spectra for (a) the uninhibited system and (b) the inhibited system for the transition from dissolved methane to methane hydrate, taken at a pressure of 31.7 MPa, using a cooling rate of 0.1 °C/min (initial *T* of 24 °C and final *T* of (a) 2.5 °C and (b) -1.9 °C).[37]

Recently Lee and coworkers used Raman spectroscopy to examine the effect that amino acids have upon gas hydrate nucleation and growth.[126] Their research aimed to investigate the proposal that KHIs function by perturbing the water structure; as such amino acids with hydrophilic side chains were selected in order to induce the maximum water structure disruption.[126] A strong relationship was found between the degree of perturbation and the consequential gas hydrate inhibition, therein providing support to the hypothesis that perturbation of water molecules may explain hydrate inhibition.

1.6.3 Computational modelling of KHI inhibition

As a development to their initial MD simulations for methane hydrate nucleation, Rodger and coworkers incorporated an octamer of PVP into the simulation as an initial probe for KHI mechanism of action.[127] Their simulations indicate that PVP does not bind to the hydrate surface, but in fact stays approximately 2 solvation shells away from hydrate clusters.[127] They found that interaction between the polymer amide groups and water molecules effectively prevents nucleation.[127] In addition, they found PVP to be ineffective at perturbing hydrate formation once clusters have reached a critical size.[127]

Trout and coworkers have reported an interesting computational simulation of inhibitor binding, proposing that the process of inhibition occurs *via* two steps:[128]

(1) The inhibitor disrupts the organisation of the water and guest molecules increasing the barrier to nucleation
(2) The inhibitor can then bind to the surface of the hydrate crystal, thereby retarding the growth along that plane.[128]

Their work provides further rationale for the efficacy of PVCap compared to PVP, through consideration of the free energy of binding for the inhibitor to the hydrate surface.[128] They found that for PVCap the binding free energy is -9.4 ± 3.8 kcal/mol whilst for PVP it is only 0.5 ± 3.7 kcal/mol; these results indicate that PVCap favours being bound to the hydrate surface, with the equilibrium shifted toward the bound state.[128] The radial distribution functions (rdf) derived from MD simulations have been examined, both for monomers of PVCap and PVP, when bound to the hydrate surface and when away in the bulk solution.[128] The rdf for the interaction between the oxygen atoms of the inhibitor and oxygen atoms of water is compared to the rdf for interaction between oxygen atoms in two water molecules. There is significantly stronger correlation between the PVCap monomer-water rdf and the water-water rdf (O-O interaction), than for the PVP analogue.[128] Consequently, the carbonyl oxygen atom of PVCap appears to readily locate itself in a water molecule lattice position, and thereby ensures a stronger binding energy than PVP.[128]

Monte Carlo simulations are reported for the inhibition of methane hydrate using PVP and are in agreement with the adsorption postulation.[129] Rodger and coworkers studied the interaction of the monomer (*N*-ethyl pyrrolidone), dimer and analogous tetramer and octamer with the hydrate surface. The smaller subunits were used due to the great difficulties that would be associated with trying to model the entire polymer.[129] The results obtained for the monomer and dimer allow for the identification of potential adsorption sites with the formation of two hydrogen bonds between the pendant hydrogen atoms on the hydrate surface and one pyrrolidone oxygen atom, as seen in Figure 1.13.[129]

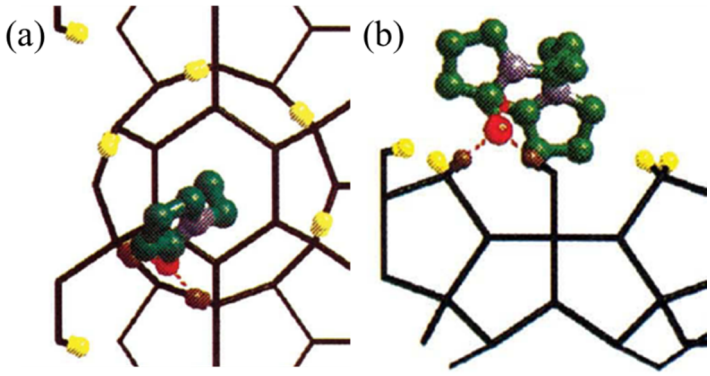

Figure 1.13: Simulation result showing the formation of two hydrogen bonds between the pyrrolidone oxygen atom and hydrogen atoms of the hydrate surface (brown = H of hydrogen-bonding hydrate) for (a) monomer binding and (b) dimer binding.[129]

Recently, English and MacElroy reviewed the developments in the use of molecular simulations in order to gain insight into clathrate hydrate formation and inhibition.[130] Their comprehensive review discusses the progress and challenges is this area, showing that whilst significant progress has been made since the initial simulations in the 1980s, many challenges remain if detailed atomistic insight is to be gained for each of the systems of interest.[130] The findings of the computational studies highlight the contrasting postulations for the KHI mechanism of action, and therein suggest that more research is required in order to fully understand these complex systems.

1.6.4 Other studies

Recently the mode of binding for PVCap to bulk water has been probed through consideration of a dimeric model compound and use of experimental and DFT computational analysis.[62] Comparisons of solution IR spectroscopic data for the dimeric model and for PVCap suggest that this model compound behaves in a similar way to the polymeric KHI.[62] DFT calculations on the interaction of water with the model compounds suggest the presence of OH···O and CH···O hydrogen bonding within a unique pocket complementary to the water molecule. This research offers a possible rationalisation for the increased ability for caprolactam carbonyl oxygen atoms to function as hydrogen bond acceptors on the basis of the high contribution to the enolate resonance form, as a result of the less strained 7-membered ring, in comparison to pyrrolidone analogues.[62] The results of the DFT analysis are shown in Figure 1.14, highlighting the binding of water to the saturated and unsaturated model compounds.[62] An X-ray crystal structure of the model dimer revealed it to be of particularly low density and lacking stabilising intermolecular interactions, suggesting a

reason for the compound's hydrophilicity.[62] This hydrophilicity may be crucial to the excellent KHI behaviour of PVCap.

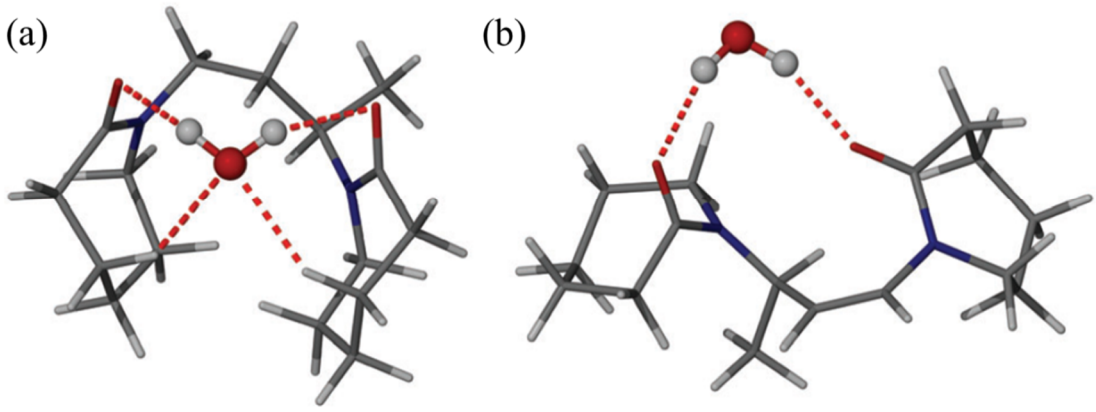

Figure 1.14: DFT structures of (a) hydrogenated and (b) unsaturated dimeric model compound derived from VCap showing binding to D_2O.[62]

Investigations using Differential Scanning Calorimetry (DSC) as a means to ascertain the effectiveness of PVCap as an inhibitor concluded that an increased concentration of PVCap enhances the inhibition properties of the polymer.[131] Analysis of the thermogram obtained from use of the emulsion system both with and without the PVCap inhibitor indicates that inclusion of the inhibitor is effective at delaying the hydrate nucleation time; this is observed by a broadening of the peak in the DSC thermogram.[131]

1.7 Anti-agglomerants

Whilst anti-agglomerants (AAs) are not the focus of the research outlined in this thesis, a brief introduction is included herein for completion.

AAs are species which interact with the liquid hydrocarbon phase and rather than inhibiting the crystallisation of clathrate hydrates, they prevent the agglomeration of small clathrate hydrate crystallites and ensure that a free-flowing slurry is maintained. The main advantage associated with the use of AAs is that performance at high subcooling is superior to that of KHIs. There is the necessity for the presence of a liquid hydrocarbon phase for AAs to function, and as such they are not suitable for all field site applications. In general, it is possible to split AAs into two types: (1) products forming a water-in-oil emulsion as produced by the French Petroleum Institute (IFP) and (2) species comprising hydrophobic tail(s) and hydrate-philic head group(s) as identified by Shell.[8, 32] As expected, these species have

different modes of action which can be addressed through a consideration of the chemistries involved.

In the late 1980s, Conoco reported that surface active agents comprising phosphonates, phosphate esters and polymers such as polyacrylamide and polyacrylates inhibit the agglomeration of clathrate hydrates.[132] In general, a high concentration of such surface active agents is required for good inhibition performance,[132] thereby reducing the economic viability of such species. Inhibition performance has since been exceeded at lower concentrations using alternative AAs, and as such further work in this area has not been reported.

IFP exploited the observation that upon mixing gas, fluid and specific amphiphilic compounds under conditions at which hydrates typically form, the mixture will thicken but no plugging occurs.[133] Thickening is due in part to the presence of the dispersed hydrate particles within the fluid, with dispersion resulting from the presence of the amphiphilic compound, but key to their functionality as an anti-agglomerant is that no blockage results.[133] To this end, IFP explored the use of non-ionic, anionic and cationic amphiphilic compounds as a means to ensure that any hydrate crystals which do form remain dispersed within the fluid mixture and thereby remain transportable.[133] Optimisation of such species concluded that non-ionic amphiphilic compounds containing amide functionality were highly successful, for example the inclusion of 0.25 wt% of coconut diethanolamide results in hydrate formation occurring at 7.5 ^{o}C with no blockage observed during the test which extended to -10 ^{o}C.[133] Results indicate that while these species allow hydrates to form, they effectively ensure that agglomeration into a plug does not occur.[134] Addition of amphiphilic compounds is economically advantageous, as less than 0.5 wt% (relative to the water phase) has proven successful.[133] Application of amphiphilic compounds results in a water-in-oil emulsion, with the hydrates confined to water droplets.[32] The confinement of hydrate particles within water droplets effectively prevents their agglomeration, a mechanism utilised to great effect by IFP.

Shell has identified that alkylarylsulfonates function successfully as gas hydrate anti-agglomerants.[135] Compound **1.22** shows the general structure of such species, where X represents H, Na or K and R is an alkyl group.[135] Whilst these compounds do act to inhibit agglomeration, inhibitor performance has since been exceeded by current AAs (*e.g.* quaternary ammonium surfactants), and thus these species are not of current application.

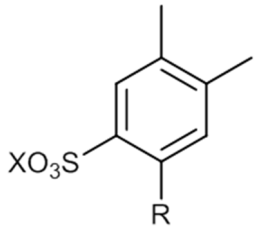

1.22

Use of quaternary tri- or tetraalkylammonium, or phosphonium, salts for inhibition activity has proved very fruitful for the petrochemical industry.[32] In the case of the tetraakyl species modification of the water structure at the hydrocarbon-water interface may further enhance inhibitor performance.[40] AAs containing an alkyl chain arm can effectively attach to the pipeline walls, thereby preventing the adhesion of hydrate particles to such surface; this will further reduce the likelihood of full pipeline blockage.[8]

Continuing with their postulate of inhibition by emulsification, IFP have synthesised an array of polymeric emulsifiers.[136-138] More specifically, their focus was on obtaining an amphiphilic compound with a hydrophilic lipophilic balance (HLB) of between 2 and 7 (maximum of 8) with molecular weights chosen in order to achieve such balance.[137] Such amphiphilic compounds can be added in concentrations ranging 0.1-5 wt% (based on the water content), thereby minimising cost. For example, the reaction between polyisobutenyl succinic anhydride with polyethylene glycol monomethyl ether (in xylene) yields a product with a HLB of 4.9, which effectively inhibits the formation of a hydrate plug for a period in excess of the 24 hours of monitoring in a mini-loop testing system.[137]

At the same time, work was being undertaken into optimising the use of quaternary AAs.[32] Due to the hydrophobicity of alkyl chain arms, it is possible to alter the solubility of the anti-agglomerant species; attachment of two "tails" leads to a more oil-soluble species, whilst one "tail" leads to increased water solubility (*e.g.* compounds **1.23** and **1.24** where R_1 = long chain; R_2 = *n*-butyl, -*n*-pentyl or isopentyl; X = spacer group).[32] Single tail AAs comprising a tail of 10-14 carbon atoms, a tributylammonium or tripentylammonium headgroup and an anion are reported as being very effective in saline conditions (subcoolings of greater than 20 ^{o}C have been achieved), however efficiency is significantly reduced in freshwater applications.[32] Whilst single-tailed AAs may appear to be the ideal species for application there are concerns with regard the toxicity and biodegradability of these compounds; the low biodegradability would result in the persistence of these toxic compounds in the environment for a prolonged time period.[32]

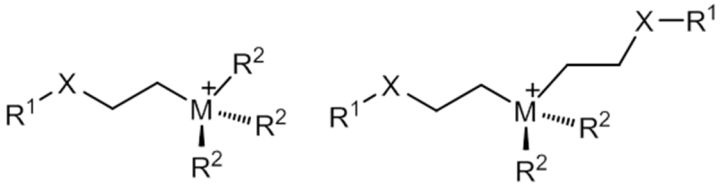

1.23 **1.24**

In an attempt to overcome the shortfalls of the single-tailed AAs, the twin-tailed analogues formed the focus of research by the Dutch Shell team.[32, 139] Inhibition performance, as measured through hydrate recirculation testing, was very encouraging for dibutyldicocylammonium bromide, with the conversion of hydrates into a very fine powder and thereby the prevention of agglomeration.[139] An important consideration for industry is whether an inhibitor remains functional following a restart if pipeline flow has been interrupted (whether scheduled or not).[140] The use of the di-ester of di-butyl-di-ethanol ammonium bromide and coconut fatty acid offers advantages as it enables pipeline flow post-restart whilst also decreasing the temperature of formation for hydrates.[140]

An array of commercially available surfactants, under the trademark name of Span™ have been found to function successfully as hydrate inhibitors, although a concentration of 3 wt% is required to achieve the desired response.[141] Span™ compounds are surfactants based on natural fatty acids and sorbitol. Sloan and coworkers explored the performance of Span 20, Span 40, Span 60 and Span 80 in contrast to analogous synthetic surfactants in order to monitor the ability to suspend hydrate particles.[141] As a measure of performance, high pressure apparatus was used with a change in the stirrer motor current being indicative of plug formation.[141] Of the species synthesised by the group, the performance of dodecyl-2-(2-caprolactamyl) ethanamide (**1.25**) was most promising due to its efficacy at very low concentration (0.75 wt%), however there are some concerns with regard the commercial viability due to the cost of synthesis of such species.[141] It seems unsurprising that this compound would act successfully as a hydrate inhibitor as we have seen earlier that the caprolactam ring functionality provides good performance (as a KHI).

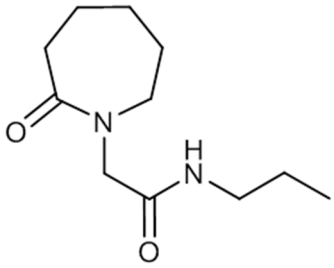

1.25

By the end of the 1990s the best high performing surfactant AAs were the quaternary surfactants with 2 or 3 butyl (or pentyl) groups, as initially discovered by Shell. Whilst other species were reported, the inhibition performance was exceeded by the quaternary ammonium surfactants (QAS) and so there has been an influx of new compounds of this type reported which perform effectively as inhibitors.[32]

The main issue associated with the use of QAS is the associated environmental impact, with toxicity remaining a concern.[32] Shell proposed that an inorganic salt (with a second polar phase) could be added to the effluent in order to enforce a phase separation whereby ionic surfactants or polymeric surfactants could be recovered.[142] The recovery of surfactants effectively reduces the associated environmental impact, although this requires the addition of further chemicals to the effluent which brings additional cost, so preference is for modification of the QAS prior to addition rather than the later recovery. Alternatively, anionic polymers such as polycarboxyic acids, polysulfonic acid, polyphosphoric acids and polyphosphonic acids have been found to successfully detoxify onium compounds with the compound remaining in the aqueous phase.[143] The potential to reduce the toxicity associated with QAS compounds further enhances their potential application and unsurprisingly a number of field trials have been reported, particularly in the Gulf of Mexico.[144] The incorporation of an ether linkage within the inhibitor compound also improves the water dispersibility.[145] More recently, Clariant have patented an array of alternative gas hydrate inhibitors incorporating ether linkages in conjunction with long alkyl chains.[146, 147]

There have been many developments in the area of AAs over the past 15 years, with optimisation of performance a current focus. The application of AAs seems encouraging with many companies maintaining considerable research investment in the development of new compounds. For a comprehensive overview of AA developments, including species which failed to reach field site application, the interested reader is directed to an excellent review by Kelland.[32]

1.8 Conclusions

Due to the many problems associated with pipeline plugging as a result of clathrate hydrate formation, the development of inhibitor compounds is of great importance. Over recent years there has been a drive towards the application of LDHIs as opposed to the traditional thermodynamic inhibitors. Use of LDHIs circumvents the need for application of large concentrations of chemical species, which has considerable economic advantages. Current industrial research is focussed on improving KHI design for application in increasingly challenging and highly regulated environments, with issues such as biodegradability, salt tolerance and high cloud point receiving increasing prominence.

As outlined, there are many complexities associated with gaining detailed insight into the mechanism of clathrate hydrate formation and inhibition. The KHI mode of action has been probed through use of a multitude of experimental techniques; however, to date there has been no conclusive determination of the precise mechanism of action of these fascinating compounds. Further work in this area would be advantageous to enable identification of optimal functionalities for future KHI development.

1.9 Project aims and overview

The aim of this thesis is to explore the critical interactions of pyrrolidone and caprolactam ligand species in the context of gas hydrate inhibition.

The initial focus will be on examining the solution-state behaviour of commercial poly(lactam) inhibitors. IR spectroscopy will be used to explore changes in the hydration behaviour upon incorporation of different moieties upon the polymer backbone. In addition, Chapter 2 aims to establish a justification for the superior performance of PVCap in contrast to PVP. Model compounds will be synthesised and explored using a range of analytical techniques, including solution IR spectroscopic titrations, NMR spectroscopic titrations and X-ray crystallography.

Chapters 3 and 4 use neutron scattering studies with the aim of enhancing the understanding of several systems related to clathrate hydrate formation and inhibition. Firstly, the liquid structures of aqueous-THF and aqueous 2-butoxyethanol will be explored. This will be followed by a neutron scattering study of aqueous-lactam systems.

In Chapters 5 to 7 the polarity of the amide carbonyl moiety is exploited in the synthesis of a series of carbonyl-bound metal complexes. X-ray crystallography is used to

provide structural insight into the short carbonyl oxygen-metal bonds. Chapters 6 and 7 report potential industrial applications of lactam coordination complexes.

1.10 References

1. A. Perrin, O. M. Musa and J. W. Steed, *Chem. Soc. Rev.*, 2013, **42**, 1996-2015.
2. A. K. Sum, C. A. Koh and E. D. Sloan, *Ind. Eng. Chem. Res.*, 2009, **48**, 7457-7465.
3. E. D. Sloan, *Nature*, 2003, **426**, 353-359.
4. E. D. Sloan, *Ind. Eng. Chem. Res.*, 2000, **39**, 3123-3129.
5. H. Davy, *Philos. Trans. R. Soc. London*, 1811, **101**, 1-35.
6. P. Villard, *Compt. Rend.*, 1888, **106**, 1602-1603.
7. P. Villard, *Compt. Rend.*, 1890, **111**, 302-305.
8. E. D. Sloan and C. A. Koh, *Clathrate Hydrates of Natural Gases Third Edition Preface*, Third edn., CRC Press, Boca Raton, 2008.
9. E. G. Hammerschmidt, *Industrial and Engineering Chemistry*, 1934, **26**, 851-855.
10. http://minesmagazine.com/388/, accessed 02/01/2012.
11. S. Y. Lee and G. D. Holder, *Fuel Process. Technol.*, 2001, **71**, 181-186.
12. I. Chatti, A. Delahaye, L. Fournaison and J.-P. Petitet, *Energy Convers. Manage.*, 2005, **46**, 1333-1343.
13. K. A. Kvenvolden, *Reviews of Geophysics*, 1993, **31**, 173-187.
14. J. P. Kennett, K. G. Cannariato, I. L. Hendy and R. J. Behl, *Methane Hydrates in Quaternary Climate Change: The Clathrate Gun Hypothesis*, American Geophysical Union, Washington, DC, 2003.
15. T. A. Strobel, K. C. Hester, C. A. Koh, A. K. Sum and E. D. Sloan, *Chem. Phys. Lett.*, 2009, **478**, 97-109.
16. J. W. Steed and J. L. Atwood, *Supramolecular Chemistry*, 2nd Edition edn., Wiley-Blackwell, Chichester, 2009.
17. K. A. Udachin, C. I. Ratcliffe and J. A. Ripmeester, *Angewandte Chemie*, 2001, **113**, 1343-1345.
18. K. A. Udachin and J. A. Ripmeester, *Nature*, 1999, **397**, 420-423.
19. C. A. Koh, *Chem. Soc. Rev.*, 2002, **31**, 157-167.
20. M. Vonstackelberg and H. R. Muller, *J. Chem. Phys.*, 1951, **19**, 1319-1320.
21. M. Vonstackelberg, *Naturwissenschaften*, 1949, **36**, 327-333.
22. W. F. Claussen, *J. Chem. Phys.*, 1951, **19**, 1425-1426.
23. L. Pauling and R. E. Marsh, *Proc. Natl. Acad. Sci. U. S. A.*, 1952, **38**, 112-118.
24. R. K. McMullan and G. A. Jeffrey, *J. Chem. Phys.*, 1965, **42**, 2725-2732.
25. T. C. W. Mak and R. K. McMullan, *J. Chem. Phys.*, 1965, **42**, 2732-2737.
26. J. A. Ripmeester, J. S. Tse, C. I. Ratcliffe and B. M. Powell, *Nature*, 1987, **325**, 135-136.
27. H. Ohno, T. A. Strobel, S. F. Dec, E. D. Sloan, Jr. and C. A. Koh, *J. Phys. Chem. A*, 2009, **113**, 1711-1716.
28. S. Alavi, J. Ripmeester and D. Klug, *J. Chem. Phys.*, 2007, **126**, 124708-124708.
29. A. P. Mehta and E. D. Sloan, *SPE Journal 53450*, 1999, **4**, 3-8.
30. P. M. Rodger, *J. Phys. Chem.*, 1990, **94**, 6080-6089.
31. Y. Rojas and X. Lou, *Asia-Pac. J. Chem. Eng.*, 2010, **5**, 310-323.
32. M. A. Kelland, *Energy Fuels*, 2006, **20**, 825-847.
33. L. M. Frostman, V. Thieu, D. L. Crosby and H. H. Downs, in *International Symposium on Oilfield Chemistry, 5-7 February 2003, Houston, Texas, SPE 80269*, Society of Petroleum Engineers, 2003.

34. Y. C. Bae, S. M. Lambert, D. S. Soane and J. M. Prausnitz, *Macromolecules*, 1991, **24**, 4403-4407.
35. S. Sun and P. Wu, *The Journal of Physical Chemistry B*, 2011, **115**, 11609-11618.
36. M. A. Kelland, T. M. Svartaas, J. ØVsthus and T. Namba, *Ann. N. Y. Acad. Sci.*, 2000, **912**, 281-293.
37. E. D. Sloan, S. Subramanian, P. N. Matthews, J. P. Lederhos and A. A. Khokhar, *Ind. Eng. Chem. Res.*, 1998, **37**, 3124-3132.
38. Y. Yeh and R. E. Feeney, *Chem. Rev.*, 1996, **96**, 601-617.
39. J. Baardsnes, L. H. Kondejewski, R. S. Hodges, H. Chao, C. Kay and P. L. Davies, *Febs Letters*, 1999, **463**, 87-91.
40. K.U. Cornelis, K.V. Raimond, R.Rene and W.A. Jacobus, *WO*9517579, 1995.
41. H. Ohno, R. Susilo, R. Gordienko, J. Ripmeester and V. K. Walker, *Chem.-Eur. J.*, 2010, **16**, 10409-10417.
42. H. Zeng, I. L. Moudrakovski, J. A. Ripmeester and V. K. Walker, *AIChE Journal*, 2006, **52**, 3304-3309.
43. C. A. Knight, A. L. Devries and L. D. Oolman, *Nature*, 1984, **308**, 295-296.
44. K.-C. Chou, *J. Mol. Biol.*, 1992, **223**, 509-517.
45. C. M. Perfeldt, P. C. Chua, N. Daraboina, D. Friis, E. Kristiansen, H. Ramløv, J. M. Woodley, M. A. Kelland and N. von Solms, *Energy Fuels*, 2014, **28**, 3666-3672.
46. R. Gordienko, H. Ohno, V. K. Singh, Z. Jia, J. A. Ripmeester and V. K. Walker, *PLoS ONE*, 2010, **5**.
47. H. Zeng, V. K. Walker and J. A. Ripmeester, *Angewandte Chemie International Edition*, 2007, **46**, 5402-5404.
48. Y. E. Kirsh, *Prog. Polym. Sci.*, 1993, **18**, 519-542.
49. E.D. Sloan, *US*5420370, 1995.
50. J. P. Long, J. P. Lederhos, A. Sum, R. L. Christiansen and E. D. Sloan, in *Proceedings of the 73rd Gas Processors Association Annual Convention*, New Orleans, LA, 1994.
51. R. O'Reilly, N. S. Ieong, P. C. Chua and M. A. Kelland, *Chem. Eng. Sci.*, 2011, **66**, 6555-6560.
52. http://www.icis.com/Articles/2005/11/26/2011322/chemical-profile-pvp.html, accessed 22/03/2012.
53. E.D. Sloan Jr., *US*5432292, 1995.
54. J. P. Lederhos, J. P. Long, A. Sum, R. L. Christiansen and E. D. Sloan, *Chem. Eng. Sci.*, 1996, **51**, 1221-1229.
55. E.D. Sloan, R.L. Christiansen, J.P. Lederhos, J.P. Long, V. Panchalingham, Y. Du and A.K.W. Sum, *US*5639925, 1997.
56. J.M. Cohen and W.D. Young, *US*6093863, 2000.
57. K.N. Bakeev, K. Harris, C.B. Argo, M.A. Drzewinski and D.E. Graham, *WO*2001004211A1, 2002.
58. K.N. Bakeev, R. Myers, J.C. Chuang, T. Winkler and A. Krauss, *US*6242518B1, 2001.
59. Y. E. Kirsh, N. A. Yanul and K. K. Kalninsh, *Eur. Polym. J.*, 1999, **35**, 305-316.
60. K.N. Bakeev, K. Harris, C.B. Argo, M.A. Drzewinski and D.E. Graham, *WO*2000032545A1, 2000.
61. A. Laukkanen, L. Valtola, F. M. Winnik and H. Tenhu, *Macromolecules*, 2004, **37**, 2268-2274.
62. J. R. Davenport, O. M. Musa, M. J. Paterson, M.O. M. Piepenbrock, K. Fucke and J. W. Steed, *Chem. Commun.*, 2011, **47**, 9891-9893.
63. E.D. Sloan Jr., *US*5880319A, 1999.
64. P. C. Chua and M. A. Kelland, *Energy Fuels*, 2012, **26**, 1160-1168.
65. H. Sefidroodi, P. C. Chua and M. A. Kelland, *Chem. Eng. Sci.*, 2011, **66**, 2050-2056.
66. K.S. Colle, R.H. Oelfke and M.A. Kelland, *US*5874660, 1999.

67. G. F. Mitchell and L. D. Talley, in *SPE Annual Technical Conference and Exhibition SPE 56770*, Society of Petroleum Engineers Houston, Texas, 1999.
68. S. B. Fu, L. M. Cenegy and C. S. Neff, in *SPE International Symposium on Oilfield Chemistry SPE 65022*, Society of Petroleum Engineers Houston, Texas, 2001.
69. K.S. Colle, C.A. Costello, R.H. Oelfke, L.D. Talley, J.M. Longo and E. Berluche, *WO*9608672, 1996.
70. M. F. Mady and M. A. Kelland, *Energy Fuels*, 2014, **28**, 5714-5720.
71. M. A. Kelland, T. M. Svartaas and L. A. Dybvik, in *SPE Annual Technical Conference and Exhibition SPE 28506*, Society of Petroleum Engineers, New Orleans, Louisiana, 1994.
72. V. Thieu, K.N. Bakeev and J.S. Shih, *US*6359047, 2002.
73. J. M. Cohen, P. F. Wolf and W. D. Young, *Energy Fuels*, 1998, **12**, 216-218.
74. J.M. Cohen, P.F. Wolf and W.D. Young, *US*5723524, 1998.
75. U.C. Klomp, *WO*2001077270A1, 2001.
76. P. Froehling, *Journal of Polymer Science Part A: Polymer Chemistry*, 2004, **42**, 3110-3115.
77. L. Del Villano and M. A. Kelland, *Chem. Eng. Sci.*, 2009, **64**, 3197-3200.
78. J. Zheng, O. M. Musa, C. Lei, M. Alexandre, Y. Zhang, R. Chuang and S. Edris, in *The 1st Annual International Congress and Exposition of Oil Field Chemicals (OFC-2010)*, Beijing, 2010.
79. O.M. Musa and L. Cuiyue, *WO*2010117660, 2010.
80. O.M. Musa and L. Cuiyue, *WO*2010114761, 2010.
81. P. C. Chua, M. Sæbø, A. Lunde and M. A. Kelland, *Energy Fuels*, 2011, **25**, 5165-5172.
82. L. Del Villano, R. Kommedal and M. A. Kelland, *Energy Fuels*, 2008, **22**, 3143-3149.
83. U. C. Klomp, in *IPTC 11374*, International Petroleum Technology Conference Dubai, U.A.E., 2007.
84. O.M. Musa and L. Cuiyue, *WO*2011130370, 2011.
85. O.M. Musa, J.C. Chuang, Y. Zhang and J. Zheng, *WO*2012054569, 2012.
86. O.M. Musa, C. Lei and K.S. Narayanan, *US*20110277844, 2011.
87. F. T. Reyes and M. A. Kelland, *Energy Fuels*, 2013, **27**, 3730-3735.
88. P. C. Chua and M. A. Kelland, *Energy Fuels*, 2012, **26**, 4481-4485.
89. F. T. Reyes and M. A. Kelland, *Energy Fuels*, 2013, **27**, 1314-1320.
90. F. T. Reyes, M. A. Kelland, N. Kumar and L. Jia, *Energy Fuels*, 2015, **29**, 695-701.
91. M. F. Mady, J. Min Bak, H.-i. Lee and M. A. Kelland, *Chem. Eng. Sci.*, 2014, **119**, 230-235.
92. F. T. Reyes, L. Guo, J. W. Hedgepeth, D. Zhang and M. A. Kelland, *Energy Fuels*, 2014, **28**, 6889-6896.
93. C. D. Magnusson, D. Liu, E. Y. X. Chen and M. A. Kelland, *Energy Fuels*, 2015.
94. G. R. Desiraju, J. J. Vittal and A. Ramanan, *Crystal Engineering - A textbook*, World Scientific Publishing, 2011.
95. J. W. Mullin, *Crystallization*, Fourth edn., Butterworth-Heinemann Ltd, 2001.
96. D. Kashchiev and A. Firoozabadi, *Journal of Crystal Growth*, 2002, **243**, 476-489.
97. C. P. Ribeiro, Jr. and P. L. C. Lage, *Chem. Eng. Sci.*, 2008, **63**, 2007-2034.
98. J. P. Long and E. D. Sloan, *Int. J. Thermophys.*, 1996, **17**, 1-13.
99. R. Tanaka, R. Sakemoto and R. Ohmura, *Cryst. Growth Des.*, 2009, **9**, 2529-2536.
100. R. L. Christiansen and E. D. Sloan, *Ann. N. Y. Acad. Sci.*, 1994, **715**, 283-305.
101. L. A. Baez and P. Clancy, *Ann. N. Y. Acad. Sci.*, 1994, **715**, 177-186.
102. R. Radhakrishnan and B. L. Trout, *J. Chem. Phys.*, 2002, **117**, 1786-1796.
103. C. Moon, P. C. Taylor and P. M. Rodger, *J. Am. Chem. Soc.*, 2003, **125**, 4706-4707.
104. M. R. Walsh, C. A. Koh, E. D. Sloan, A. K. Sum and D. T. Wu, *Science*, 2009, **326**, 1095-1098.

105. R. W. Henning, A. J. Schultz, V. Thieu and Y. Halpern, *J. Phys. Chem. A*, 2000, **104**, 5066-5071.
106. C. A. Koh, J. L. Savidge and C. C. Tang, *J. Phys. Chem.*, 1996, **100**, 6412-6414.
107. C. A. Koh, R. P. Wisbey, X. P. Wu, R. E. Westacott and A. K. Soper, *J. Chem. Phys.*, 2000, **113**, 6390-6397.
108. M. R. Walsh, J. D. Rainey, P. G. Lafond, D.-H. Park, G. T. Beckham, M. D. Jones, K.-H. Lee, C. A. Koh, E. D. Sloan, D. T. Wu and A. K. Sum, *PCCP Phys. Chem. Chem. Phys.*, 2011, **13**, 19951-19959.
109. J. Vatamanu and P. G. Kusalik, *PCCP Phys. Chem. Chem. Phys.*, 2010, **12**, 15065-15072.
110. L. C. Jacobson and V. Molinero, *J. Am. Chem. Soc.*, 2011, **133**, 6458-6463.
111. G.-J. Guo, Y.-G. Zhang, C.-J. Liu and K.-H. Li, *PCCP Phys. Chem. Chem. Phys.*, 2011, **13**, 12048-12057.
112. P. Englezos, N. Kalogerakis, P. D. Dholabhai and P. R. Bishnoi, *Chem. Eng. Sci.*, 1987, **42**, 2647-2658.
113. J. H. Vanderwaals and J. C. Platteeuw, *Adv. Chem. Phys.*, 1959, **2**, 1-57.
114. W. R. Parrish and Prausnit.Jm, *Industrial & Engineering Chemistry Process Design and Development*, 1972, **11**, 26-35.
115. J. B. Klauda and S. I. Sandler, *Ind. Eng. Chem. Res.*, 2000, **39**, 3377-3386.
116. E. Dendy Sloan, *The Journal of Chemical Thermodynamics*, 2003, **35**, 41-53.
117. N. Daraboina, J. Ripmeester, V. K. Walker and P. Englezos, *Energy Fuels*, 2011, **25**, 4398-4404.
118. H. Ohno, I. Moudrakovski, R. Gordienko, J. Ripmeester and V. K. Walker, *J. Phys. Chem. A*, 2012, **116**, 1337-1343.
119. N. Daraboina, J. Ripmeester, V. K. Walker and P. Englezos, *Energy Fuels*, 2011, **25**, 4392-4397.
120. N. Daraboina, P. Linga, J. Ripmeester, V. K. Walker and P. Englezos, *Energy Fuels*, 2011, **25**, 4384-4391.
121. R. Larsen, C. A. Knight and E. D. Sloan, *Fluid Phase Equilibria*, 1998, **150**, 353-360.
122. M. J. Cloninger, B. Bilgicer, L. Li, S. L. Mangold, S. T. Phillips and M. L. Wolfenden, in *Supramolecular Chemistry: From Molecules to Nanomaterials*, eds. P. A. Gale and J. W. Steed, John Wiley & Sons Ltd., 2012, vol. 1, pp. 95-115.
123. J. S. Zhang, C. Lo, A. Couzis, P. Somasundaran, J. Wu and J. W. Lee, *J Phys. Chem. C*, 2009, **113**, 17418-17420.
124. H. E. King, J. L. Hutter, M. Y. Lin and T. Sun, *J. Chem. Phys.*, 2000, **112**, 2523-2532.
125. A. K. Sum, R. C. Burruss and E. D. Sloan, *J. Phys. Chem. B*, 1997, **101**, 7371-7377.
126. J.H. Sa, G.H. Kwak, K. Han, D. Ahn and K.-H. Lee, *Sci. Rep.*, 2015, **5**.
127. C. Moon, R. W. Hawtin and P. M. Rodger, *Faraday Discussions*, 2007, **136**, 367-382.
128. B. J. Anderson, J. W. Tester, G. P. Borghi and B. L. Trout, *J. Am. Chem. Soc.*, 2005, **127**, 17852-17862.
129. T. J. Carver, M. G. B. Drew and P. M. Rodger, *J. Chem. Soc.-Faraday Trans.*, 1995, **91**, 3449-3460.
130. N. J. English and J. M. D. MacElroy, *Chem. Eng. Sci.*, 2015, **121**, 133-156.
131. J. W. Lachance, E. D. Sloan and C. A. Koh, *Chem. Eng. Sci.*, 2009, **64**, 180-184.
132. R.R. Matthews and C.R. Clark, *EP*309210, 1989.
133. A. Sugier, P. Bourgmayer, E. Behar and E. Freund, *US*4915176, 1990.
134. A. Sugier, P. Bourgmayer and R. Stern, *US*4973775, 1990.
135. H.M. Muijus, N.C.M. Beers, N.M. Van Os, C.A. Kind and M.J. Anselme, *EP*457375A1, 1991.
136. A. Sugier, P. Bourgmayer and J.P. Durand, *US*5244878, 1993.
137. J.P. Durand, P. Gateau, A.S. Baley and A. Sugier, *US*5434323, 1995.
138. M. Thomas, A.S. Baley and J.P. Durand, *US*5426258, 1995.

139. U.C. Klomp and R. Reijnhart, *US*5879561, 1999.
140. U.C. Klomp, *WO*9913197, 1999.
141. Z. Huo, E. Freer, M. Lamar, B. Sannigrahi, D. M. Knauss and E. D. Sloan, *Chem. Eng. Sci.*, 2001, **56**, 4979-4991.
142. G.C. Blytas and V.R. Kruka, *US*7033504, 2006.
143. G.T. Rivers, L.M. Frostman, J.L. Pryzbyliski and J.A. McMahon, *US*2003/0146173 A1, 2003.
144. L. M. Frostman, in *SPE Annual Technical Conference and Exhibition, SPE 63122*, Society of Petroleum Engineers, Dallas, Texas, 2000.
145. C.R. Milburn and G.M. Sitz, *US*6444852, 2002.
146. U. Dahlmann and M. Feustel, *US*20040164278 A1, 2004.
147. U. Dahlmann and M. Feustel, *US*20040163306 A1, 2004.

2 Solution and structural analysis of lactam species

2.1 Introduction

KHI mechanism of action remains a large area of uncertainty within the petrochemical industry due, in part, to complexities associated with gaining solution and structural information on polymers through conventional analytical techniques. While computational studies of monomeric species are reported within the literature showing the adsorption of the small lactam species onto the hydrate surface,[1] these fail to take into account cooperativity due to adjacent lactam rings as within polymeric inhibitors. The Steed group have previously shown that dimeric model compound 1,3-bis(caprolactamyl) but-1-ane (**2.1**), represents an appropriate model for PVCap and provides insight into the hydration behaviour of the parent polymer.[2]

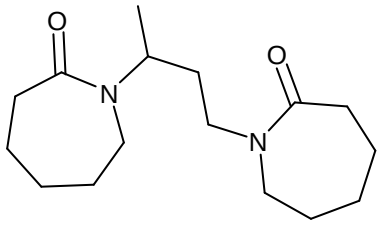

2.1

It has been postulated that hydration of the highly polar amide carbonyl moiety within KHIs leads to disruption of water structure and therein prevents the formation of gas hydrate cages.[2, 3] Upon hydration the cyclic lactam species undergoes a shift to the enolate resonance form, resulting in a reduction in electron density on the carbonyl group. Infrared (IR) spectroscopy enables mapping of the resulting shift of the carbonyl stretching band to lower wavenumber. Precedence for the use of IR spectroscopy to analyse solvation and hydration behaviour of polymers has long been established.[4-7] In 2002, Maeda *et al.* reported some insight into the solution behaviours of PVCap and PVP.[5] Their work used D_2O rather than H_2O in order to avoid overlapping of the water bending mode with the amide carbonyl stretching band (specifically within PVCap); this concept will be utilised in the following chapter, *vide infra*.[5]

This chapter highlights the solution and crystallographic behaviour of a series of lactam, bis(lactam) and poly(lactam) species. X-ray single crystal data, IR spectroscopy and ^1H NMR spectroscopy are all brought together in order to explore the behaviour of this

fascinating series of compounds. Particular emphasis is placed upon examining changes in hydration upon incorporating different functionalities upon the aliphatic backbone in an attempt to establish a justification for the superior inhibition performance of some polymers. Firstly, a systematic comparison of the hydration behaviour of several commercial KHIs is detailed. This is followed by development and analysis of a series of model compounds, whereby hydration behaviour is verified relative to the parent polymer. For completeness, the behaviour of relevant monomeric lactams is also examined.

2.2 Poly(lactam) species

Ashland Inc. supply a series of poly(lactam) KHIs, with different functionalities incorporated to provide specific field-site performance.[8] Commercial samples are supplied as 50 wt% mixtures in 2-butoxyethanol to ease application and enhance performance. In order to ensure consistency the polymers were first isolated in powder form by precipitation with diethyl ether which acts as an anti-solvent followed by filtration. The samples were thoroughly dried within the drying pistol (held under vacuum heated by refluxing toluene) and purity confirmed using ^{1}H NMR spectroscopy and IR spectroscopy. PVP samples were supplied as white powders and were analysed after intensive drying; two PVP analogues were examined in order to explore the effects of molecular weight upon hydration behaviour. PVP K12 (low molecular weight polymer MW ~3500) was purchased from Acros Organics and PVP K30 (high molecular weight species MW ~ 65,000) was supplied by Ashland Inc.

Solution IR spectroscopic titrations with D_2O were performed by dissolving the dry KHI polymer powder in anhydrous acetonitrile (MeCN) to generate a homogeneous solution of known concentration. Acetonitrile was selected as it is only a weak hydrogen bond donor and therefore should not interfere with the hydration process. Measurements were conducted using a Perkin Elmer Spectrum 100 FT-IR spectrometer fitted with a Specac solution IR cell. A 0.05 mm spacer was used to separate the CaF_2 windows and enclose the liquid samples. Throughout this chapter, the equivalents of the guest, D_2O, are calculated relative to the monomeric repeat unit in the lactam polymer. Table 2.1 details the composition of the polymer samples studied.

Name	Functionalities
PVP K12	Poly vinyl pyrrolidone
PVP K30	Poly vinyl pyrrolidone
PVCap	Poly vinyl caprolactam
P(VCap/VOH)	Vinylcaprolactam-vinyl alcohol copolymer (82:18)
P(VCap/VP)	Vinylcaprolactam-vinyl pyrrolidone copolymer (95:5)
P(VCap/VP)	Vinylcaprolactam-vinyl pyrrolidone copolymer (50:50)
P(VCap/HEMA)	Vinylcaprolactam-(hydroxyethyl)methacrylate co-polymer (95:5)

Table 2.1 Compositions and names of commercial KHI polymers under investigation

Comparisons between the solid and solution-state behaviours of PVCap (MW ~ 3000) and PVP K12 (MW ~ 3500) are reported herein, in an attempt to establish a justification for the superior hydrate inhibitor performance of PVCap.[9] For consistency, an initial 5.38 x 10^{-5} moles/mL acetonitrile solution was used for both KHIs; use of solutions of higher concentration was not possible because the polymers cloud out at higher concentration.

The amide I carbonyl stretching frequency (υ(C=O)) of PVP K12 occurs at 1668 cm^{-1} in the solid-state and at 1682 cm^{-1} in anhydrous MeCN solution. In comparison, for PVCap the C=O stretch occurs at 1629 cm^{-1} in the solid state and at 1637 cm^{-1} in anhydrous MeCN. Increased strain within the pyrrolidone ring reduces the contribution to the enolate resonance form, resulting in greater carbonyl double bond character than within the more flexible 7-membered species. This is observed in the IR spectra by the significantly higher υ(C=O) in PVP. The differences between the solid-state and aprotic solution spectra for both polymers suggests stronger CH···O hydrogen bonding in the solid-state leading to weaker C=O bonds. Upon addition of up to 500 equivalents of D_2O per monomer unit in MeCN solution there is notable shift and broadening of the C=O stretch in both PVP and PVCap to 1658 cm^{-1} and 1616 cm^{-1} respectively, as seen in Figure 2.1.

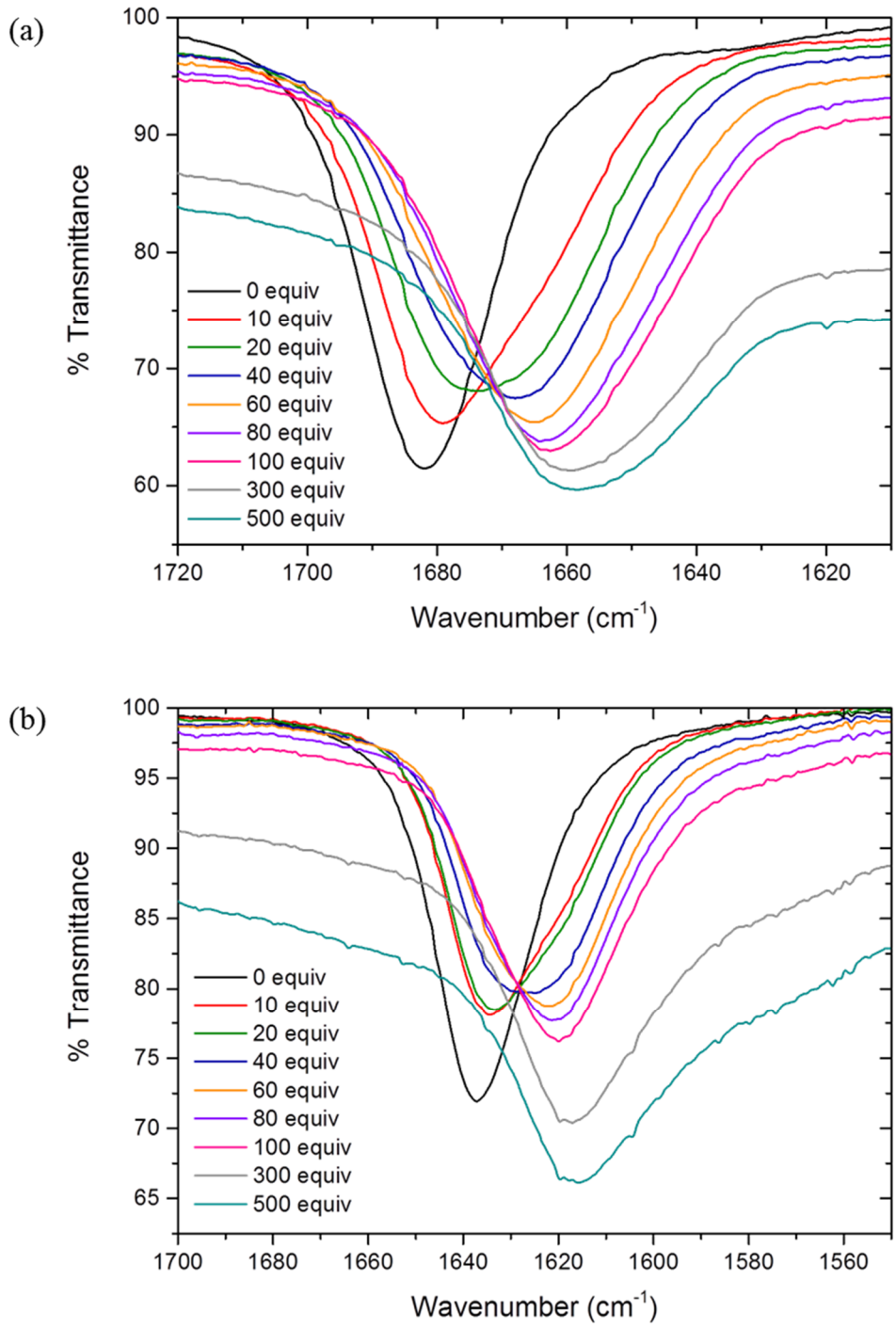

Figure 2.1: Solution IR titration results for (a) PVP K12 and (b) PVCap. Starting acetonitrile solutions were at a concentration of 5.38×10^{-5} moles/mL. D_2O molar equivalents are based per monomer unit.

Figure 2.2 shows the cumulative υ(C=O) shifts for PVP and PVCap during the titration, totalling 24 cm^{-1} for PVP and 22 cm^{-1} for PVCap following addition of 500 D_2O equivalents. However, when taking into account the spectrometer resolution of 1 cm^{-1}, the calculated cumulative shifts for PVP and PVCap are within instrument error of one another. This

suggests that the carbonyl stretching band behaves analogously in the 5 and 7-membered rings, despite the different ring properties.

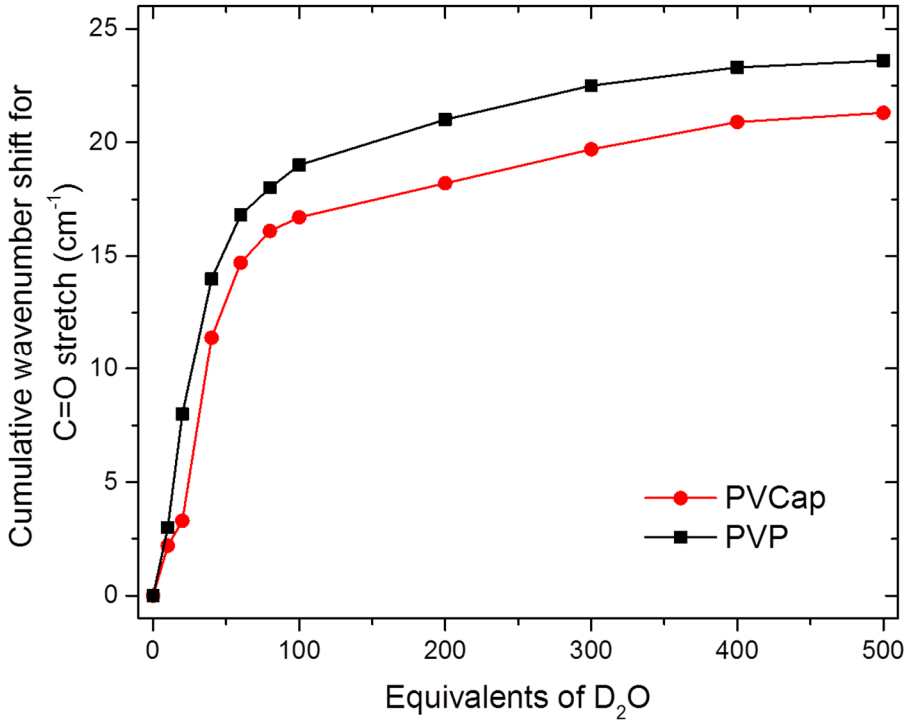

Figure 2.2: Cumulative υ(C=O) shifts (cm^{-1}) as a function of the number of molar equivalents of D_2O for PVP K12 and PVCap.

While the cumulative wavenumber shifts give some information about the hydration behaviour, it is perhaps more useful to identify the number of distinct hydrated carbonyl bands present during the titration and to monitor the transition between these bands. Some of the spectra in Figure 2.1 are significantly broadened, a phenomenon that has been attributed to multiple overlapping C=O bands as a result of multiple carbonyl environments.[10] This phenomenon is easily observed in the spectra for PVP in the presence of 20 equivalents of D_2O. The band asymmetry may be calculated according to the equation reported by Kirsh *et al.*:[10]

$$g = \left(\frac{[(\nu_h - \nu_0) - (\nu_0 - \nu_l)]}{(\nu_h - \nu_l)} \right) x\ 100\%$$

Where v_o is the wavenumber at band maximum, v_h and v_l are measured at half-height and represent the high and low frequencies of the band.[11] Figure 2.3 shows a schematic representation of the calculations and the resulting expected asymmetry sign.

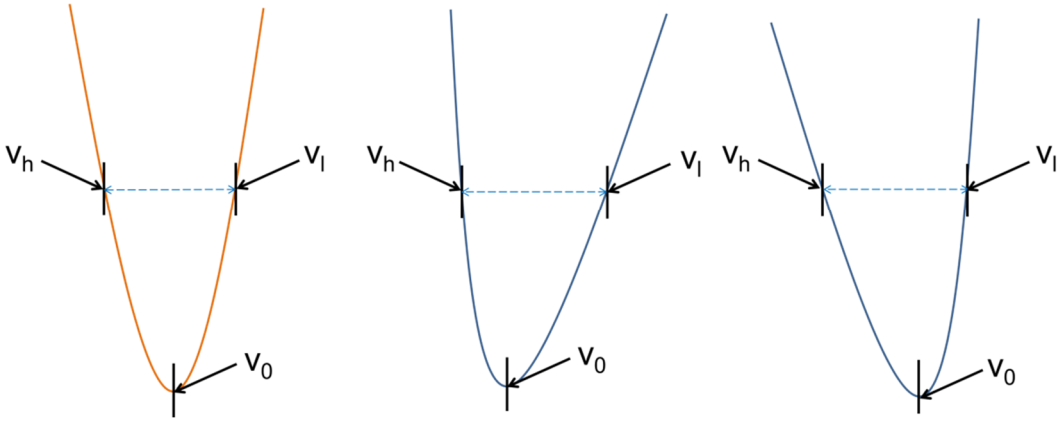

Figure 2.3: Calculation of carbonyl band asymmetry signs (a) zero, (b) negative and (c) positive

A significant change in the gradient of the plot of the band asymmetry is attributed to the transition to a different hydrated carbonyl environment. In this work the asymmetry is used to monitor the evolution of the carbonyl stretch during hydration, and to enable systematic comparison between the polymer series. Broadened stretches may be crudely thought of as representing two (or more) different hydrated carbonyl bands.[5, 12, 13] A broadened band is generally followed by a more symmetric band as a result of transition to the next hydrated state. Figure 2.4 shows the correlation between the titration data and the calculated carbonyl band asymmetry for PVP K12, with the numbers representing the different hydrated carbonyl environments.

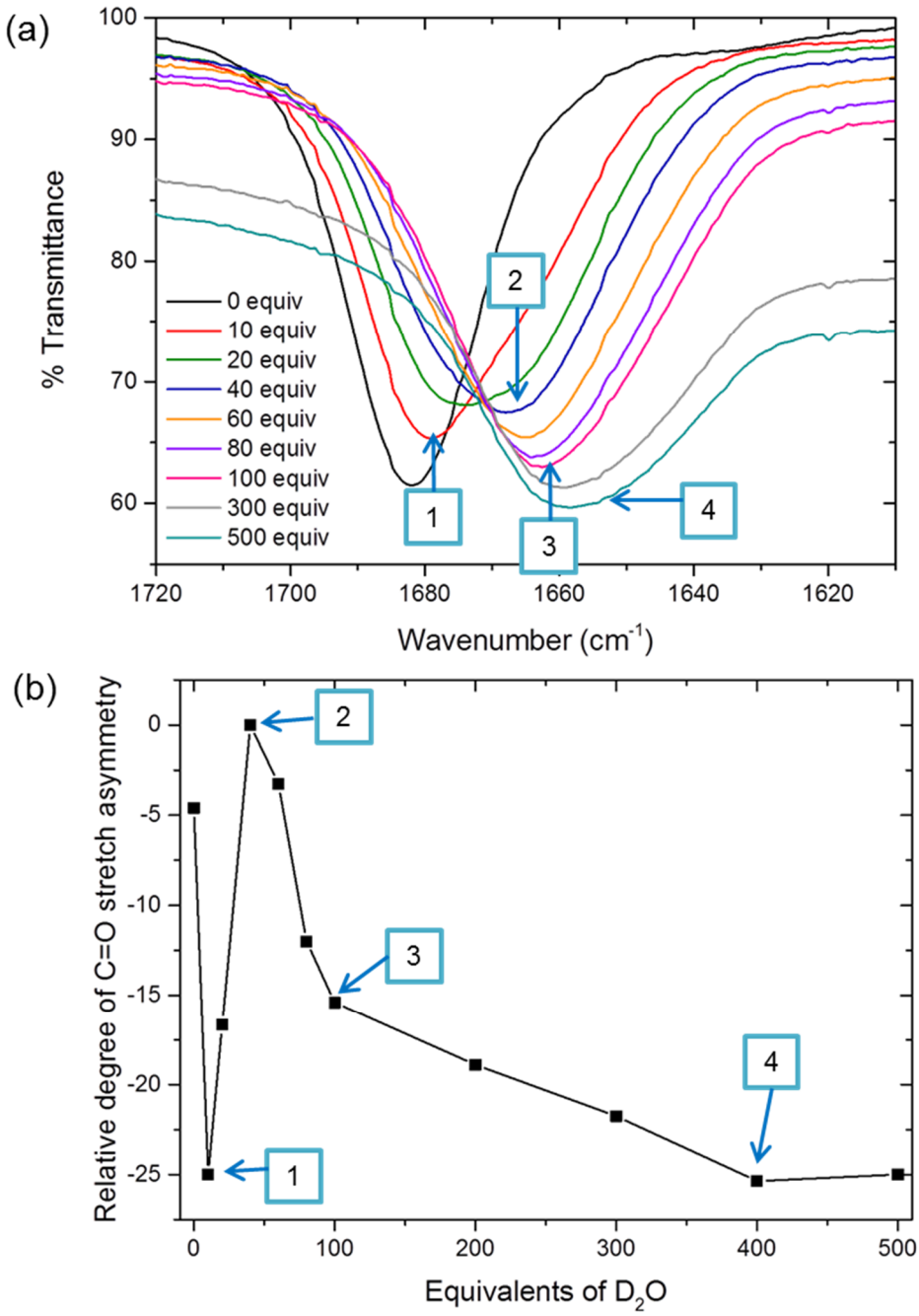

Figure 2.4: Shows the correlation between the titration data and the relative degree of carbonyl stretch asymmetry for PVP K12. Where (a) highlights the transition to the next hydrated environment during the titration and (b) shows a plot of the C=O band asymmetry for PVP K12 during the titration; numbers correspond to the transitions observed in (a)

Based on these spectroscopic titrations, the relative degree of carbonyl stretch asymmetry has been calculated for PVP and PVCap, and shows a high dependence on the amount of D_2O added, as shown in Figure 2.5. The gradient of the plots change four times for

both PVP and PVCap, testifying to the existence of three or four individual hydrated-υ(C=O) bands.

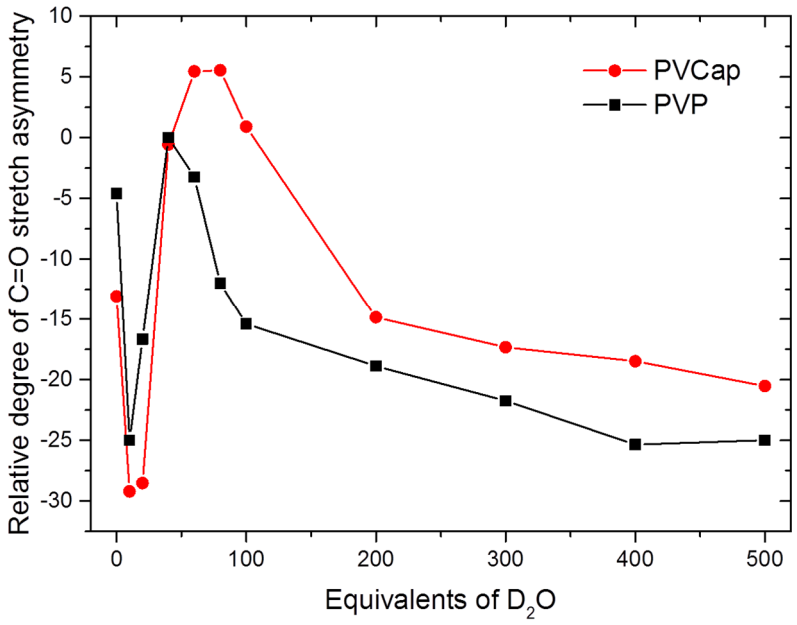

Figure 2.5: Relative degree of asymmetry of the C=O stretch in PVP and PVCap *vs* molar equivalents of D_2O

For completeness, the IR spectra were deconvoluted using Pseudo-Voigt fitting in an attempt to isolate the individual components within the broadened carbonyl bands. Figure 2.6 shows the resultant fitting for PVP and PVCap following addition of a range of D_2O equivalents (as stated in each plot key). The plots show the original spectroscopic data in black, fitted peaks in red and green, and the overall cumulative fit obtained by Pseudo-Voigt fitting in blue. As established above, there are likely to be multiple components which overlap to give the broadened carbonyl band appearance. In this work the carbonyl bands are deconvoluted into 2 peaks, as consistent with 2 hydrated states. Whilst it is anticipated that many more hydrated states may be present, fitting 3 or 4 (or more) peaks to each of the broadened carbonyl bands proved challenging, with large errors associated with the fitted data. Therefore, it was concluded that modelling the data as two components provided the most reliable results, and will at least enable comparison between polymer hydration behaviours.

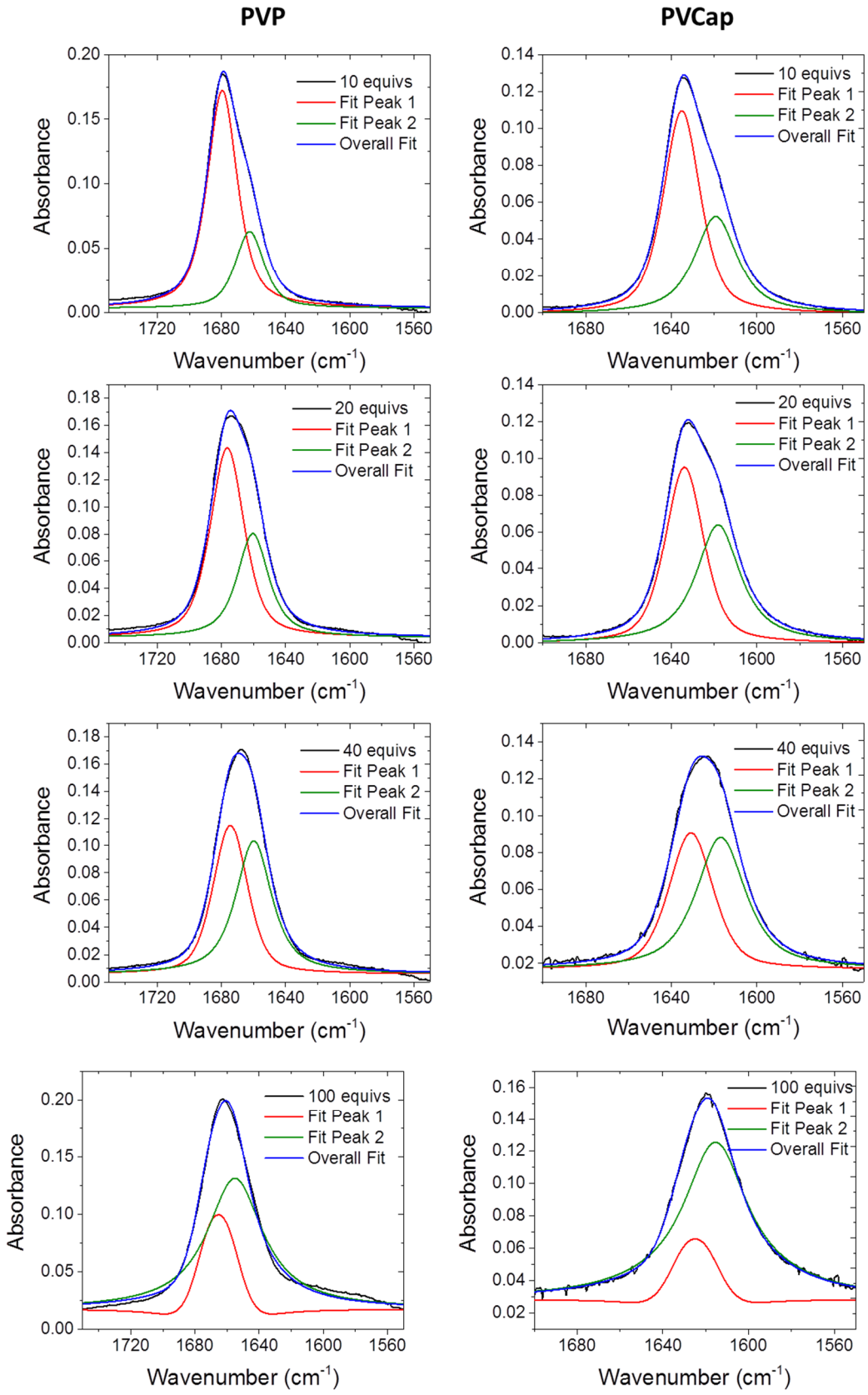

Figure 2.6: Pseudo-Voigt fitting for PVP and PVCap IR spectroscopic data. Black line = original data; blue line = cumulative fit deconvoluted bands; red/green lines = deconvoluted bands

In all instances the overall fit is in good agreement with the original spectroscopic data. Upon addition of 10 and 20 D_2O equivalents the carbonyl bands split into a major component (at higher wavenumber) and a minor shoulder component (at lower wavenumber). The lower wavenumber component corresponds to an increasingly hydrated state, and the integral of this peak increases upon addition of further water. At 40 D_2O equivalents, the carbonyl bands are split into two peaks of similar intensity, thought to represent an equal distribution of states. As further water is added to both polymers the band at lower wavenumber becomes increasingly dominant, and shifts further to lower wavenumber, consistent with carbonyl hydration.

Whilst the deconvolution of spectra provides further support for the comparable hydration behaviour of PVP and PVCap, little additional insight is gained than previously outlined in the asymmetry discussion. It is well established that the hydration behaviour of these important polymers are complex, and is likely to occur *via* multiple hydration states as opposed to the rather simplified analysis of a non-hydrated and hydrated state switching, as implied in the Voigt fitting. It is believed that there exist a range of degrees of hydration that favours the more hydrated state as further water is added to the system. Due to the complexity of the long chain polymers and the reasonably weak water binding, in all instances a small population of non-hydrated carbonyl groups are thought to exist, and this cannot reliably be taken into account through the process of spectral deconvolution but rather using the asymmetry analysis. To this end, calculation of the carbonyl band asymmetry is likely to provide more useful insight into the overall behaviour of the carbonyl group as this takes into consideration the many states without the need to resolve the broad bands. Therefore, calculation and discussion of asymmetry will be the main source of comparison hereafter.

IR spectroscopic measurements of D_2O solutions of the lactam species removes any dilution effects as a result of using MeCN solvent, and should therein provide the υ(C=O) for the fully hydrated species. The absence of dissociable protons within PVP and PVCap means that the IR bands should be equivalent in H_2O and D_2O.[5] In 1, 5 and 10 wt% PVP-D_2O solutions the υ(C=O) occurs at 1645 cm^{-1} and remains unaffected by dilution, as seen in Figure 2.7. In addition, the absence of a carbonyl stretch at 1682 cm^{-1} confirms the lack of dehydrated carbonyl groups in the solution. This indicates that the carbonyl group hydrates, as seen by the shift to lower wavenumber, but is then not further affected following the addition of

extra water molecules. It is meaningless to examine solutions of higher concentration due to saturation of the %Transmittance in the spectrum.

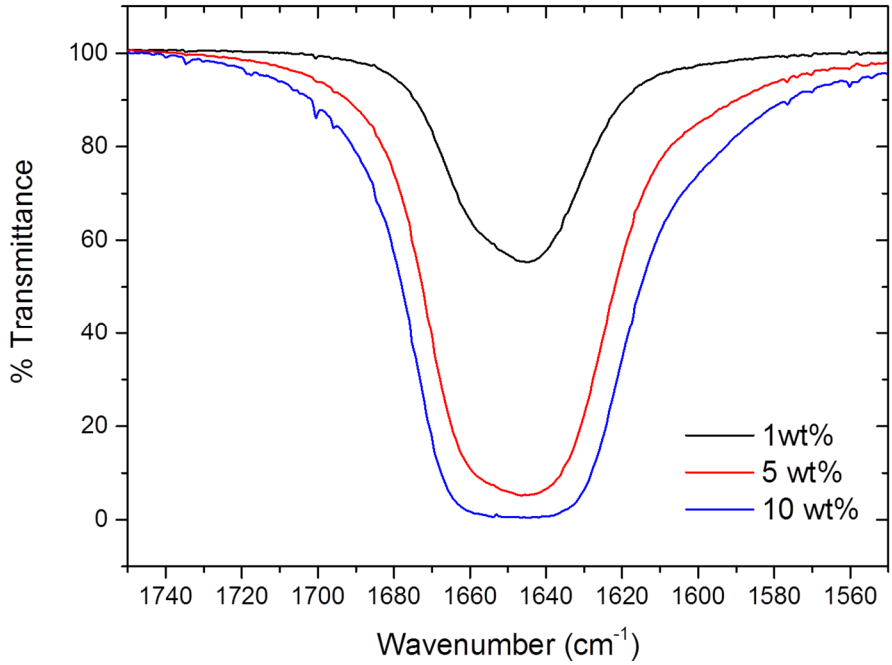

Figure 2.7: Carbonyl stretch within PVP in different wt% D_2O solutions

It is worth noting that the υ(C=O) occurs at 1645 cm^{-1} in a 1 wt% D_2O solution of PVP in contrast to 1658 cm^{-1} in MeCN + 500 D_2O equivalents, therein highlighting the competitive effect of the aprotic solvent. For comparison, the υ(C=O) occurs at 1609 cm^{-1} in a 1 wt% D_2O solution of PVCap, and at 1616 cm^{-1} in the PVCap-MeCN solution after addition of 500 equivalents of D_2O.

While considering the interactions of PVP and PVCap with solvent, it is also interesting to examine the interactions between polymer and 2-butoxyethanol. This is industrially relevant because many KHIs are supplied commercially as 50 wt% mixtures in this alcohol. The high polarity of the amide carbonyl moiety in the presence of an alcohol solvent provokes the question of whether some degree of hydrogen-bonding interaction between solvent and polymer occurs. Figure 2.8 shows the solution IR titration of PVCap with 2-butoxyethanol in acetonitrile solution. The most prominent carbonyl stretch occurs at 1637 cm^{-1} and remains largely unaffected by the presence of 2-butoxyethanol. Addition of more than 50 molar equivalents of 2-butoxyethanol results in a broad shoulder at ~1620 cm^{-1}, which increases in prominence as further solvent is added. It is postulated that this shoulder corresponds to a hydrogen-bonded species within solution. During commercial application inhibitors are

dissolved in 50 wt% 2-butoxyethanol, but this mixture is then diluted considerably in sea-water. Therefore, these IR data suggest that at the solvent concentrations experienced in industrial applications the 2-butoxyethanol has no significant hydrogen bonding interaction with the inhibitor.

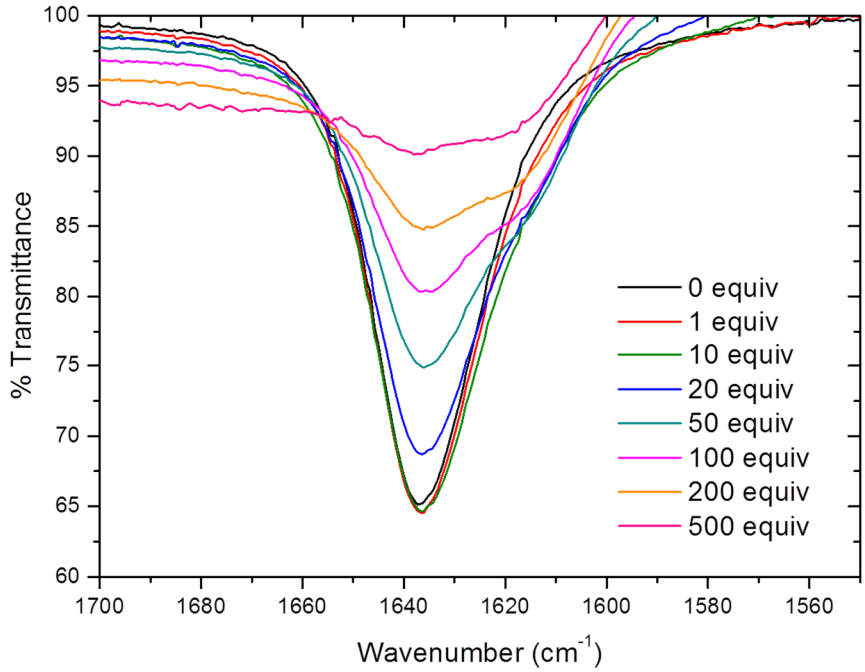

Figure 2.8: Solution IR titration of PVCap with 2-butoxyethanol in acetonitrile (initial PVCap-MeCN concentration = 5.38 × 10^{-5} moles/mL). Equivalents of 2-butoxyethanol are calculated per monomer unit in the polymer.

The pyrrolidone solution studies outlined in this section so far use the low molecular weight K12 analogue. For completeness, the solution behaviour of high molecular weight PVP K30 (MW ~ 65,000) was also examined in order to establish the influence of molecular weight upon hydration behaviour. Acetonitrile solutions of the same host concentration (5.39 x 10^{-5} moles/mL) were studied, confirming that molecular weight has no significant effect upon the hydration mode or ability of PVP. Figure 2.9 shows the cumulative υ(C=O) shift in K12 and K30, totalling 24 cm^{-1} and 22 cm^{-1} respectively. It appears that the higher MW analogue saturates at a lower number of D_2O equivalents than K12, with 100 D_2O equivalents having a more significant effect upon the carbonyl group in K30. However, as further D_2O is added (up to 500 equivalents) the υ(C=O) shifts comparably in both pyrrolidone polymers.

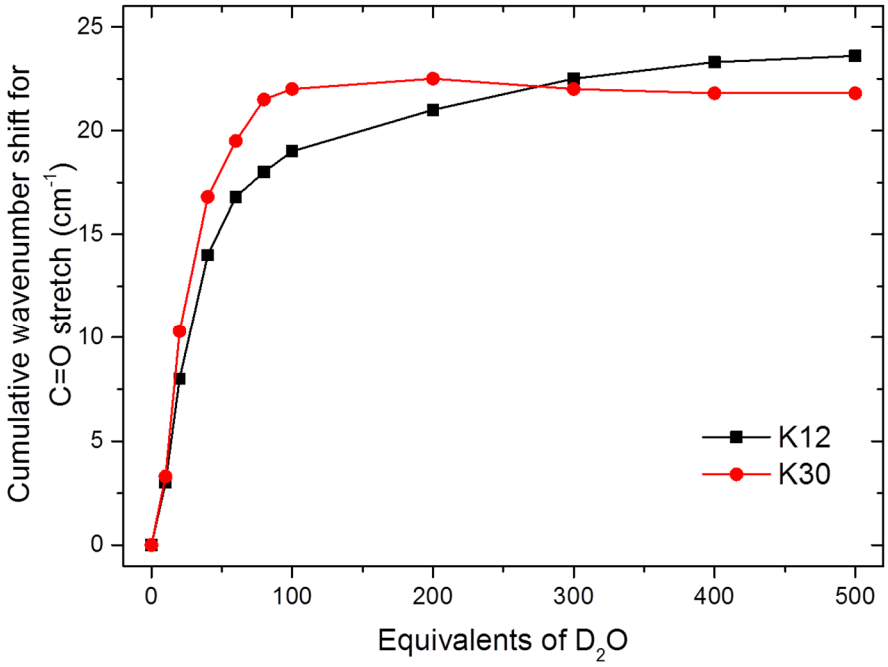

Figure 2.9: Cumulative υ(C=O) shift during the addition of D_2O to MeCN solutions of PVP K12 and K30.

In addition, changes in the carbonyl band asymmetry are similar between the two PVP species as seen in Figure 2.10. Work by Kelland and co-workers had shown that high MW PVP functions well by adsorbing to the hydrate surface, while low MW PVP has a greater effect upon gas hydrate nucleation.[14] This work shows similar hydration behaviour at the carbonyl moiety of both polymers in the solution.

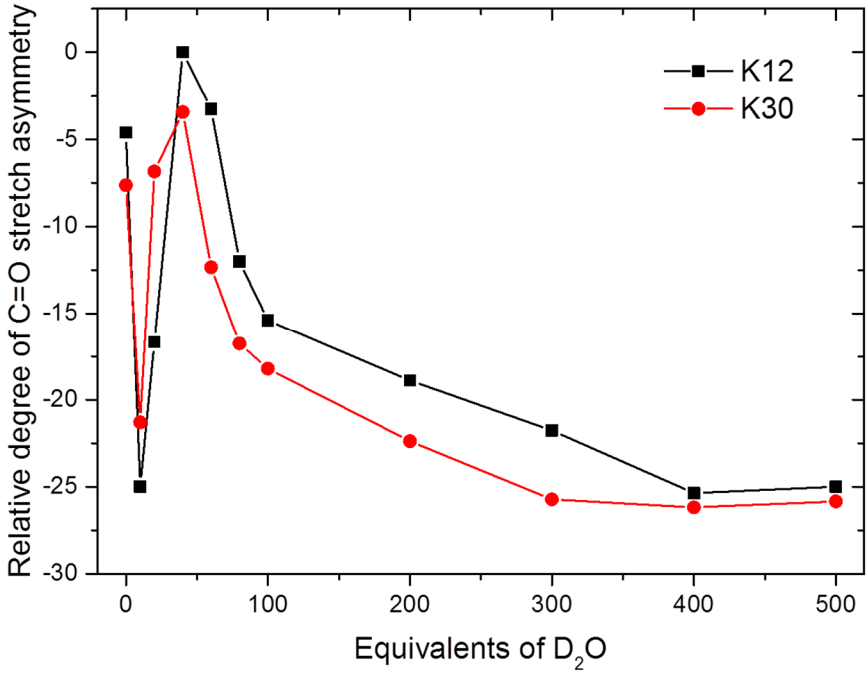

Figure 2.10: Relative degree of C=O stretch asymmetry in PVP K12 and K30 following addition of known equivalents of D_2O into MeCN-polymer solutions.

In conclusion, this work confirms hydration at the carbonyl moiety and shows that by monitoring the shift in the υ(C=O) we can ascertain insight into these fascinating polymers, through behavioural comparison between different species. The changes in the carbonyl stretch asymmetry during titration indicate that three/four hydration states are achieved for both PVP and PVCap. Finally, this shows no apparent explanation for the superior inhibition performance of PVCap compared to PVP, if one assumes that the polymers were only to function by binding solvent water. Table 2.2 summarises the hydration behaviour for PVP and PVCap.

Polymer	***v*(C=O) (cm^{-1})**				
	Solid	**MeCN**	**MeCN + 500 D_2O**	**MeCN + 1000 D_2O**	**1 wt% D_2O**
PVP K12	1668	1682	1658	1653	1645
PVCap	1629	1637	1616	1614	1609

Table 2.2: υ(C=O) for PVP K12 and PVCap in various states

Two vinyl caprolactam-vinyl pyrrolidone copolymers have also been studied; namely the 50:50 and 95:5 species. These copolymeric species are reported to have a high cloud point (72 ^{o}C) and reasonable salt tolerance, making them appealing for warm field sites.[15] Solution studies were undertaken in order to examine the consequence of moving away from a

homopolymeric species and to establish whether this affects the hydration process and to probe any cooperativity between the two types of monomer. The pyrrolidone and caprolactam carbonyl components are both pronounced in the MeCN solution of the 50:50 copolymer, occurring at 1680 cm^{-1} and 1635 cm^{-1}, respectively. Upon addition of 500 D_2O equivalents the υ(C=O) shifts to 1658 cm^{-1} for the pyrrolidone component and 1614 cm^{-1} for the caprolactam moiety, as shown in Figure 2.11.

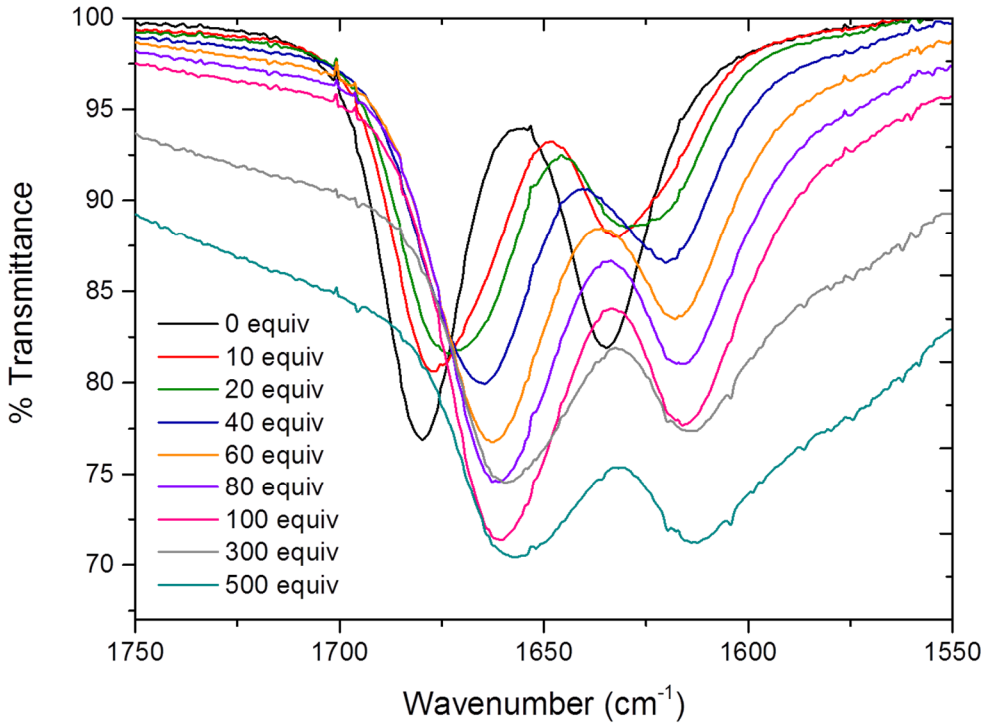

Figure 2.11: Solution IR titration showing addition of D_2O into an MeCN solution of the 50:50 VP/VCap copolymer. Starting solution concentration = 5.43×10^{-5} moles/mL.

Independently tracing the shifts in the υ(C=O) for the pyrrolidone and caprolactam components within the 50:50 copolymer enables comparison to PVP and PVCap, as seen in Figure 2.12. Upon addition of 500 equivalents of D_2O to the copolymer solution, the pyrrolidone υ(C=O) shifts by 23 cm^{-1} whilst the caprolactam υ(C=O) shifts by 22 cm^{-1}. Once again, taking into account instrument resolution error, it can be concluded that the carbonyl moieties behave in an analogous manner in the copolymer as within the respective homopolymers.

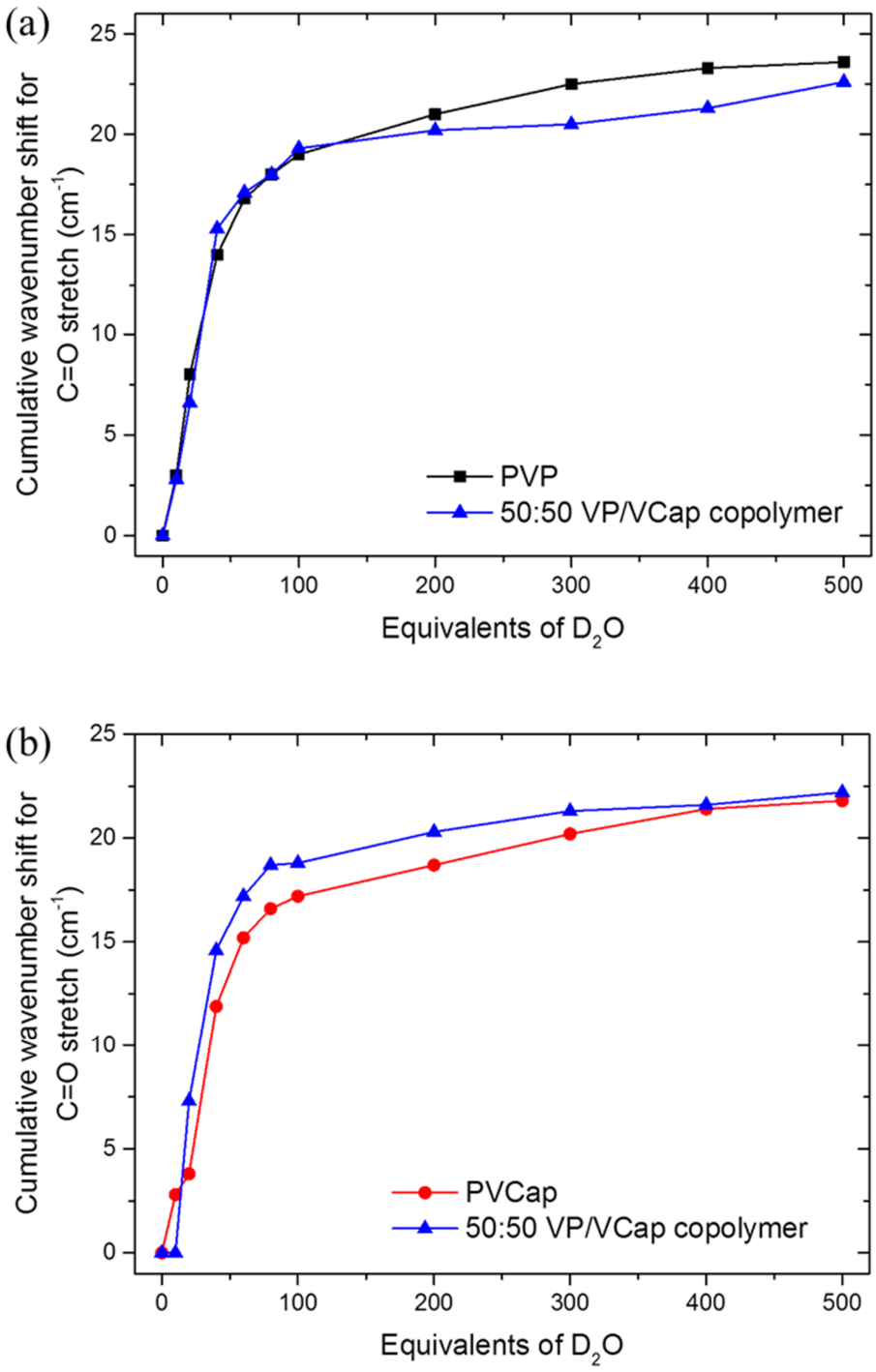

Figure 2.12: Cumulative υ(C=O) shifts in the 50:50 copolymer *vs* (a) PVP and (b) PVCap.

In addition, changes in the relative degree of carbonyl band asymmetry highlights that the C=O band evolves in a similar manner in the copolymer and respective homopolymers, as seen in Figure 2.13. The pyrrolidone component in the copolymer seems unaffected by the presence of the 7-membered ring, having a near-identical asymmetry trend to that of PVP. While the trend in the asymmetry of the caprolactam carbonyl stretch differs

between the copolymer and PVCap, the gradient of the plots both change four times, testifying to their comparable behaviour. This suggests that the additional polymer asymmetry as a result of the combination of 5 and 7 membered rings has no significant effect upon the number of hydrated carbonyl environments attained.

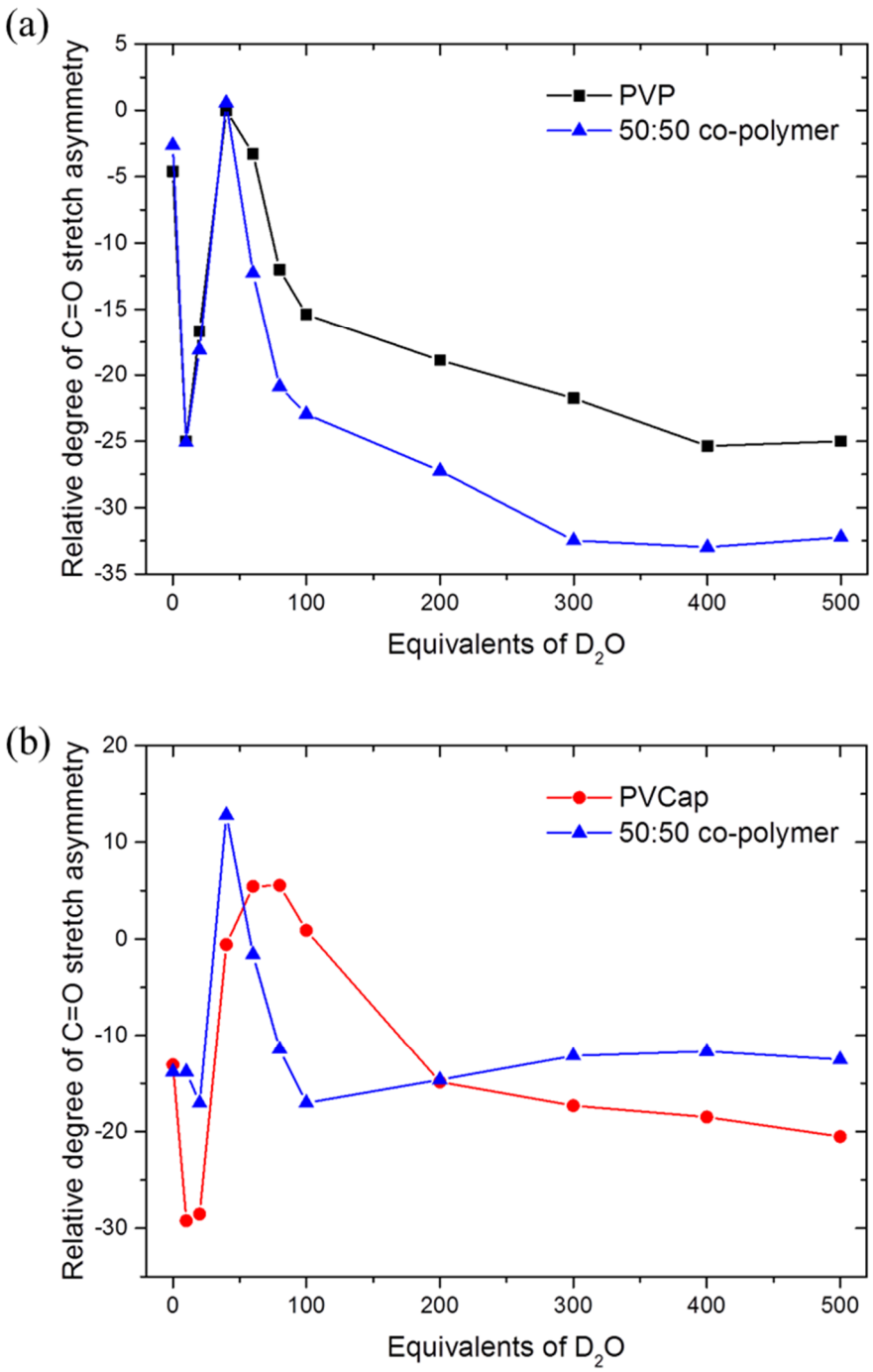

Figure 2.13: Relative degree of C=O stretch asymmetry in the 50:50 copolymer *vs* PVP and PVCap for (a) pyrrolidone component and (b) caprolactam component.

The carbonyl region in the IR spectrum of the 95:5 VCap/VP copolymer is dominated by the caprolactam component, with the pyrrolidone stretch appearing as a broad shoulder throughout the titration, as seen in Figure 2.14. Prior to hydration the carbonyl stretches occur at 1676 cm^{-1} and 1636 cm^{-1} for the pyrrolidone and caprolactam groups respectively. It was not possible to accurately trace the shift in the pyrrolidone *v*(C=O) during the hydration process due its broad nature. As anticipated, the behaviour of the caprolactam band mirrors the behaviour of PVCap.

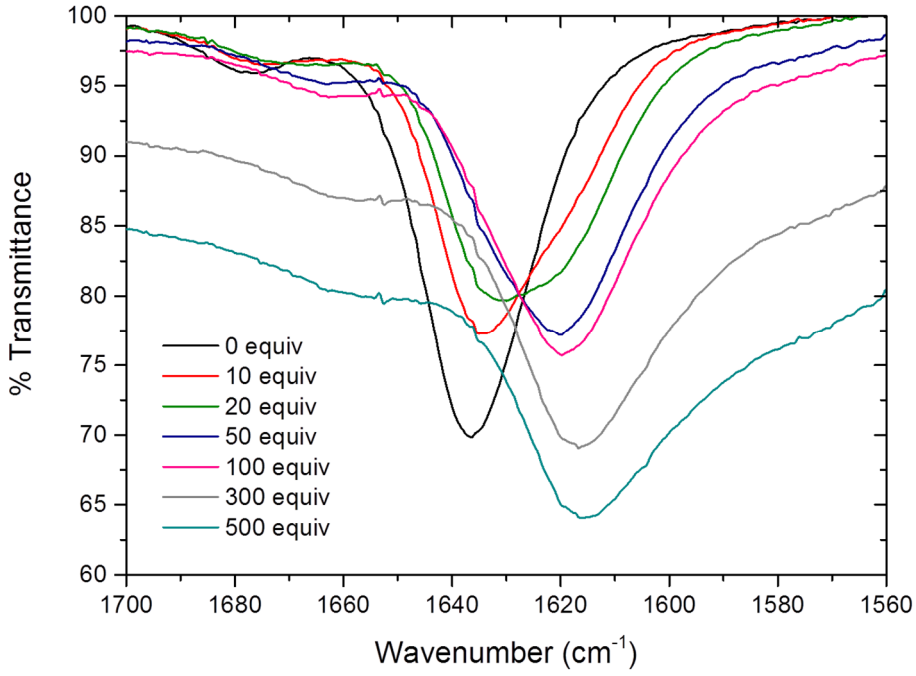

Figure 2.14: Solution IR Titration showing addition of D_2O into an MeCN solution of the 95:5 VCap/VP copolymer.

In conclusion, the transitions of the carbonyl stretch during hydration are similar in all of the polymers studied. This suggests that the hydrated carbonyl environments are unaffected by the incorporation of both 5 and 7-membered rings upon the aliphatic backbone relative to the homopolymers. Three/four hydrated carbonyl bands are observed within the IR spectra for the pyrrolidone and caprolactam functionalities within the copolymers, as previously observed for PVP and PVCap.

Moving away from copolymers containing only lactam functionalities, leads on to the vinyl alcohol-vinyl caprolactam copolymer (VOH/VCap). As outlined in Chapter 1, this species maintains KHI performance relative to PVCap, whilst having improved biodegradability. The powdered KHI was isolated through repeated washing with diethyl ether and proved to be

less soluble than PVCap in anhydrous MeCN. The solid-state IR spectrum shows a broad carbonyl stretch with a band maximum occurring at 1613 cm^{-1}, as seen in Figure 2.15. This low *v*(C=O) wavenumber represents a hydrogen-bonded species, akin to previous examples, however in this instance the shift to the enolate resonance form is believed to be as a result of intra-molecular hydrogen bonding interactions with the polymer OH functionalities. Such an interaction is expected to reduce the hydration potential of the polar C=O group. The carbonyl stretch is broad in the solid-state, indicating the presence of multiple carbonyl environments, but most notably contains a shoulder at higher wavenumber (approximately 1633 cm^{-1}) which is assigned to a "free" non-hydrogen bonded carbonyl stretching mode. In addition, a broad OH stretch occurs at 3500-3150 cm^{-1}, as expected for a hydrogen-bonded species.[16] Dissolution in MeCN, is likely to disrupt the intra-molecular interactions and expose a greater proportion of the carbonyl functionalities. The MeCN solution IR spectrum of the VOH/VCap copolymer has a broad carbonyl stretch at 1635 cm^{-1} with the shoulder occurring at lower wavenumber in this solution, as seen in Figure 2.15. Finally, the OH stretch within the acetonitrile solution is shifted to higher wavenumber, and is split into two sharper peaks; this may indicate the presence of free OH groups in addition to those hydrogen-bonding to the C=O.

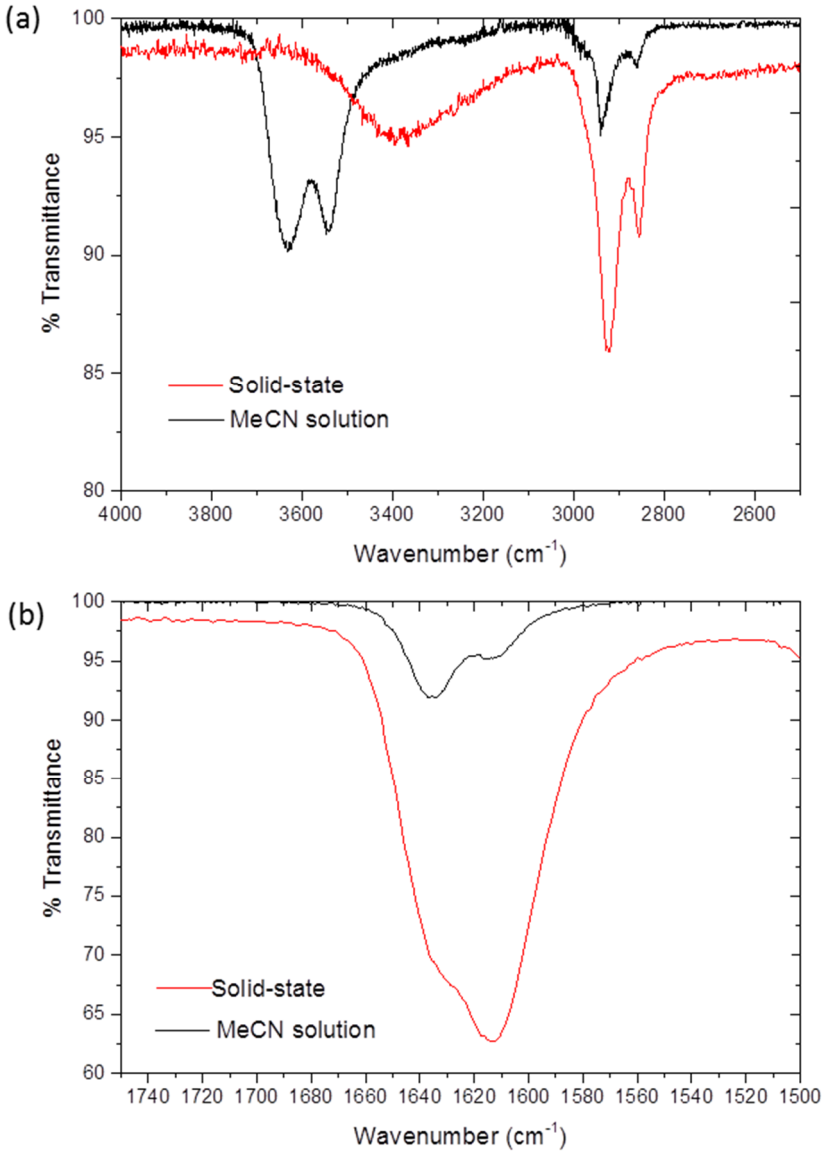

Figure 2.15 IR spectra of VCap/VOH copolymer in the solid-state and as an acetonitrile solution at a concentration of 3.28×10^{-5} moles/mL showing (a) *ν*(OH) and (b) *ν*(C=O)

The low solubility of the VCap/VOH copolymer in acetonitrile led to the use of a solution of lower concentration than in the analogous PVCap and PVP spectra resulting in relatively noisy spectra, as seen in Figure 2.16. Addition of D_2O causes a shift in the carbonyl stretch maximum to lower wavenumber, resulting in a single band at 1609 cm^{-1} following addition of 500 equivalents of D_2O. Carbonyl stretch asymmetry calculations are not reported for this copolymer as a result of the broad nature of this feature.

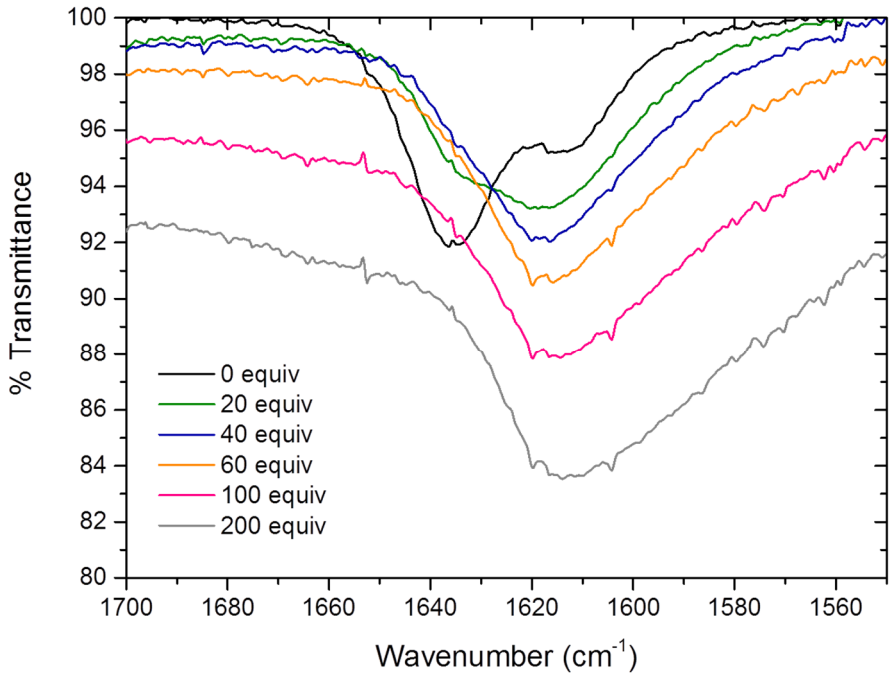

Figure 2.16: Solution IR titration showing addition of D_2O into an acetonitrile solution of the VCap/VOH copolymer.

Finally, Ashland Inc. supply a biodegradable vinyl caprolactam – (hydroxyethyl) methacrylate (VCap/HEMA) copolymer (95:5), as seen in Figure 2.17.[17]

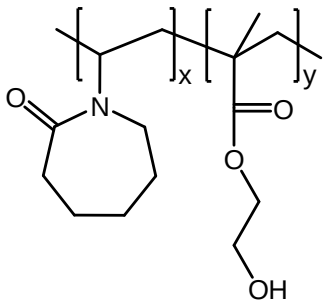

Figure 2.17: Vinyl-caprolactam – (hydroxyethyl) methacrylate (VCap/HEMA) copolymer

Both the caprolactam C=O and HEMA C=O functionalities are apparent in the IR spectrum of an acetonitrile solution of this KHI, occurring at 1636 cm^{-1} and 1720 cm^{-1} respectively, as seen in Figure 2.18. The HEMA component is present in relatively small amounts within the copolymer, and as such is only observed as a broad shoulder of low intensity. During the titration the HEMA carbonyl stretch becomes too broad to accurately determine its shift and asymmetry.

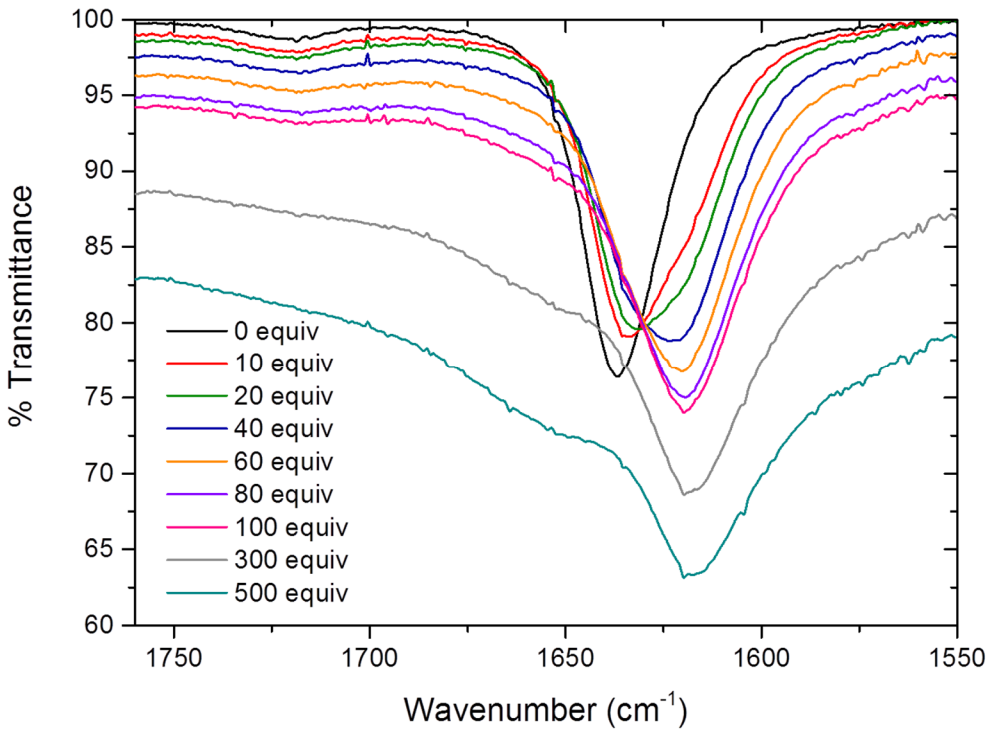

Figure 2.18: Solution IR titration of D_2O into an acetonitrile solution of the VCap/HEMA copolymer at a concentration of 5.38×10^{-5} moles/mL. The HEMA C=O stretch originates at 1720 cm^{-1}.

The caprolactam carbonyl moiety, however, is found to behave analogously to PVCap in terms of wavenumber shift and asymmetry behaviour, as shown in Figure 2.19. This suggests that the appended HEMA arm does not affect the hydration ability of the key caprolactam carbonyl group.

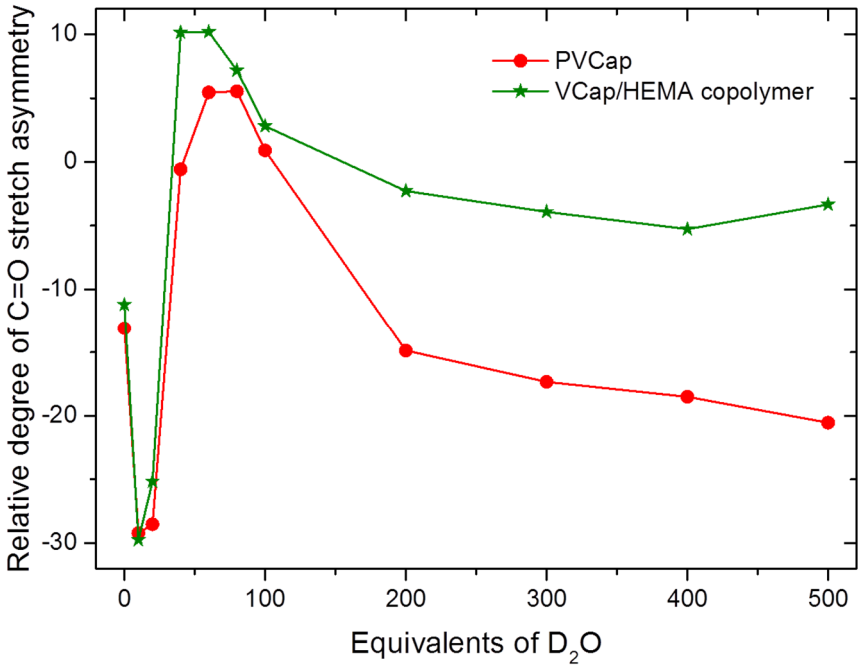

Figure 2.19: Relative degree of C=O stretch asymmetry following addition of D_2O to acetonitrile solutions of the VCap/HEMA copolymer and PVCap.

Finally, Figure 2.20 shows the compilation of the carbonyl stretch asymmetry behaviour during hydration for the KHIs outlined within this Chapter. The relative degree of carbonyl stretch asymmetry is plotted as a function of guest mass/host mass. The ratio of guest mass/host mass is used to allow direct comparison of the KHIs based directly upon the mass of polymer powder used. In conclusion, the solution studies reported highlight the consistent hydration behaviour of the carbonyl moiety within the lactam group of all KHIs examined. The behaviour of this key group is not affected by the incorporation of different functionalities upon the polymer backbone. The change in asymmetry suggests the existence of three/four different hydrated carbonyl environments during the titration in all species.

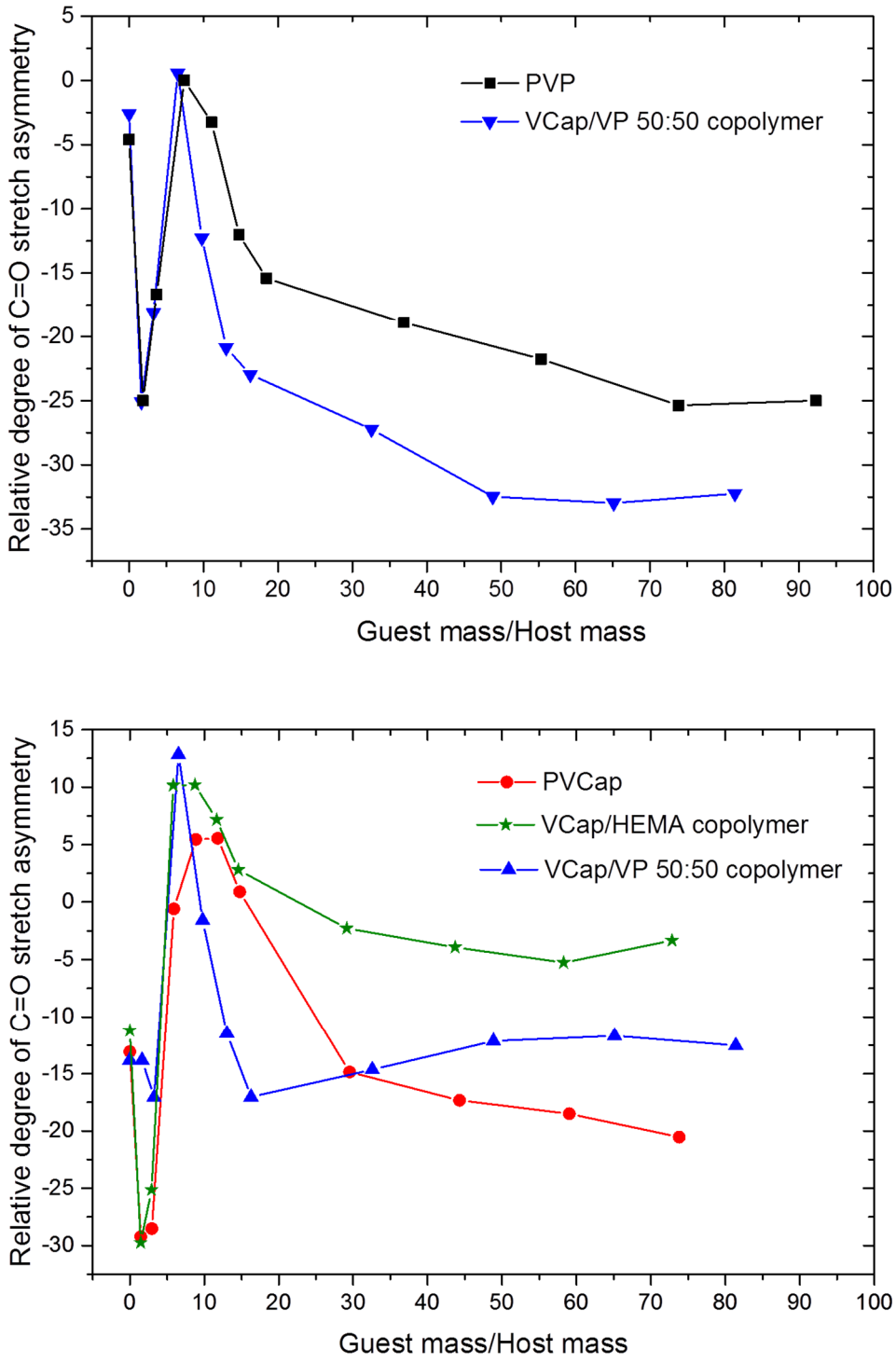

Figure 2.20: Compilation of carbonyl stretch asymmetry *vs* guest mass/host mass for all KHIs examined.

While this work shows no apparent explanation for the superior KHI performance of PVCap, it confirms that different functionalities can be incorporated upon the polymer backbone in order to meet field-conditions without a consequential effect upon the lactam carbonyl hydration.

2.3 Model Compounds

This section reports the synthesis and analysis of a series of small molecule model compounds developed in order to overcome the complexities associated with gaining quantitative information on the solution behaviour of polymers. The model compounds contain the key functionalities from the parent polymer, and in general are bis(lactam) species. As elucidated in Chapter 1, there are a multitude of studies based on monomers, oligomers and polymers looking at the behaviours of these commercially-important compounds. The computational studies by Carver *et al.* into the adsorption behaviours of monomeric and oligomeric units with hydrate cages show that the strongest adsorption occurred when each pyrrolidone oxygen atom formed two hydrogen bonding interactions with the hydrate surface.[1] In addition, Carver found that computational studies of monomeric and dimeric analogues provided sufficient inhibition insight when examining the {001} surfaces of a methane hydrate model.[1] The remainder of this chapter focusses on the experimental solid-state and solution behaviour of dimeric model compounds, and should therefore take into account cooperativity as a result of adjacent lactam units. Such cooperativity effects may be highly significant within the long polymeric units. In addition, where appropriate the behaviours of relevant monomers is included and compared; Figure 2.21 shows the compounds examined in this work.

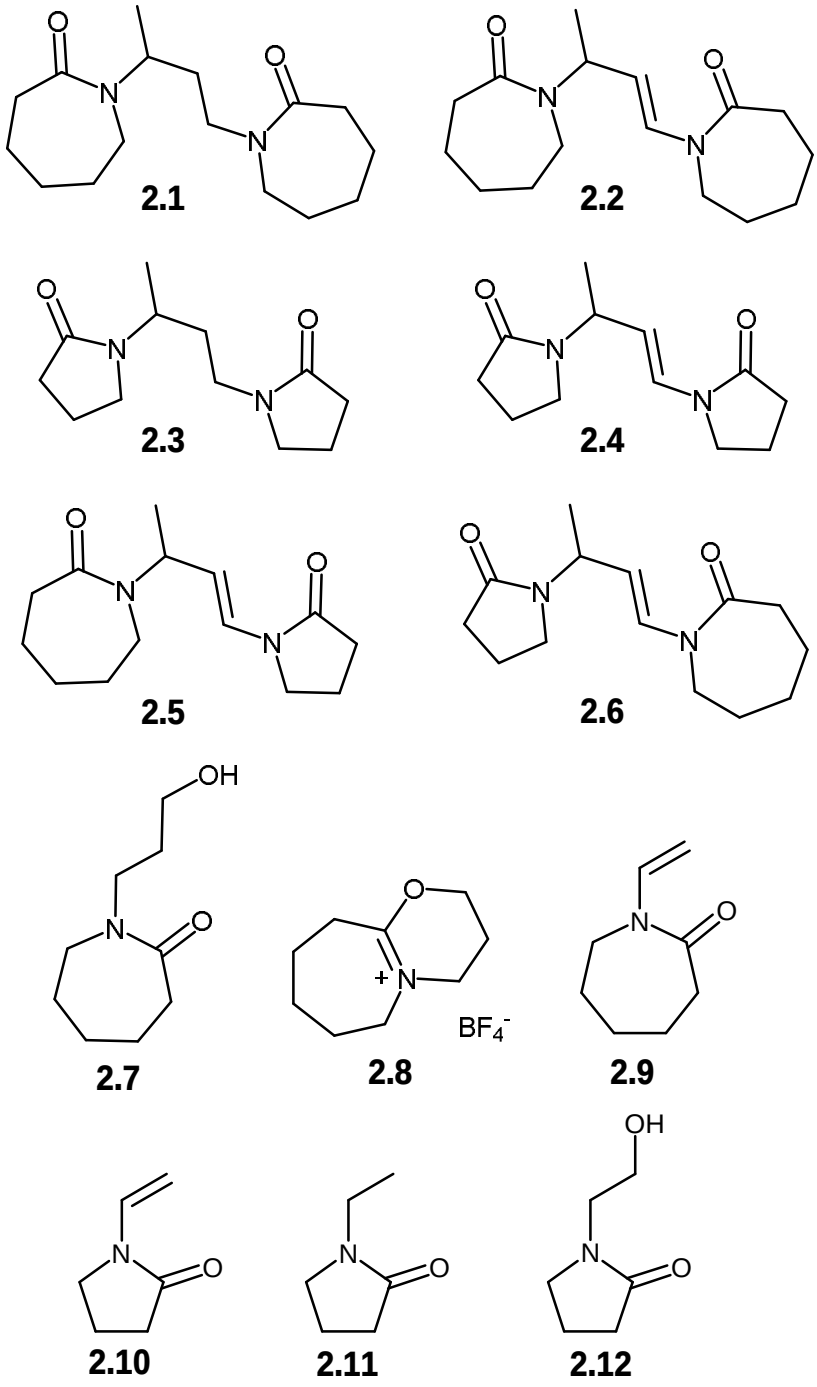

Figure 2.21: Compilation of compounds studied

2.3.1 Synthesis

Previous work within the Steed group established 1,3-bis(caprolactamyl) but-1-ane (**2.1**) as a representative model for the performance of PVCap.[2] A sample of compound **2.1** was supplied by Ashland Inc., and was analysed after extensive drying by holding the sample under vacuum surrounded by refluxing toluene (Abderhalden drying pistol). In this work, an updated synthetic procedure was used to isolate the unsaturated analogue 1,3-

bis(caprolactamyl) but-1-ene (**2.2**), involving use of a trifluoroacetic acid catalyst in hexane solution. This reaction results in the clean isolation of compound **2.2**, which precipitates as a white powder in good yield.

Analogous model compounds 1,3-bis(pyrrolidin-2-on-1-yl) but-1-ane (**2.3**) and 1,3-bis(pyrrolidin-2-on-1-yl) but-1-ene (**2.4**) were chosen to represent PVP. Whilst the saturated analogue **2.3** is expected to be a closer representation of the polymer due to the greater degree of rotational freedom along the methylene backbone, it was interesting to examine the solution behaviour of unsaturated compound **2.4** for comparison. A sample of model **2.3** was kindly supplied by Ashland Inc., and was analysed after extensive drying by holding the sample under vacuum surrounded by boiling toluene.

Zhuo *et al.* have previously reported the synthesis of compound **2.4** through the acid catalysed dimerization of 1-vinyl-2-pyrrolidone (**2.10**) using trifluoroacetic acid in DCM.[18] However, replication of this procedure resulted in an incomplete reaction and the presence of impurities, as confirmed by ^{1}H NMR spectroscopy. Alternatively, reaction of 1-vinyl-2-pyrrolidone with sulphuric acid in cyclohexane results in isolation of **2.4** in good yield. The product is isolated as a viscous yellow oil and despite considerable efforts to crystallise this small molecule no crystalline material was isolated.

Model compounds were also developed for the commercial 50:50 VP/VCap copolymer based on VP/VCap heterodimer analogues. Reaction of a stoichiometric mixture of 1-vinyl-2-pyrrolidone and vinyl-caprolactam in cyclohexane with H_2SO_4 results in a viscous brown oil containing homodimers **2.2** (caprolactam analogue) and **2.4** (pyrrolidone analogue) in addition to heterodimers 1-pyrrolidonyl,3-caprolactamyl but-1-ene (**2.5**) and 1-caprolactamyl,3-pyrrolidonyl but-1-ene (**2.6**). Saturated analogues of **2.5** and **2.6** are the desired model compounds in this work; it was anticipated that following isolation of **2.5** and **2.6** the samples could be hydrogenated using a ThalesNano H-Cube® Continuous-flow hydrogenation reactor. The ^{1}H NMR spectrum of the reaction mixture confirms the ratio of products as shown in Table 2.3.

Product	**2.2**	**2.4**	**2.5**	**2.6**
Composition	20 %	34%	38%	8%

Table 2.3: Distribution of products in the reaction mixture as determined by ^{1}H NMR spectroscopy.

Isolation of the heterodimer components was not trivial as a result of the similarity between the members of this series of compounds. Considerable efforts were made to establish an appropriate solvent system for silica column chromatography, with many solvents resulting in product co-elution. A mixture of ethyl acetate:acetone (3:1) was found to provide the best degree of separation using TLC; however product decomposition occurred upon scaling up from TLC to a preparative column. Therefore, an aqueous aliquot of the reaction mixture was examined using Analytical-HPLC. The mixture was screened using an acetonitrile gradient and a methanol gradient; with both solvents resulting in comparable separation. Three dominant peaks are seen in the chromatograph, with elution times of 3.52, 4.48 and 5.43 minutes corresponding to molecular weights of 223.2, 251.2 and 279.2 respectively, as seen in Figure 2.22. This confirms that separation of these compounds should be achievable. The Mass Spectra for the elution of each compound (Figure 2.22) shows not only a peak corresponding to the molecular ion, but also that of 2M (where M = compound **2.2**, **2.4** – **2.6**). It is believed that molecular aggregation occurs within the mass spectrometer.

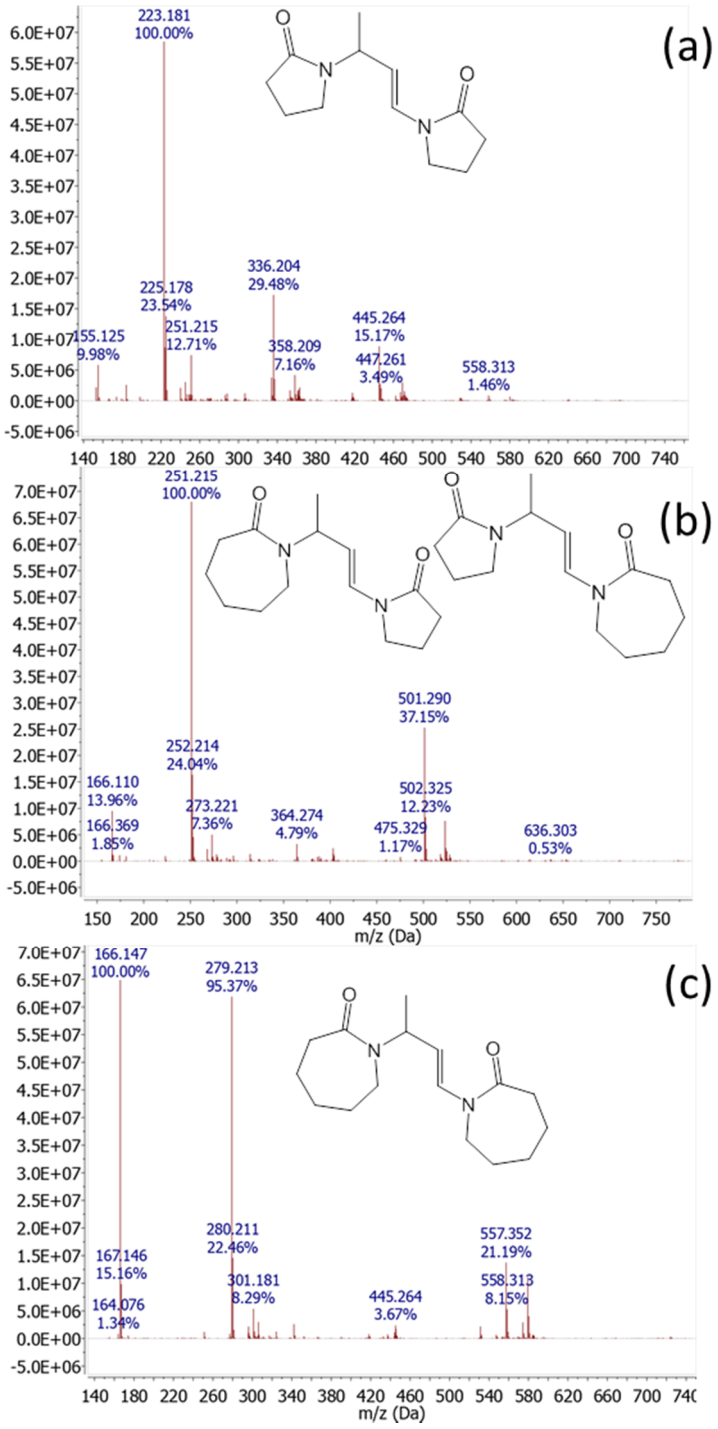

Figure 2.22: Mass Spectra showing HPLC elution products: (a) **2.4** at 3.52 minutes; (b) **2.5** and **2.6** at 4.48 minutes and (c) **2.2** at 5.43 minutes.

The purification was scaled up using Preparative-HPLC with a reverse-phase acetonitrile eluent. Fortunately, each of the compounds contains a chromophore thereby enabling product elution to be monitored by changes in the UV absorbance (λ = 236 nm). The ^{1}H NMR spectra of the evaporated fractions confirmed separation of **2.2** and **2.4**, in addition to the co-elution of heterodimers **2.5** and **2.6**. The heterodimers are expected to behave

analogously within HPLC because they have the same molecular weight and very similar polarity. Separation of the heterodimer isomers was deemed unnecessary because upon saturation the species would be near-identical, differing only in the position of the methyl substituent. Figure 2.23 shows the partial ^{1}H NMR spectra of the reaction mixture in addition to the individual components following HPLC, confirming clean separation. The main differences in the spectra are found in the position of the alkene and NCH protons.

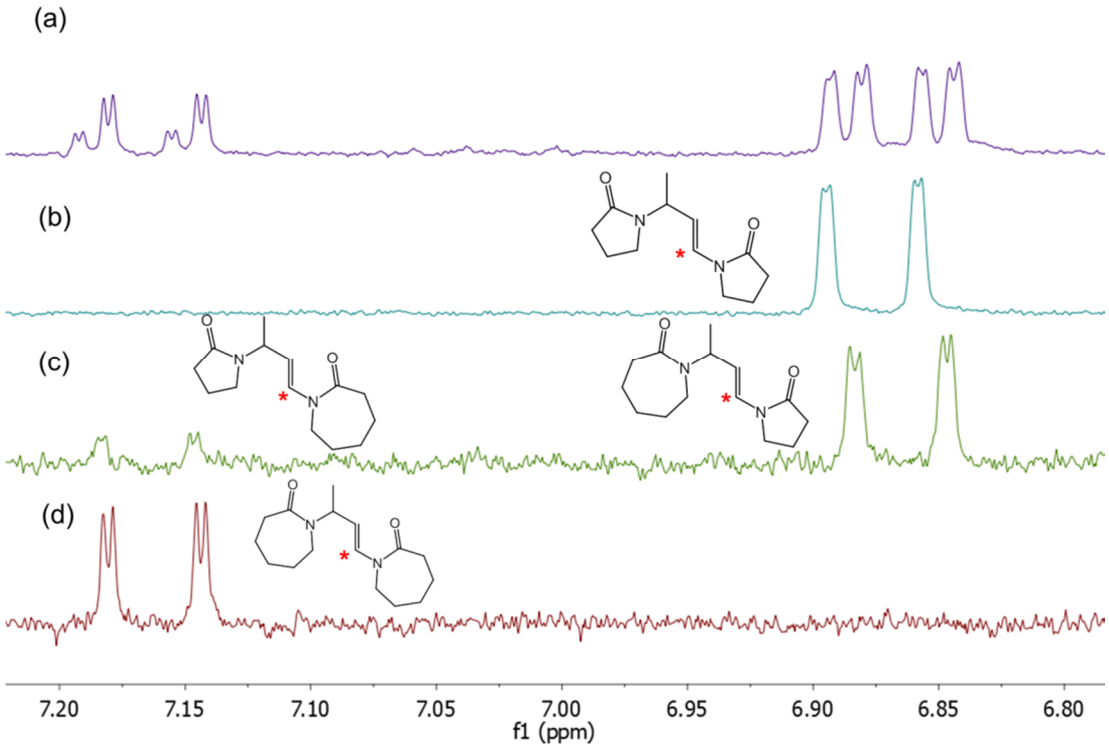

Figure 2.23: Partial ^{1}H NMR spectra highlighting the position of the NCH proton in (a) the reaction mixture and (b)→(d) each of the dimers illustrated.

Unfortunately, HPLC instrument problems prevented the isolation of sufficient material of compounds **2.5** and **2.6**. Therefore, the desired solution analysis was not possible, and work upon these species was concluded. It was possible to isolate good quality single crystals of heterodimer **2.5**, and the X-ray crystal structure is included in Section 2.3.2 (*vide infra*). Detailed analysis of these analogues will form part of the future work.

Finally, hexahydro-1-(3′-hydroxypropyl)-*2H*-azepin-2-one (**2.7**) was chosen as the model compound for the commercial vinyl alcohol-vinyl caprolactam copolymer. Compound **2.7** was synthesised according to the procedure reported by Gracias *et al*. as shown in Scheme 2.4.[19]

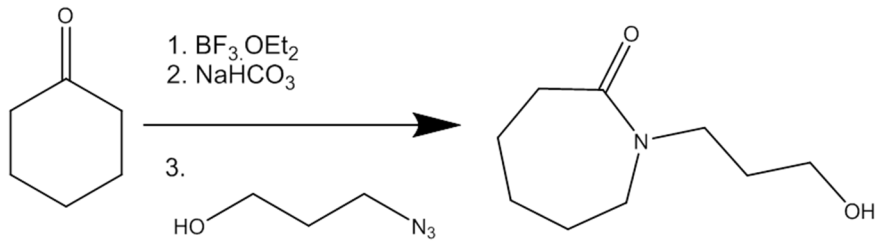

Scheme 2.4: Reaction of cyclohexanone with 3-azido-1-propanol for the formation of compound **2.7**

The reaction was undertaken in two stages; firstly involving the *in situ* formation of 3-azido-propanol, followed by reaction with cyclohexanone. 3-azido-propanol was synthesised from sodium azide and 3-chloro-propanol according to the procedure reported by Sumerlin *et al.*,[20] however, for safety reasons[1] the reaction was performed on a small scale and at higher dilution. As a result of the reduced product concentration, there were difficulties in extraction using diethyl ether, with much of the small organic azide remaining in the aqueous phase, and thereby limiting the overall reaction yield. Fortunately, Sigma-Aldrich made 3-azido-propanol commercially available during the period of study, thereby removing the need for the first step in the synthetic scheme.

The second stage of the reaction proceeds by a ring expansion process *via* a bicyclic intermediate, namely 2,3,4,5,6,7,8,9-octahydro-1-oxa-4a-azonia-benzocycloheptene tetrafluoroborate (**2.8**).[19, 21] The $BF_3.OEt_2$ acts as a Lewis acid in order to facilitate the reaction, and forms the counteranion (BF_4^-) in the intermediate species **2.8**. Recrystallization of the crude reaction mixture from DCM/diethyl ether *via* slow evaporation enables isolation of good quality crystals of compound **2.8**. The X-ray single crystal structure is shown in Figure 2.24. Fenster *et al*. reported the hydrolysis pathway for the ring opening of this intermediate to enable isolation of the final product.[21] The oxygen atom present in intermediate **2.8** transforms into the pendant alcohol arm in the final product, while the carbonyl oxygen atom originates from addition of aqueous sodium bicarbonate.[21]

[1] Sodium azide and small organic azides are known to be unstable and potentially explosive compounds. Additional precautions were taken including the use of a blast shield throughout the experiment. It is worth noting that no problems were experienced with this reaction.

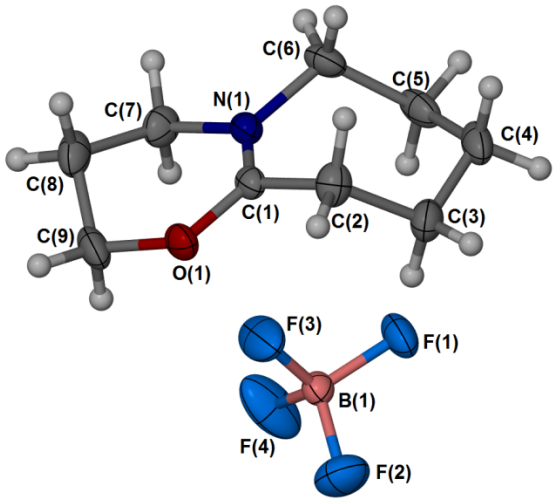

Figure 2.24: X-ray single crystal structure of the reaction intermediate (**2.8**). Thermal ellipsoids are shown at 50% probability.

Further washing of the intermediate with sodium bicarbonate ensures complete hydrolysis and yields the product as a yellow oil. A minor impurity (~10%) is visible in the ^{1}H NMR spectrum, removable through silica column chromatography using an ethyl acetate eluent. The final product was rigorously dried under vacuum at 110 ^{o}C in an Abderhalden drying pistol.

2.3.2 Structural Analysis

This section outlines the X-ray crystallographic analysis for the lactam compounds summarised in Figure 2.21, as applicable. While X-ray crystallography provides insight into the solid-state arrangement of molecules, the key interactions highlighted by this analysis may enhance the understanding of the solution behaviour of such species. Most notably, crystallographic analysis highlights the polarity of the amide carbonyl moiety (*vide infra*), which is believed to be crucial to polymer KHI performance.

The Steed group have previously reported the single crystal X-ray structures of compounds **2.1** and **2.2** in their pure form,[2] showing strong CH···O interactions between the C=O group and an alkene proton within the unsaturated compound **2.2**. Crystals of pure **2.1** were isolated by extensive drying of the oily product, while recrystallization from acetone produced crystals of **2.2**.[2] The isolation of a hydrated or solvated crystalline analogue would provide additional information into the hydration modes of the carbonyl moieties. With this target in mind, a series of recrystallizations of **2.1** and **2.2** were undertaken. A plethora of solvents were used, with crystalline material of compound **2.2** isolated upon evaporation of

2-propanol, acetonitrile, 2-butanone and ethyl acetate, in addition to acetone. However, unit cell determination of the resulting crystals showed that the known solid forms were obtained in all cases. *In situ* crystallization is an alternative technique used to grow single crystals directly from liquid samples *via* a freeze-melt process.[22] This technique was used for aqueous solutions of compounds **2.1** and **2.2**, of varying concentration. Crystalline material was isolated, however, the unit cell determination confirmed formation of hexagonal ice in all instances.

Despite considerable efforts to crystallize compounds **2.3** and **2.4**, no crystalline material was formed. It is believed that the hygroscopicity of these species makes crystallization unlikely resulting in the substances occurring as oily residues in all instances. However, a metal-bound coordination complex of compound **2.3** is reported in Chapter 5, providing insight into the polarity of the pyrrolidone carbonyl moiety.

In contrast, it did prove possible to isolate diffraction quality crystals of heterodimer **2.5** and the X-ray molecular structure is shown in Figure 2.25. This heterodimer analogue crystallises concomitantly with compound **2.2** from an acetone/hexane mixture following slow evaporation of solvent. Due to the small crystal size, samples were analysed using I19 at Diamond, Oxford, by Dr. K. Fucke. The nitrogen-carbonyl bond distances are shorter than the N-C(ring) distances as consistent with the partial double bond character for the N-C(O) bond upon transition to the enolate resonance form. The bond distance for N(1)-C(1) at 1.365(2) Å is marginally shorter than that for N(2)-C(11) (1.373(2) Å), although the difference is not statistically significant at the 3σ level.

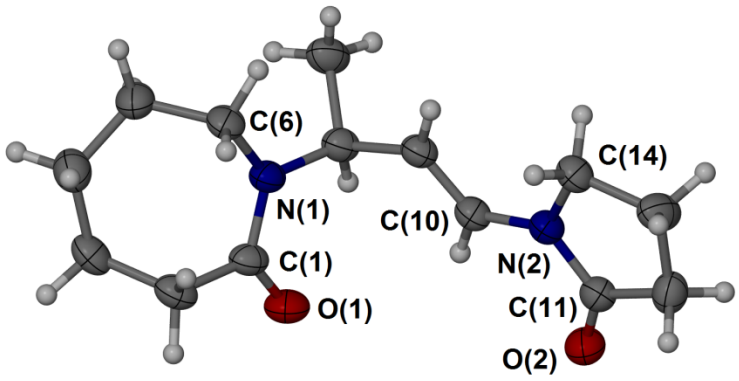

Figure 2.25: X-ray molecular structure of 1-pyrrolidonyl,3-caprolactamyl but-1-ene (**2.5**). Thermal ellipsoids are shown at 50% probability. Selected bond distances (Å): N(1)-C(1) 1.365(2), N(1)-C(6) 1.473(2), N(1)-C(7) 1.487(2), C(1)-O(1) 1.236(2), N(2)-C(10) 1.407(2), N(2)-C(11) 1.373(2), N(2)-C(14) 1.469(2), C(11)-O(2) 1.231(2).

The crystal packing in this compound, shown in Figure 2.26, is based on CH···O interactions between the pyrrolidone carbonyl group and hydrogen atoms of a neighbouring pyrrolidone (with C···O distances of 3.461(3) Å and 3.490(3) Å), in addition to CH···O interactions between the caprolactam carbonyl functionality and the alkene group. The caprolactam carbonyl moiety is a better acceptor than the pyrrolidone analogue, and as such interacts with the stronger hydrogen bond donor of the alkene group rather than a ring-CH_2. The caprolactam carbonyl-alkene interaction is marginally longer than that within the caprolactam homodimer, with distances of 3.390(3) Å and 3.320 Å for compounds **2.5** and **2.2**[2] respectively.

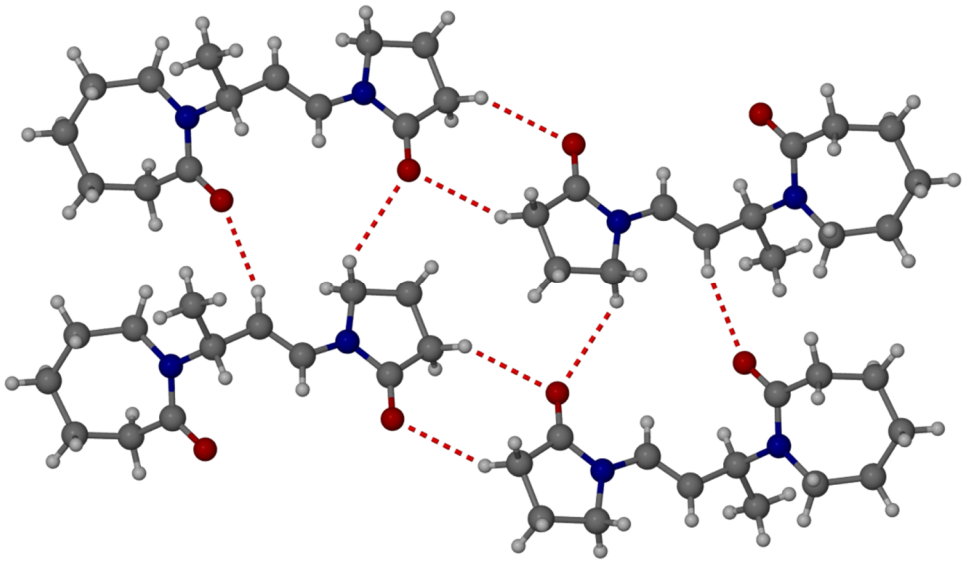

Figure 2.26: Crystal packing of compound **2.5**.

The asymmetric nature of this compound results in less optimal packing than within unsaturated homodimer **2.2**, as established by the densities of 1.207 g/cm^3 and 1.231 g/cm^3 for **2.5** and **2.2**[2] respectively (both at 120 K). Hirshfeld surfaces are a commonly used visualisation tool implemented within the crystallography community to enable the examination of intermolecular interactions and packing in a crystal.[23] The surfaces outlined in this work were generated by Crystal Explorer, using the finalised *.cif* for each molecule of interest. As seen in Figure 2.27, a 3D surface is mapped onto the X-ray molecular structure. The surface is generated by the software suite, taking into consideration the electron distribution in the individual molecule and over the entire crystal. The red-white-blue colour scheme shows the comparison of intermolecular contacts.

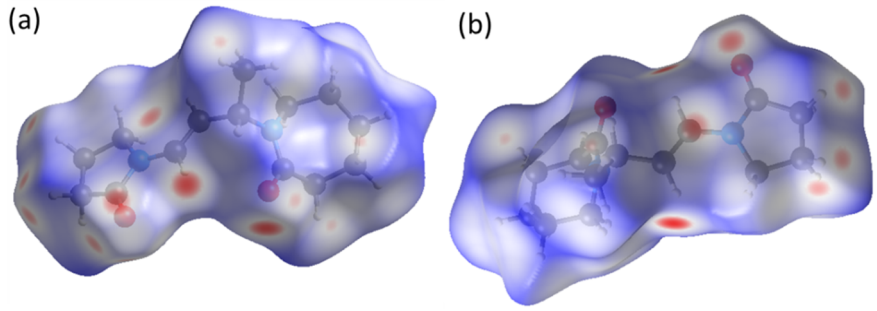

Figure 2.27: Hirshfeld surface mapped onto the X-ray crystal structure for compound **2.5**, red colouration shows interactions at (a) carbonyl moieties and (b) alkene CH group.

For ease of comparison, the surfaces are often examined following generation of a 2D fingerprint plot, as seen in Figure 2.28; these plots allow the interactions to be compared amongst the series of molecules. The fingerprint plot shows d_e vs d_i where d_e represents the distance from the surface to the nearest nucleus outside of the surface, and d_i represents the distance from the surface to the nearest nucleus inside of the surface.[23] This work is focussed on examining interactions at the lactam carbonyl moieties, as these are believed to be of most interest in the consideration of inhibitor behaviour. The Hirshfeld surface fingerprint plots, shown in Figure 2.28, illustrate the dominance of the intermolecular CH···O interactions (arrows), appearing more pronounced in compound **2.2** than **2.5**. In addition, the fingerprint plot for **2.5** has two "wings" as a result of CH···π interactions.

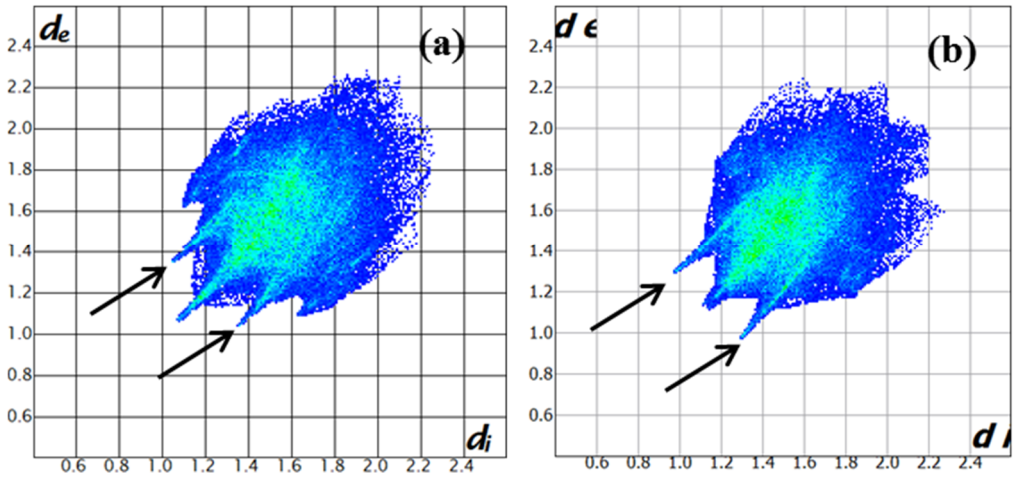

Figure 2.28: Hirshfeld surface fingerprint analysis for (a) **2.5** and (b) **2.2**. Black arrows show the CH···O interactions. Two "wings" in (a) correspond to CH···π interactions.

The X-ray crystal structure of 1-vinyl-2-pyrrolidone (**2.10**) was also obtained and offers additional insight into pyrrolidone interactions in the solid-state. Compound **2.10** was purchased from Sigma-Aldrich as a pale yellow liquid, with a reported melting point of 13-14

°C. *In situ* crystallization performed by loading the liquid sample into a borosilicate glass capillary and subjecting the sample to a series of heating and cooling cycles induces the formation of a crystalline sample suitable for single crystal X-ray analysis (see Experimental section for details). Two datasets were collected, at 260 K and 150 K, and the material proved to be the same phase at both temperatures. Figure 2.29 shows the X-ray crystal structure at 150 K.

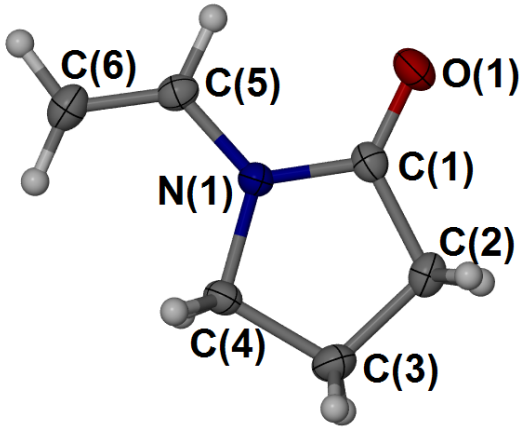

Figure 2.29: X-ray molecular structure of 1-vinyl-2-pyrrolidone (**2.10**) at 150 K. Thermal ellipsoids are shown at 50% probability.

The carbonyl oxygen atom forms a bifurcated acceptor CH···O hydrogen-bond to two hydrogen atoms of the alkene functionality, with C···O distances of 3.3519(13) Å (C5-O1) and 3.3837(15) Å (C6-O1), as shown in Figure 2.30. In addition, there is a longer interaction between the carbonyl oxygen atom of one molecule with a lactam-CH_2 functionality on an alternative molecular plane. The Hirshfeld surface fingerprint plot is shown in Figure 2.33 alongside compounds **2.9** and **2.12** (*vide infra*).

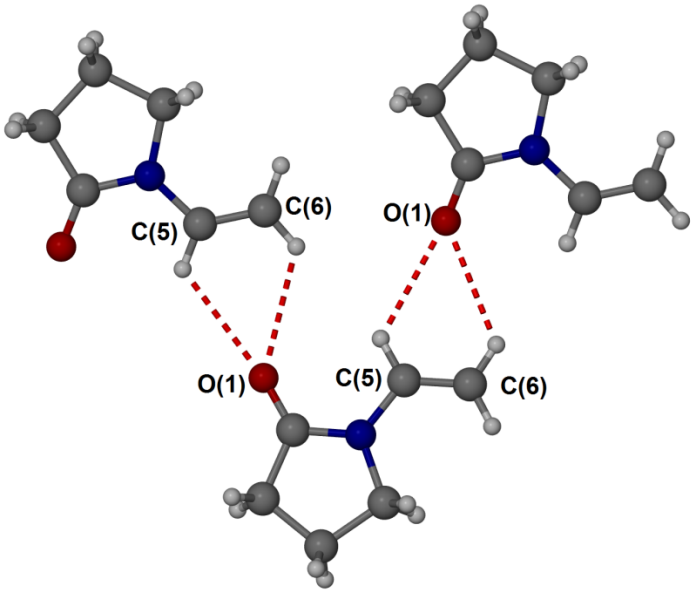

Figure 2.30: Crystal packing in 1-vinyl-2-pyrrolidone (**2.10**) at 150 K

Comparison between this unsaturated small lactam species with the 7-membered analogue is possible using the X-ray crystal structure of *n*-vinyl caprolactam (**2.9**) reported by Tishchenko *et al*. in 1997 (CSD refcode NUQYED).[24] Interestingly, the crystal packing differs from the pyrrolidone analogue, with a notable absence of a hydrogen bonding interaction between the caprolactam carbonyl moiety and the alkene-NCH proton, as seen in Figure 2.31. The X-ray crystallographic analysis for **2.9** was conducted at room temperature; therefore it is not reliable to draw comparisons to compound **2.10** or to elucidate many conclusions from the occurrence of longer C···O interactions (3.461 Å) in **2.9**.

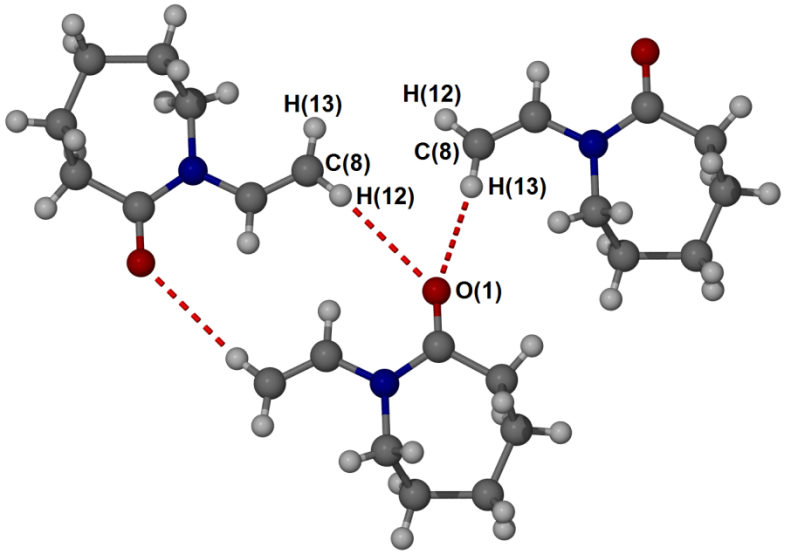

Figure 2.31: Crystal packing of *N*-vinyl caprolactam (**2.9**) as reported by Tishchenko *et al*.[24]

Single crystals of 1-ethyl-2-pyrrolidone (**2.11**) could not be isolated through *in situ* liquid crystallization, and repeated melt-freeze cycles resulted in the formation of a glass at low temperature. The lower melting point of -77 ^{o}C for this compound, lack of a good hydrogen-bond donor, in addition to the flexibility and rotational freedom of the saturated ethyl arm may impede crystallisation. In addition, a series of mixtures of **2.10**/**2.11** and 1-(2-hydroxyethyl)-2-pyrrolidone (**2.12**)/**2.11** were cooled within glass capillaries in an attempt to isolate a co-crystal, however, this also proved unsuccessful due to the formation of a glass in all instances.

While it was not possible to isolate crystalline material of the hydroxy-caprolactam compound **2.7**, it is anticipated that the solid-state structure of the pyrrolidone analogue **2.12** may provide insight into potential interactions in copolymers based on this type of repeat unit, particularly regarding the issue of intramolecular as opposed to intermolecular hydrogen bonding interactions, as noted in the VCap/VOH copolymer in Section 2.2. Flash cooling of **2.12** using a dry ice/acetone bath resulted in crystallisation of the yellow liquid. The hygroscopic nature of this lactam is highlighted by the rapid liquification of this crystalline material upon exposure to atmosphere. This process is apparently a result of the compound's deliquescence (dissolution of the solid material in absorbed atmospheric water). When crystalline material is held in a sealed environment, at room temperature, it remains solid indefinitely; however dissolution occurs within 15 minutes upon exposure to air. The X-ray crystal structure, collected at 120 K, demonstrates the presence of a short intermolecular

hydrogen-bond between the hydroxyl donor and lactam carbonyl acceptor, with an O···O bond distance of 2.747(2) Å, Figure 2.32.

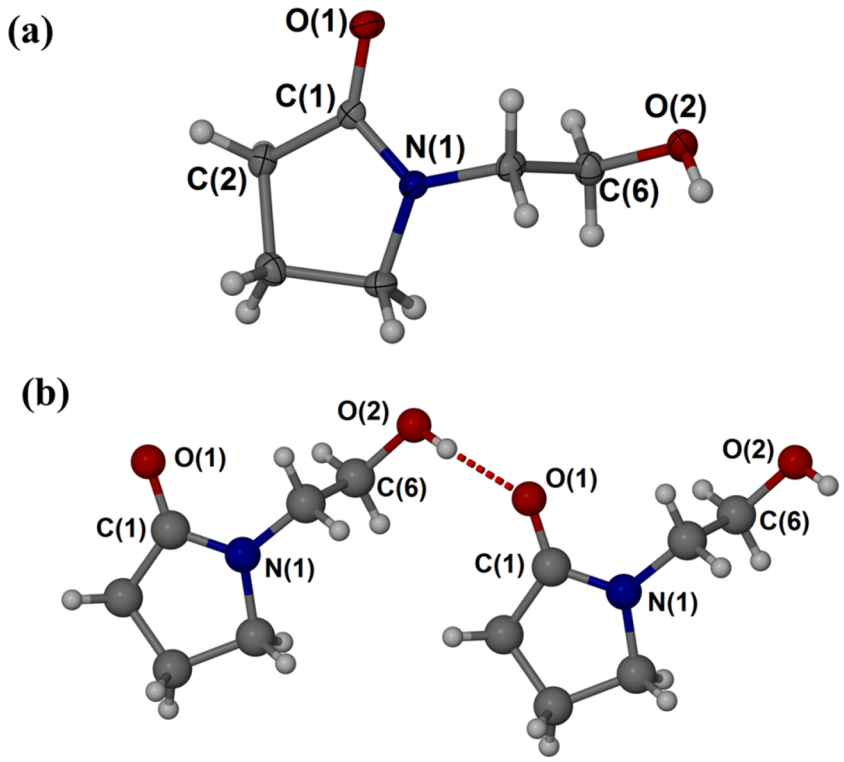

Figure 2.32: X-ray crystal structure of **2.12** collected at 120 K, (a) asymmetric unit (thermal ellipsoids are shown at 50 % probability), (b) intermolecular hydrogen bonding interaction between two molecules.

The Hirshfeld surface fingerprint plot for **2.12** is dominated by the intermolecular OH···O interactions, as seen in Figure 2.33. Assuming that similar intermolecular interactions occur in the 7-membered analogue **2.7** and also in the VCap/VOH copolymer may explain the reduced solubility of the polymeric KHI in solvent. Intermolecular interactions would reduce the availability of the polar functionalities, and may lead to increased polymer aggregation with the polar groups inside the aggregate and an outward facing shell of greater hydrophobicity. In addition, such interactions would likely reduce the hydration potential of the species.

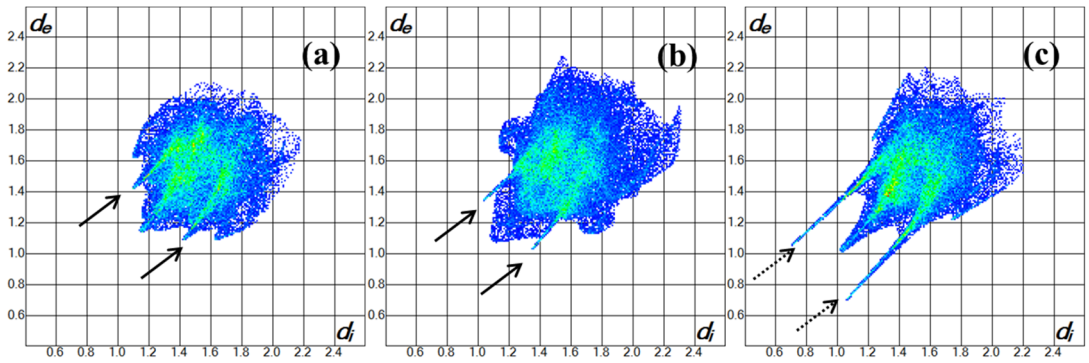

Figure 2.33: Hirshfeld surface fingerprint plots for (a) **2.10**, (b) **2.9** and (c) **2.12**. Solid black arrows on (a) and (b) show CH···O interactions, dashed black arrow on (c) highlights the OH···O interactions. The two "wings" in (b) represent CH···π interactions.

2.3.3 Solution Analysis

Having established the importance of the amide carbonyl group for lactam interactions within the solid-state, the hydration behaviour of this key moiety was monitored using IR spectroscopy and ^{1}H NMR spectroscopy. Details of the hydration behaviour of caprolactam dimers **2.1** and **2.2** have been reported previously by the Steed group,[2] however, the solution analysis for the saturated analogue has been repeated within this work to ensure consistency with the present experiments and enable direct comparison to the other compounds within the series. The conclusions of this work are included later in this section in a comparison to the 5-membered analogue **2.3** (*vide infra*).

Hydration of dimeric pyrrolidone species **2.3** and **2.4** has not previously been investigated. While the saturated analogue is expected to be a closer representation of PVP due to the greater degree of rotational freedom along the aliphatic backbone, it was interesting to examine the solution behaviour of the unsaturated species for comparison. The IR spectrum of an acetonitrile solution of compound **2.4** contains two carbonyl stretches, at 1701 cm^{-1} and 1680 cm^{-1}, as a result of the two distinct carbonyl functionalities. Unfortunately, the *v*(C=C) band occurs at 1663 cm^{-1} in MeCN, and hence overlaps with the carbonyl stretches upon hydration, as seen in Figure 2.34. It is therefore not possible to accurately trace the *v*(C=O) shifts during the titration.

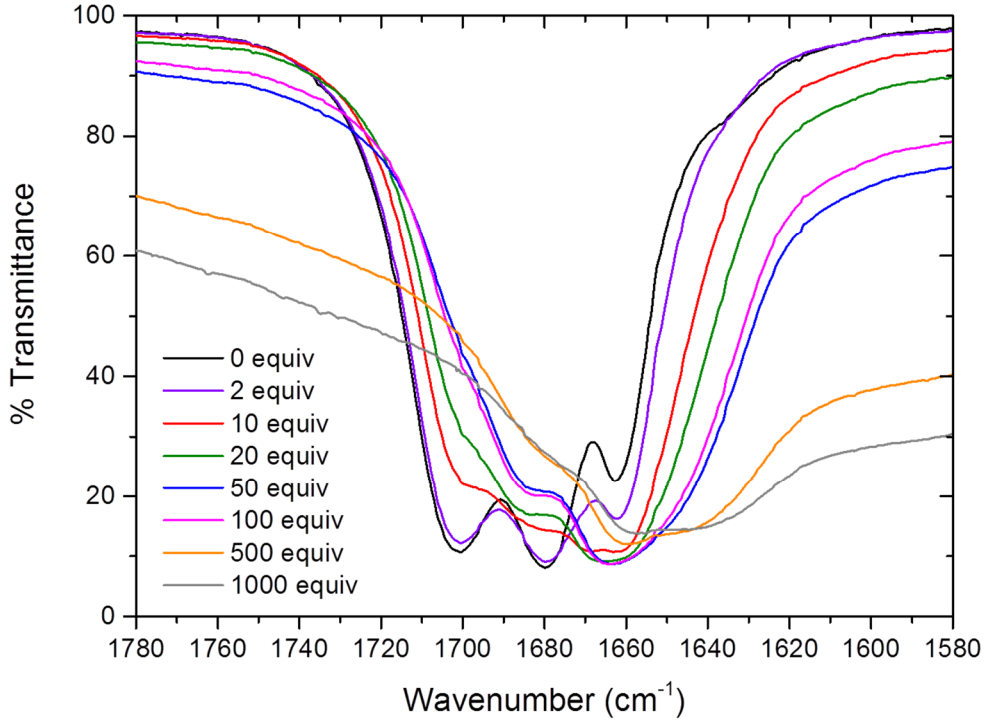

Figure 2.34: Solution IR titration showing addition of D_2O into an MeCN solution of 1,3-bis(pyrrolidin-2-on-1-yl) but-1-ene (**2.4**). Starting solution concentration = 1.098×10^{-4} moles/mL.

IR spectroscopic measurements on saturated **2.3** as a neat film shows *v*(C=O) at 1654 cm^{-1} and at 1639 cm^{-1} as a 1wt% D_2O solution; these are shifted to lower wavenumber in comparison to PVP (1668 cm^{-1} and 1645 cm^{-1}) potentially due to a greater degree of hydrogen bonding interactions within the small molecule. However, the carbonyl stretch occurs at 1681 cm^{-1} in anhydrous MeCN solution, the same wavenumber as PVP K12, indicating that the apolar solvent successfully disrupts intermolecular hydrogen bonding within the species and enables the ν(C=O) in **2.3** to appear equivalent to the parent polymer. For ease of comparison, the equivalents of D_2O are calculated with respect to equivalents per lactam moiety in order to allow direct comparison between PVP and model compounds. Hydration of the carbonyl moiety is observed by a shift from 1681 cm^{-1} to 1647 cm^{-1} upon addition of 500 molar equivalents of D_2O per lactam group, as seen in Figure 2.35. The greater accessibility of the carbonyl functionalities within the small dimer molecule may enable the binding of additional water, in contrast to the more sterically hindered polymer. This is further highlighted by the greater cumulative wavenumber shift for **2.3** of 33 cm^{-1} compared to 24 cm^{-1} for PVP.

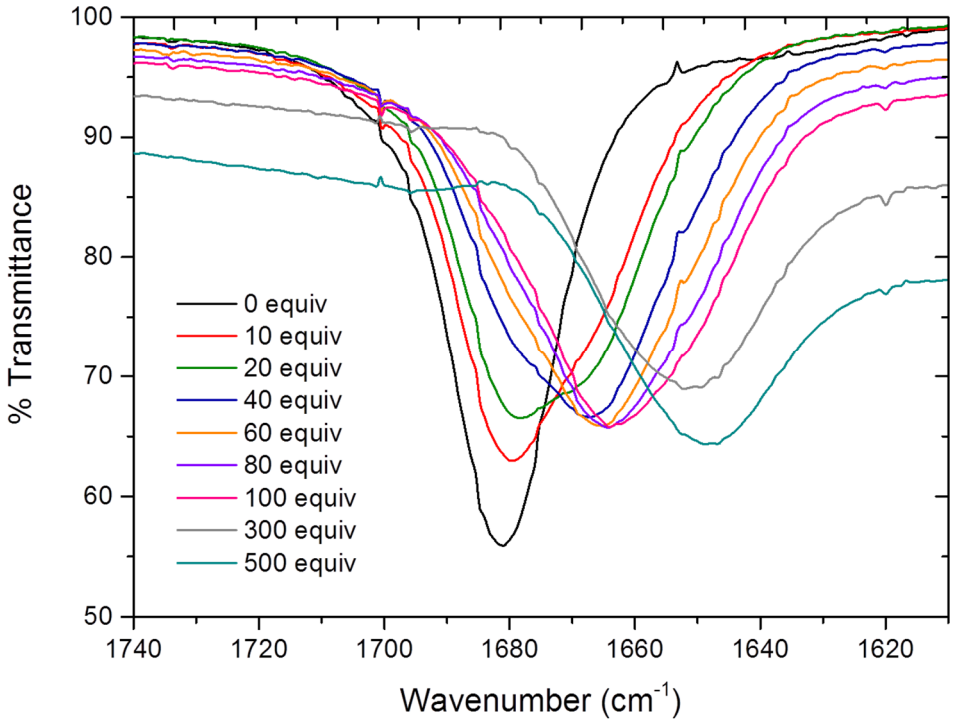

Figure 2.35: Solution IR spectroscopic titration showing addition of D_2O into an MeCN solution of compound **2.3**. Equivalents of D_2O are calculated per lactam moiety.

In the literature the behaviour of pyrrolidone monomers **2.10** and **2.11** have been computationally modelled to provide insight into the mode of action of KHIs.[1, 3] In order to examine the reliability of use of these monomeric lactam species as model compounds, their solution behaviour was investigated. The *v*(C=O) bands occur at 1704 cm^{-1} and 1681 cm^{-1} in anhydrous MeCN solutions of **2.10** and **2.11** respectively. This indicates greater carbonyl double bond character in unsaturated vinyl-pyrrolidone, which may be as a result of some delocalisation of the nitrogen lone pair by conjugation with the alkene functionality.[7] Therefore, saturated **2.11** is expected to be better than **2.10** as a model for PVP due to the absence of the double bonded vinyl group. Figure 2.36 shows the IR titration data tracing the addition of D_2O to an acetonitrile solution of ethyl-pyrrolidone (**2.11**).

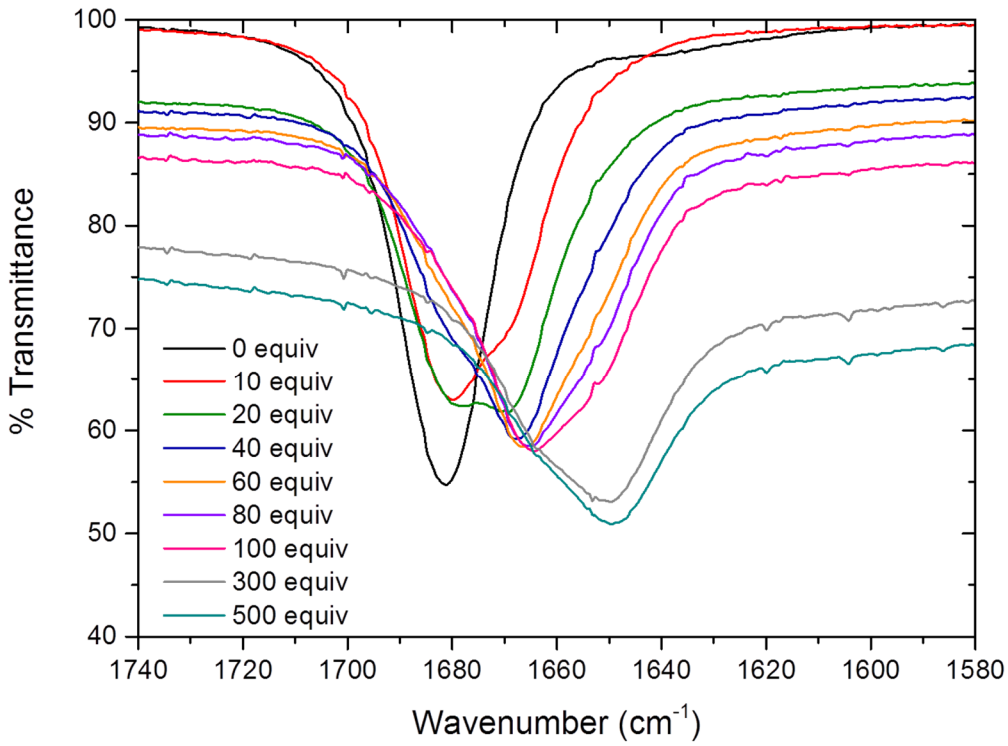

Figure 2.36: Solution IR titration showing addition of D_2O into an MeCN solution of ethyl pyrrolidone **2.11**. Starting solution concentration = 5.3×10^{-5} moles/mL.

Changes in the relative degree of carbonyl stretch asymmetry during titration validates the use of compound **2.3** as a model for PVP, as shown in Figure 2.37, alongside the data for saturated monomer **2.11**. The asymmetry trend for **2.3** upon addition of up to 100 D_2O equivalents closely mirrors that for PVP during the same initial hydration, with both plots showing three gradient changes. While the plot of the monomer data also shows three changes in gradient following addition of up to 100 D_2O equivalents, the second hydrated carbonyl stretch occurs at lower D_2O equivalents than for PVP and **2.3**, occurring at 20 equivalents in **2.11** and at 40 equivalents for the dimer and polymer. The reduced steric hindrance in the monomer may make the carbonyl moiety more accessible to water, and therefore hydration could occur more readily. However, it is worth noting that further hydration (100 – 500 D_2O equivalents) results in an additional two hydrated carbonyl environments for the monomer and dimer, whilst only one further environment for PVP. Overall it appears that the dimeric compound is more suitable as a model for the hydration behaviour of PVP, particularly when considering the first three hydrated environments.

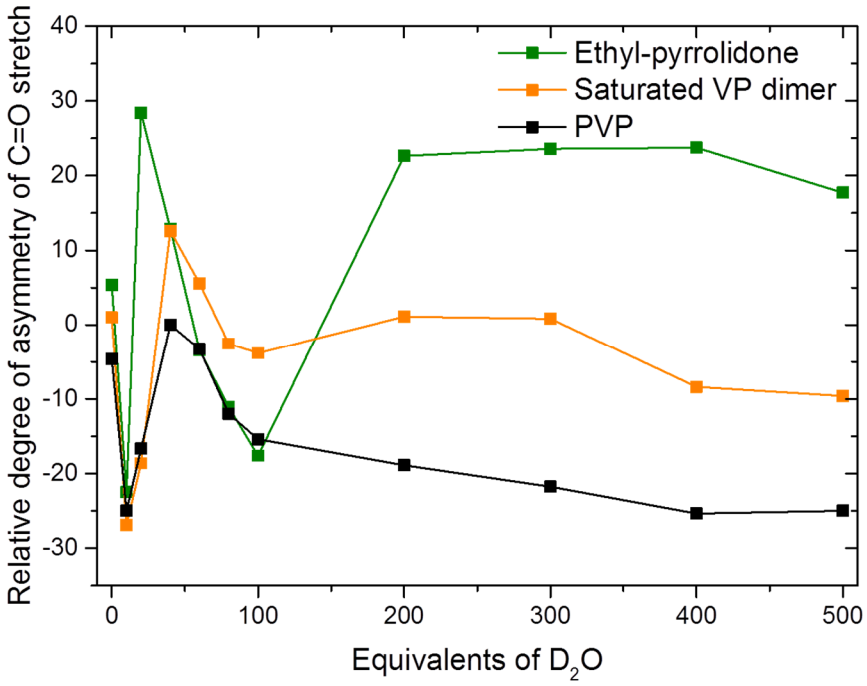

Figure 2.37: Comparison between the changes in the relative degree of carbonyl stretch asymmetry for PVP, **2.3** and **2.11**. Equivalents of D_2O are quoted per lactam unit.

Quantitative insight into guest binding may also be obtained through use of ^1H NMR spectroscopic titration.[25] In this work, the model compound is considered to be the host (H) whilst D_2O is the guest (G). Titrations were performed by dissolving the dried lactam species in anhydrous acetonitrile-d_3 to generate a homogeneous solution of known concentration. Known equivalents of D_2O were added, the sample thoroughly mixed and spectra analysed with chemical shifts (ppm) referenced to the residual solvent. D_2O equivalents are based on the entire molecule, in order to gain insight on a single guest bridging both carbonyl groups, in addition to water molecules binding to separate functionalities. Upon hydration, the amide functionality will undergo a change in resonance form, with donation of the lone pair of electrons from the nitrogen atom causing a partial negative charge to be localised on the carbonyl oxygen atom. This would result in a slight change in the shielding of the nearby protons, which can then be monitored as changes in the chemical shifts. It is anticipated that the reduced ring strain in the caprolactam group (in comparison to the pyrrolidone ring) would result in a significantly greater contribution to the enolate resonance form.

In the pyrrolidone species a shift to the enolate resonance form results in slight deshielding of the protons adjacent to the pyrrolidone carbonyl group, as seen by the small positive chemical shift changes in Figure 2.38. The unsaturated alkene arm of compound **2.10** appears to reduce the changes in the ring during hydration in comparison to saturated **2.11**,

as seen by the chemical shift changes of protons at position (a) in Figure 2.38. The two pyrrolidone rings in compound **2.4** experience different chemical shift changes upon hydration due to the position of the alkene group, with those labelled (a) behaving analogously with the saturated dimer and ethyl-pyrrolidone, whilst (b) behaves similarly to **2.10**. In contrast, the protons within the saturated species (**2.3**) experience greater chemical shift changes, in comparison to **2.4**, due to the absence of the alkene functionality ensuring there is no reduction in the hydration potential of the molecule. However, it is worth noting that the changes in the chemical shifts during hydration are relatively small in all compounds. Finally, the difference between the saturated and unsaturated species indicates that ethyl-pyrrolidone is a better model for PVP hydration than vinyl-pyrrolidone, if a monomer study is required.

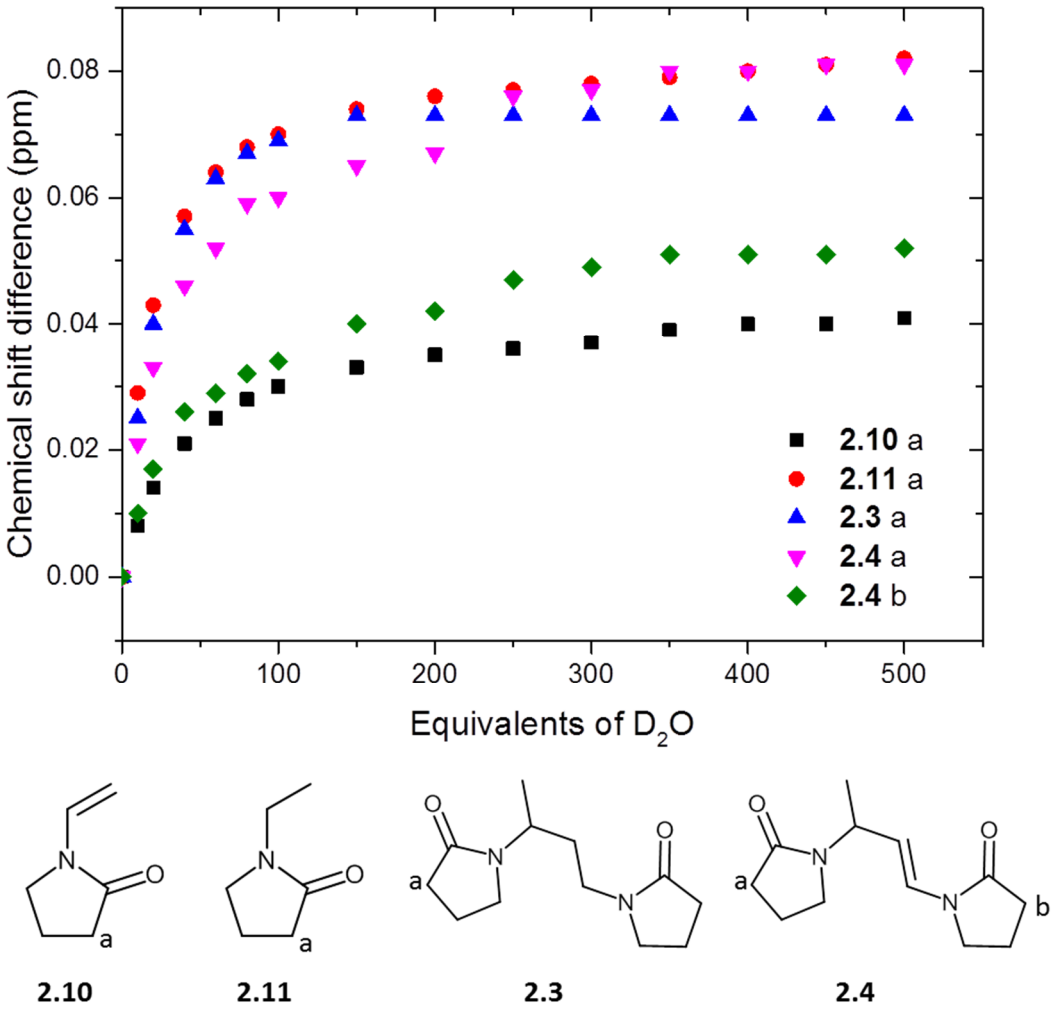

Figure 2.38: Chemical shift differences (ppm) for protons 'a' and 'b' adjacent to the carbonyl moiety in compounds **2.10**, **2.11**, **2.3** and **2.4**. Equivalents of D_2O are based on the entire lactam compound.

Equilibrium binding constants were calculated by non-linear least squares regression using the HypNMR2006 program, and are given in Table 2.4.[26] IR spectroscopic titrations highlighted the occurrence of multiple guest binding, therefore when modelling the ^{1}H NMR titration isotherms it is necessary to assume a stoichiometry model involving binding more than one water molecule to each carbonyl group. However, given the weak binding it is not possible to unambiguously determine more than two equilibrium constants and hence a compromise 1:2 (H:G) stoichiometry model was adopted. In the case of dimeric compounds **2.3** and **2.4**, the K_{11} binding constant corresponds to a single water molecule binding to one dimer molecule (possibly bridging between the two carbonyl groups), whilst K_{12} represents the binding of a second water molecule to give one water molecule per lactam carbonyl group. The titration isotherm for compound **2.10** fits a 1:1 stoichiometry, with a low binding constant of 0.05 M^{-1}, therein confirming its poor hydration ability. The saturated monomer **2.11** shows a much greater propensity for hydration than **2.10**, as seen in the stronger binding constant. This compound fits a combined 1:1 and 1:2 stoichiometry, in agreement with the multiple hydrated states confirmed by IR spectroscopy. For this monomer compound this corresponds to the binding of two water molecules to the same carbonyl group. It is surprising that the unsaturated VP dimer (**2.4**) has a marginally stronger binding constant than the saturated analogue (**2.3**), but this may indicate that the molecule is locked by the alkene group in a favourable conformation for water complexation. However, it is worth noting that the reported *K* values are weak in all four compounds studied, and upon taking into account the errors associated with the log β_{11} values (3 x e.s.d) the constants for **2.3** and **2.4**, in addition to **2.4** and **2.11** are not significantly different. The *K* values are therefore used only as a measure of overall water affinity, indicating that the less sterically hindered saturated monomer hydrates most readily.

Compound	**2.3**	**2.4**	**2.10**	**2.11**
Logβ_{11}	-0.37(2)	-0.22(6)	-1.25(4)	-0.20(3)
K_{11}/M^{-1}	0.42	0.60	0.05	0.62
Logβ_{12}	-1.85(4)	-1.59(8)		-1.38(4)
K_{12}/M^{-1}	0.03	0.04		0.07

Table 2.4: D_2O Binding constants for **2.3**, **2.4**, **2.10** and **2.11** by titration of up to 500 molar equivalents of D_2O into acetonitrile solutions of each compound.

Having established and compared the solution behaviours of the pyrrolidone series, we will now examine the differences between the pyrrolidone and caprolactam dimers. The caprolactam dimer **2.1** has a very similar water binding constant to the pyrrolidone analogue,

as seen in Table 2.5. One possible reason for the more effective nature of PVCap as a KHI compared to PVP is the greater polarity of the carbonyl group as a result of reduced ring strain in comparison to the pyrrolidone analogue. However, this difference is not sufficiently large to be reflected in the NMR data in these measurements.

Compound	**2.1**	**2.3**
Logβ_{11}	-0.29(4)	-0.37(2)
K_{11}/M^{-1}	0.50	0.42
Logβ_{12}	-1.86(5)	-1.85(4)
K_{12}/M^{-1}	0.03	0.03

Table 2.5: D_2O Binding constants for **2.1** and **2.3** by titration of up to 500 molar equivalents of D_2O into acetonitrile solutions of each compound.

IR spectroscopic measurements on the caprolactam-vinyl alcohol model compound **2.7** as a neat film show the broad carbonyl stretch occurs at 1620 cm^{-1}. This is similar to the VCap/VOH copolymer (1613 cm^{-1}), in which the broadness is thought to arise from multiple carbonyl environments due to varying intramolecular and/or intermolecular hydrogen bonding interactions. Upon dissolution in anhydrous acetonitrile, the broad carbonyl stretch resolves into two distinct bands, as shown in Figure 2.39. The band at higher wavenumber in MeCN solution (1637 cm^{-1}) is assigned to the "free" carbonyl groups, while that at lower wavenumber (1620 cm^{-1}) is thought to represent the carbonyl groups experiencing significant hydrogen bonding interactions from the OH functionalities in the molecule. It is not clear whether these are inter- or intramolecular interactions, however, the intermolecular interactions present in the crystal structure of the pyrrolidone analogue (**2.12**) provides indirect evidence for intermolecular hydrogen bonding.

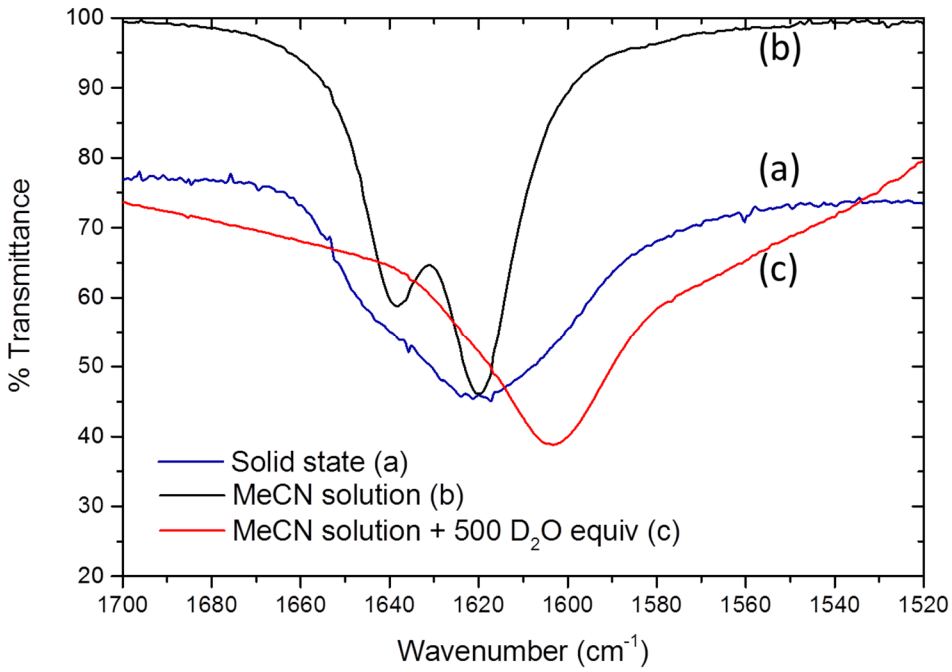

Figure 2.39: Partial IR spectra showing the carbonyl stretching band of compound **2.7** in (a) the solid state, (b) as an MeCN solution and (c) following addition of 500 D_2O equivalents to an MeCN solution.

Figure 2.40 compares the carbonyl stretch in acetonitrile solutions of the VCap/VOH copolymer and in model compound **2.7**. In both species the carbonyl stretch is resolved into two distinct bands of similar wavenumber. The band at higher wavenumber (1635 cm^{-1}) is dominant in the polymer, while the lower wavenumber band (1620 cm^{-1}) dominates in the model compound. This indicates that there is a greater degree of hydrogen-bonding interaction within the model compound than in the copolymer, potentially as a result of the higher caprolactam:alcohol ratio in **2.7** (1:1 in **2.7** in comparison to 82:18 in the copolymer). Therefore it is postulated that the hydration behaviour of the caprolactam moiety of compound **2.7** may be an underestimate of that in the polymer.

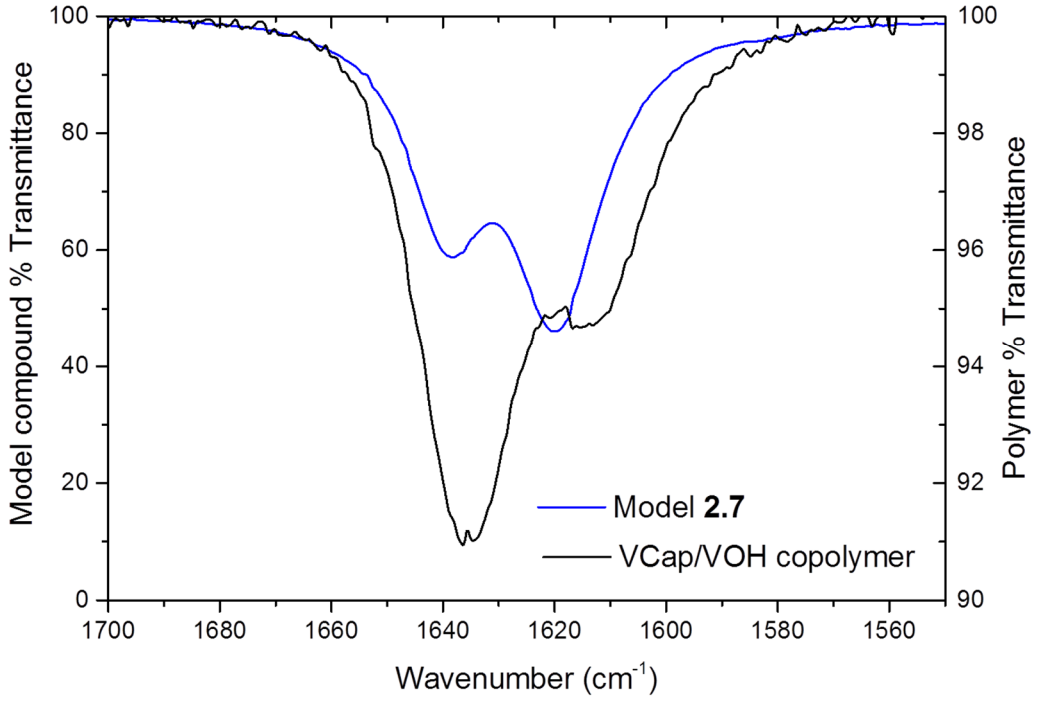

Figure 2.40: Comparison between the carbonyl stretch in MeCN solutions of (a) Model compound **2.7** and (b) VCap/VOH copolymer.

The stepwise hydration of compound **2.7** was monitored through solution IR spectroscopic titration, as seen in Figure 2.41. Addition of only 10 D_2O molar equivalents results in a significant reduction in the prominence of the stretch at 1637 cm^{-1}, indicating transition to a hydrogen bonded carbonyl environment. Furthermore, the carbonyl stretch is then broadened at 40 D_2O equivalents, indicating transition to the next hydrated state. The carbonyl stretch occurs at 1603 cm^{-1} following addition of 500 D_2O equivalents; this is lower than within the copolymer, indicating additional hydrogen bonding interactions in the small lactam compound. The hydration behaviour of **2.7** is complex due to the two potential hydration sites (C=O and OH), and the existence of two carbonyl bands in the MeCN solution. Unfortunately, due to the complications as a result of the presence of two bands little insight is gained by tracing the band asymmetry.

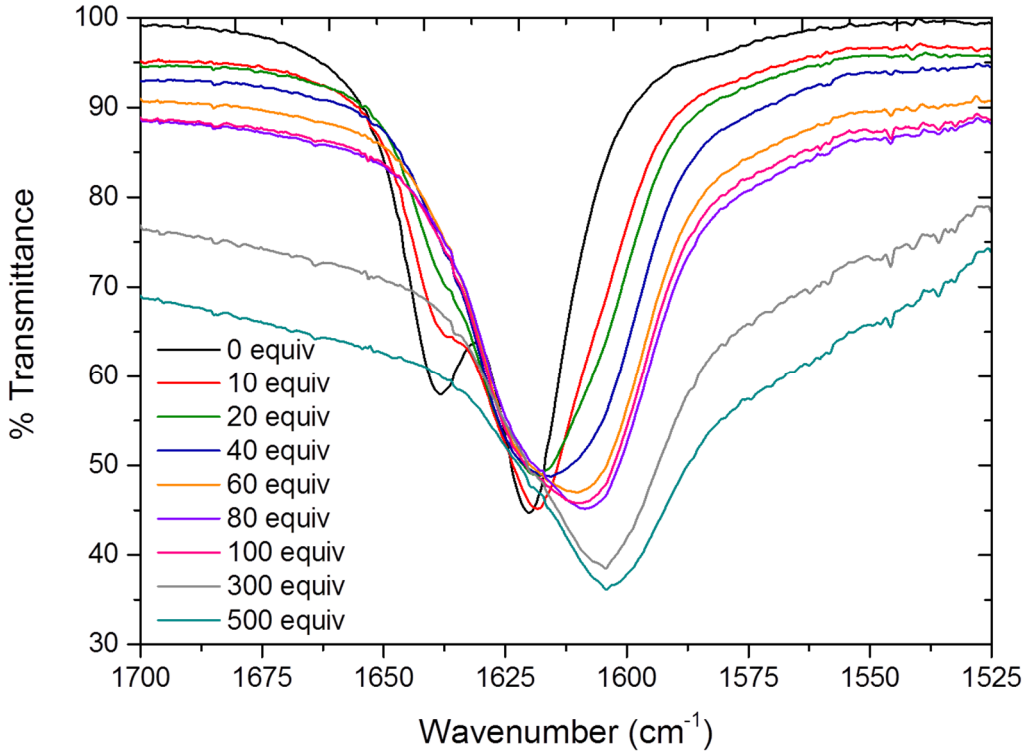

Figure 2.41: Solution IR titration showing addition of D_2O into an MeCN solution of compound **2.7**. Starting solution concentration = 5.84×10^{-5} moles/mL.

The ^1H NMR spectroscopic titration for compound **2.7** shows shifts in all protons, as seen in Figure 2.42. The figure shows increasing D_2O equivalents from bottom to top, ranging from 0 to 500, with D_2O equivalents calculated relative to compound **2.7**. The dominant peak which shifts significantly during the titration from 2.25 ppm to 4.3 ppm corresponds to residual HDO in the D_2O solvent being added. Shifts in this peak are not taken into account when calculating binding constants; however, all other traceable chemical shift changes are accounted for in the calculation, including the OH proton.

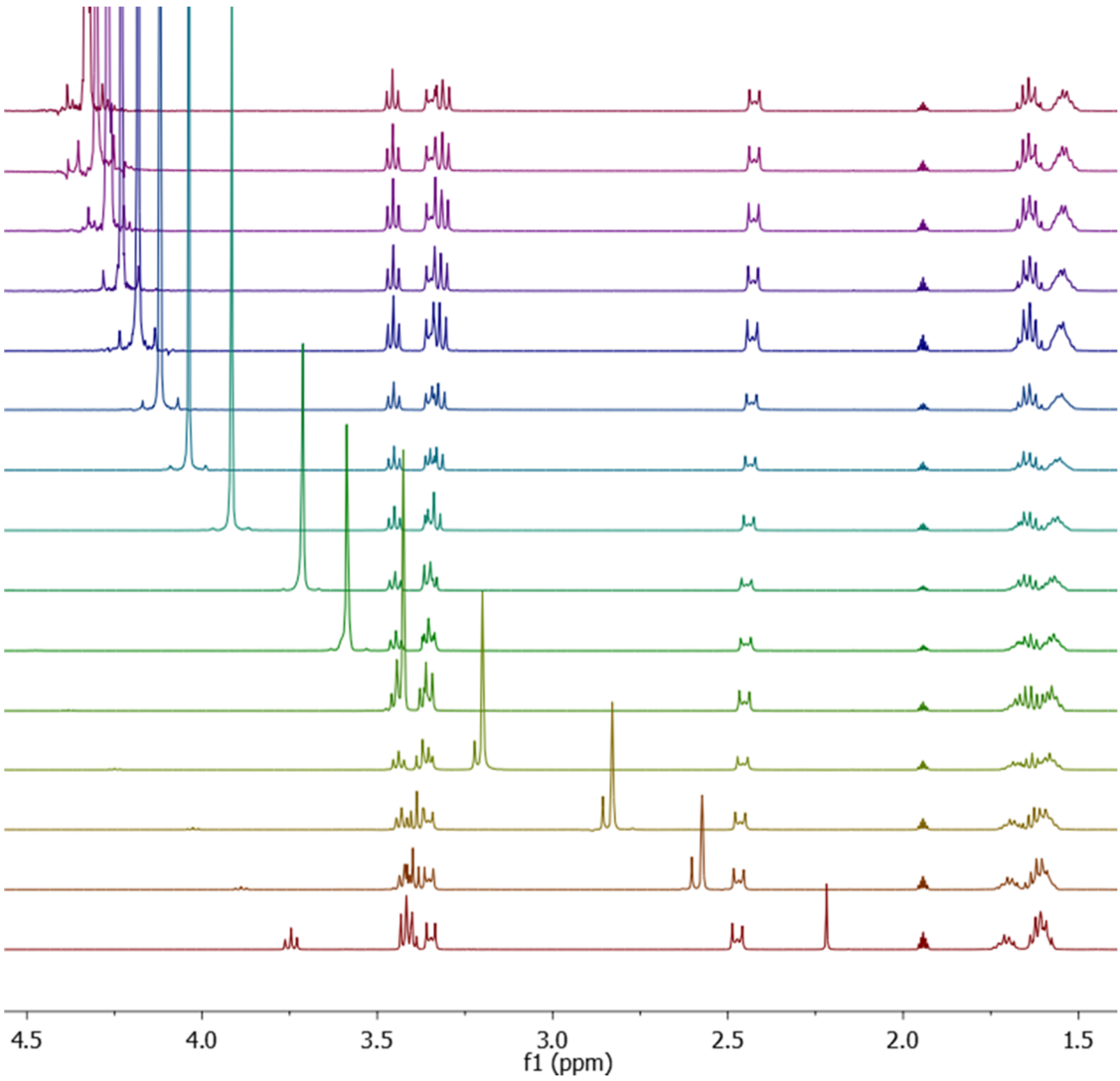

Figure 2.42: Partial ^{1}H NMR spectra recorded during addition of D_2O to a d_3-MeCN solution of **2.7**. Equivalents of D_2O increase from bottom (0) to top (500), as follows 0, 10, 20, 40, 60, 80, 100, 150, 200, 250, 300, 350, 400, 450 and 500 equivalents.

The alcoholic OH proton originates as a well-defined triplet at 3.74 ppm, and shifts downfield and broadens upon addition of D_2O as a result of hydrogen bonding interactions. It is possible to trace this resonance until addition of 250 D_2O equivalents, after which point the peak cannot be distinguished from the baseline because of exchange with deuterium. The resulting titration isotherm fits a combined 1:1 and 1:2 host:guest stoichiometry, with $\log\beta_{11}$ equalling 0.106(9) and $\log\beta_{12}$ equalling -0.757(9), and therefore giving binding constants of 1.28 M^{-1} and 0.14 M^{-1} for K_{11} and K_{12} respectively. These binding constants are reasonably weak despite the presence of two potential water binding sites, this further supports the presence of inter/intramolecular interactions reducing the propensity for molecule hydration. It is anticipated that the copolymeric KHI has stronger water binding properties than compound **2.7**.

For comparison, the hydration behaviour of the alcohol-pyrrolidone species (**2.12**) is included. The carbonyl stretch in an acetonitrile solution of **2.12** is broadened, as seen in Figure 2.43, with a stretch maximum at 1683 cm^{-1} in addition to a shoulder at lower wavenumber. In this species the most prominent carbonyl stretch, at higher wavenumber, represents the "free" carbonyl moieties. While the occurrence of intermolecular interactions has been established by the X-ray crystal structure (Figure 2.32), the shortened aliphatic arm (as opposed to in **2.7**) may reduce the potential for intramolecular interaction; hence the shoulder at lower wavenumber is of reduced intensity.

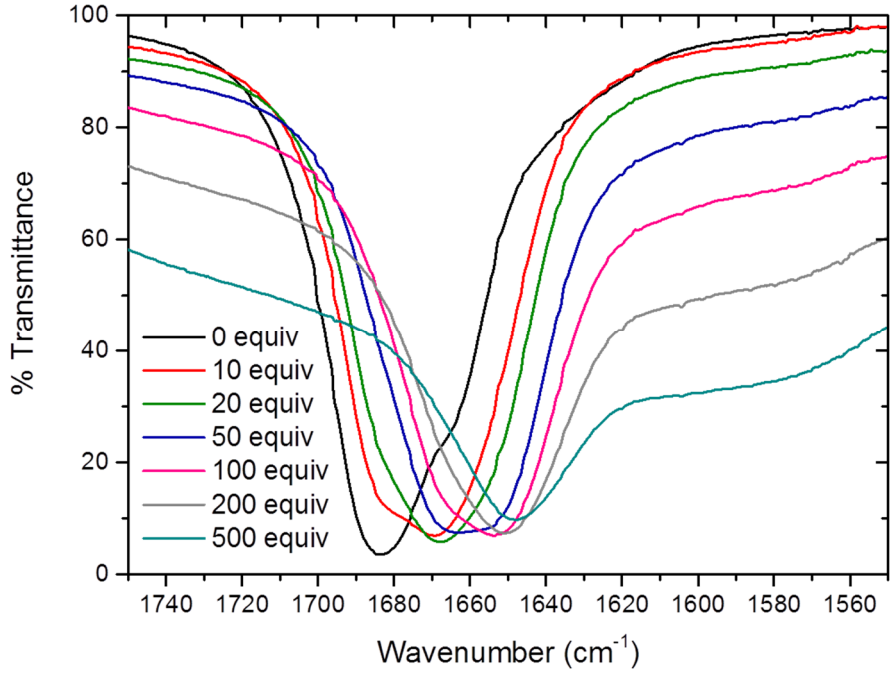

Figure 2.43: Solution IR titration following addition of D_2O in an acetonitrile solution of 1-(2-hydroxyethyl)-2-pyrrolidone (**2.12**). D_2O equivalents are based on the entire **2.12** compound.

Finally, for completeness the solution behaviour of *N*-vinyl caprolactam (**2.9**) is compared to the 5-membered analogue (**2.10**) in an attempt to establish a reason for the superior KHI performance of the caprolactam moiety. Changes in the protons affected by a shift in enolate form are mapped in Figure 2.44 following addition of D_2O. In **2.9** and **2.10** the alkene-NCH proton is shifted upfield during titration indicating an increase in shielding, with this effect greatest for VCap. Interestingly, protons (a) and (e) in **2.9** experience a slight upfield shift during the titration, this is in contrast to the downfield shifts observed in **2.10** and **2.11**.

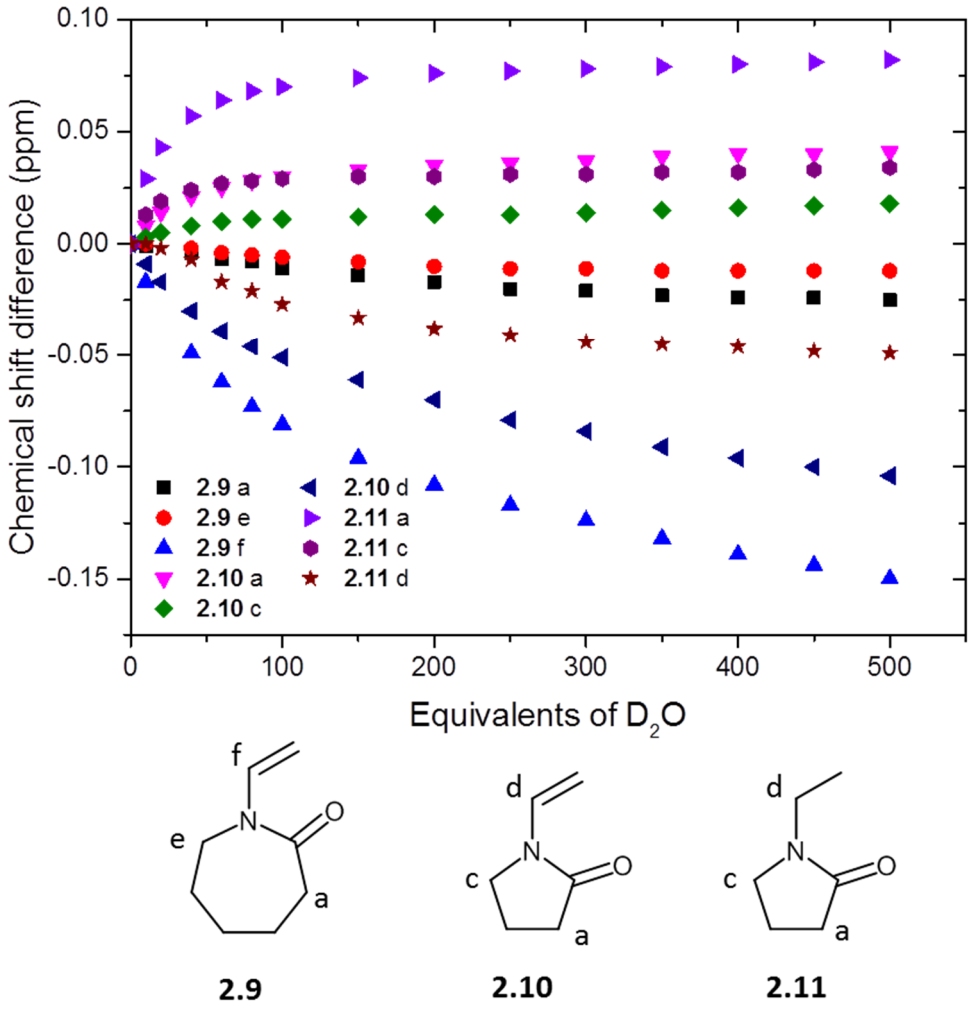

Figure 2.44: Chemical shift differences (ppm) for protons adjacent to the amide moiety in compounds **2.9**, **2.10** and **2.11**

The titration isotherms for **2.9** and **2.10** both fit 1:1 host:guest stoichiometry. They both have low binding constants, as reported in Table 2.6, highlighting their poor hydration ability. In contrast the binding constants for compound **2.7** are much higher, confirming the improved hydration ability of saturated caprolactam compounds. The binding constants for **2.11** are included in the table for completeness.

Compound	**2.7**	**2.9**	**2.10**	**2.11**
Logβ_{11}	0.106(9)	-1.25(3)	-1.25(4)	-0.20(3)
K_{11}/M^{-1}	1.28	0.05	0.05	0.62
Logβ_{12}	-0.757(9)			-1.38(4)
K_{12}/M^{-1}	0.14			0.06

Table 2.6: D_2O Binding constants for **2.7**, **2.9**, **2.10** and **2.11** by titration of up to 500 molar equivalents of D_2O into acetonitrile solutions of each compound.

2.4 Conclusions

In conclusion, IR spectroscopy has been utilised to gain insight into hydration of the carbonyl moiety in a series of commercially available KHIs. Titrations indicate that all inhibitors experience multiple hydrated-carbonyl environments, which may be crucial to their industrial performance. The amide carbonyl moiety appears to hydrate analogously amongst the species, irrespective of the identity of additional functionality. This may be important for industrial application as may enable specific moieties to be incorporated along the aliphatic chain in order to provide specific field-site performance, whilst not compromising on the hydration potential of the lactam rings.

In addition, a selection of model compounds have been developed to represent the polymeric inhibitors in order to elucidate quantitative insight into water binding. Solution and solid-state studies are reported for a series of lactam species, highlighting the polarity of the carbonyl moiety and it's propensity for water complexation. Detailed and systematic comparisons are outlined, alongside verification of the performance relative to parent polymers. This work suggests that the alkene group significantly affects the hydration ability of monomeric *n*-vinyl caprolactam and vinyl-pyrrolidone, and suggests that use of saturated analogues of these monomers would provide a more realistic representation of the polymer hydration, if a monomeric study is required. The equilibrium binding constants are relatively weak in all compounds; however, the K_{11} and K_{12} values provide a crude measure of overall water affinity for each of the species examined.

Finally, one postulate for the KHI mechanism of action suggests that inhibitors bind to water in solution, disrupt the formation of a cage and therein prevent the formation of clathrate hydrates. If this inhibition mechanism were to be the sole mode of functionality we would anticipate there to be a difference in the hydration behaviour of the series, wherein PVCap would hydrate most readily, either binding water most strongly or having more hydrated environments. The absence of significant differences in the water binding properties of PVP and PVCap (and related model compounds) suggests that this KHI mechanism of action, if correct, could not be the sole mechanistic explanation. However, to verify this theory further examination of the solution behaviour should be conducted as a function of temperature and in the presence of the other pipeline components including NaCl and gas/oil molecules.

2.5 Experimental

Methods and materials

Samples of commercial KHIs were provided by Ashland Inc. as mixtures in 2-butoxyethanol. 1-(2-hydroxyethyl)-2-pyrrolidone (**2.12**) was supplied by Ashland Inc. All other reagents and solvents were purchased from standard commercial sources and used without further purification. All NMR spectra were performed on a Varian Mercury-400 MHz (^{1}H, ^{13}C) and Bruker Advance-400MHz (^{1}H, ^{13}C) and were referenced to residual solvent. Fourier transform infrared spectra were recorded using a Perkin Elmer Spectrum 100 ATR spectrometer. For each solid-state spectrum, 16 scans were conducted over a spectral range 4000 to 600 cm^{-1} with a resolution of 1 cm^{-1}. For solution measurements a Specac solution IR cell was used, which was fitted with CaF_2 windows using a 0.05 mm spacer. The analysis was carried out using the Perkin Elmer Spectrum Express 1.01 software. Electrospray (ES) mass spectrometry was recorded on a Thermo-Finnigan LTQ instrument.

HPLC was performed using a Waters Mass Directed Auto-Purification system equipped with an XBridge Prep C18 column (100 x 19 mm, 5um) with a linear gradient elution from 90% water with 0.1% formic acid and 10% acetonitrile with 0.1% formic acid to 5% water with 0.1% formic acid and 95% acetonitrile with 0.1% formic acid over 10 minutes.

Crystals suitable for single crystal X-ray diffraction structure determination were selected, soaked in perfluoropolyether oil and mounted on a preformed tip. Single crystal X-ray data were collected at 120 K (unless otherwise specified) on an Agilent Gemini S-Ultra diffractometer equipped with Cryostream (Oxford Cryosystems) open-flow nitrogen cryostats, using graphite monochromated Mo$K\alpha$-radiation (λ = 0.71073 Å). All structures were solved using direct methods and refined by full-matrix least squares on F^2 for all data using SHELXL[27] and OLEX2[28]. All non-hydrogen atoms were refined with anisotropic displacement parameters. CH hydrogen atoms were placed in calculated positions, assigned an isotropic displacement factor that is a multiple of the parent carbon atom and allowed to ride. H-atoms attached to oxygen were located on the difference map when possible, or placed in calculated positions.

General procedure for ^{1}H NMR spectroscopic titrations

All chemical shifts are reported in ppm relative to residual solvent. A solution of the host species of known concentration was made up in a single NMR tube using d_3-acetonitrile. D_2O (the guest) was added in 10 μL aliquots using a Hamilton microliter syringe and the spectra were recorded after addition.

The mathematical analysis of ^{1}H NMR data was performed using HypNMR2006.[26] The solution is considered as a host-guest equilibria system, with the lactam species treated as the host and D_2O as the guest. The chemical shifts for each lactam proton are traced during the titration, and the peak positions (in ppm) are tabulated as a function of host and guest concentration. These tabulated datasets were analysed by the HypNMR software suite, whereby a binding isotherm is calculated and refined simultaneously for all of the chemical shift data available. Where a 1:1 and 1:2 stoichiometry was selected the simultaneous refinement was performed for a combined 1:1 and 1:2 stoichiometry.

Following isotherm convergence a log β value was output in addition to the associated standard error for this value, and an overall chi-squared parameter. Upon attainment of a suitably converged and reliable binding constant, the log β values were converted as required to isolate the K_{11} and K_{12} values. Examples of the titration isotherms are included in the Appendix.

Compound	Mass used/g	Moles	Host solution volume/mL
2.1	0.0155	5.53×10^{-5}	0.5
2.3	0.0125	5.6×10^{-5}	0.6
2.4	0.0124	5.6×10^{-5}	0.6
2.7	0.0095	5.55×10^{-5}	0.5
2.9	0.0077	5.53×10^{-5}	0.5
2.10	0.0062	5.49×10^{-5}	0.5
2.11	0.0063	5.57×10^{-5}	0.5

General procedure for solution IR spectroscopic titrations

Solution Infrared measurements were conducted using a Perkin Elmer Spectrum 100 FTIR spectrometer fitted with a Specac solution IR cell with CaF_2 windows. An acetonitrile solution of the host species of known concentration was made up in a vial. The guest, D_2O, was then added in 10 μL aliquots until the desired equivalents were added. The solution was sonicated for 1 minute to ensure homogeneity and then syringed into the solution IR cell. All infrared

measurements were taken at a resolution of 1 cm^{-1} and 16 scans, using a 0.05 mm spacer within the liquid cell.

Compound	Mass used/g	Moles of monomeric unit	Host solution volume/mL
PVP K12	0.003	2.7×10^{-5}	0.5
PVP K30	0.003	2.7×10^{-5}	0.5
PVCap	0.00375	2.69×20^{-5}	0.5
P(VP/VCap) (50:50)	0.0034	2.72×10^{-5}	0.5
P(VP/VCap) (5:95)	0.00375	2.69×10^{-5}	0.5
P(VCap/VOH)	0.002	1.64×10^{-5}	0.5
P(VCap/HEMA)	0.0038	2.74×10^{-5}	0.5
2.1	0.0032	2.28×10^{-5}	0.5
2.3	0.003	2.67×10^{-5}	0.5
2.4	0.025	1.12×10^{-4}	1.0
2.7	0.01	5.84×10^{-5}	1.0
2.10	0.0125	1.12×10^{-4}	1.0
2.11	0.003	2.65×10^{-5}	0.5
2.12	0.0125	9.68×10^{-5}	1.0

Polymer isolation

Detailed below is the procedure used for the isolation of PVCap. The same method allows isolation of each of the polymers outlined in Chapter 2.2.

A commercial sample of viscous orange/brown oil comprising 50 wt% PVCap in 2-butoxyethanol was placed into a vial, and diethyl ether added until a cream precipitate formed. The mother liquor was decanted to isolate a cream powder. The powder was washed with additional diethyl ether, dried and ground using a Retsch MM200 ball mill. This process was repeated until all of the 2-butoxyethanol was removed (as confirmed by ^{1}H NMR spectroscopy).

IR (ν/cm^{-1}) : 2925-2856 (C-H stretch), 1616 (C=O), 1478 (C-N), 1440-1442 (C-H).

Model Compound synthesis

1,3-Bis(caprolactam-2-on-1-yl) but-1-ene (**2.2**)

N-vinyl caprolactam (2.0 g, 14.4 mmol) and dry hexane (10 mL) were placed into a 3-neck round bottom flask fitted with a stirrer bar, reflux condenser and nitrogen inlet/outlet. The reaction mixture was heated to 50 ^{o}C and TFA (4 drops) was added through the sidearm. The

temperature was increased to 60 °C and held for 3 h. The mixture was allowed to cool to room temperature, under nitrogen, whereby two layers were visible. Hexane (40 mL) was added and a white precipitate formed. The solid product was isolated using Büchner filtration. The product was washed with cold hexane if residual *n*-vinyl caprolactam remained.

^{1}H NMR spectrum in agreement with published work.[2]

1,3-Bis(pyrrolidin-2-on-1-yl) but-1-ene (**2.4**)

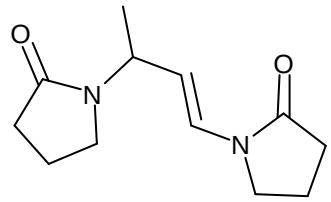

N-vinyl pyrrolidone (12 g, 108 mmol) was placed into a 2-neck flask under an atmosphere of nitrogen, and anhydrous cyclohexane (5 mL) was added. The reaction mixture was heated to 60 °C with stirring. Concentrated sulphuric acid (3 μL) was added and the temperature was increased to 70 °C. The reaction mixture was held at 70 °C, under nitrogen, for 6 h. The mixture was then allowed to cool to room temperature, and the solvent removed upon the rotary evaporator. Residual solvent and acid were removed by addition of hexane (20 mL) followed by rotary evaporation. Prior to analysis, the sample was held in the drying pistol at 110 °C for 3 h.

^{1}H NMR (400 MHz, $CDCl_3$) δ 6.98 (d, *J* = 13.6 Hz, 1H, NCH), 4.95 – 4.83 (m, 2H, CH=CH), 3.49 – 3.43 (m, 2H, NCH_2), 3.31 – 3.23 (m, 2H, NCH_2), 2.47 (t, *J* = 8.2 Hz, $COCH_2$), 2.40 – 2.33 (m, 2H, $COCH_2$), 2.10 (d, *J* = 7.4 Hz, 2H, CH_2), 2.01 – 1.93 (m, 2H, CH_2), 1.27 (d, *J* = 6.8 Hz, 3H, CH_3).

^{13}C{^{1}H} NMR (100 MHz, $CDCl_3$) δ 174.36, 173.42, 125.26, 110.89, 46.15, 45.35, 42.55, 31.65, 31.34, 18.11, 17.58, 17.11

IR (*ν*/cm^{-1}): 1673.8 (C=O), 1658.4 (C=O).

1-caprolactamyl,3-(2-pyrrolidone-1-yl) but-1-ene (**2.5**)

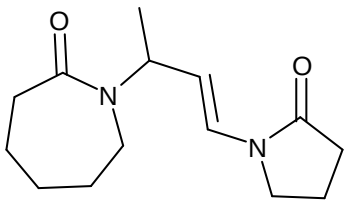

n-vinyl caprolactam (2.0 g, 14.4 mmol) and *n*-vinyl pyrrolidone (1.6g, 14.4 mmol) were added to a 3-neck round bottom flask fitted with a stirrer bar, reflux condenser and nitrogen inlet and outlet. Trifluoroacetic acid (8 drops) was added through the sidearm, and the reaction mixture was stirred at room temperature for 3 hours, under N_2, resulting in a viscous yellow oil. Dry hexane (10 mL) was added, and the reaction mixture was heated to 50 ^oC and held for 19 hours. Upon cooling to room temperature, the hexane layer was decanted to isolate a thick yellow/orange oil. Silica column chromatography using an acetone/hexane (3:1) solvent system results in the isolation of compound **2.5**. Compound **2.5** crystallises concomitantly with 1,3-caprolactamyl-but-1-ene (**2.2**).

X-ray crystallography data were collected at I19 Synchrotron by Dr. Katharina Fucke.

^{1}H NMR (400 MHz, $CDCl_3$) δ 6.96 (dd, *J* = 1.7, 14.8 Hz, 1H, vinyl NCH), 5.40 (m, *J* = 3.4, 5.9, 10.1 Hz, 1H, NCH), 4.90 (dd, *J* = 5.0, 14.8 Hz, 1H, vinyl CH), 3.50-3.43 (m, 2H, CH_2), 3.19 – 3.11 (m, 2H, CH_2), 2.55 – 2.44 (m, 4H, 2 x CH_2), 2.09 (m, *J* = 7.6, 14.8 Hz, 2H, CH_2), 1.68 – 1.66 (m, 6H), 1.22 (d, *J* = 6.9 Hz, 3H, CH_3).

^{13}C{^{1}H} NMR (100 MHz, $CDCl_3$) δ 175.74, 173.58, 125.44, 112.32, 48.46, 45.58, 43.49, 37.91, 31.55, 30.34, 30.05, 23.79, 17.73, 16.99.

MS (GC ES-) *m/z* : 249.1 (M-H)

IR (cm^{-1}) 1622 (C=C), 1658 (C=O) and 1690 (C=O).

Crystal data for $C_{14}H_{22}N_2O_2$, *M* = 250.34, colourless block, 0.30 x 0.10 x 0.05 mm^3, triclinic, space group $P\bar{1}$ (no. 2), *a* = 6.353(3) Å, *b* = 8.231(4) Å, *c* = 14.087(10) Å, α = 102.473(8)^o, β = 96.293(8)^o, γ = 103.742(5)^o, *V* = 688.5(7) Å^3, *Z* = 2, D_c = 1.207 g/cm^3, F_{000} = 272, CCD area detector, synchrotron radiation, λ = 0.68890 Å, *T* = 120(2)K, $2\theta_{max}$ = 54.7^o, 6733 reflections collected, 3173 unique (R_{int} = 0.0340). Final *GooF* = 1.056, *R1* = 0.0626, *wR2* = 0.1712, *R* indices based on 2674 reflections with I>2σ(I) (refinement on F^2), 165 parameters, 0 restraints.

Hexahydro-1-(3'-hydroxypropyl)-*2H*-azepin-2-one (**2.7**)

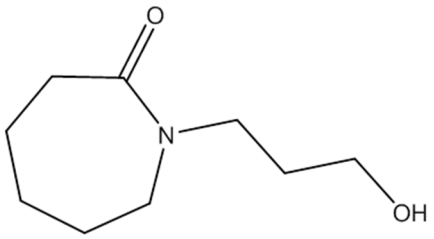

Procedure 1: Sodium azide (0.675 g, 10.4 mmol) and tetrabutyl ammonium hydrogen sulphate (0.0144 g) were dissolved in water (20 mL). 3-chloropropanol (0.434 mL, 0.4908 g, 5.1916 mmol) was added through the sidearm. The mixture was stirred at 80 ^{o}C for 24 hours, and then stirred at room temperature for a further 15 hours. The solution was extracted with DCM (3 x 10 mL) and dried over $MgSO_4$. The solution was filtered into a dry 3-neck flask and held under N_2 to give 3-azidopropanol (assumed 0.496 g, 4.88 mmol). Cyclohexanone (0.4 g, 0.422 mL, 4.04 mmol) was added through the sidearm. The mixture was stirred and cooled to 0 ^{o}C. $BF_3.OEt_2$ (1.04 mL, 8.08 mmol) was added dropwise, noting some gas evolution. The solution was warmed to room temperature over 30 minutes, and then stirred at room temperature for an additional 3 hours. The solution was concentrated, saturated $NaHCO_3$ (20 mL) added and the mixture stirred at room temperature for 60 minutes. The organic layer was separated, dried (using $MgSO_4$) and concentrated to a viscous oil.

Procedure 2: 3-azido-1-propanol (0.5 g, 4.94 mmol) was added to a solution of cyclohexanone (0.485 g, 4.94 mmol) in dry DCM (12 mL) under N_2. The mixture was stirred and cooled to 0 ^{o}C. $BF_3.OEt_2$ (1.22 mL, 9.89 mmol) was added dropwise over 5 minutes, noting some gas evolution. The solution was warmed to room temperature over 30 minutes, and then stirred at room temperature for an additional 3 hours. The solution was concentrated, saturated $NaHCO_3$ (20 mL) added and the mixture stirred at room temperature for 60 minutes. DCM (80 mL) was added then the organic layer was separated, dried (using $MgSO_4$) and concentrated to a viscous oil. Silica column chromatography, with an ethyl acetate eluent, enables clean isolation of product **2.7** as a yellow oil (0.603 g, 3.52 mmol, 71 %).

^{1}H NMR (400 MHz, CD_3CN) δ 3.74 (t, 1H, OH), 3.44 – 3.39 (m, 4H, C$\underline{H_2}$OH, ring-NC$\underline{H_2}$), 3.36 – 3.34 (m, 2H, NC$\underline{H_2}$), 2.49-2.46 (m, 2H, COC$\underline{H_2}$), 1.74 – 1.69 (m, 2H, C$\underline{H_2}$CH_2OH), 1.64 – 1.58 (m, 6H, ring-C$\underline{H_2}$).

$^{13}C\{^{1}H\}$ NMR (100 MHz, CD_3CN) δ 177.60, 58.80, 50.22, 45.16, 37.57, 31.23, 30.54, 29.16, 24.30.

IR (ν/cm^{-1}): 3380 (br) (OH), 2925-2855 (C-H stretch), 1620 (C=O), 1490 (C-N), 1445-1424 (C-H).

2,3,4,5,6,7,8,9-octahydro-1-oxa-4a-azonia-benzocycloheptene tetrafluoroborate (**2.8**)

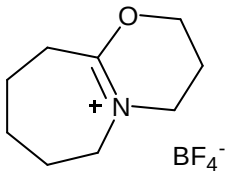

Sodium azide (0.675 g, 10.4 mmol) and tetrabutyl ammonium hydrogen sulphate (0.0144 g) were dissolved in water (20 mL). 3-chloropropanol (0.434 mL, 0.4908 g, 5.1916 mmol) was added through the sidearm. The mixture was stirred at 80 ^{o}C for 24 hours, and then stirred at room temperature for a further 15 hours. The solution was extracted with DCM (3 x 10 mL) and dried over $MgSO_4$. The solution was filtered into a dry 3-neck flask and held under N_2 to give 3-azidopropanol (assumed 0.496 g, 4.88 mmol). Cyclohexanone (0.4 g, 0.422 mL, 4.04 mmol) was added through the sidearm. The mixture was stirred and cooled to 0 ^{o}C. $BF_3.OEt_2$ (1.04 mL, 8.08 mmol) was added dropwise, noting some gas evolution. The solution was warmed to room temperature over 30 minutes, and then stirred at room temperature for an additional 3 hours. A small aliquot of the reaction mixture was held in a small vial. The vial was placed inside a larger vial containing ether and sealed. Vapour diffusion at room temperature resulted in single crystals within 48 hours.

Crystal data for $C_9H_{16}NOBF_4$: M = 241.04, colourless block, 0.3113 x 0.2851 x 0.1784 mm^3, monoclinic, space group $P2_1/c$ (No. 14), a = 7.5172(5) Å, b = 14.1150(6) Å, c = 10.7302(7) Å, α = 90.00 ^{o}, β = 102.856(7) ^{o}, γ = 90.00 ^{o}, V = 1109.99(11) Å^3, Z = 4, D_c = 1.442 g/cm^3, F_{000} = 504, Xcalibur, Sapphire3, Gemini ultra, MoKα radiation, λ = 0.71073 Å, T = 120K, $2\theta_{max}$ = 52.0^{o}, 4808 reflections collected, 2183 unique (R_{int} = 0.0375). Final *GooF* = 1.055, *R1* = 0.0573, *wR2* = 0.1393, *R* indices based on 1629 reflections with I>2σ(I) (refinement on F^2), 145 parameters, 0 restraints. Lp and absorption corrections applied, μ = 0.136 mm^{-1}.

1-vinyl-2-pyrrolidone (**2.10**)

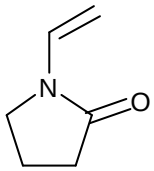

Crystallisation: A sample of 1-vinyl-2-pyrrolidone was purchased from Sigma-Aldrich and used without further purification. Sample was loaded within a borosilicate capillary and mounted at 290K, and then cooled at 120 deg/h to 230K. Flash cooling (touch of liquid nitrogen) was performed when the sample was at 236 K, resulting in the formation of polycrystalline material filling the capillary. The sample was warmed to 280 K, at 120 deg/h, and melted by direct heat application (touch), noting that the crystalline material quickly re-formed. The sample was warmed to 283 K at 60 deg/h and again direct heat applied to fully melt the sample. The slow regrowth of crystalline material resulted in the formation of a good single crystal. The sample was cooled to 260 K at 60 deg/h and data collected. The sample was cooled to 150 K at 120 deg/h and a second dataset collected.

In situ liquid crystallisation performed with assistance from Dr. Dmitry Yufit.

Crystal data for C_6H_9NO: M = 111.14, capillary crystallisation, 0.3 x 0.3 x 0.5 mm^3, monoclinic, space group $P2_1/c$ (no. 14), a = 7.6926(5) Å, b = 11.5789(5) Å, c = 7.7886(6) Å, α = 90.00^o, β = 118.977(10)^o, γ = 90.00^o, V = 607.10(8) Å^3, Z = 4, D_c = 1.216 g/cm^3, F_{000} = 240, Xcalibur, Sapphire3, MoKα radiation, λ = 0.71073 Å, T = 260K, $2\theta_{max}$ = 52.0^o, 4186 reflections collected, 1186 unique (R_{int} = 0.0172). Final *GooF* = 1.048, *R1* = 0.0351, *wR2* = 0.0895, *R* indices based on 1033 reflections with I>2σ(I) (refinement on F^2), 110 parameters, 0 restraints. Lp and absorption corrections applied, μ = 0.083 mm^{-1}.

1-(2-hydroxyethyl)-2-pyrrolidone (**2.12**)

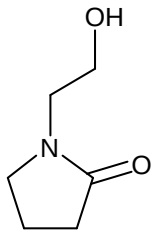

A sample of 1-(2-hydroxyethyl)-2-pyrrolidone was supplied by Ashland Inc. as a viscous yellow oil, and used without further purification. The sample was placed within a sealed vial, and submerged in a dry ice/acetone bath for 4 minutes, resulting in formation of crystalline material. A single crystal was selected and mounted upon the diffractometer.

Crystal data for $C_6H_{11}NO_2$: M = 129.16, colourless block, 0.387 x 0.2127 x 0.1366 mm^3, orthorhombic, space group $Pca2_1$ (No. 29), a = 9.9709(3) Å, b = 6.6979(2) Å, c = 10.0174(3) Å, α = 90.00^o, β = 90.00^o, γ = 90.00^o, V = 669.01(4) Å^3, Z = 4, D_c = 1.282 g/cm^3, F_{000} = 280, Xcalibur, Sapphire3, Mo$K\alpha$ radiation, λ = 0.71073 Å, T = 120K, $2\theta_{max}$ = 51.9^o, 4780 reflections collected, 1301 unique (R_{int} = 0.0281). Final *GooF* = 1.056, *R1* = 0.0252, *wR2* = 0.0600, *R* indices based on 1234 reflections with I>2σ(I) (refinement on F^2), 83 parameters, 1 restraint. Lp and absorption corrections applied, μ = 0.096 mm^{-1}.

2.6 References

1. T. J. Carver, M. G. B. Drew and P. M. Rodger, *J. Chem. Soc.-Faraday Trans.*, 1995, **91**, 3449-3460.
2. J. R. Davenport, O. M. Musa, M. J. Paterson, M.-O. M. Piepenbrock, K. Fucke and J. W. Steed, *Chem. Commun.*, 2011, **47**, 9891-9893.
3. B. J. Anderson, J. W. Tester, G. P. Borghi and B. L. Trout, *J. Am. Chem. Soc.*, 2005, **127**, 17852-17862.
4. Y. E. Kirsh, N. A. Yanul and K. K. Kalninsh, *Eur. Polym. J.*, 1999, **35**, 305-316.
5. Y. Maeda, T. Nakamura and I. Ikeda, *Macromolecules*, 2002, **35**, 217-222.
6. Y. Maeda, T. Nakamura and I. Ikeda, *Macromolecules*, 2002, **35**, 10172-10177.
7. I. Száraz and W. Forsling, *Polymer*, 2000, **41**, 4831-4839.
8. A. Perrin, O. M. Musa and J. W. Steed, *Chem. Soc. Rev.*, 2013, **42**, 1996-2015.
9. M. A. Kelland, *Energy Fuels*, 2006, **20**, 825-847.
10. Y. Kirsh, *Water soluble Poly-N-Vinylamides - Synthesis and Physiochemical Properties*, John Wiley & Sons Ltd, 1998.
11. I. Chatti, A. Delahaye, L. Fournaison and J.-P. Petitet, *Energy Convers. Manage.*, 2005, **46**, 1333-1343.
12. S. Sun and P. Wu, *The Journal of Physical Chemistry B*, 2011, **115**, 11609-11618.

13. J. Spevacek, J. Dybal, L. Starovoytova, A. Zhigunov and Z. Sedlakova, *Soft Matter*, 2012, **8**, 6110-6119.
14. R. O'Reilly, N. S. Ieong, P. C. Chua and M. A. Kelland, *Chem. Eng. Sci.*, 2011, **66**, 6555-6560.
15. http://www.ashland.com/Ashland/Static/Documents/ASI/Energy-Oil%20and%20Gas%20Technologies/PC-11724_Inhibex_Series_Sheet.pdf, accessed 05/02/2015.
16. http://www2.ups.edu/faculty/hanson/Spectroscopy/IR/IRfrequencies.html, accessed 24/3/2015.
17. O.M. Musa and L. Cuiyue, *WO*2010117660, 2010.
18. J. C. Zhuo, *Molecules*, 1999, **4**, M117.
19. V. Gracias, G. L. Milligan and J. Aube, *J. Am. Chem. Soc.*, 1995, **117**, 8047-8048.
20. B. S. Sumerlin, N. V. Tsarevsky, G. Louche, R. Y. Lee and K. Matyjaszewski, *Macromolecules*, 2005, **38**, 7540-7545.
21. E. Fenster, B. T. Smith, V. Gracias, G. L. Milligan and J. Aube, *J. Org. Chem.*, 2008, **73**, 201-205.
22. M. T. Kirchner, D. Blaeser and R. Boese, *Chem.-Eur. J.*, 2010, **16**, 2131-2146.
23. M. A. Spackman and D. Jayatilaka, *Crystengcomm*, 2009, **11**, 19-32.
24. G. N. Tishchenko, N. E. Zhukhlistova and Y. E. Kirsh, *Crystallogr. Rep.*, 1997, **42**, 626-630.
25. P. Thordarson, *Chem. Soc. Rev.*, 2011, **40**, 1305-1323.
26. C. Frassineti, S. Ghelli, P. Gans, A. Sabatini, M. S. Moruzzi and A. Vacca, *Anal. Biochem.*, 1995, **231**, 374-382.
27. G. M. Sheldrick, *Acta Crystallogr. Sect. A*, 2008, **64**, 112-122.
28. O. V. Dolomanov, L. J. Bourhis, R. J. Gildea, J. A. K. Howard and H. Puschmann, *J. Appl. Crystallogr.*, 2009, **42**, 339-341.

3 Neutron scattering of water solvent mixtures

3.1 Introduction

Neutron scattering studies offer many advantages over the more conventional X-ray diffraction, particularly when studying compounds with high hydrogen content.[1] The neutron scattering power of each atom is not correlated to the atomic number, enabling isotopic substitutions to be distinguished. This provides a unique opportunity to examine hydrogen positions within solution because hydrogen and deuterium can be readily exchanged and have vastly different scattering cross sections.[1] Probing the structure of disordered systems has become an important application of neutron studies, enabling atomistic-level structural insight into solvent and liquid samples. Atomistic insight is critical in understanding the hydration behaviour of solution species, enabling hydrogen-bonding interactions to be probed directly.[2]

Such techniques have provided information about a plethora of interesting systems including aqueous tertiary butanol,[3] THF[4, 5] and glycerol[6] in addition to many others[7, 8]. One particularly relevant clathrate hydrate neutron study by Koh, Soper and coworkers examines the hydration shell of methane molecules during methane hydrate formation.[9] Interestingly, the report suggests that the hydration shell of methane is different in the liquid and crystalline states.[9]

THF hydrate forms a structure II type clathrate and is synthesised from a 1:17 molar ratio of THF:water at temperatures below 4 ^{o}C. As mentioned in Chapter 1, THF hydrate is commonly used as a model clathrate hydrate within inhibition studies in order to overcome difficulties with the relatively low aqueous solubility of natural gas. Bowron *et al.* studied the structure of liquid THF[5] and aqueous THF[4] using neutron scattering data, showing the atomistic interactions of the THF ring with surrounding molecules. Bowron combined neutron scattering data with Empirical Potential Structure Refinement (EPSR) simulations to explore the presence of voids within solution as a result of the intrinsic packing of THF molecules.[4, 5] This chapter aims to build on these previous findings to develop a model for the liquid behaviour of a potentially clathrate forming solution, as a function of temperature.

Furthermore, this chapter also extends this work to the structure of aqueous 2-butoxyethanol. 2-butoxyethanol is commonly used as the solvent for KHI application, and is

known to have synergistic effects upon the KHI and hence improve inhibitor performance.[10] *N*-alkoxyethanols ($ROCH_2CH_2OH$) have been species of considerable interest in the literature, due in part to the formation of molecular aggregates within aqueous solution.[11, 12] The latter part of this chapter will explore the liquid structure of aqueous 2-butoxyethanol, in addition to exploring the effect of PVCap addition upon the structure of aqueous 2-butoxyethanol.

3.2 Experiment Theory

In this work neutron diffraction data were collected at the ISIS pulsed neutron source at the Rutherford Appleton Laboratory, Oxford, using the Small Angle Neutron Diffractometer for Amorphous and Liquid Samples (SANDALS)[13] and the Near and Intermediate Range Order Diffractometer (NIMROD)[14]. NIMROD and SANDALS are both optimised for the study of hydrogen/deuterium containing samples, with NIMROD taking advantage of high energy neutrons[15] and SANDALs having many detectors at low angles.[16]

Data collected during neutron scattering experiments are measured as a function of the exchanged wave vector Q, where $Q = (4\pi\sin\theta)/\lambda$, with λ corresponding to the incident wavelength and 2θ representing the scattering angle.[17] It is this value which determines the scale probed during the experiment, with an inverse relationship between length-scale and Q.[18] The physical quantity measured by the diffractometer shows the differential scattering cross section (DSCS), $d\sigma/d\Omega$, as a function of Q, according to Equation 1.[18] In this equation σ represents the scattering cross section and Ω represents the solid angle element.[1, 18]

$$\frac{1}{\mathrm{N}}\frac{\mathrm{d}\sigma}{\mathrm{d}\Omega} = \sum\nolimits_{\alpha} c_\alpha b_\alpha^2 + \sum\nolimits_{\alpha,\beta\geq\alpha} (2-\delta_{\alpha\beta}) c_\alpha c_\beta b_\alpha b_\beta [S_{\alpha\beta}(Q)-1] \quad (1)$$

The first term in the equation ($\sum_\alpha c_\alpha b_\alpha^2$) represents the self-scattering term, whilst the remainder of the equation corresponds to the distinct (or interference) scattering.[18] The c_α and c_β terms represent the atomic concentrations, whilst the b_α and b_β terms correspond to the scattering lengths. Finally, the $S_{\alpha\beta}(Q)$ term represents the partial structure factors. Handling of the data uses the GudrunN package[18], enabling determination of total structure factor, $F(Q)$, as described in Equation 2:[5]

$$\mathrm{F}(Q) = \sum\nolimits_{\alpha,\beta\geq\alpha} (2-\delta_{\alpha\beta}) c_\alpha c_\beta b_\alpha b_\beta [S_{\alpha\beta}(Q)-1] \quad (2)$$

$S_{\alpha\beta}(Q)$ is the term of interest in the above equation, and is the Fourier transform of the atomic pair distribution function ($g(r)$). The mathematical transformations from $S(Q)$ to

g(*r*) are performed by the software package,[18] based upon the information input regarding densities and atomic composition. The *g*(*r*) function shows how atomic densities vary as a function of radial distance, *r*, from any particular atom, and is represented by Equation 3.[17]

$$g(r) = \frac{1}{(2\pi)^3 \rho} \int 4\pi Q^2 F(Q) \frac{\sin Qr}{Qr} dQ \qquad (3)$$

The *g*(*r*) plot provides detailed insight into the arrangement of atoms within the solution, both showing the nearest-neighbours in addition to the longer-range structure.[19] Figure 3.1 is adapted from Soper and coworkers showing a schematic representation of the correlation between a typical g(r) plot with a 2-dimensional liquid structure.[19] The peaks in the *g*(*r*) profile, labelled (a) and (b), represent the distance from the central purple atom (circle) to the first and second atomic shells respectively. It is worth noting that the schematic shows a well ordered system, with greater disorder expected for liquid samples, increasing the complexity of analysis.

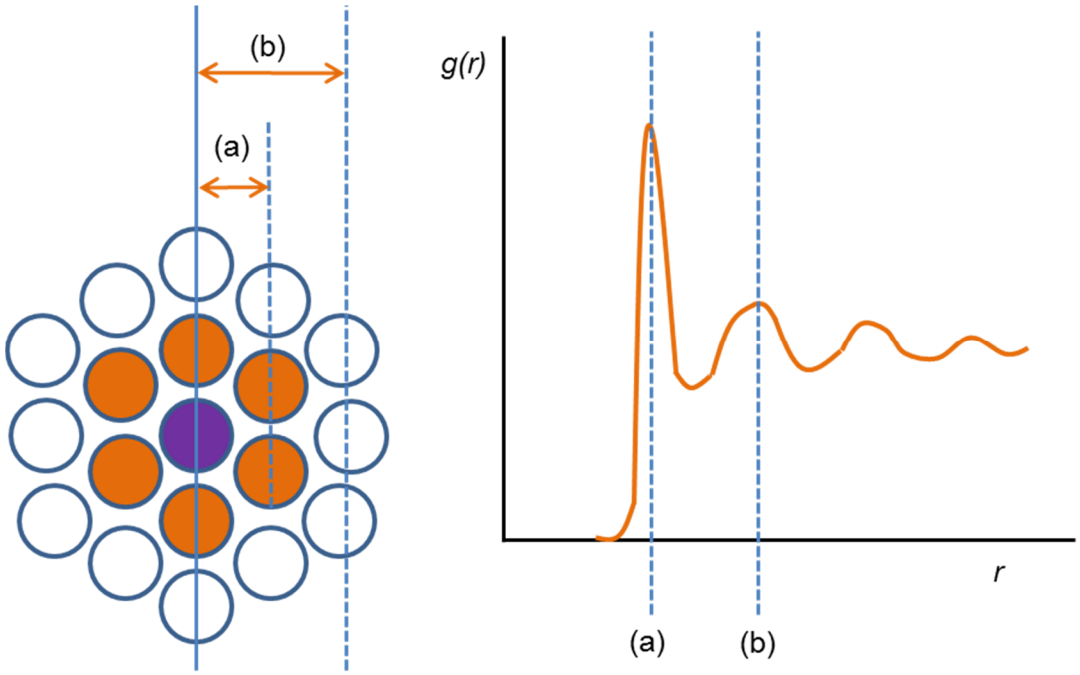

Figure 3.1: Schematic representation of the relationship between *g*(*r*) *vs* r plot and the two-dimensional liquid structure. This figure is adapted from Soper and coworkers.[19]

The disordered nature of liquid systems brings with it inherent challenges when trying to obtain atomistic insight, due to the absence of a regular crystal lattice. Many computational modelling packages are in regular use and can be used to simulate liquid structure; however, in general these are based upon theoretical information rather than

physical experimental data. A software suite entitled EPSR can be used to assemble a three-dimensional model of liquid mixtures. EPSR uses a Monte Carlo process to generate a modelled liquid box with a simulated differential scattering cross section that is consistent with the input experimental neutron data.[20] Minimisation of the difference between the experimental and simulated DSCS is the driving force for the iterative refinement.

EPSR simultaneously equilibrates the simulated differential scattering cross section to the neutron data collected for each of the isotopic substitutions included. Therefore it is advantageous to maximise the number of distinct samples studied in order to enhance the model accuracy. Once equilibrated the refinement information is assembled and averaged, enabling the generation of a single three-dimensional model that is in agreement with the data for each of the isotopic substitutions. From this model, it is possible to extract real-space pair distribution functions and gain insight into hydration shells of molecules.

3.3 Experimental details

Deuterated and protic water, deuterated and protic THF and protic 2-butoxyethanol were purchased from Sigma-Aldrich and used without further purification. Butoxyethanol-1,1,2,2-d_4 was purchased from QMX Laboratories Ltd, and used without further purification. This research was conducted in collaboration with Dr Samantha Callear and Prof. Alan Soper (STFC-ISIS).

In order to provide sufficient scattering contrast a series of solutions of different isotopic mixtures were assembled, and were injected into the sample cans, as seen in Figure 3.2. Each sample can is made of a Titanium-Zirconium alloy ($Ti_{0.68}Zr_{0.32}$) , is a flat plate with internal dimensions of 1 mm by 35 mm by 35 mm and has a wall thickness of 1.1 mm.[4] Each TiZr can contains approximately 1.2 mL of liquid sample. The opposite phase of scattered neutrons by Ti and Zr results in negligible coherent scattering.[18] Sample cans were held on an autosampler, under vacuum, in the neutron beam. Temperature was controlled remotely through use of an attached julabo.[21]

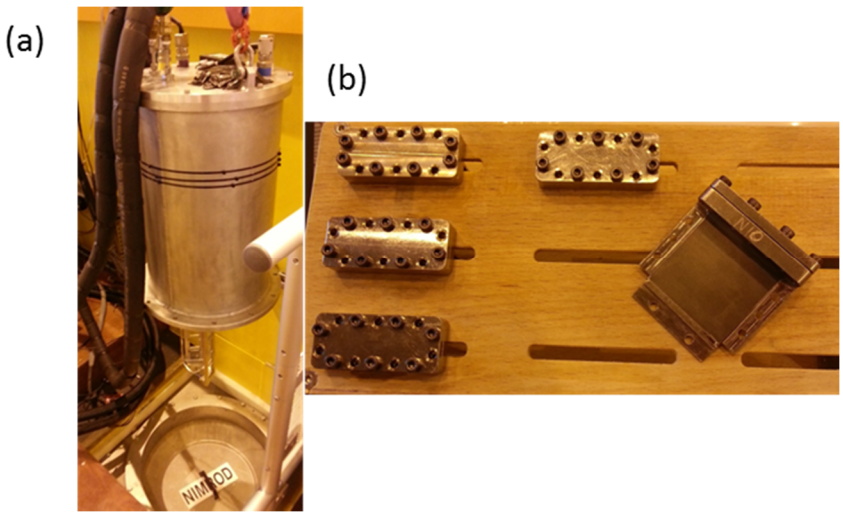

Figure 3.2: Photographs showing instrumentation at ISIS (a) NIMROD sample changer and (b) TiZr sample cans.

Raw experimental data were corrected and normalised using GudrunN, taking account of the background (TiZr can and instrument) and inelastic scattering.[18] Inelastic scattering is most problematic with hydrogen and deuterium atoms, and occurs due to energy exchange upon impact of the neutron to the atom, as described by Soper.[22] Corrections for inelastic scattering were performed iteratively using GudrunN, taking care to avoid subtraction of scattering due to the system of interest.

3.4 Aqueous THF (1:17 molar ratio)

Four isotopically distinct systems were studied in order to ensure sufficient scattering contrast, namely THF/H_2O, TDF/H_2O, THF/D_2O and TDF/D_2O. Neutron scattering data were collected well above the clathrate forming temperature and just elevated from it (20 ^oC and 6 ^oC respectively) to examine whether clustering occurs prior to clathrate development. The data were fully corrected and normalised using GudrunN[18] taking into account the necessary corrections for inelastic scattering. Plots showing the raw data are included in the Appendix.

The EPSR system was assembled containing water and THF molecules, of the correct concentration, within a cubic box at the appropriate temperature. The primary focus of this work was to elucidate the structure of the aqueous-THF system at 6 ^oC as this would be the structure most similar to that just prior to clathrate formation. The THF molecule was modelled and minimised using *.jmol*, ensuring that each atom was given an independent label to allow for individual atomic information to be incorporated, in a similar way to the work of Bowron *et al*.[4, 5] Figure 3.3 shows the labelling system used for the THF molecules.

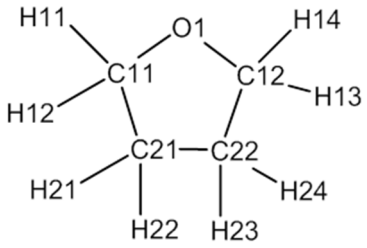

Figure 3.3: Atomic labelling used for the THF molecules

Bowron *et al.* have reported the Lennard-Jones parameters (ε and σ) and coulomb charges (e) for the THF molecule, as seen in Table 3.1 with atomic labels consistent with those in Figure 3.3.[4, 5] The same values are included within this work, and are important for seeding the simulation and ensuring an appropriate simulation starting point.

Atom	**ε (kJ/mol)**	**σ (Å)**	**q (e)**
O1	0.586	2.90	-0.4000
C11	1.251	3.21	0.140
C12	1.251	3.21	0.140
C21	1.251	3.21	0.000
C22	1.251	3.21	0.000
H11	0.791	2.58	0.030
H12	0.791	2.58	0.030
H13	0.791	2.58	0.030
H14	0.791	2.58	0.030
H21	0.791	2.58	0.000
H22	0.791	2.58	0.000
H23	0.791	2.58	0.000
H24	0.791	2.58	0.000

Table 3.1: Initial simulation parameters for THF molecules in the EPSR simulation.

The minimum bond distance values are also included in the EPSR simulation to ensure that the THF molecule maintains a chemically correct geometry, in addition to ensuring chemically feasible inter-molecule non-bonded distances. Once again, the values used are the same as those reported by Bowron *et al.* as shown in Table 3.2.[4, 5]

d/Å	**O1**	**C11**	**C12**	**C21**	**C22**	**H11**	**H12**	**H13**	**H14**	**H21**	**H22**	**H23**	**H24**
O1		1.42	1.42	2.33	2.37	2.06	2.08	2.08	2.05	3.29	2.7	2.88	3.28
C11			2.31	1.53	2.33	1.1	1.1	3.07	3.03	2.2	2.17	2.69	3.32
C12				2.36	1.53	2.82	3.22	1.1	1.1	3.34	2.72	2.17	2.2
C21					1.52	2.17	2.19	3.28	2.87	1.1	1.1	2.16	2.19
C22						2.69	3.32	2.19	2.17	2.2	2.16	1.1	1.1
H11							1.8	3.27	3.76	2.45	3.08	2.58	3.76
H12								4.03	3.74	2.69	2.46	3.76	4.21
H13									1.8	4.15	3.79	2.37	2.78
H14										3.92	2.81	3.05	2.38
H21											1.82	2.43	2.71
H22												3.06	2.45
H23													1.81
H24													

Table 3.2: Minimum bond distance constraints used for the THF molecule.[4, 5]

Following simulation equilibration, the potential energy was systematically modified in order to promote convergence between the simulated and experimental data. EPSR iteratively modifies the simulation in order to minimise the differences between datasets and attempt generation of a consistent and representative model. The potential energy was varied using a process of trial-and-error, monitoring changes in the overall error value as a measure of the quality of fit. A fine balance exists between providing sufficient energy to allow simulation convergence whilst not artificially over-fitting the data. Once the datasets had converged, the simulations were accumulated for several thousand iterations, until the plots of the partial site-site distributions had reduced noise levels. Figure 3.4 shows the fit of the EPSR model to the experimental neutron data for each of the isotopically distinct systems; the solid black line represents the experimental data whilst the open purple dashes represent the model data. Overall the quality of the fit is good especially at $Q > 2$, although there are some apparent deviations in the fit at low Q. Soper and Bowron report that differences in low Q are generally found to correspond to low frequency components which in real-space correspond to unphysically short interatomic distances and are therefore unimportant.[4]

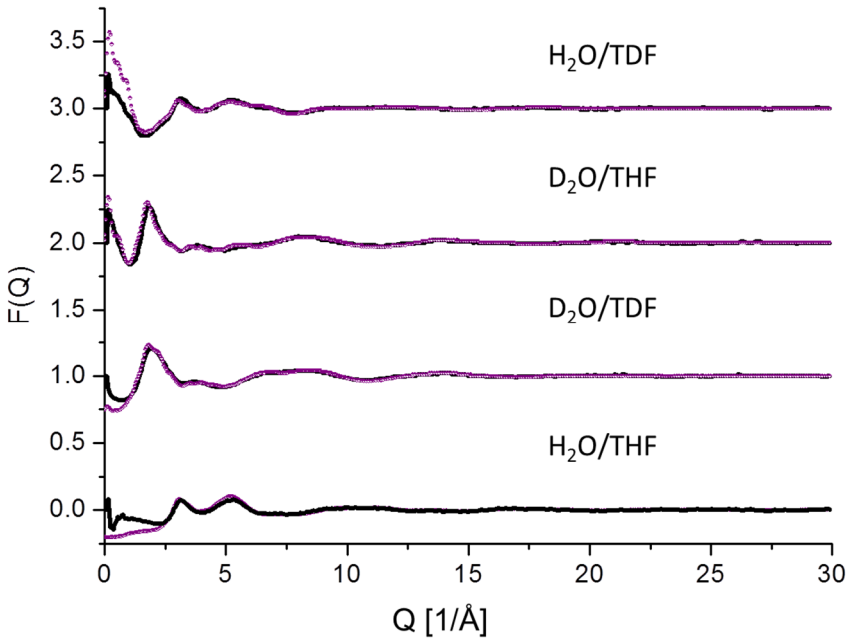

Figure 3.4: Quality of fit for EPSR simulation to experimental data, viewed in Q space. Black line represents the experimental neutron data and purple circles represent the simulated data from EPSR. This data is taken at 6 °C. Data are vertically offset at F(Q) = 0,1,2,3.

The results can then be viewed in real-space, as seen in Figure 3.5. The quality of the fit is sufficiently adequate to allow reliable detailed structural analysis.

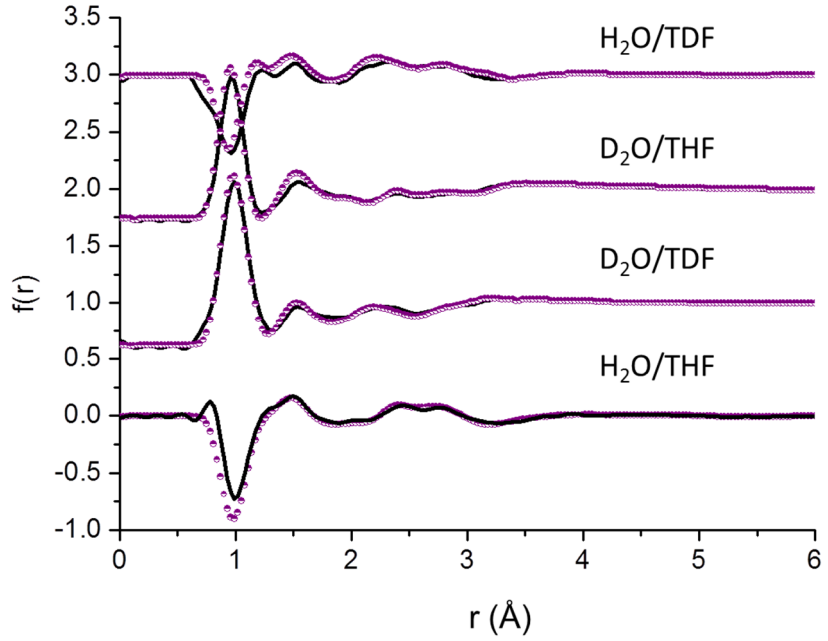

Figure 3.5: Quality of fit of EPSR simulation to experimental data, viewed in real-space. Black line represents the experimental neutron data and purple circles represent the simulated data from EPSR. Temperature = 6 °C.

Once the datasets are accumulated, the EPSR software suite allows for the calculation of site-site distribution functions, atomic coordination numbers and spatial density functions. Figure 3.6 shows the EPSR generated partial site-site distribution functions for the water molecules in the THF/water (1:17) systems at both 6 °C and 20 °C. The labels OW and HW are given to the oxygen and hydrogen atoms of the water molecules. In simple terms, the $g_{OW\text{-}OW}(r)$ *vs* r plot shows the atomic distribution of neighbouring water oxygen atoms in relation to a central water oxygen atom, highlighting how the hydration shell varies as a function of distance. Temperature appears to have no effect upon the water structuring, indicating that significant changes do not occur as the clathrate hydrate forming temperature is approached.

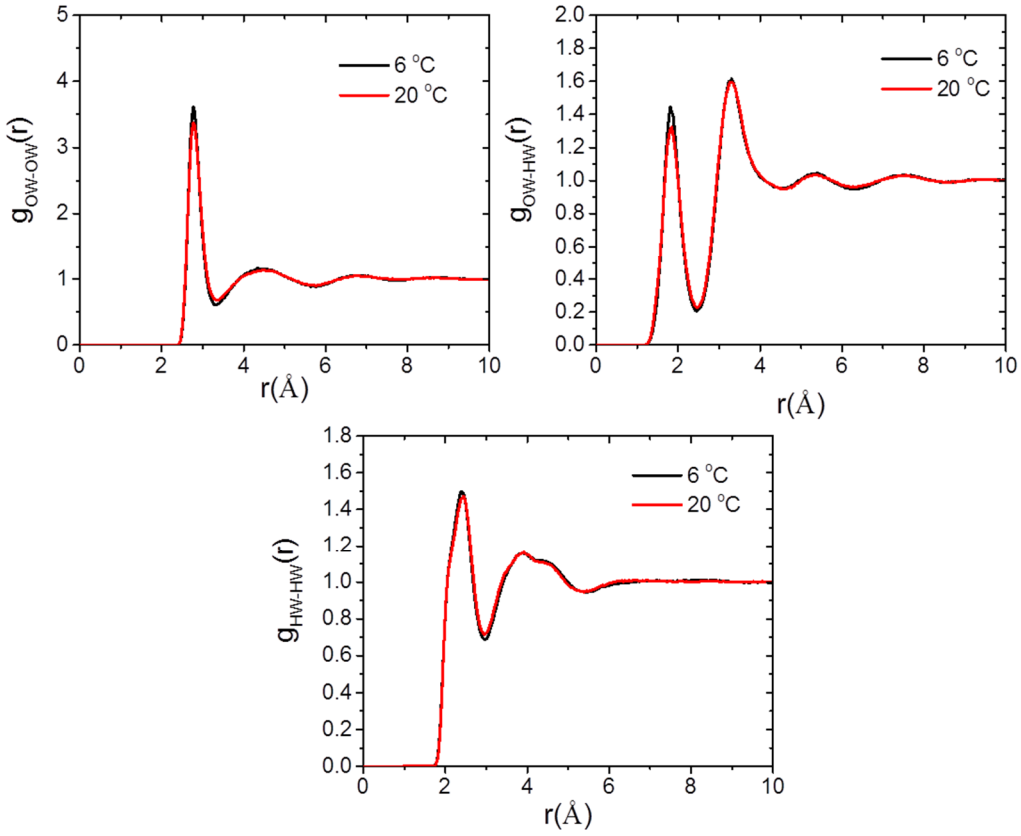

Figure 3.6: EPSR generated partial atomic distribution functions for (a) OW-OW, (b) OW-HW and (c) HW-HW interactions.

For comparison, Figure 3.7 shows the analogous partial site-site distribution functions reported by Bowron *et al.* for the 0.23 mole fraction THF/water mixture at 20 °C (solid lines) and pure water (dashed lines).[4]

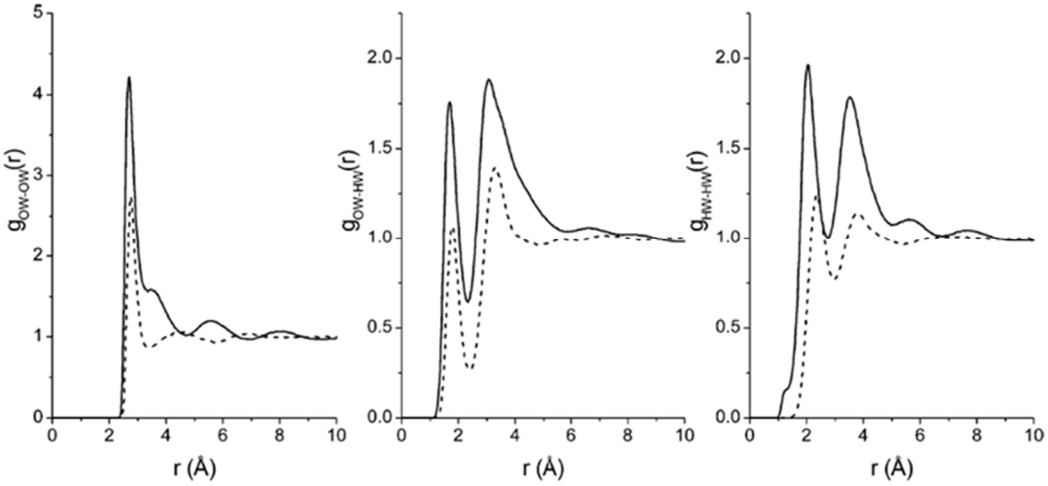

Figure 3.7: EPSR generated partial site-site distribution functions reported by Bowron *et al.* for 0.23 mole fraction THF/water system (solid lines) and pure water (dashed lines).[4]

As anticipated the distribution functions calculated in this work are different to those reported by Bowron *et al*., appearing to be an intermediate value between that of the THF-rich and pure water functions. Water-THF mixtures are known to possess an unusual closed-loop phase diagram, with interesting liquid-liquid immiscibility observed under specific conditions of concentration and temperature.[4] This propensity for phase separation indicates the potential for non-ideal solution behaviour. Whilst the composition of the system studied in this work is below the immiscibility limit it is worth noting that such a separation phenomenon can exist for mixtures of these solvents.

Bowron *et al.* studied a 0.23 mole fraction THF-water system at room temperature and ambient pressure, which also constituted a system below the immiscibility limit due to being insufficiently heated. Bowron noted the rise at low *r* for the aqueous-solvent mixture in comparison to pure water, attributing this to the mixture undergoing some degree of spatial confinement wherein the water molecules are confined and partially segregated in the overall mixture.[4] A similar, if less intense, rise is also observed in the 1:17 systems. This implies that even at this low THF concentration, and low temperature, well below the immiscibility limit for the aqueous THF mixture, there still appears a tendency for some degree of segregation. Figure 3.8 shows selected partial distribution functions for the interactions involving the ether oxygen atom of the THF ring, namely HW-O1 and OW-O1, confirming the formation of hydrogen bonding interactions at this moiety.

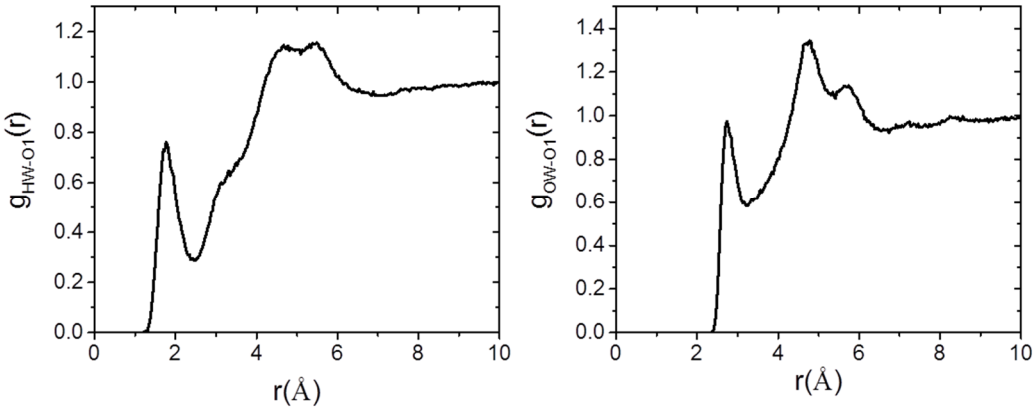

Figure 3.8: Partial distribution functions for water-ether oxygen atom interactions

While the site-site distribution functions provide insight into the density distributions of one atom in relation to another, the coordination numbers for each atom pair provide quantitative insight into the hydration numbers. Figure 3.9 is a schematic representation of the coordination number determination for the OW-OW shells, where the r_{min} and r_{max} are specified in order to allow integration of the area under each part of the curve. In this example (1) covers a radius range 2.4 – 3.3 Å (first shell), and then (2) covers 3.3 – 5.6 Å; by specifying the r_{min} and r_{max} it is possible to gain insight into each hydration shell, as opposed to just calculating an overall coordination number.

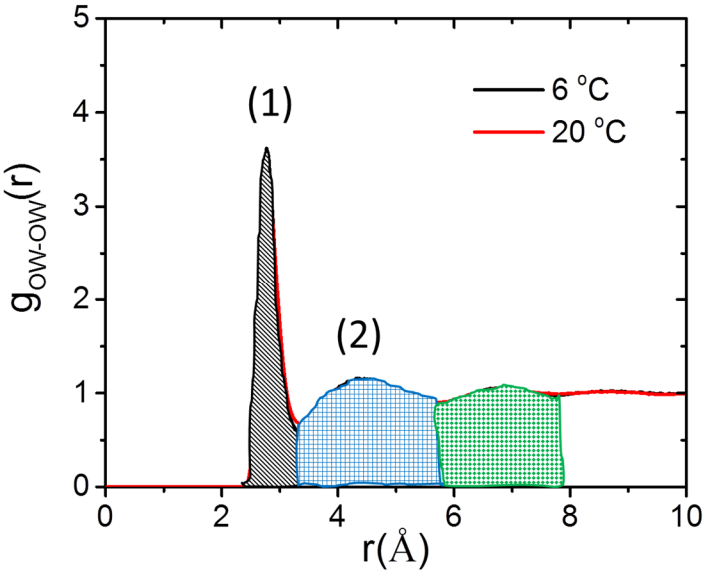

Figure 3.9: Calculation of the coordination numbers for OW-OW. Specific r_{min} and r_{max} are outlined as follows (1) 2.4 – 3.3 Å and (2) 3.3 – 5.6 Å.

The calculated coordination numbers for the interactions of interest are reported in Table 3.3. The r_{min} and r_{max} are selected in agreement with the work published by Bowron *et*

al. in order to enable comparison between systems.[4] The first atom in the correlation list is considered the central atom, for example O1-OW is considering the shell of OW atoms surrounding a central O1 atom, while OW-O1 examines how many O1 atoms are surrounding a central OW atom. The coordination numbers are considerably lower in the latter correlation than in the former, as the numbers are calculated as an average of the simulation box which is dominated by water molecules. The coordination numbers indicate that, on average, approximately one water molecule hydrogen atom is strongly associated with the ether oxygen atom of the THF molecule.

Correlation	R_{min} (Å)	R_{max} (Å)	Coordination no. (atoms)	ESD
O1-O1	2.4	4.0	0.18	0.39
O1-O1	4.0	7.3	1.92	1.34
O1-H11	2.3	3.6	0.09	0.29
O1-H12	2.3	3.6	0.06	0.24
O1-H13	2.3	3.8	0.13	0.34
O1-H14	2.3	3.5	0.09	0.28
O1-OW	2.3	3.3	1.53	0.69
O1-OW	3.3	4.4	4.09	1.73
O1-OW	4.4	5.35	8.70	2.45
O1-OW	5.35	6.7	16.35	3.51
OW-O1	2.3	3.3	0.09	0.30
OW-O1	3.3	4.4	0.24	0.48
OW-O1	4.4	5.35	0.51	0.69
OW-O1	5.35	6.7	0.96	0.93
O1-HW	1.2	2.46	1.19	0.56
O1-HW	2.46	3.6	3.61	1.52
HW-O1	1.2	2.46	0.04	0.19
HW-O1	2.46	3.6	0.11	0.32
H11-OW	2.3	3.7	3.560	1.43
H12-OW	2.3	3.7	3.66	1.46
H13-OW	2.3	3.7	3.61	1.40
H14-OW	2.3	3.7	3.61	1.45
OW-OW	2.4	3.3	3.83	0.91
OW-OW	3.3	5.6	15.09	2.9
OW-OW	2.4	5.6	18.92	3.09
OW-HW	1.2	2.5	1.82	0.61
HW-OW	1.2	2.5	0.91	0.38
HW-HW	1	2.93	4.36	1.29
HW-HW	2.93	5.13	24.75	4.65

Table 3.3: Coordination numbers for selected correlations in the THF/water EPSR simulation at 6 ^{o}C.

Finally, to aid with visualising the three-dimensional structure, the spatial density functions ($g_c(r,\Omega)$) have been calculated within the EPSR software suite, according to the schematic shown in Figure 3.10. In such plots an atom is placed at the origin, in this case the ether oxygen atom of the THF molecule, and then a three-dimensional map is generated to show the density of other molecules in relation to this origin atom as a function of radial distance (r) and orientation ($\Omega = \theta,\phi$).

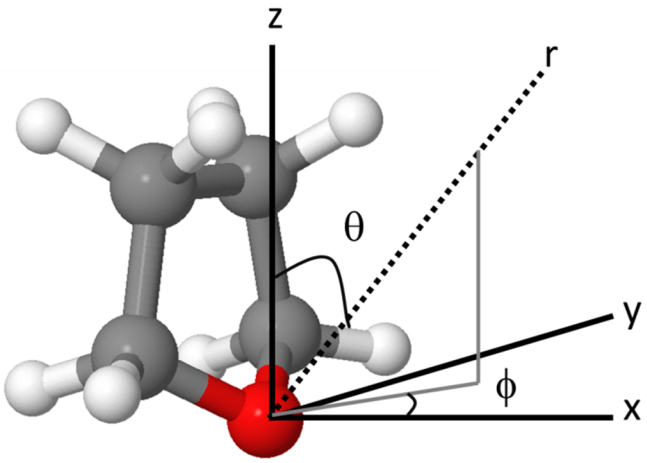

Figure 3.10: Reference coordinate axes for the spatial density function calculations involving the THF molecule. Schematic is based upon that reported by Bowron *et al*.[4]

By plotting the spatial density function of water oxygen atoms (OW) surrounding the THF ether oxygen origin, it is possible to generate an image of the THF hydration sphere. Figure 3.11 shows a 3D plot of the shell of O1-OW interactions at (a) 2.0 – 3.0 Å and (b) 3.0 – 4.1 Å; these images give an idea of the first and second hydration shells of the THF molecules within the liquid system. The isosurface levels show the most likely region that would be occupied by the specified percentage of neighbouring molecules; so in (a) the image shows the most probable 50% of neighbouring water molecules surrounding the ether oxygen atom.

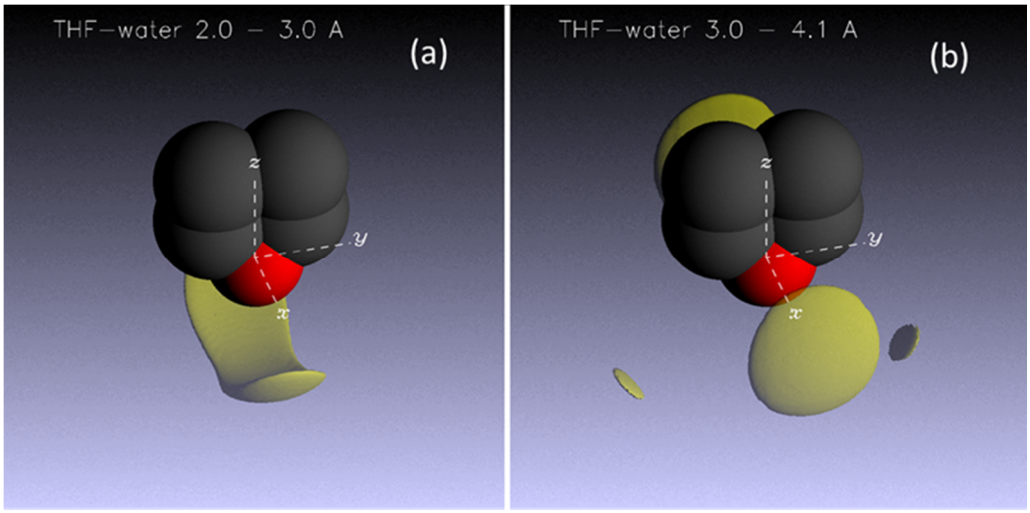

Figure 3.11: EPSR derived spatial density functions for the aqueous THF (1:17) mixture at 6 ^{o}C: (a) $g(r,\Omega)$ in the distance range 2.0-3.0 Å at an isosurface level of 50%; (b) $g(r,\Omega)$ in the distance range 3.0-4.1 Å at an isosurface level of 15%

For completeness, the 3D spatial density function for the water-water interactions (OW-OW interactions), at a distance range 2.0 – 3.5 Å is shown in Figure 3.12. This provides insight into the first hydration shell of the water molecules in the aqueous-THF mixture.

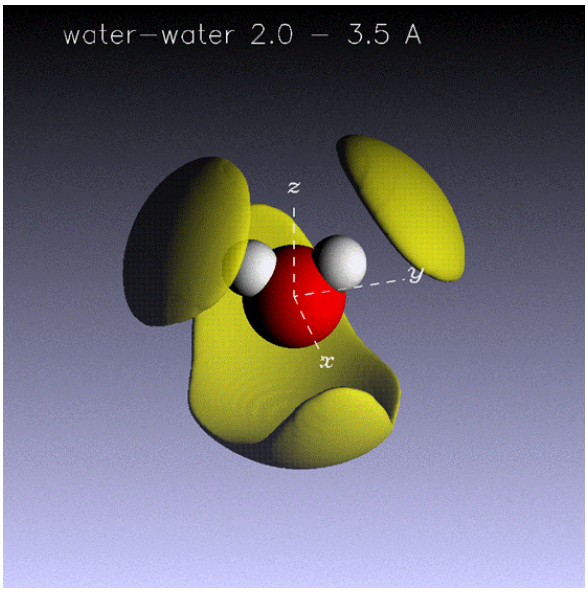

Figure 3.12: EPSR derived spatial density functions for the water-water interactions in the THF-water (1:17) mixture at 6 ^{o}C in the distance range 2.0 – 3.5 Å at an isosurface level of 50%.

To conclude, these data indicate that significant re-structuring does not occur as the temperature is lowered from 20 ^{o}C to 6 ^{o}C, implying an absence of transition to a “clathrate-like” structure. It is worth noting that literature articles disclosing the synthesis of THF hydrate at 4 ^{o}C report the application of cold-sources (*i.e.* cold copper wire) in order to

initiate nucleation.[23] This may explain why little change is observed as the temperature is lowered in this investigation, in addition to deliberately avoiding cooling to, and below 4 ^{o}C. Therefore, it does not appear that formation of THF hydrate is intrinsic, and that artificial nucleation initiation is necessary to induce transformation from liquid to crystalline material. Finally, the coordination numbers and spatial density functions confirm the hydrogen bonding interactions between the THF and water molecules, in addition to the water-water interactions.

3.4.1 THF hydrate inhibition

The formation of THF hydrate is well established at temperatures below 4 ^{o}C,[23] and therefore the work outlined previously was undertaken at 6 ^{o}C to ensure a homogeneous liquid solution was present throughout. However, a crude snapshot of the inhibition ability of PVCap was gained by applying several cooling and heating cycles to the samples. In the knowledge that initiation is required in order to induce crystallization, the samples were flash cooled to -15 ^{o}C, noting transition to ice. Following this, the samples were heated to 15 ^{o}C, with the neutron scattering data confirming the transition to homogeneous liquid samples. Finally, the temperature of the samples was slowly reduced to 3 ^{o}C to promote hydrate formation, and neutron scattering data were recorded. As seen in Figure 3.13 the TDF/D_2O sample (at 3 ^{o}C) has multiple sharp Bragg peaks, therein indicating that THF hydrate (a crystalline species) has formed. In contrast, the sample containing PVCap/TDF/D_2O has a smooth differential scattering cross section, indicative of a liquid sample. This shows that the presence of the PVCap inhibitor successfully prevented the formation of THF hydrate at 3 ^{o}C.

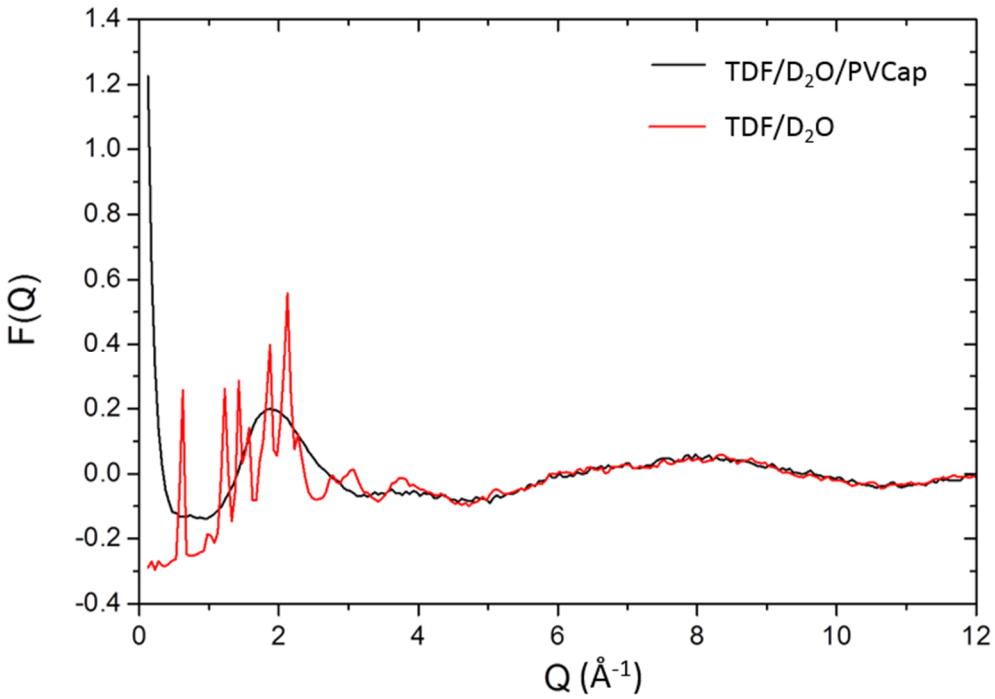

Figure 3.13: Experimental neutron data for (a) TDF/D_2O and (b) PVCap/TDF/D_2O at 3 °C

While additional datasets were collected for the ternary PVCap-aqueous THF systems (a range of isotopic substitution using deuterated and protic water and THF in combination with protic PVCap) little information could be elucidated from these data. It was not possible to develop a reliable EPSR simulation for the ternary mixture, due to the highly complex nature of this liquid system. Generation of EPSR simulation models for this, and other similar ternary mixtures, may provide further insight into the inhibitor mode of action, however, this was not possible using current knowledge and software.

3.5 Aqueous 2-butoxyethanol

There is considerable empirical evidence that 2-butoxyethanol acts as a "promoter" of hydrate inhibitor activity and it has been shown that KHI performance is markedly improved in the presence of this co-solvent.[10] The behaviour of dilute solutions of 2-butoxyethanol in water have long been recognised to be of interest, with evidence for the aggregation and surfactant-like behaviour and there have already been some SANS studies on the system, albeit not in a hydrate inhibition context.[11, 12, 24] Giordano and Teixeira suggested that the propensity of 2-butoxyethanol to form surfactant-like aggregates is unsurprising considering the similarities in chemical structure and phase diagram to the more traditional chained non-ionic surfactants.[11] Early studies using ultrasonic measurements indicate that water/2-

butoxyethanol mixtures possess temperature and concentration behaviour similar to the critical micelle concentration (CMC) curves of surfactant analogues.[25]

Yoshida *et al.* combined SANS and neutron spin echo (NSE) studies to probe concentration fluctuations within an aqueous 2-butoxeythanol system as a function of temperature.[24] They attributed the observed fluctuations to the formation of 2-butoxyethanol clusters taking the form of incomplete micelles.[24] It was postulated that the micelles contain a hydrophobic core, and that the hydroxyl functionalities retain the ability to form hydrogen bonds with neighbouring water species.[24] The hydration state of 2-butoxyethanol micelles was probed by Arikawa *et al.*, showing a decrease in hydration number upon transition from free 2-butoxyethanol molecules to spherical micelles.[26] More recently, Zhanpeisov *et al*. combined DFT calculations with Raman data to explore hydration of 2-butoxyethanol, with hydration occurring at both the alcohol and ether oxygen atoms.[27]

However, no attempt has previously been made to derive a detailed molecular level model using EPSR simulation. This work focusses on the neutron scattering data collected using NIMROD for a 0.05 mole fraction aqueous 2-butoxyethanol system at 6 ^{o}C. Such a sample composition was chosen as this should provide sufficient solute scattering while limiting molecule aggregation.

In order to provide sufficient scattering contrast a combination of five isotopically distinct systems were studied, using both protic and deuterated 2-butoxyethanol and water. It was not possible to purchase a fully deuterated analogue of 2-butoxyethanol, and as such this work used Butoxyethanol-1,1,2,2-d_4 (hereafter labelled DBut), which is deuterated between the ether and alcohol moieties but contains a protic butyl tail. Data were collected for the following systems: (1) H_2O/HBut, (2) D_2O/HBut, (3) D_2O/DBut, (4) H_2O/DBut (5) H_2O/D_2O(50:50)/HBut and (6) H_2O/D_2O(50:50)/DBut.

As previously outlined, the neutron data were corrected and fully normalised using GudrunN[18], taking into account corrections for inelastic scattering and background. A large rise at low *Q* is observed, as seen in Figure 3.14, which can be attributed to the occurrence of aggregates within the system, potentially as a result of solute micelle formation. The presence of such small-angle scattering is consistent with that reported by D'Arrigo *et al.*[11, 12] Figure 3.14 also highlights that PVCap appears to have little overall effect on the large-scale structures, with little change in the degree of small-angle scattering. In order to gain additional insight into the shape of the large-scale structures, detailed SANS analysis can be

undertaken focussing on this large rise at low Q. However, this is outside of the remit of this current work, but will form the focus of future collaborative projects with STFC-ISIS.

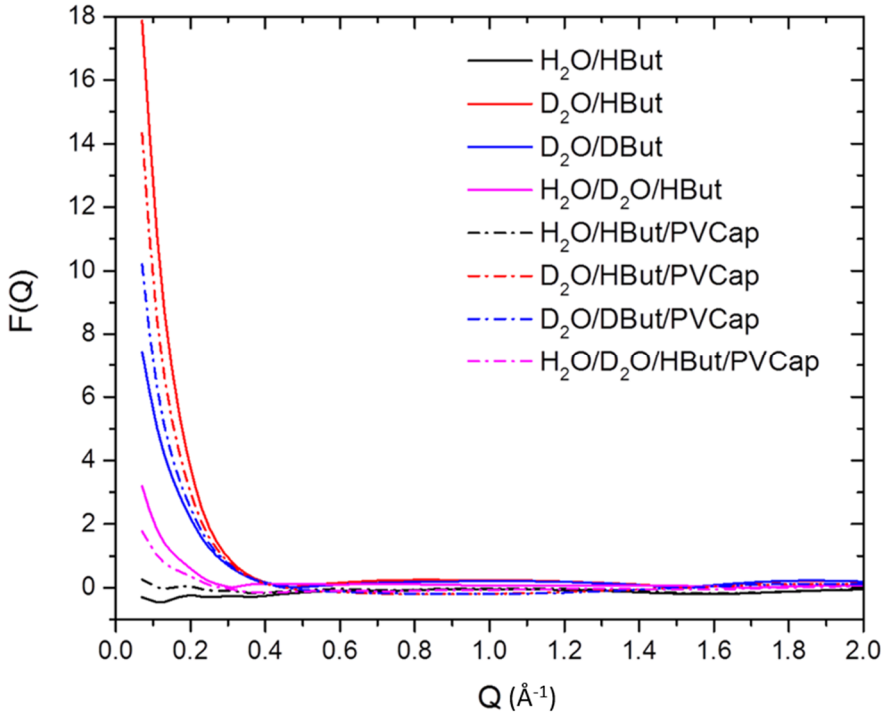

Figure 3.14: Small-angle neutron scattering data for aqueous butoxyethanol systems at 6 ^{o}C.

While PVCap appears to have little effect upon the aggregation behaviour of 2-butoxyethanol, the polymer does have a more pronounced effect on the atomic interactions as seen in the overall atomic pair distribution functions (Figure 3.15). It is unsurprising that PVCap does not prevent solute micelle formation, as the polymer does not participate in significant hydrogen bonding interactions with 2-butoxyethanol, as established in Chapter 2. The atomic pair distribution functions are dominated by the water component, due to the low concentration of solutes added. Therefore, it is postulated that such atomistic differences upon addition of PVCap are a result of polymer-water interactions as opposed to polymer-2-butoxyethanol interactions. In order to fully probe this theory, it would be desirable to develop an EPSR model for the tertiary mixture, however, this proved challenging due to the many system variables and unknowns about the polymer species; further work in this area would be advantageous. Overall, it is therefore possible to think of the aqueous KHI system as having two interactions of interest: (1) 2-butoxyethanol-water interactions and (2) KHI-water interactions. The remainder of this chapter will focus on exploring the interactions between water and 2-butoxyethanol, while Chapter 4 will focus on the aqueous-polymer system.

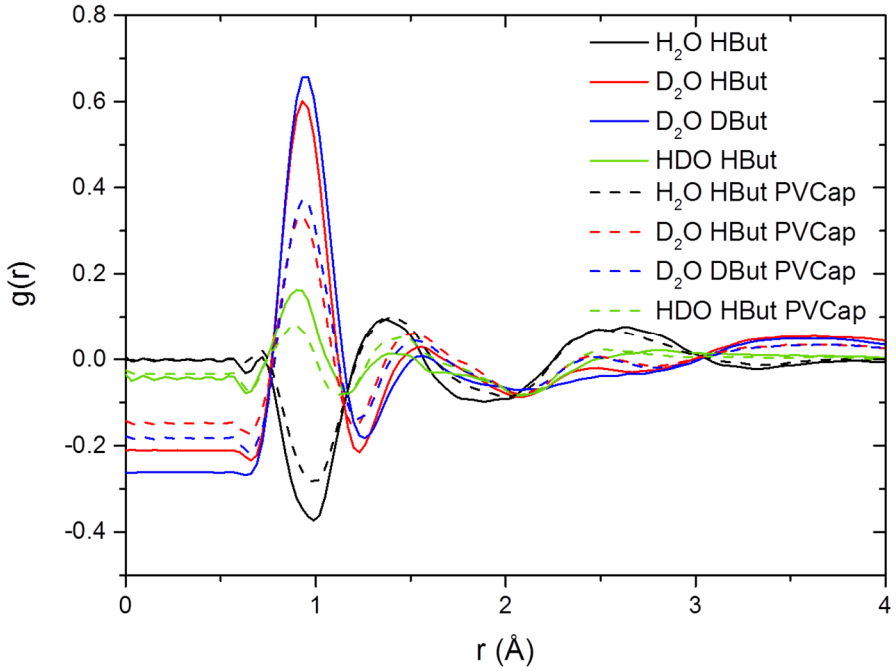

Figure 3.15: Experimental total pair distribution functions for aqueous butoxyethanol and aqueous-butoxyethanol-PVCap systems for data collected at 6 °C

An EPSR simulation was compiled, containing 247 water molecules and 13 molecules of 2-butoxyethanol, in an attempt to establish atomistic information about the liquid structure of aqueous 2-butoxyethanol. However, it should be noted that the software is unable to model large-scale structures, and will therefore not provide insight into the aggregates. A model of 2-butoxyethanol was generated using *.jmol* and optimised using MOPAC. Once again, distinct atom environments were given independent labels, and each atomic label given relevant Lennard-Jones and charge parameters, as seen in Figure 3.16 and Table 3.4.

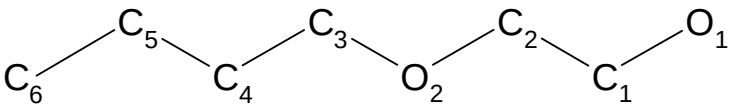

Figure 3.16: Atom labelling system used for 2-butoxyethanol in EPSR

Atom	ε (kJ/mol)	σ (Å)	q (e)
O1	0.71	3.12	-0.68
O2	0.59	2.9	-0.38
C1	0.28	3.5	0.2
C2	0.28	3.5	0.2
C3	0.28	3.5	0.2
C4	0.28	3.5	-0.07
C5	0.28	3.5	-0.07
C6	0.28	3.5	-0.07
H1	0	0	0.05
H2	0	0	0.07
H3	0	0	0.06
H4	0	0	0.06
H5	0	0	0.06
H6	0	0	0.06
H7	0.065	1.8	0

Table 3.4: Initial simulation parameters for 2-butoxyethanol molecules in the EPSR simulation

Attempts to develop an accurate and reliable EPSR model proved challenging, due in part to the complexities imparted by the presence of larger structures within solution. Figure 3.17 shows the fit of the most accurate simulation model alongside the experimental neutron data for each of the isotopic substitutions.

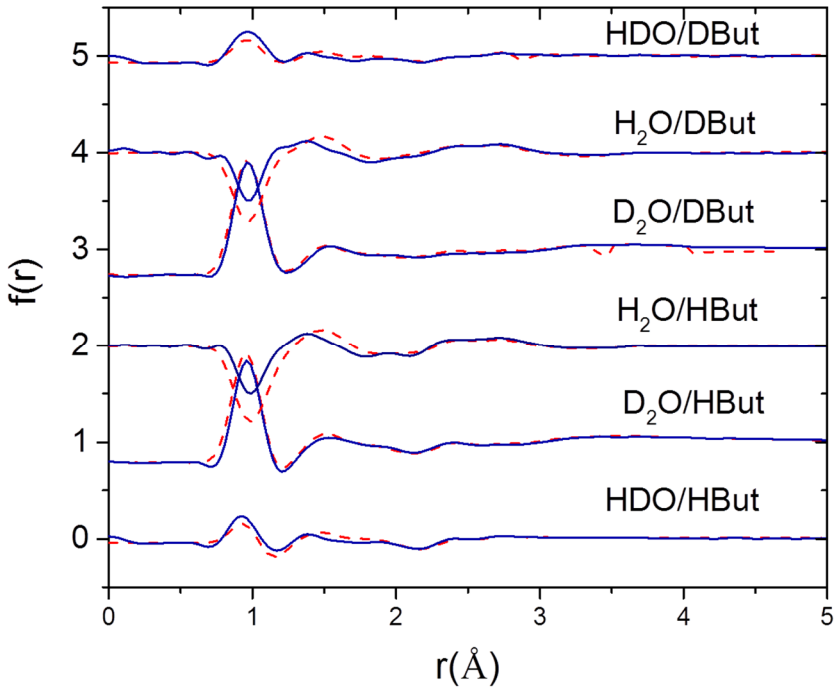

Figure 3.17: Quality of fit of EPSR simulation to experimental data for the aqueous 2-butoxyethanol system. Blue line shows the experimental neutron data and the red dashes show the simulated data generated from the EPSR simulation.

Although the fit of the model to the experimental data is reasonable, further work would be advantageous in order to incorporate information regarding the large structures as this would have an influence upon the interactions between 2-butoxyethanol and water. Some of the important EPSR calculated partial site-site distribution functions are shown in Figure 3.18, highlighting the water-water and water-solute interactions of interest. The expected hydrogen bonding interactions are observed between the alcohol moiety and water molecules (O1-OW and O1-HW). In addition, Zhanpeisov *et al*. identified the formation of hydrogen bonding interactions between the ether moiety and water molecules, through DFT calculations.[26] Therefore, ether-water interactions have been probed in the system of study (O2-OW), and are shown below.

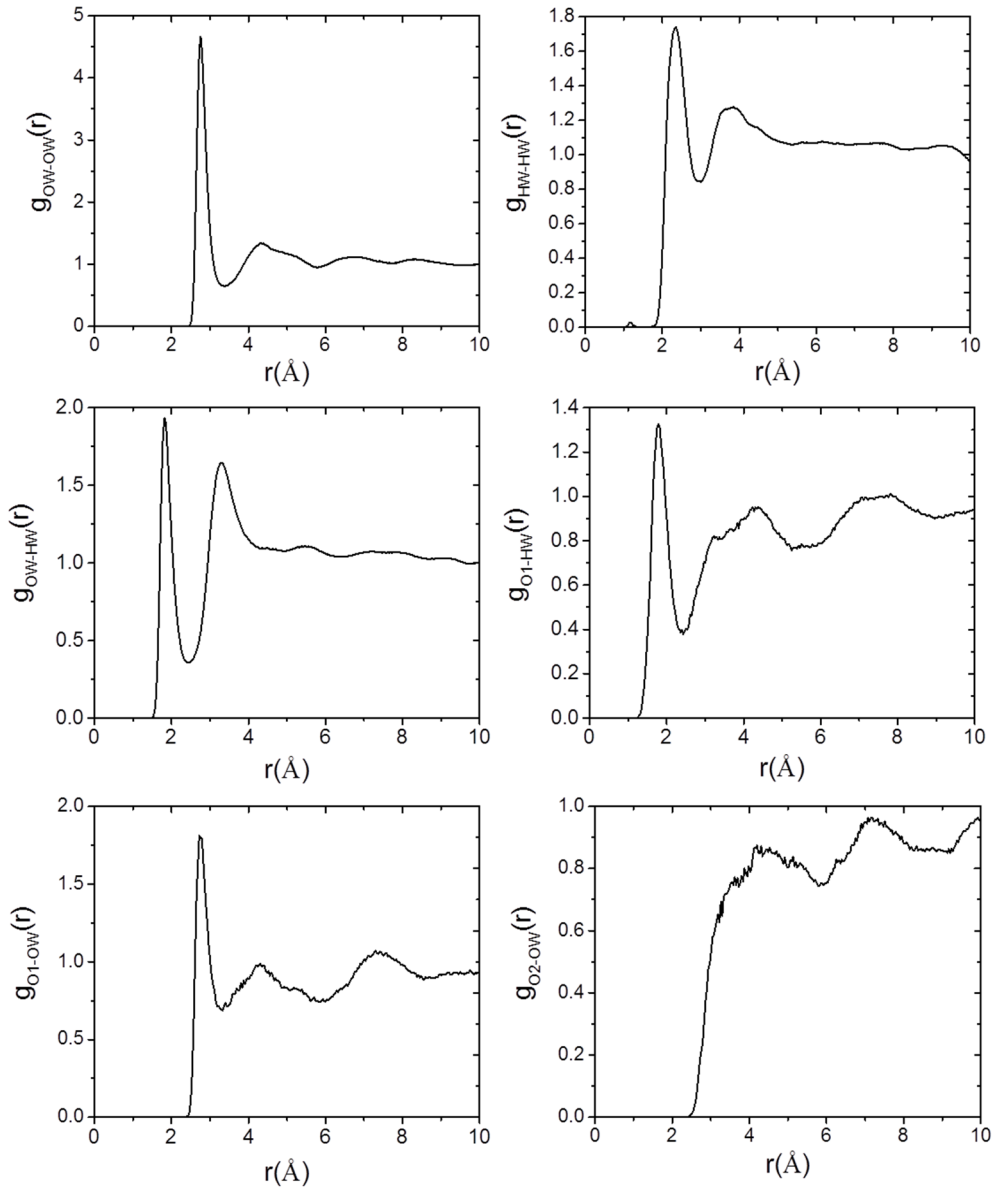

Figure 3.18: Selected partial site-site distribution functions for interactions in the 0.05 mole fraction aqueous 2-butoxyethanol system at 6 ^{o}C.

The first peak in the OW-OW distribution function, in Figure 3.18, is more intense than that reported previously in the aqueous-THF systems and also that for pure water (as reported by Bowron[4] and shown in Figure 3.7). This supports the idea that this system undergoes partial segregation wherein the water molecules undergo some degree of spatial confinement (*i.e.* some separation from the solute), thereby enhancing the density of close water-water interactions. It is postulated that aggregation of 2-butoxyethanol molecules and the consequential formation of large-scale structures, would cause the solute-solvent separation, and therein increase the close water-water interactions.

Absence of the ether-water interaction (O2-OW), as reported by Zhanpeisov,[26] may be as a consequence of solute micelle formation. It is anticipated that the ether moiety would be encapsulated in large-scale structures, therein making it less available for hydration. However, the inability of EPSR to model the formation of large scale structures limits the atomistic information available, and goes some way to explaining the differences between the simulated and experimental neutron data.

3.6 Conclusion

This chapter highlighted the variety of information available from combining neutron scattering experiments with EPSR modelling, providing insight into complex liquid systems. Investigations into THF-water (1:17) mixtures reported no re-structuring as the clathrate hydrate temperature is approached. Akin to earlier work by Bowron, the system appears to experience some degree of spatial confinement, wherein the water and THF molecules are partially separated within the liquid system resulting in clustering of the individual components.

Neutron scattering data for the aqueous 2-butoxyethanol systems are in agreement with those reported in the literature, showing small-angle scattering attributable to the formation of molecular aggregates. Exploration of the shape of these large-scale structures will form the focus of future collaborations, but is however outside of the remit of this project. Addition of PVCap does not appear to prevent 2-butoxyethanol aggregation, which is unsurprising as the polymer is not believed to interact with the alcoholic solute, as identified in Chapter 2. However, the overall atomic pair distribution functions differ between the aqueous 2-butoxyethanol systems with and without PVCap, indicating that the polymer does alter the atomic interactions in the solution. Therefore atomistic differences between these systems are largely attributed to polymer-water interactions as opposed to polymer-2-butoxyethanol interactions. Chapter 4 aims to examine the aqueous PVCap system in more detail.

3.7 References

1. S.M.Bennington, A.C.Hannon and S.E.Rogers, in *ISIS Neutron Training Course*.
2. F. Foglia, M. J. Lawrence, C. D. Lorenz and S. E. McLain, *J. Chem. Phys.*, 2010, **133**.
3. J. L. Finney, D. T. Bowron and A. K. Soper, *J. Phys. Condes. Matter*, 2000, **12**, A123-A128.
4. D. T. Bowron, J. L. Finney and A. K. Soper, *J. Phys. Chem. B*, 2006, **110**, 20235-20245.

5. D. T. Bowron, J. L. Finney and A. K. Soper, *J. Am. Chem. Soc.*, 2006, **128**, 5119-5126.
6. J. J. Towey, A. K. Soper and L. Dougan, *PCCP Phys. Chem. Chem. Phys.*, 2011, **13**, 9397-9406.
7. S. E. Pagnotta, S. E. McLain, A. K. Soper, F. Bruni and M. A. Ricci, *J. Phys. Chem. B*, 2010, **114**, 4904-4908.
8. N. H. Rhys, A. K. Soper and L. Dougan, *J. Phys. Chem. B*, 2012, **116**, 13308-13319.
9. C. A. Koh, R. P. Wisbey, X. P. Wu, R. E. Westacott and A. K. Soper, *J. Chem. Phys.*, 2000, **113**, 6390-6397.
10. J. M. Cohen, P. F. Wolf and W. D. Young, *Energy Fuels*, 1998, **12**, 216-218.
11. G. D'Arrigo, R. Giordano and J. Teixeira, *Physica Scripta*, 1992, **1992**, 248.
12. G. D'Arrigo, J. Teixeira, R. Giordano and F. Mallamace, *J. Chem. Phys.*, 1991, **95**, 2732-2737.
13. http://www.isis.stfc.ac.uk/instruments/sandals/sandals6929.html.
14. http://www.isis.stfc.ac.uk/instruments/nimrod/nimrod2468.html.
15. D. T. Bowron, A. K. Soper, K. Jones, S. Ansell, S. Birch, J. Norris, L. Perrott, D. Riedel, N. J. Rhodes, S. R. Wakefield, A. Botti, M. A. Ricci, F. Grazzi and M. Zoppi, *Rev. Sci. Instrum.*, 2010, **81**, 033905.
16. C. Benmore and A. Soper, *The SANDALS manual. A guide to performing experiments on the small angle neutron diffractometer for amorphous and liquid samples at ISIS*, Council for the Central Lab. of the Research Councils (CLRC), Chilton (United Kingdom). Rutherford Appleton Lab, 1998.
17. D. Keen, *J. Appl. Crystallogr.*, 2001, **34**, 172-177.
18. A. Soper, *GudrunN and GudrunX. Programs for correcting raw neutron and x-ray total scattering data to differential cross section*, ISIS, Rutherford Appleton Laboratory, Oxford, 2012.
19. J. L. Finney and A. K. Soper, *Chem. Soc. Rev.*, 1994, **23**, 1-10.
20. A. K. Soper, *Chem. Phys.*, 1996, **202**, 295-306.
21. http://www.isis.stfc.ac.uk/sample-environment/low-temperature/water-baths/water-baths9789.html.
22. A. K. Soper, *Mol. Phys.*, 2009, **107**, 1667-1684.
23. T. Y. Makogon, R. Larsen, C. A. Knight and E. D. Sloan, *J. Cryst. Growth*, 1997, **179**, 258-262.
24. K. Yoshida, T. Yamaguchi, T. Otomo, M. Nagao, H. Seto and T. Takeda, *J. Mol. Liq.*, 2005, **119**, 125-131.
25. G. D'Arrigo, F. Mallamace, N. Micali, A. Paparelli and C. Vasi, *Physical Review A*, 1991, **44**, 2578 – 2587.
26. T. Arikawa, M. Nagai and K. Tanaka, *Chem. Phys. Lett.*, 2009, **477**, 95-101.
27. N. U. Zhanpeisov, S. Takanashi, S. Kajimoto and H. Fukumura, *Chem. Phys. Lett.*, 2010, **491**, 151-155.

4 Neutron scattering of water – lactam mixtures

4.1 Introduction

As outlined in Chapter 1, a multitude of research exists exploring clathrate hydrate formation and KHI mode of action. Of most relevance to this chapter is the literature outlining use of computational modelling[1-3] and neutron scattering experiments.[4-6] Due to the large number of atoms present in clathrate hydrate and KHI-containing simulations, undertaking a purely computational study can be arduous and computationally expensive.[7] However, Rodger and co-workers have used Molecular Dynamics (MD) simulations to show that inhibitors appear to reduce the degree of structuring of water molecules, therein delaying or preventing hydrate nucleation.[1, 8] In a similar manner, Anderson *et al.* computationally examined the radial distribution functions of several KHIs during the binding of inhibitor to the hydrate surface.[2] The recent review by MacElroy and English[7] highlights the significant developments made in using molecular simulations to gain insight into clathrate hydrate systems, and describes huge advancements since the initial computational simulations completed by Tse in 1983. [9] In addition, the authors also emphasise the immense challenges that still remain within this field in order to achieve reliable and detailed insight into these fascinating systems.[7]

Use of neutron scattering to understand the behaviour of KHIs can be found within the literature. In particular, Hutter and King report SANS data for several polymer systems.[4, 5] Their work explores the conformation of polymers in potentially hydrate forming systems, identifying the formation of aggregates upon the hydrate crystal surface.[4, 5] They postulate that binding of the polymer to the hydrate surface effectively prevents crystal growth. A limited length-scale was studied in their work, that did not extend to molecule scale. However, these results are encouraging from the view-point of using neutron scattering tools to probe industrially relevant polymers such as the systems of interest in the present work.

The work reported in this chapter builds upon the foundations outlined in Chapter 3. As established in the previous chapter, there are many advantages to using neutron scattering experiments to gain atomistic insight into aqueous-solute systems. In addition, the literature highlights the plausibility of gaining atomistic insight into KHI related systems. This chapter builds upon these concepts and probes a broader length-scale in order to examine

the aqueous behaviour of PVCap and related model compound (1,3-biscaprolactamyl but-1-ane, **2.1**) as a function of temperature.

4.2 Aqueous lactam systems experimental data

Neutron scattering data were collected at 6 ^{o}C and 20 ^{o}C for 10 wt% aqueous-PVCap and aqueous-1,3-bis(caprolactamyl) but-1-ane (**2.1**, dimer) systems, using NIMROD.[10] The two temperatures were selected in order to examine whether water re-structuring occurs as the temperature is lowered in the presence of clathrate hydrate inhibitors. While use of a 10 wt% KHI solution is not directly representative of pipeline conditions, this higher-than-commercial concentration is required to ensure that the solute (lactam species) provides sufficient scattering contribution to be seen within the solvent. In order to gain the most information regarding solvent-solvent, solute-solvent and solute-solute interactions, the hydrogen atoms within the solute should ideally represent approximately 10 % of the total atoms in the mixture. As a 10 wt% PVCap solution, the hydrogen atoms in the polymer represent approximately 5 % of the total atoms and 5.5 % in the dimer system. Use of a higher solute concentration would improve the signal; however, this was not possible because both of the lactam species begin to cloud out of solution at higher concentration.

Three isotopically distinct samples were measured: (1) lactam in H_2O, (2) lactam in D_2O and (3) lactam in a 1:1 mixture of H_2O and D_2O. It was not possible to obtain a deuterated analogue of the lactam species, therefore only the water component was varied.

Figure 4.1 shows the experimentally measured total structure factor as a function of *Q*. It is worth noting that Figure 4.1 shows only the low *Q* region in order to highlight the differences between mixtures, however data up to *Q* of 50 Å^{-1} is available and is incorporated in the EPSR model. A *Q* range of 0.05 to 50 Å^{-1} was analysed, using a step size of 0.02 Å^{-1}. Notable differences are apparent in the degree of scattering at low *Q* for the D_2O/PVCap system in comparison to the D_2O/Dimer system. Small angle scattering is due to a contrast in the scattering density from larger sized objects, therefore the rise at low *Q* within PVCap may be due to the presence of larger structures within solution which scatter negatively within the positive scattering of the D_2O solvent. This may indicate that the polymer is forming small aggregates which are not observed within the dimer solution – this seems reasonable as the polymer is held together and may coil, whilst the dimer molecules would be more freely scattered. Differences between the polymer and dimer systems are not readily observed

when examining the protic water systems, due to the reduced contrast in these samples, since both the lactam species and water scatter negatively.

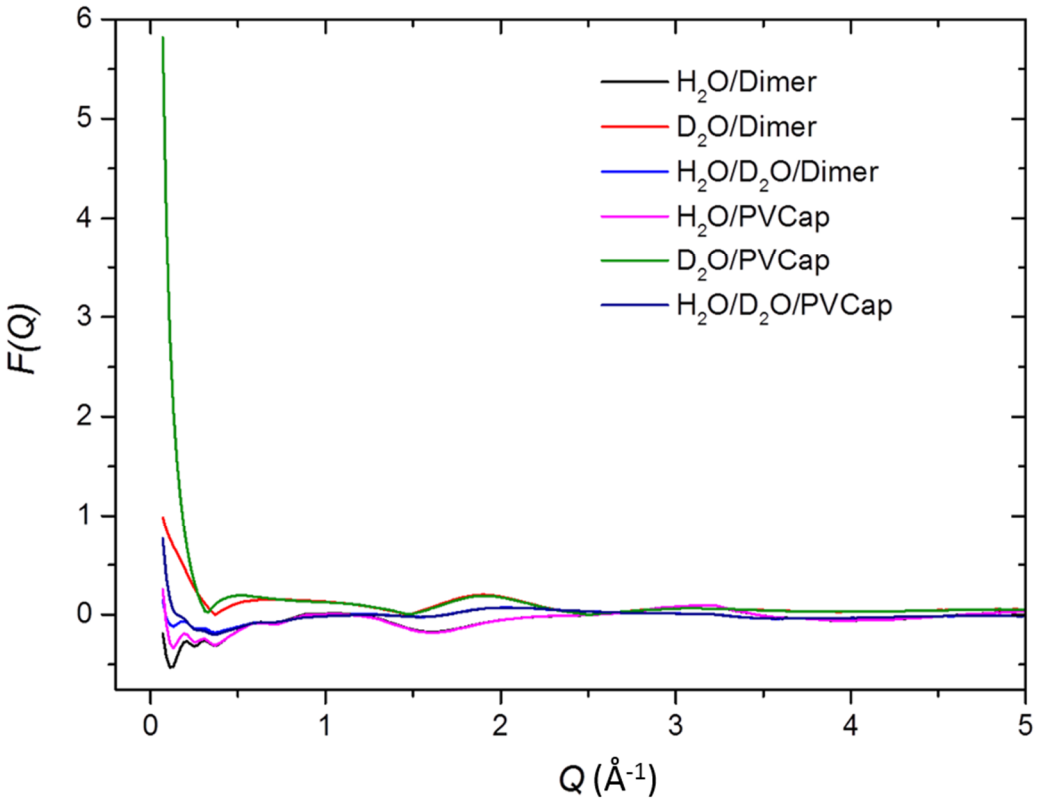

Figure 4.1: Plots of experimentally measured total structure factor as a function of *Q* for the aqueous-lactam systems studied. Plot is limited to $Q < 5$ Å^{-1} in order to highlight differences in low *Q* scattering.

On the atomic scale, however, the interactions of the dimer and polymer with water are expected to be very similar, as verified previously in Chapter 2. Figure 4.2 shows the total pair distribution functions (G(r) *vs* r plots) for the aqueous-polymer and aqueous-dimer systems. The data are consistent in real-space, indicating that despite differences in the large-scale structures (low *Q* or high r), the general local structuring is comparable.

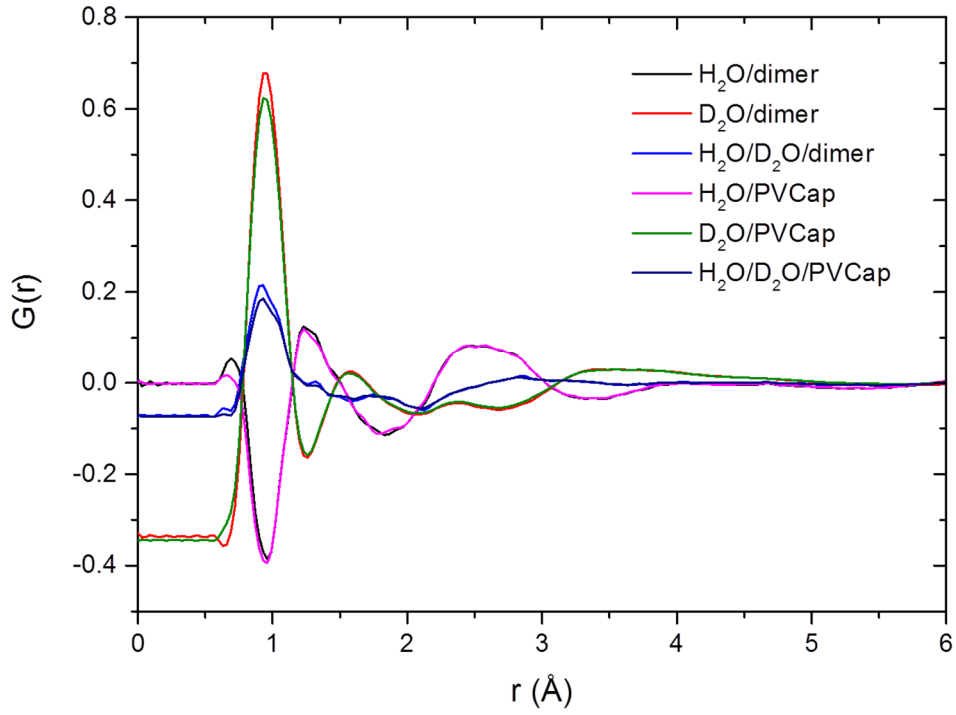

Figure 4.2: Plot of the total pair distribution functions for both aqueous-lactam systems studied. Data recorded at 20 °C.

Further, Figure 4.3 shows the total pair distribution functions for the aqueous dimeric model compound systems at both temperatures. The data are similar as a function of temperature, indicating that significant restructuring does not occur as the temperature is reduced.

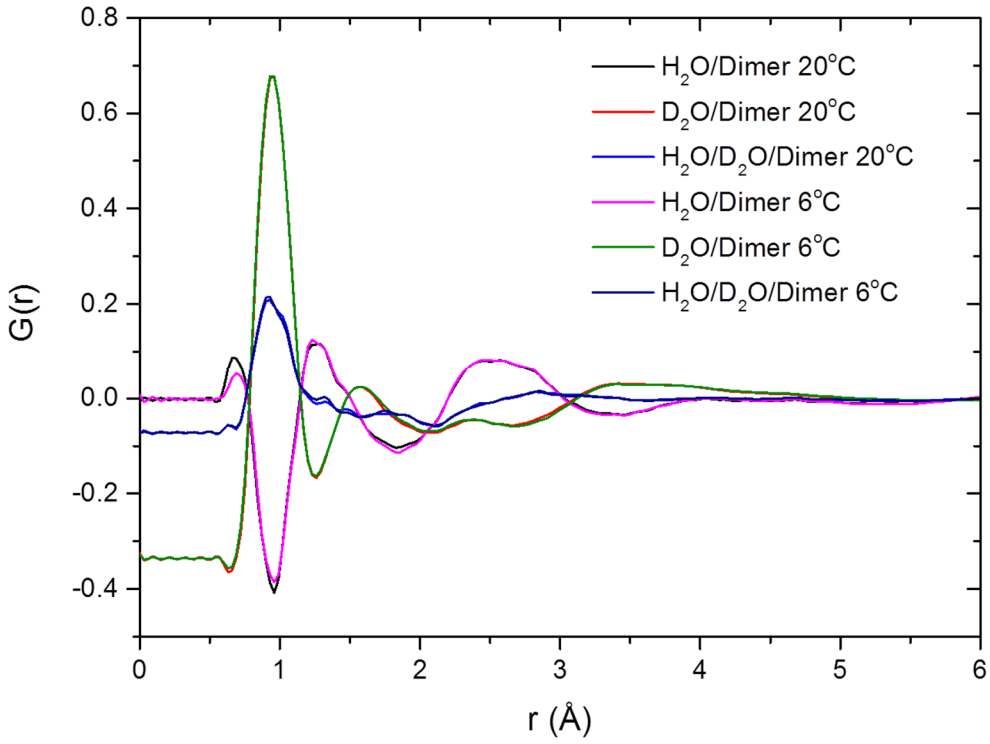

Figure 4.3: Plot of the total pair distribution functions in real-space for the aqueous-dimer systems at 6 °C and 20 °C.

Having established similarity between the systems at different temperatures, it is possible to compare these data with pure water systems in order to confirm the effect of the inhibitor species. Subtle differences are apparent in the total pair distribution functions of pure water and aqueous inhibitor solutions, as seen in Figure 4.4. Once again, differences are more pronounced between D_2O/lactam systems and pure D_2O than the protic analogues as a result of the differences in isotopic scattering. There exists a small broad peak in the D_2O-lactam systems at approximately 2.4 Å that is absent in the pure D_2O system; this may correspond to an interaction between the solute and solvent or may relate to an intramolecular distance in the lactam species.

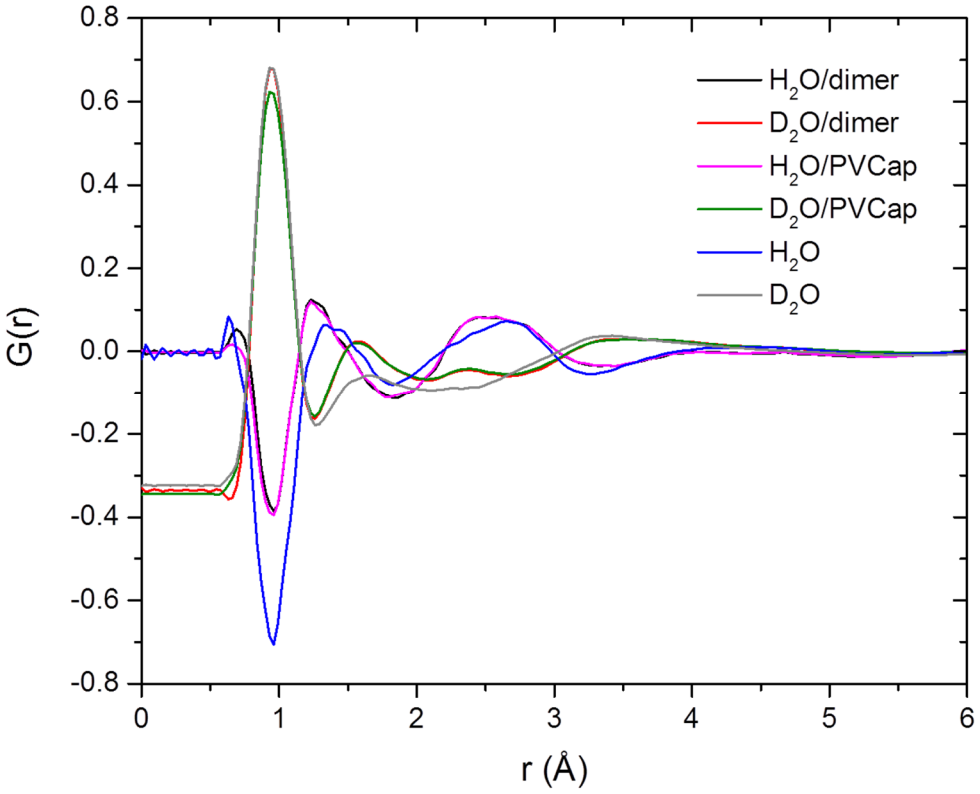

Figure 4.4: Comparison between the total pair distribution functions for aqueous lactam and pure water systems at 6 °C.

The subtlety of difference in these data indicates that the presence of the lactam species at this concentration has little effect on the overall solution structure. It is worth noting that these plots of the partial atomic distribution functions take into account the overall system, which in this instance is dominated by water molecules. Therefore, in order to fully probe the subtle differences the data need to be modelled and analysed using EPSR. More specifically, examining the hydration shell of the carbonyl oxygen atom can be achieved through extraction of the atomic pair distribution function O1-OW from the EPSR model, where O1 represents the carbonyl oxygen atom of the lactam and OW the oxygen atom of water. In addition, the water hydration shell can be investigated in order to determine whether the local water structure differs upon addition of a clathrate hydrate inhibitor.

It is well established that X-ray scattering data complements neutron data, and can provide additional information for model refinement in EPSR.[11] X-ray scattering data were collected for the H_2O-lactam systems loaded within a glass capillary, using the Ag source diffractometer in the Disordered Materials Group, ISIS, operated by Dr. Sam Callear.[12] These data were corrected and fully normalised using GudrunX,[13] and the finalised plots are shown in Figure 4.5. The scattering behaviour is similar between the polymer and dimer systems,

adding further support to the representative behaviour of the model compound. The finalised X-ray data are incorporated in the EPSR model.

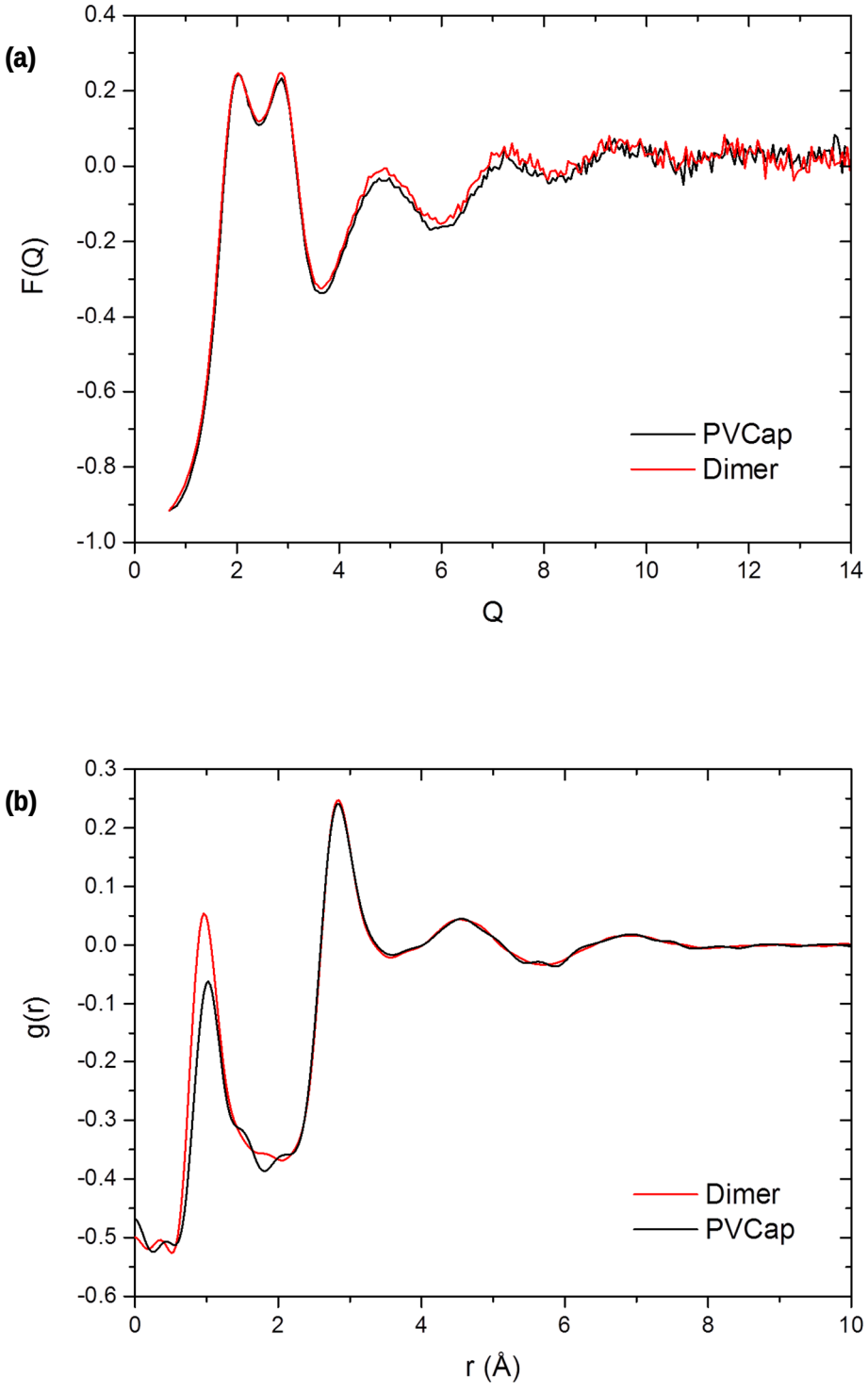

Figure 4.5: X-ray scattering data for the aqueous lactam systems (a) interference scattering and (b) total pair distribution functions.

4.3 Data modelling

EPSR has been used to generate a three-dimensional model of the liquid structure of the aqueous-dimer and aqueous-PVCap systems. The simulation aims to investigate the subtle differences between pure water and aqueous solute systems for the data collected at 6 ^{o}C. The raw data indicates that the lactam species have little effect upon perturbing the overall water structure, however, it was hoped that using EPSR would enable exploration of the hydration shell of the carbonyl functionality.

A computational model of the caprolactam dimer was developed using the *.jmol* interface within the EPSR software suite. The molecule geometry was optimised using MOPAC, and intramolecular distances were incorporated based upon the X-ray single crystal structure[14] in order to ensure that a chemically feasible geometry was maintained. Figure 4.6 shows a schematic representation of the dimer molecule, with individual atom labelling as necessary to allow incorporation of appropriate parameters.

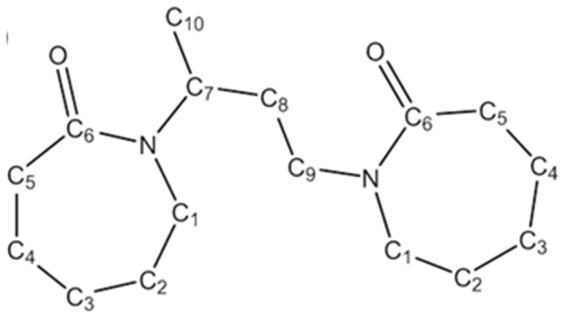

Figure 4.6: Schematic showing atomic labelling for the dimer molecule

The Lennard-Jones parameters (ε and σ) used to seed the simulation are shown in Table 4.1. No such parameters are reported in the literature for PVCap and related oligomers, therefore the simulation was compiled using parameters based upon the optimised potentials for liquid simulation (OPLS) all-atom field work undertaken by Jörgensen *et al*.[15] Parameters for representative functional groups are incorporated in this work. The atomic sites of water molecules were assigned the labels OW and HW for the water oxygen and hydrogen atoms respectively.

Atom Label	ε	σ	Atomic charges	
			MOPAC PM3	Gaussian
C1	0.276	3.5	-0.073357	-0.153
C2	0.276	3.5	-0.1299655	-0.258
C3	0.276	3.5	-0.0997895	-0.2615
C4	0.276	3.5	-0.092452	-0.2635
C5	0.276	3.5	-0.1241755	-0.354
C6	0.439	3.75	0.258866	0.5735
C7	0.276	3.5	-0.036475	0.006
C8	0.276	3.5	-0.152156	-0.264
C9	0.276	3.5	-0.061731	-0.145
C10	0.276	3.5	-0.138347	-0.4545
N1	0.711	3.25	-0.0671025	-0.4145
O1	0.879	2.96	-0.369379	-0.523
H1	0.06	2.42	0.06350375	0.149
H2	0.126	2.5	0.0610665	0.141
H3	0.126	2.5	0.05323575	0.133
H4	0.126	2.5	0.05775425	0.146
H5	0.06	2.42	0.07530375	0.158
H6	0.06	2.42	0.048488333	0.1495
H7	0.126	1.8	0.104749	0.191
H8	0.126	2.5	0.069843	0.1445
H9	0.126	2.5	0.0750315	0.1645

Table 4.1: Lennard-Jones parameters (ε and σ) used to seed aqueous dimer EPSR simulation. Atom labels correspond to those in Figure 4.6.

In addition, the EPSR simulation requires atomic charge information to be included in order to approximate valid structural characteristics. Once again, there was an absence of reported charge values for representative compounds in the literature. Therefore, as part of this work the effect of the partial atomic charges on the EPSR simulation was explored. Simulations were compiled using charge values based upon (a) similar functionalities reported in the work by Jörgensen[15], (b) charges output by the MOPAC calculation (using PM3 hamiltonian) and (c) charges based on DFT calculations. It is worth noting that EPSR requires the molecule to possess overall charge neutrality. Upon using the Jörgensen based charge values, the simulation failed to tend towards convergence, whilst also showing an absence of hydrogen bonding at the carbonyl moiety. It is believed that these charge values, based on individual functionalities, fail to take into account the overall molecular properties and are therefore less representative of the system. ESPR simulation results using the charges based on MOPAC and DFT are comparable. Gaussian calculations for the caprolactam dimer, using the crystal structure geometry and optimised geometry, were undertaken by Dr. Mark Fox (Durham University), and the results of the partial charge calculations are shown in Figure 4.7.

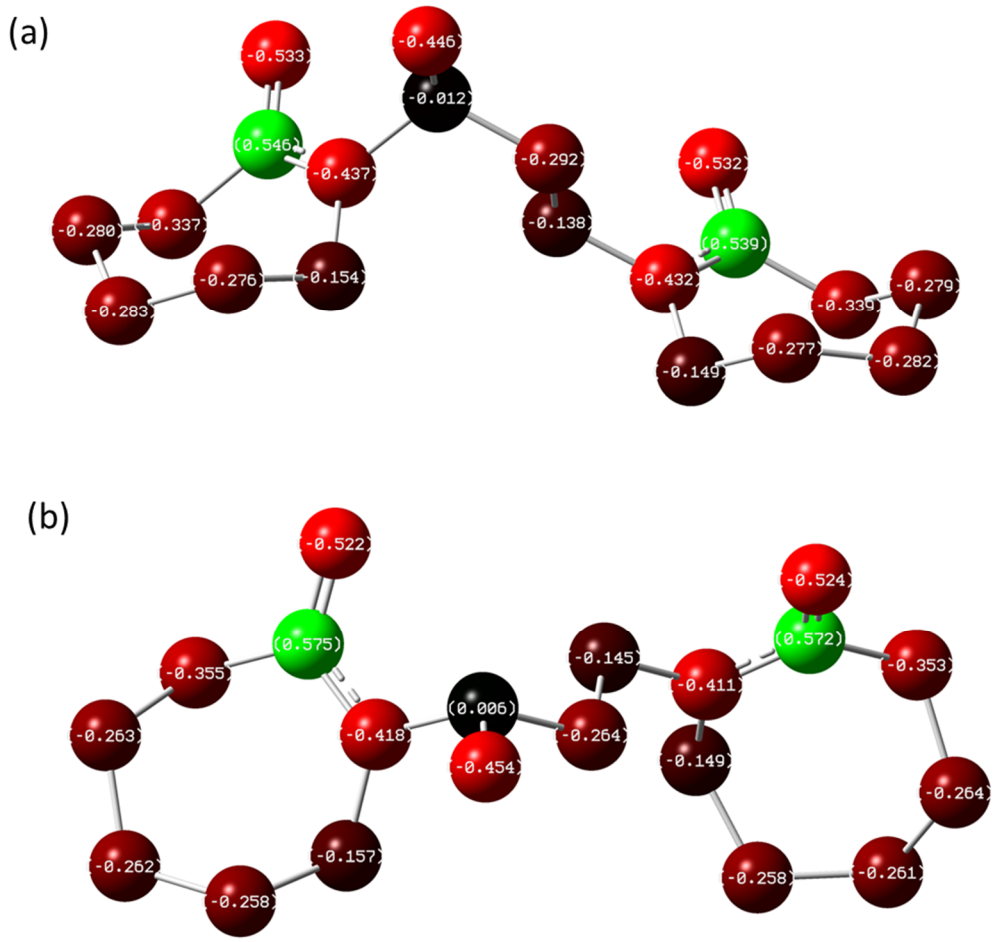

Figure 4.7: Partial atomic charges in saturated VCap dimer at B3LYP 6-31G* (H atoms removed for clarity, but averaging a charge of 0.15). (a) Shows the charges for the crystal structure geometry whilst (b) shows the charges for the optimised geometry

A cubic simulation box containing 10 dimer molecules and 1400 water molecules was assembled at 6 ^{o}C, corresponding to a representative atomic density of 0.101 atoms/Å^{3}. The finalised neutron scattering data was introduced as a constraint, and the simulation was equilibrated. Following equilibration, the potential energy of the system was systemically modified in order to promote convergence between the simulated and experimental data. EPSR iteratively modifies the simulation in order to minimise the differences between datasets and attempt generation of a consistent and representative model. The potential energy was varied using a process of trial-and-error, monitoring changes in the overall error value. As discussed in Chapter 3, a fine balance exists between providing sufficient energy to allow simulation convergence whilst not artificially over-fitting the data. Following convergence, the datasets were accumulated and averaged, in order to improve the model and reduce simulation fluctuations. Figure 4.8 shows a snapshot of the simulation box during the refinement, hydrogen atoms have been removed for clarity.

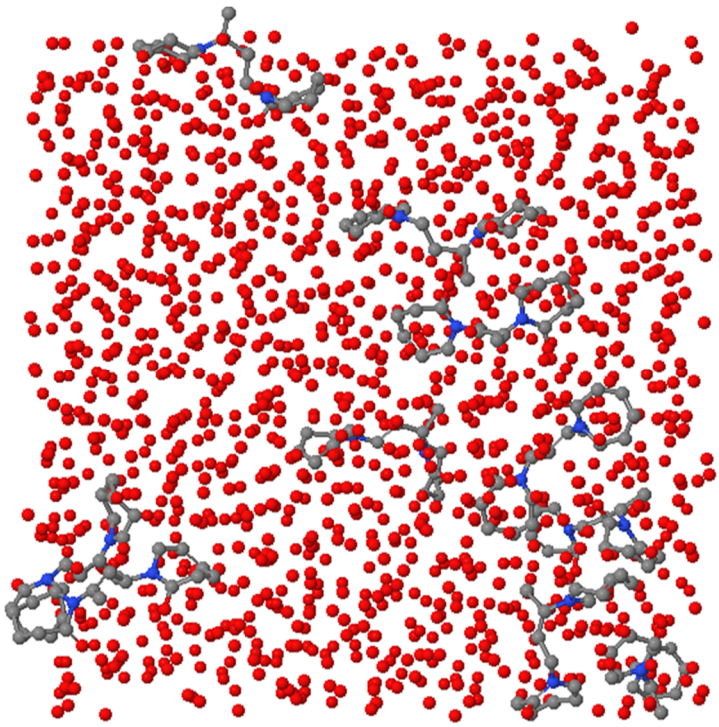

Figure 4.8: Image showing the simulation box containing 10 dimer molecules and 1400 water molecules. Hydrogen atoms have been removed for clarity.

Despite considerable efforts to accurately model the neutron data for the aqueous-dimer system, there remain issues with the simulation fitting, and therefore it is not possible to draw meaningful conclusions at this stage. In this instance the simulation-to-data fit was deemed unacceptable for detailed analysis, as the hydration shells of individual components could not be unequivocally distinguished.

It is believed that the challenges with data modelling are due to the limited isotopic substitutions used, as a result of the lack of a deuterated dimer analogue, in addition to the low solute concentration in the systems of study. In general, use of a wider variety of isotopic substitutions enables greater contrast variations to be established, and allows for easier and more accurate data modelling. While it would be desirable to obtain neutron data for systems of higher solute concentration in order to see a greater degree of scattering caused by the lactam species, the relatability to industrial application then reduces.

In an attempt to assess the viability of performing the analogous simulation for the aqueous-PVCap system, an initial simulation box was generated of the appropriate concentration. Challenges were encountered immediately with the generation of a representative model for the polymer within the EPSR software shell, due to the large and complex nature of the polymer and software issues. The method for creating a polymer

model was unknown within the Disordered Materials Group at the time of this work. As a result of collaboration with Prof. Alan Soper (STFC-ISIS), it was possible to create a model of syndiotactic PVCap. It is not possible to generate a polymeric model directly within the software, but instead each repeat unit was created separately in addition to both end caps, as seen in Figure 4.9.

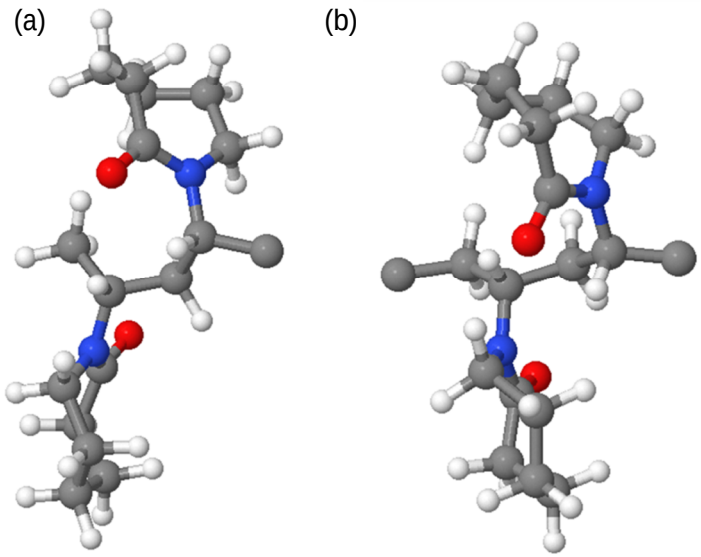

Figure 4.9: Individual repeat units used to generate PVCap. (a) shows the end cap with the first two repeat units and (b) shows the central repeat units.

The caps and repeat units were then "docked" together within the software package to enable generation of PVCap with 20 monomer repeat units, as seen in Figure 4.10. All atoms with unique environments were independently labelled in the same manner as previously reported with the dimer compound; this was done in order to enable the future incorporation of individual Lennard-Jones parameters.

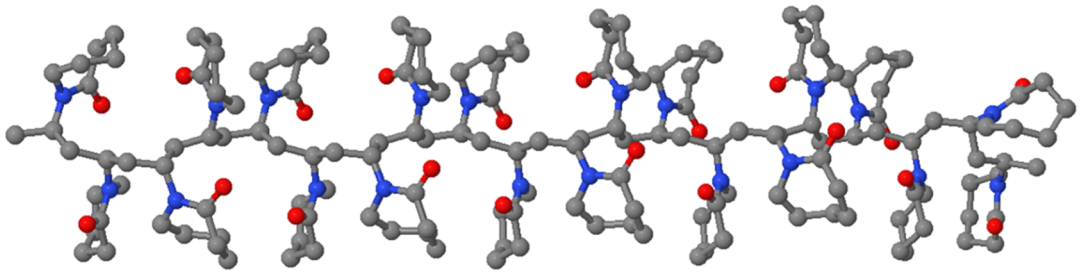

Figure 4.10: Model of PVCap. Hydrogen atoms are omitted for clarity

The simulation containing water and polymer molecules of the correct ratio was allowed to run for several thousand iterations. However, unsurprisingly the same challenges

were encountered as previously reported with the dimer molecule, and therefore it was not possible to generate a reliable simulation to fit the aqueous-polymer data. Furthermore, the large size of the polymer significantly increased the time taken to complete each iteration, which had major implications when trying to systematically vary the potential energy of the system in order to promote convergence. Ideally, the future work would focus on synthesising deuterated analogues of the dimer and polymer in order to allow additional isotopic mixtures to be probed. In addition, it may be necessary to use a supercomputer in order to run simulations on new data as this should increase the data output and reduce the iteration times.

4.4 Conclusions

Neutron scattering data have been outlined for two aqueous lactam systems in order to explore the postulation that addition of KHIs results in water restructuring and therein prevents the formation of pipeline plugs. The raw data indicates that the local structures of the aqueous PVCap and aqueous caprolactam dimer are similar. The raw data output shows the averaged atomic pair distribution functions, and due to the high water concentration it is difficult to establish differences caused by the lactam species, in comparison to pure water. Therefore, in order to quantitatively probe these small scattering differences a simulated model based upon experimental neutron data was developed using the EPSR software suite. EPSR has been used in an attempt to develop a model consistent with both neutron and X-ray scattering data. However, significant difficulties were encountered in producing a reliable model. Therefore it was not possible to unequivocally elucidate a cause of the subtle solution differences, or establish the hydration shell of the amide carbonyl moiety.

This work highlights that neutron scattering may provide unique atomistic insight into the molecular structuring of liquid systems. While it was not possible to establish detailed information on the systems of study, this does highlight that further work in this area would be advantageous, most importantly using a wider selection of deuterated species to ensure optimum scattering contrast. In addition, undertaking detailed computational studies on the systems of interest would be advantageous, with the aim of elucidating appropriate Lennard-Jones parameters for seeding initial EPSR simulations. Future work in this area must remain mindful if samples are studied at higher concentration, because whilst this would increase the scattering from the lactam solute, the relatability to KHI application would reduce.

4.5 References

1. C. Moon, P. C. Taylor and P. M. Rodger, *Can. J.Phys.*, 2003, **81**, 451-457.
2. B. J. Anderson, J. W. Tester, G. P. Borghi and B. L. Trout, *J. Am. Chem. Soc.*, 2005, **127**, 17852-17862.
3. T. J. Carver, M. G. B. Drew and P. M. Rodger, *J. Chem. Soc.-Faraday Trans.*, 1995, **91**, 3449-3460.
4. H. E. King, J. L. Hutter, M. Y. Lin and T. Sun, *J. Chem. Phys.*, 2000, **112**, 2523-2532.
5. J. L. Hutter, H. E. King and M. Y. Lin, *Macromolecules*, 2000, **33**, 2670-2679.
6. C. A. Koh, R. P. Wisbey, X. P. Wu, R. E. Westacott and A. K. Soper, *J. Chem. Phys.*, 2000, **113**, 6390-6397.
7. N. J. English and J. M. D. MacElroy, *Chem. Eng. Sci.*, 2015, **121**, 133-156.
8. T. J. Carver, M. G. B. Drew and P. M. Rodger, *J.Chem. Soc., Faraday Transactions*, 1996, **92**, 5029-5033.
9. J. S. Tse, M. L. Klein and I. R. McDonald, *J. Phys. Chem.*, 1983, **87**, 4198-4203.
10. D. T. Bowron, A. K. Soper, K. Jones, S. Ansell, S. Birch, J. Norris, L. Perrott, D. Riedel, N. J. Rhodes, S. R. Wakefield, A. Botti, M.-A. Ricci, F. Grazzi and M. Zoppi, *Rev. Sci. Instrum.*, 2010, **81**.
11. A. K. Soper, *J. Phys. Condes. Matter*, 2007, **19**.
12. http://www.isis.stfc.ac.uk/support-laboratories/xrd/xrd9446.html.
13. A. Soper, *GudrunN and GudrunX. Programs for correcting raw neutron and x-ray total scattering data to differential cross section*, ISIS, Rutherford Appleton Laboratory, Oxford, 2012.
14. J. R. Davenport, O. M. Musa, M. J. Paterson, M.O. M. Piepenbrock, K. Fucke and J. W. Steed, *Chem. Commun.*, 2011, **47**, 9891-9893.
15. W. L. Jorgensen, D. S. Maxwell and J. TiradoRives, *J. Am. Chem. Soc.*, 1996, **118**, 11225-11236.
16. D. T. Bowron, J. L. Finney and A. K. Soper, *J. Phys. Chem. B*, 2006, **110**, 20235-20245.

5 Metal ion complexation by highly polar podands

5.1 Introduction

Amides are an important class of compounds encountered in a vast array of chemistries as a consequence of the high polarity of the carbonyl moiety. As established in Chapter 2, while the mechanism of action of poly(lactam) KHIs is not conclusively determined, it is believed that the polarity of the amide carbonyl functionality is critical to the inhibition behaviours.[1, 2] As a result of such functionality and good solubility, poly(lactam) species have found use in a wide variety of applications including ceramics, cosmetics and adhesives.[3] In addition, the polarity of the carbonyl moiety enables such species to function as effective solvents, such as in dimethylformamide (DMF) and dimethylacetamide (DMA), while also enabling metal complexation.[4] An array of oxygen-bound metal complexes containing DMF, DMA and diamide ligands are reported in the literature, incorporating transition metal and lanthanide metal cations.[4-8]

Ashland Inc. have recently reported the compositions and uses of a selection of *N*-alkyl lactam ethers, reporting a plethora of potential commercial applications.[9] This chapter focuses mainly on a bis *N*-ethyl pyrrolidone ether ligand (**5.1**), as outlined below. The presence of the ether linkage and the general composition leads to analogies to the popular crown ethers and acyclic podands.[10-12] On the basis of these analogies, we postulate that formation of alkali metal coordination complexes with bis(lactam) ligands may hold some potential. Support for the metal coordination behaviour of lactam ligands can be found in the literature, in early work involving metal complexation of ε-caprolactam and pyrrolidinone.[13, 14] In addition, Goodgame *et al.* reported several transition metal and lanthanide metal coordination complexes containing bis(lactam) ligands.[15-17] Recently, PVP and related co-polymers were studied in relation to the purification of heavy metals from waste water using a process of polymer enhanced ultrafiltration, reporting that PVP expresses selectivity for binding nickel ions in solution.[18] This highlights the potential commercial versatility of these interesting lactam ligands.

This work reports the synthesis and study of a series of metal-bound pyrrolidone coordination complexes, in order to exploit and examine the polarity of the amide carbonyl moiety. 1-{2-[2-(2-oxo-pyrrolid-1-yl)-ethoxy]-ethyl}-pyrrolid-2-one (**5.1**) and 1,3-

bis(pyrrolidin-2-on-1-yl) but-1-ane (**2.3**) are the bis(lactam) ligands of choice, both containing two carbonyl groups for metal complexation. In addition, the sodium metal complexation of mono(lactam) 1-(2-hydroxyethyl)-2-pyrrolidone (**2.12**) is explored. Several of the complexes included in this chapter were published by the author in 2014.[19]

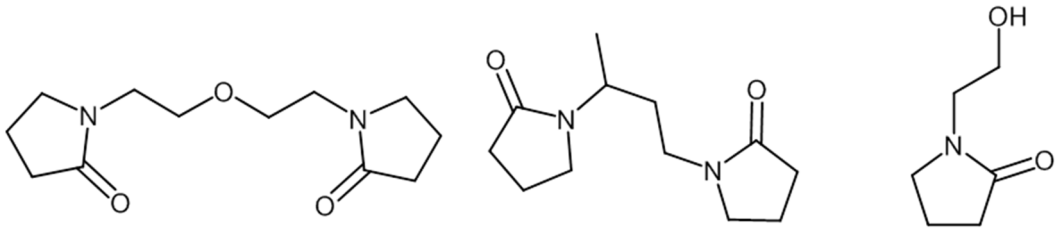

5.1 **2.3** **2.12**

5.2 Sodium complexes

Reaction of ligand **5.1** with sodium hexafluorophosphate ($NaPF_6$) in acetonitrile followed by solvent evaporation at room temperature results in the isolation of three crystalline coordination complexes; $[Na(\mathbf{5.1})_2]PF_6$ (**5.2**), $\{[Na_3(\mu_3\text{-}\mathbf{5.1})_2(\mu_2\text{-}\mathbf{5.1})_2](PF_6)_3\}_n$ (**5.3**) and $[Na_3(H_2O)_2(\mu\text{-}\mathbf{5.1})_2](PF_6)_3$ (**5.4**). Ligand-to-metal ratio determines the crystal composition, resulting in metal:ligand stoichiometries of 1:2, 3:4 and 3:2, respectively. Complex characterisation was undertaken using X-ray crystallography, IR spectroscopy, elemental analysis and thermogravimetric analysis (TGA). $NaPF_6$ was chosen primarily due to the relatively non-coordinating nature of the PF_6^- anion and the reasonable metal salt solubility.

The X-ray molecular structure of **5.2** comprises a sandwich complex containing two ligand molecules bound to a distorted octahedral Na^+ centre, as shown in Figure 5.1. The high polarity of the lactam carbonyl groups is exemplified by the considerably shorter metal-oxygen bond distances at 2.36 Å (average), in comparison to the longer metal-ether bond of 2.5364(10) Å.

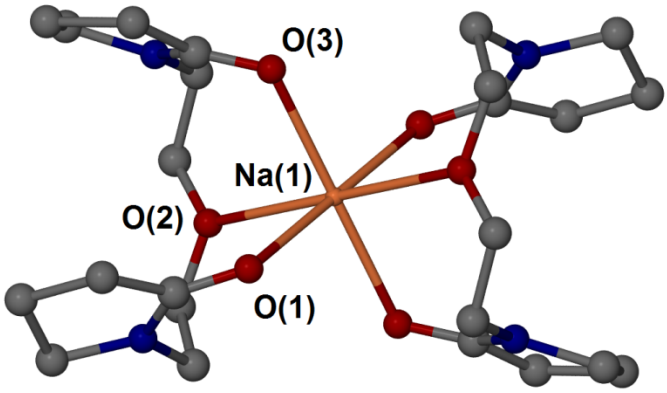

Figure 5.1: X-ray molecular structure of the cation in [Na(**5.1**)$_2$]PF$_6$ (**5.2**). Hydrogen atoms are omitted for clarity. Selected bond lengths (Å): Na(1)-O(1) 2.3697(9), Na(1)-O(2) 2.5366(9), Na(1)-O(3) 2.3524(9).

The PF_6^- anion is not coordinated to the metal centre, but instead is held in pockets by a number of CH···F hydrogen bond interactions[20,21] with surrounding ligand molecules, as shown in Figure 5.2. The carbonyl stretching mode for dried ligand **5.1** as a neat film occurs at 1674 cm^{-1}, and shifts to 1661 cm^{-1} in metal complex **5.2**. The shift to lower wavenumber indicates a shift to the enolate resonance form upon complexation, in a similar manner to that established in Chapter 2.

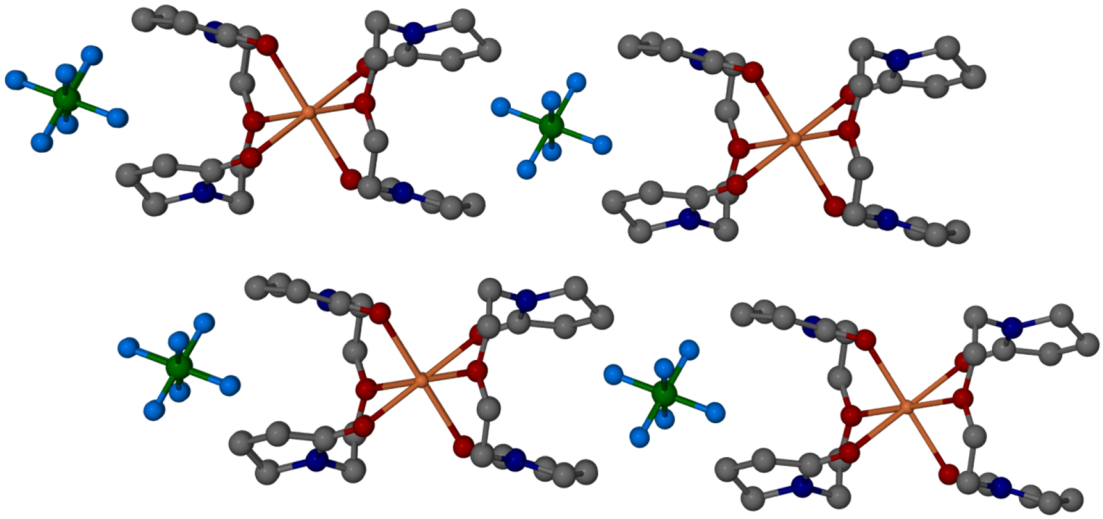

Figure 5.2: Packing of molecules in [Na(**5.1**)$_2$]PF$_6$ (**5.2**) as viewed down the *a* axis.

The X-ray molecular structure of {[Na$_3$(μ_3-**5.1**)$_2$(μ_2-**5.1**)$_2$](PF$_6$)$_3$}$_n$ (**5.3**) exhibits a 3:4 metal-ligand ratio and highlights ligand binding in the presence of a dearth of metal salt, Figure 5.3. There are three distinct metal environments in the complex; Na(1) has a unique

coordination sphere while Na(2) and Na(3) have similar environments. Na(1) binds to four pyrrolidone carbonyl groups of the central cluster, in addition to two carbonyl oxygen atoms of the ligand bridging adjacent clusters (O(1) and O(3)). The bridging ligand joins adjacent Na_3 clusters to form an overall 1D coordination polymer, however, the ether oxygen atom does not coordinate to a metal cation. The remaining sodium centres, Na(2) and Na(3), are sandwiched by three ligand molecules in a similar manner to complex **5.2**, binding to carbonyl oxygen atoms and ether groups. This complex highlights the versatility of ligand **5.1**, with it acting as both a double and triply bridging molecule in this coordination polymer. Akin to complex **5.2**, the PF_6^- anions are held in pockets by CH···F hydrogen bond interactions.

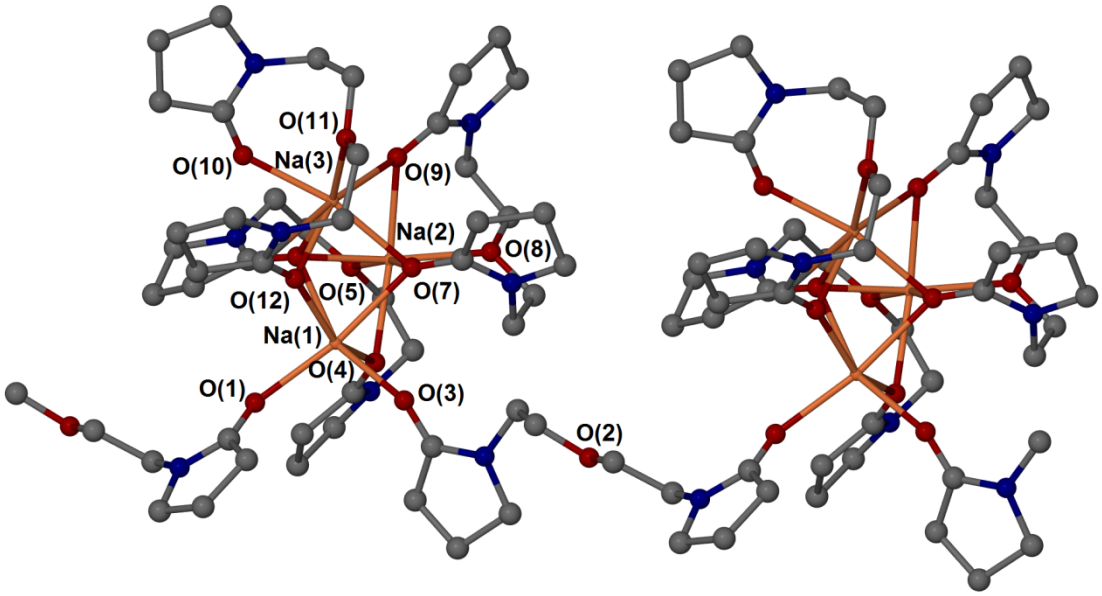

Figure 5.3: X-ray molecular structure of $\{[Na_3(\mu_3\text{-}\mathbf{5.1})_2(\mu_2\text{-}\mathbf{5.1})_2](PF_6)_3\}_n$ (**5.3**) Anions and hydrogen atoms are omitted for clarity. Selected bond lengths (Å): Na(1)-O(1) 2.2739(19), Na(1)-O(3) 2.287(2), Na(1)-O(4) 2.4719(18), Na(1)-O(6) 2.6537(18), Na(1)-O(7) 2.4392(18), Na(1)-O(12) 2.336(2), Na(2)-O(4) 2.3588(18), Na(2)-O(5) 2.4417(18), Na(2)-O(6) 2.2665(18), Na(2)-O(7) 2.3662(18), Na(2)-O(8) 2.3568(18), Na(2)-O(9) 2.4281(19), Na(3)-O(6) 2.3244(18), Na(3)-O(7) 2.3728(17), Na(3)-O(9) 2.6290(19), Na(3)-O(10) 2.2749(19), Na(3)-O(11) 2.5044(19), Na(3)-O(12) 2.376(2).

In contrast, the X-ray molecular structure of $[Na_3(H_2O)_2(\mu\text{-}\mathbf{5.1})_2](PF_6)_3$ (**5.4**) shows optimisation of ligand binding when exposed to an excess of metal salt (Figure 5.4). This hydrated 3:2 complex comprises two distinct metal environments. Na(1) is sandwiched between two ligand molecules, bound by interactions with the carbonyl and ether oxygen atoms of both ligand molecules. The carbonyl-metal bond distances are comparable to those in **5.2** at an average of 2.35 Å. In addition, the metal-ether bond distance of 2.418(6) Å is considerably shorter than in complex **5.2**. The remaining two Na^+ cations (Na(2)) bind to both

carbonyl oxygen atoms of a single ligand species, in addition to a single carbonyl group of the other ligand molecule. Overall, this results in both ligand molecules having one doubly bridging carbonyl functionality, and one triply bridging carbonyl group. Finally, the coordination spheres of these metal cations are completed by a bound water molecule, a terminal PF_6^- anion and a bridging PF_6^- anion.

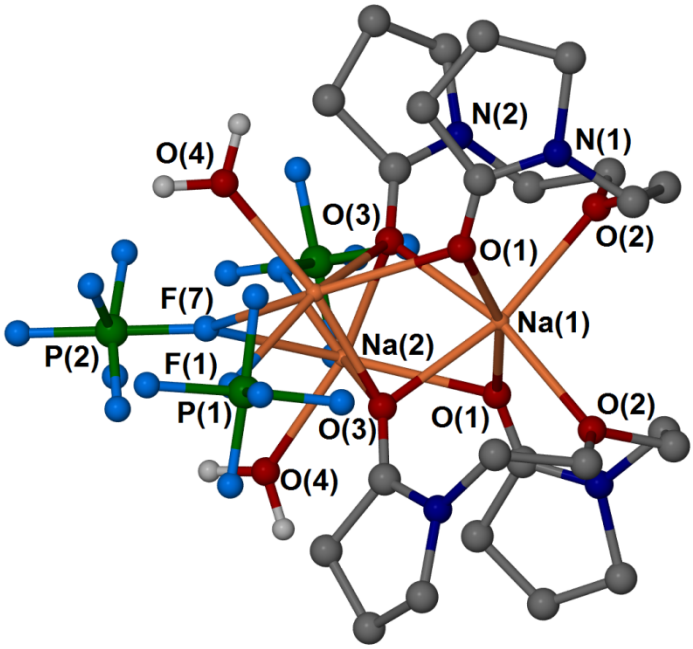

Figure 5.4: X-ray molecular structure of $[Na_3(H_2O)_2(\mu\text{-}\mathbf{5.1})_2](PF_6)_3$ (**5.4**). Hydrogen atoms are omitted for clarity with the exception of water molecules. Selected bond lengths (Å): Na(1)-O(1) 2.338(8), Na(1)-O(2) 2.418(6), Na(1)-O(3) 2.364(6), Na(2)-O(1) 2.509(9), Na(2)-O(4) 2.279(10), Na(2)-F(1) 2.418(10), Na(2)-F(7) 2.644(11).

Complex **5.4** confirms that hydration at the Na^+ centre is possible in conjunction with ligand binding. Use of methanol or 2,2-dimethoxypropane allows isolation of a solvated 1:1 complex $[Na_2(\mu\text{-}\mathbf{5.1})_2(MeOH)_2](PF_6)_2$ (**5.5**). In the latter case, it is postulated that the incorporated methanol solvent originates from acid hydrolysis of 2,2-dimethoxypropane. Both tridentate ligand molecules bind *via* the carbonyl and ether oxygen atoms, where once again the ether-metal bond is longer than the carbonyl-metal bond. One carbonyl oxygen atom of each ligand binds solely to a single Na^+ cation (O(1)) while the remaining carbonyl group (O(3)) forms a bridge between the two metal centres. The octahedral coordination sphere of each metal centre is completed by a molecule of methanol and a coordinated PF_6^- anion. The molecule of methanol is strongly hydrogen bonded to the non-bridging carbonyl oxygen atom, with an O(4)···O(1) distance of 2.79 Å.

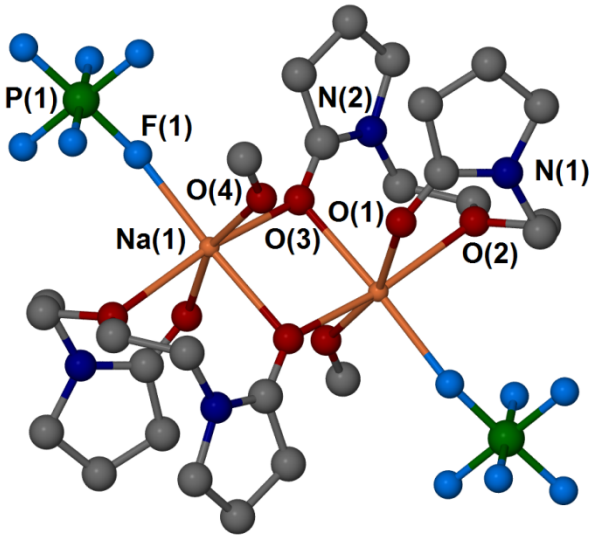

Figure 5.5: X-ray molecular structure of $[Na_2(\mu\text{-}\mathbf{5.1})_2(MeOH)_2](PF_6)_2$ (**5.5**). Hydrogen atoms are omitted for clarity. Selected bond lengths (Å): Na(1)-O(1) 2.428(2), Na(1)-O(2) 2.496(2), Na(1)-O(3)' 2.322(2), Na(1)-O(3) 2.438(2), Na(1)-O(4) 2.329(3), Na(1)-F(1) 2.295(2).

The TGA thermogram shows a weight loss of 7.3 % upon heating from room temperature to 183 °C, this corresponds to the loss of two molecules of methanol per dimer complex (calculated 7.27%), Figure 5.6. A sharp decrease in weight is observed upon further heating, and is attributed to thermal decomposition.

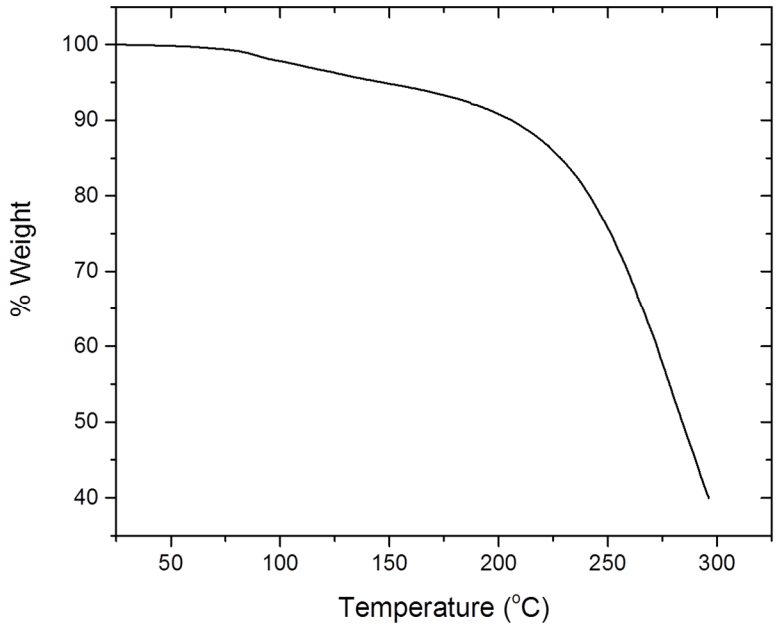

Figure 5.6: Thermogravimetric trace for $[Na_2(\mu\text{-}\mathbf{5.1})_2(MeOH)_2](PF_6)_2$ (**5.5**).

Despite the weakly coordinating nature of the PF_6^- anion, metal-anion coordination is found in complexes **5.4** and **5.5**. Therefore, complexation of ligand **5.1** with sodium tetraphenylborate ($NaBPh_4$) was explored in order to further reduce the potential for anion binding and maximise the interaction of the metal with the lactam ligand. Good quality single crystals of the centrosymmetric dimer complex $[Na_2(\mu\text{-}\mathbf{5.1})_2(H_2O)_4](BPh_4)_2$ (**5.6**) were isolated from a stoichiometric mixture of $NaBPh_4$ and ligand **5.1**. Crystals formed at room temperature from aqueous solution within 24 hours. The complex was characterised by X-ray crystallography and the molecular structure is reported in Figure 5.7. Ligand-metal binding is analogous to complex **5.5**, with one carbonyl oxygen atom (O(2)) bridging the two Na^+ centres while the remaining carbonyl oxygen atom and ether donor bind solely to a single metal cation. Once again, the ether-metal bond distance is longer than the pyrrolidone carbonyl oxygen-metal bond distance. Each metal coordination sphere is completed by two bound water molecules, held in position by hydrogen bonding interactions with the non-bridging pyrrolidone carbonyl group (O(3)···O(4) at 2.79 Å) and OH···π interactions with the counter-anion. The unusual occurrence of OH···π interactions is reported in the literature based on neutron diffraction work for alternative compounds.[22] The BPh_4^- anion does not coordinate to the metal centre, but is found at the periphery of the dimer complex.

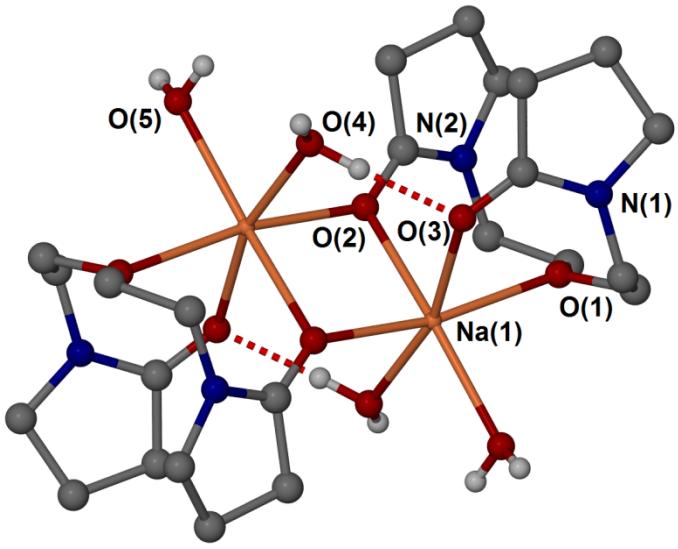

Figure 5.7: X-ray molecular structure of the cation in $[Na_2(\mu\text{-}\mathbf{5.1})_2(H_2O)_4](BPh_4)_2$ (**5.6**). Selected hydrogen atoms are omitted for clarity. Selected bond lengths (Å): Na(1)-O(1) 2.4652(12), Na(1)-O(2) 2.4434(13), Na(1)-O(2)' 2.3293(13), Na(1)-O(3) 2.3876(13), Na(1)-O(4) 2.3726(15), Na(1)-O(5) 2.3971(17) Å.

In addition, reaction of ligand **5.1** with $NaBPh_4$, in ethanol, at a 2:1 ligand-metal ratio results in the crystallization of a product of formula $[Na_2(\mathbf{5.1})_2(\mu\text{-}\mathbf{5.1})_2](BPh_4)_2$ (**5.7**), which was

characterised by X-ray crystallography (Figure 5.8) and IR spectroscopy. In this dimer complex, two molecules of **5.1** act as tridentate ligands and bind through all three oxygen atoms in a similar manner to complex **5.6**, with O(1) bridging the two Na^+ cations. However, the additional two ligand molecules each bind to the metal centre through only one carbonyl oxygen atom (O(4)). Surprisingly, the ether donor and remaining carbonyl group of these ligands (O(5) and O(6)) are not coordinated. Therefore unlike all previous examples, the sodium cation is five coordinate. There are three carbonyl stretching modes in the solid-state IR spectrum of complex **5.7**, occurring at 1679 cm^{-1}, 1666 cm^{-1} and 1642 cm^{-1}, corresponding to the non-coordinated, singly bound and bridging carbonyl groups.

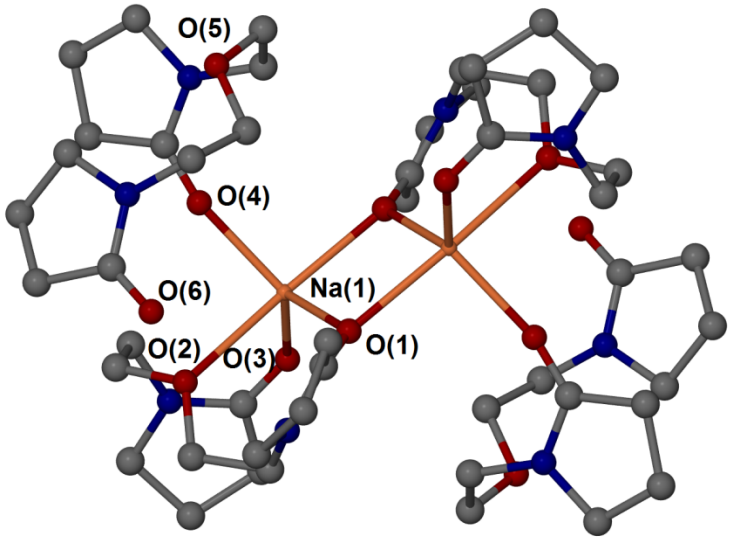

Figure 5.8: X-ray molecular structure of the cation in $[Na_2(\mathbf{5.1})_2(\mu\text{-}\mathbf{5.1})_2](BPh_4)_2$ (**5.7**).Selected bond lengths (Å): Na(1)-O(1) 2.3033(15), Na(1)-O(2) 2.4976(14), Na(1)-O(3) 2.2769(15) and Na(1)-O(4) 2.2363(16) Å.

5.3 Potassium complexes

Reaction of ligand **5.1** with KPF_6 in a 2:1 ratio in acetonitrile (at room temperature) results in the crystallization of a sandwich complex of formula $[K(\mathbf{5.1})_2]PF_6$ (**5.8**), which was characterised by X-ray crystallography. This complex is isomorphous with the sodium analogue **5.2** and hence is not pictured. The carbonyl oxygen-metal bond distances are significantly longer in the potassium analogue than in the sodium complex (2.64 Å (av.) *vs* 2.36 Å (av.) respectively) due to the larger ionic radius of K^+.

Reaction of equimolar solutions of ligand **5.1** with KPF_6 results in the crystallization of several closely related tetrameric coordination complexes. A simple hydrate is isolated from

acetonitrile at room temperature, namely $[K_4(\mu_4\text{-}H_2O)(\mu\text{-}\mathbf{5.1})_4](PF_6)_4$ (**5.9**) (Figure 5.9), while reaction in methanol results in an alternative polymorph. The X-ray crystal structures of both polymorphs of complex **5.9** proved to be disordered, with the pyrrolidone rings adopting two positions. Due to the limited precision of the data it was not possible to perform detailed quantitative comparisons; however, the gross structural features can be easily distinguished. Overall, each ligand molecule binds through all three oxygen atoms, with both carbonyl functionalities bridging two metal cations. In the centre of the cluster exists a quadruply bridging disordered water molecule. While these complexes are unique in that it highlights the formation of a tetrameric complex, the ligand binding mode is consistent with that seen in the previous metal complexes. Solid-state IR spectroscopy shows that the carbonyl stretching modes are shifted in the potassium complexes to 1650-1666 cm^{-1} (*vs* 1674 cm^{-1} for the free ligand). Degradation of the crystalline material is observed over time as a result of the hygroscopicity of these complexes, notable by the conversion from single crystals to a viscous oil.

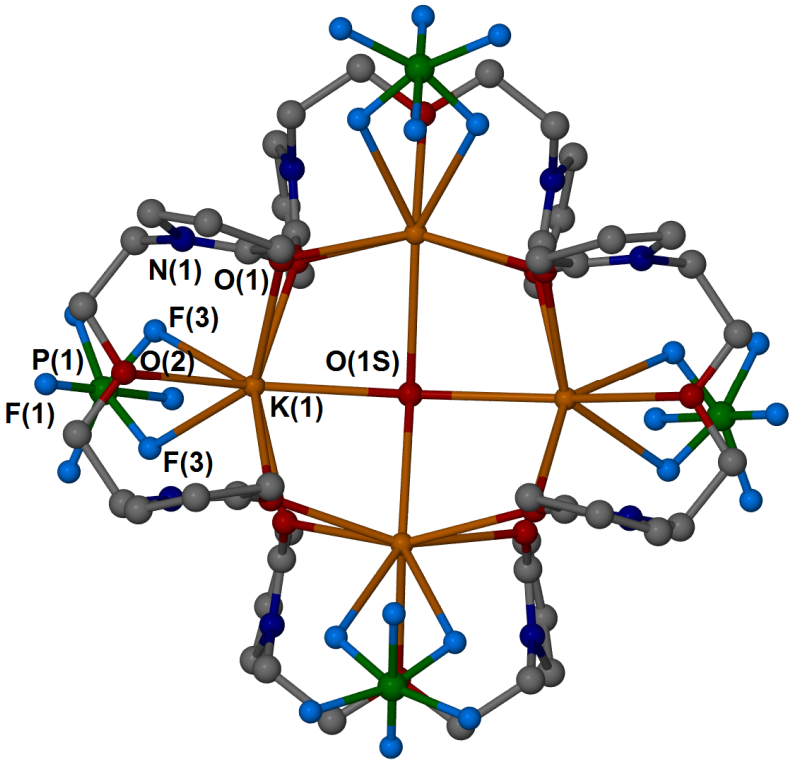

Figure 5.9: X-ray structure of one of the crystallograhically unique tetranuclear complexes $[K_4(\mu_4\text{-}H_2O)(\mu\text{-}\mathbf{5.1})_4](PF_6)_4$ (**5.9**). Hydrogen atoms are omitted for clarity.

5.4 Protonation

Attempts were made to isolate a lithium complex of ligand **5.1**, using $LiNO_3$, LiI, LiCl and LiBr, but no crystalline material was obtained. Reaction of a stoichiometric mixture of ligand **5.1** with $LiPF_6$, in methanol, results in the surprising crystallization of a monoprotonated ligand complex, **5.1**·HPF_6 (**5.10**). The complex was analysed using X-ray crystallography, as shown in Figure 5.10. Adjacent molecules interact through hydrogen bonding interactions between the monoprotonated carbonyl group of one ligand molecule and the carbonyl group of a neighbouring ligand species, with an O(1)···O(3) distance of 2.443(2) Å. This short hydrogen bonding distance is indicative of a strong interaction, and results in the formation of an overall 1D zigzag chain. Precedence for the protonation of carbonyl functionalities can be found in the literature in the ionic co-crystal of *N*-methylpyrrolidone and *N*-methylpyrrolidonium tribromide.[23] The solvated nature of Li^+ in methanol offers some explanation for the absence of a coordinated metal cation in this complex.[24] The PF_6^- anion does not coordinate or make a close approach and is therefore not shown in Figure 5.10. The carbonyl stretching mode is significantly shifted and broadened in the solid-state IR spectrum, occurring at 1642 cm^{-1}.

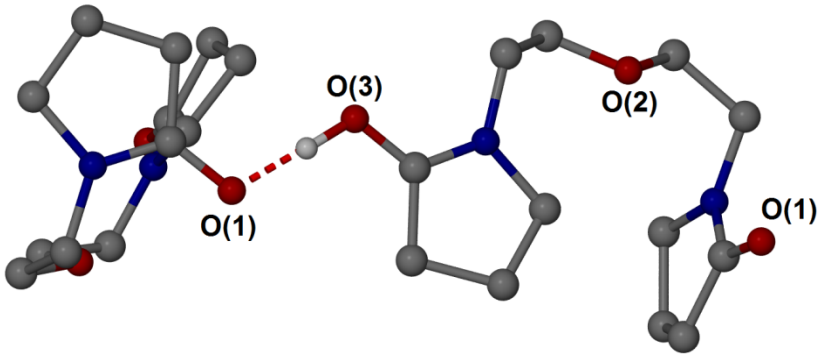

Figure 5.10: X-ray crystal structure of **5.1**·HPF_6 (**5.10**). The PF_6^- anion is removed for clarity. Hydrogen bond distance O(1)···O(3) 2.443(2) Å.

5.5 Zinc complex

Slow evaporation of acetone from an equimolar solution of ligand **5.1** and zinc (II) chloride results in the crystallization of a 1D coordination polymer of formula {[$ZnCl_2$(μ-**5.1**)]}$_n$ (**5.11**). The two carbonyl groups of each ligand molecule join to adjacent zinc centres *via* short bonds, consistent with the small and polarising nature of Zn(II). The ether oxygen atom does not coordinate to the metal centre, allowing the chloride ions to remain metal-bound, and

therein enabling a tetrahedral geometry at the Zn^{2+} centre. Further evidence for the high polarising ability of the metal dication is seen in the considerable shift in the carbonyl stretching mode in the IR spectrum, occurring at 1611 cm^{-1} in this coordination complex.

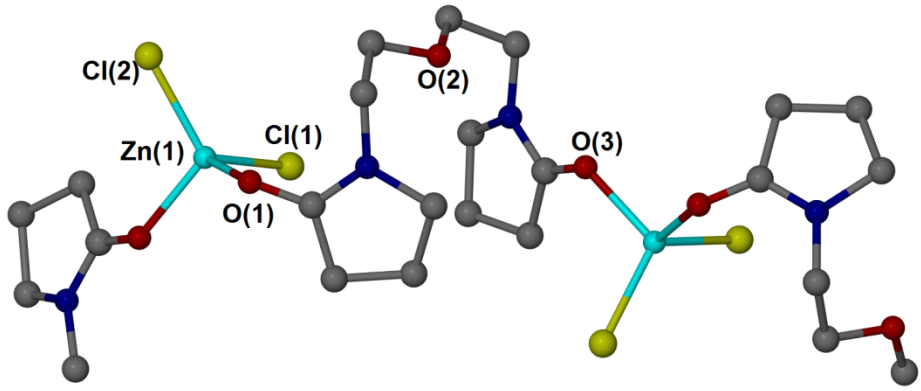

Figure 5.11: X-ray crystal structure of {[$ZnCl_2$(μ-**5.1**)]}$_n$ (**5.11**). Hydrogen atoms are omitted for clarity. Selected bond lengths (Å): Zn(1)-O(1) 1.9958(18), Zn(1)-O(3) 1.9952(18), Zn(1)-Cl(1) 2.2368(7) and Zn(1)-Cl(2) 2.2116(7).

Addition of an equimolar quantity of ligand **5.1** directly to $ZnCl_2$, followed by addition of acetone, results in a crystalline precipitate immediately upon sonication. The precipitate was isolated using Büchner filtration and analysed using PXRD. Comparison between the experimental powder pattern and the calculated powder pattern based on the single crystal data for **5.11** indicates the formation of a new compound, as seen in Figure 5.12. Analysis by IR spectroscopy and TGA indicates that the precipitate is not simply a solvated analogue of complex **5.11**, with a weight loss of only 1.4% upon heating from room temperature to 250 ^{o}C. Elemental analysis indicates that a 1:1 complex is present, and therefore it is postulated that direct addition of the ligand to the metal salt results in the formation of an alternative polymorph or isomer of **5.11**. Due to the absence of single crystals, it is not possible to unequivocally establish the identity of this material.

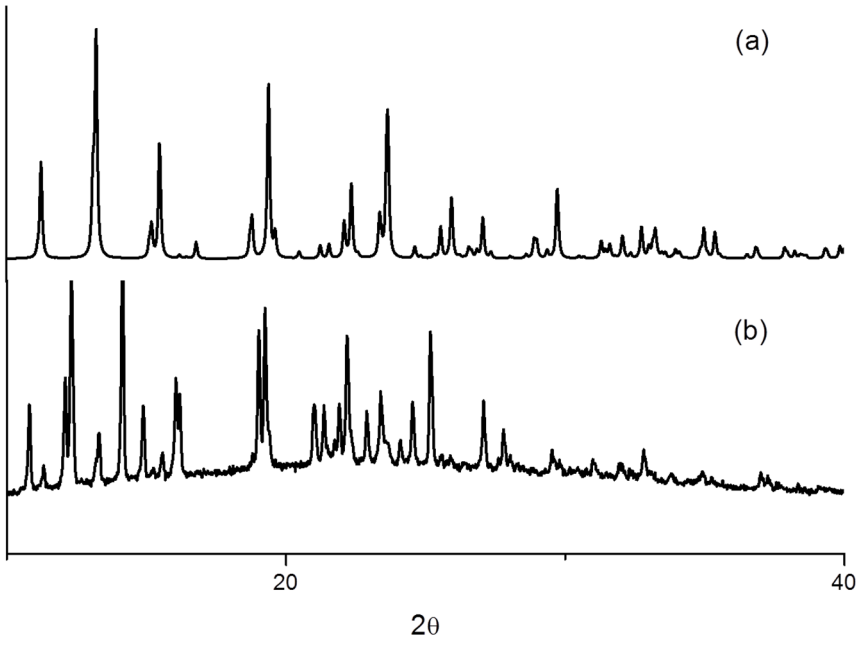

Figure 5.12: (a) calculated PXRD pattern based on the single crystal structure of {[$ZnCl_2$(μ-**5.1**)]}$_n$ (**5.11**) and (b) experimental PXRD pattern of alternative zinc chloride product.

5.6 Other ligands

All of the complexes reported to date are based on the bis(pyrrolidone) ligand **5.1**, showing metal complexation at the carbonyl oxygen and ether donor groups. For comparison, the sodium metal complexation behaviour of 1,3-bis(pyrrolidin-2-on-1-yl) but-1-ane (**2.3**) is reported, in an attempt to explore metal binding in the absence of the ether functionality. Reaction of ligand **2.3** with $NaPF_6$ in methanol results in the crystallization of an unusual 2:3 trigonal 1D coordination polymer {[Na_2(μ-**2.3**)$_3$](PF_6)$_2$}$_n$ (**5.12**). The asymmetric unit contains three ligand molecules and two alkali metal centres, arranged into two independent polymeric chains of opposing handedness, as seen in Figure 5.13. Each carbonyl oxygen atom bridges two metal centres, with Na-O bond distances in the range 2.43-2.57 Å, considerably longer than in the complexes of **5.1** as a result of increased steric strain in the smaller ligand. IR spectroscopy confirms a shift to the enolate resonance form upon complexation, as seen by a shift from 1663 cm^{-1} to 1645 cm^{-1}. Isolation and characterisation of complex **5.12** confirms that the ether functionality is not essential for complexation, highlighting that the polar nature of the carbonyl moiety is crucial to the performance of these species.

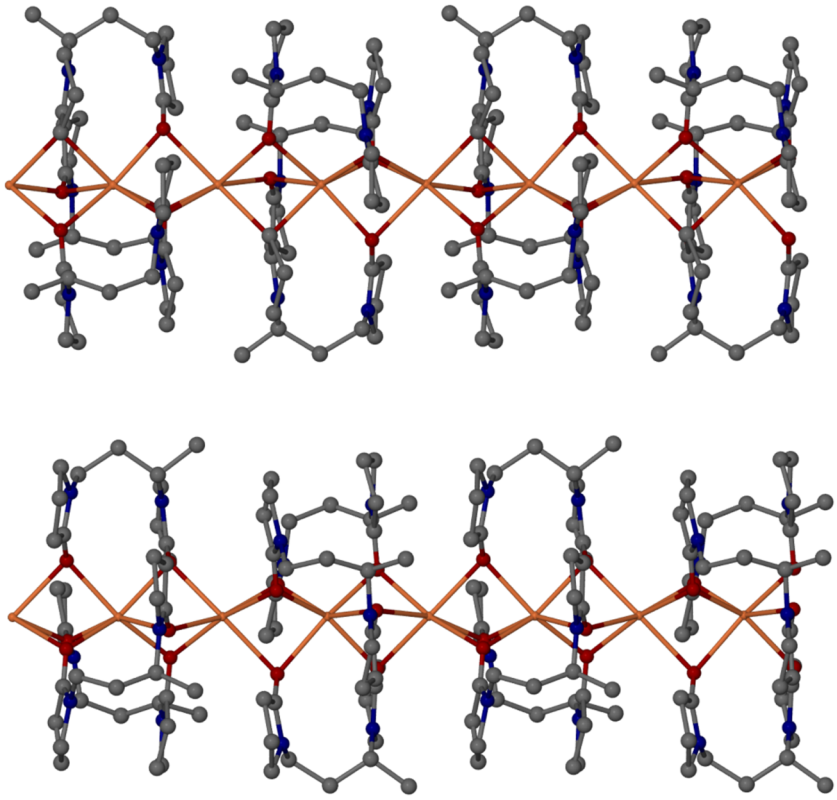

Figure 5.13: X-ray crystal structure of {[Na_2(μ-**2.3**)$_3$](PF_6)$_2$]$_n$ (**5.12**). Hydrogen atoms and counter anions are omitted for clarity.

Finally, the sodium complexation of mono(lactam) 1-(2-hydroxyethyl)-2-pyrrolidone (**2.12**) was explored in order to examine whether having two carbonyl moieties is crucial to the coordination behaviour. The high polarity of the carbonyl moiety in the pyrrolidone ring enables formation of a hydrated 1:1 complex with $NaBPh_4$, namely [Na_2(μ-**2.12**)$_2$(H_2O)$_3$](BPh_4)$_2$ (**5.13**), Figure 5.14. The dimer complex is similar to complex **5.6** (analogous ligand **5.1** complex), with the carbonyl oxygen atoms bridging the metal centres. While the ether donor binds to a single metal centre in complex **5.6**, in this instance the alcohol moiety of ligand **2.12** binds to a single sodium cation. The carbonyl-metal bond distance is shorter than in complex **5.6** due to the smaller ligand size. The octahedral coordination sphere of each metal centre is completed by three molecules of water.

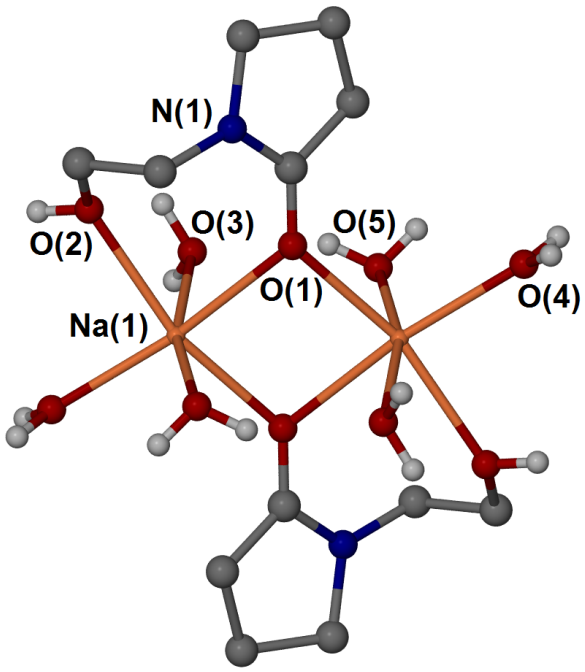

Figure 5.14: X-ray molecular structure of the cation in $[Na_2(\mu\text{-}\mathbf{5.3})_2(H_2O)_3](BPh_4)_2$ (**5.13**). Hydrogen atoms are omitted with the exception of water molecules. Selected bond distances (Å): Na(1)-O(1) 2.4001(19), Na(1)-O(1)' 2.3121(17), Na(1)-O(2) 2.4113(19), Na(1)-O(3) 2.424(2), Na(1)-O(4) 2.298(2), Na(1)-O(5) 2.4066(19) Å.

5.7 Conclusions

The isolation and characterisation of a series of metal-bound coordination complexes provides support for the high polarity of the pyrrolidone carbonyl moiety. The bis(pyrrolidone) ether ligand (**5.1**) shows great versatility in binding mode, exhibiting both terminal and bridging interactions. The surprising isolation of the protonated form of the ligand highlights the basicity of the polar pyrrolidone carbonyl group. This characteristic is also exemplified by the short carbonyl oxygen-metal bond distances, in comparison to the ether-metal analogues. The complex with the bis(pyrrolidone) ligand lacking an ether linkage (**2.3**) indicates that the C=O groups are fundamental for the coordination behaviours, and that the ether donor is not essential. This is further supported by the sodium complex of 1-(2-hydroxyethyl)-2-pyrrolidone (**2.12**).

In conclusion, this work has exploited the highly polar pyrrolidone carbonyl group in the formation of a plethora of metal complexes, which may have further application. It is postulated that this characteristic of the C=O functionality may be crucial to the interesting behaviour of these ligands and related species.

5.8 Experimental

5.8.1 General

1-{2-[2-(2-oxo-pyrrolid-1-yl)-ethoxy]-ethyl}-pyrrolid-2-one (**5.1**), 1,3-bis(pyrrolidin-2-on-1-yl) but-1-ane (**2.3**) and 1-(2-hydroxyethyl)-2-pyrrolidone (**2.12**) were supplied by Ashland Inc., and used without further purification. Sodium hexafluorophosphate, sodium tetraphenylborate, potassium hexafluorophosphate, lithium hexafluorophosphate and zinc chloride were purchased from Sigma-Aldrich and used without further purification.

IR spectra were measured with a Perkin-Elmer 100 FT-IR spectrometer, using an ATR attachment. Thermogravimetric analysis was conducted using a Perkin Elmer Pyris 1 TGA with purge gas specified at 40 mls per minute. TGA temperature was increased at 10 ^{o}C per minute up to the temperature specified.

Crystals suitable for single crystal X-ray diffraction structure determination were selected, soaked in perfluoropolyether oil and mounted on a preformed tip. Single crystal X-ray data were collected at 120 K on an Agilent Gemini S-Ultra diffractometer equipped with the Cryostream (Oxford Cryosystems) open-flow nitrogen cryostats, using graphite monochromated MoKα-radiation (λ = 0.71069 Å). All structures were solved using direct methods and refined by full-matrix least squares on F^2 for all data using SHELXL[25] and OLEX2[26]. All non-hydrogen atoms were refined with anisotropic displacement parameters. CH hydrogen atoms were placed in calculated positions, assigned an isotropic displacement factor that is a multiple of the parent carbon atom and allowed to ride. H-atoms attached to oxygen were located on the difference map when possible, or placed in calculated positions. In some cases disordered H atoms could not be included in the model. Elemental analysis was performed using an Exeter Analytical inc. CE-400 Elemental Analyser. Powder diffraction was performed on glass slides using a Bruker AXS D8 Advance diffractometer, with a Lynxeye Soller PSD Detector, using CuKα radiation at a wavelength of 1.5406 Å.

5.8.2 Synthesis of coordination complexes

Complexes **5.4** and **5.5** were synthesised by Dominic Myers, a summer student, under the direct supervision of Andrea Perrin. X-ray crystallographic analysis of complexes **5.3**, **5.4**, **5.9**, **5.11** and **5.12** were performed by Dr. Katharina Fucke and observed by Andrea Perrin.

[Na(**5.1**)$_2$]PF_6 (**5.2**).

1-{2-[2-(2-oxo-pyrrolid-1-yl)-ethoxy]-ethyl}-pyrrolid-2-one (**5.1**) (0.286 g, 1.19 mmol) was added to $NaPF_6$ (0.1 g, 0.595 mmol) dissolved in acetonitrile (2 mL). The resulting mixture was sonicated for 1 minute. Colourless crystals formed upon evaporation of the solvent at room temperature (Yield = 0.276 g, 0.425 mmol, 71 %). Analysis calc. for $C_{24}H_{40}N_4O_6NaPF_6$: C 44.45, H 6.22, N 8.64%, found: C 44.38, H 6.26, N 8.57%; IR (υ/ cm^{-1}): 1661 (C=O), 1120 (C-O, ether). Crystal data for $C_{24}H_{40}N_4O_6NaPF_6$: M = 648.56, colourless plate, 0.497 × 0.2891 × 0.1196 mm^3, triclinic, space group $P\bar{1}$ (No. 2), a = 7.0768(4), b = 8.5945(5), c = 12.9170(7) Å, α = 77.011(5), β = 77.346(4), γ = 74.071(5) °, V = 725.67(7) Å^3, Z = 1, D_c = 1.484 g/cm^3, F_{000} = 340, Xcalibur, Sapphire3, Gemini ultra, Mo Kα radiation, λ = 0.7107 Å, T = 120.0K, 2θ_{max} = 55.0°, 12472 reflections collected, 3330 unique (R_{int} = 0.0337). Final *GooF* = 1.064, *R1* = 0.0377, *wR2* = 0.0956, *R* indices based on 2945 reflections with I >2σ(I) (refinement on F^2), 212 parameters, 0 restraints. Lp and absorption corrections applied, μ = 0.194 mm^{-1}.

{[Na_3(μ_3-**5.1**)$_2$(μ_2-**5.1**)$_2$](PF_6)$_3$}$_n$ (**5.3**).

1-{2-[2-(2-oxo-pyrrolid-1-yl)-ethoxy]-ethyl}-pyrrolid-2-one (**5.1**) (0.0975 g, 0.406 mmol) was added to $NaPF_6$ (0.0511 g, 0.304 mmol) dissolved in acetonitrile (1 mL). The resulting mixture was sonicated for 1 minute. Colourless crystals formed upon evaporation of the solvent at room temperature (Yield = 0.1291 g, 0.088 mmol, 28.96 %). Analysis calc. for $C_{48}H_{80}N_8O_{12}Na_3P_3F_{18}$: C 39.35, H 5.50, N 7.65%, found: C 39.33, H 5.61, N 7.69%; IR (υ/ cm^{-1}): 1655 (C=O), 1117 (C-O, ether). Crystal data for $C_{48}H_{80}N_8O_{12.28}Na_3P_3F_{18}$: M = 1469.61, colourless plate, 0.7422 × 0.4462 × 0.1434 mm^3, triclinic, space group $P\bar{1}$ (No. 2), a = 13.2010(4), b = 13.6768(4), c = 18.1009(5) Å, α = 85.700(2), β = 84.890(2), γ = 88.882(2) °, V = 3245.65(16) Å^3, Z = 2, D_c = 1.504 g/cm^3, F_{000} = 1525, Xcalibur, Sapphire3, Gemini ultra, Mo Kα radiation, λ = 0.7107 Å, T = 120.0K, 2θ_{max} = 55.0°, 76405 reflections collected, 14788 unique (R_{int} = 0.0868). Final *GooF* = 1.029, *R1* = 0.0563, *wR2* = 0.1197, *R* indices based on 10349 reflections with I>2σ(I) (refinement on F^2), 894 parameters, 0 restraints. Lp and absorption corrections applied, μ = 0.226 mm^{-1}.

[Na_3(H_2O)$_2$(μ-**5.1**)$_2$](PF_6)$_3$ (**5.4**).

1-{2-[2-(2-oxo-pyrrolid-1-yl)-ethoxy]-ethyl}-pyrrolid-2-one (**5.1**) (0.0487 g, 0.202 mmol) was added to $NaPF_6$ (0.0511 g, 0.304 mmol) dissolved in acetonitrile (1 mL). The resulting mixture was sonicated for 1 minute. Colourless crystals formed upon evaporation of the solvent at

room temperature (Yield = 0.0481 g, 0.0471 mmol, 23.26 %). Analysis calc. for $C_{24}H_{44}N_4O_8Na_3P_3F_{18}$: C 28.26, H 4.35, N 5.49%, found: C 28.38, H 4.18, N 5.58%; IR (υ/ cm^{-1}): 1650 (C=O), 1123 (C-O, ether). Crystal data for $C_{24}H_{44}N_4O_6Na_3P_3F_{18}$: M = 1020.51, clear light colourless irregular, 0.2738 × 0.1334 × 0.0759 mm^3, monoclinic, space group $C2/c$ (No. 15), a = 13.848(2) , b = 17.969(3), c = 16.913(3) Å, α = 90.00, β = 107.686(18), γ = 90.00 °, V = 4009.8(11) Å^3, Z = 8, D_c = 1.690 g/cm^3, F_{000} = 2080, Xcalibur, Sapphire3, Gemini ultra, Mo Kα radiation, λ = 0.7107 Å, T = 120K, $2\theta_{max}$ = 58.6°, 32122 reflections collected, 5004 unique (R_{int} = 0.1991). Final *GooF* = 1.310, *R1* = 0.1745, *wR2* = 0.4286, *R* indices based on 2014 reflections with I >2σ(I) (refinement on F^2), 274 parameters, 0 restraints. Lp and absorption corrections applied, μ = 0.314 mm^{-1}.

[Na_2(μ-**5.1**)$_2$($MeOH)_2$]($PF_6)_2$ (**5.5**).

1-{2-[2-(2-oxo-pyrrolid-1-yl)-ethoxy]-ethyl}-pyrrolid-2-one (**5.1**) (0.05 g, 0.208 mmol) was added to $NaPF_6$ (0.035 g, 0.208 mmol) dissolved in 2,2-dimethoxypropane (1 mL). The resulting mixture was sonicated for 1 minute. Pale yellow crystals formed upon evaporation of the solvent at room temperature (Yield = 0.0654 g, 0.0743 mmol, 36 %). The sample for analysis was dried *in vacuo* for 2 h at 110 °C resulting in loss of the coordinated methanol. Analysis calc. for $C_{12}H_{20}N_2O_3NaPF_6$: C 35.30, H 4.94, N 6.86%, found: C 35.62, H 5.06, N 6.78%; IR (υ/ cm^{-1}): 1650 (C=O), 1123 (C-O, ether). Crystal data for $C_{26}H_{48}N_4O_8Na_2P_2F_{12}$, M = 880.60, colourless plate, 0.2888 × 0.1892 × 0.0992 mm^3, monoclinic, space group $P2_1/c$ (No. 14), a = 11.1886(5), b = 13.3508(5), c = 13.6275(6) Å, α = 90.00, β = 111.547(5), γ = 90.00 °, V = 1893.37(14) Å^3, Z = 2, D_c = 1.545 g/cm^3, F_{000} = 912, Xcalibur, Sapphire3, Gemini ultra, Mo Kα radiation, λ = 0.7107 Å, T = 120.0K, $2\theta_{max}$ = 55.0°, 13061 reflections collected, 4262 unique (R_{int} = 0.0515). Final *GooF* = 1.043, *R1* = 0.0618, *wR2* = 0.1266, *R* indices based on 2880 reflections with I >2σ(I) (refinement on F^2), 248 parameters, 2 restraints. Lp and absorption corrections applied, μ = 0.247 mm^{-1}.

[Na_2(μ-**5.1**)$_2$($H_2O)_4$]($BPh_4)_2$ (**5.6**).

1-{2-[2-(2-oxo-pyrrolid-1-yl)-ethoxy]-ethyl}-pyrrolid-2-one (**5.1**) (0.05 g, 0.20 mmol) was added to $NaBPh_4$ (0.071 g, 0.20 mmol) dissolved in water (1 mL). The resulting mixture was sonicated for 1 minute. Colourless crystals formed within 24 hours at room temperature (Yield = 0.0807 g, 0.065 mmol, 32.62 %). Analysis calc. for $C_{72}H_{88}B_2N_4Na_2O_{10}$: C 69.90, H 7.18, N 4.53 %, found: C 70.06, H 7.11, N 4.64 %; IR (υ/ cm^{-1}): 1668, 1643 (C=O), 1120 (C-O, ether). Crystal data for $C_{72}H_{88}B_2N_4Na_2O_{10}$, M = 1237.06, colourless block, 0.5581 × 0.241 × 0.1241

mm^3, triclininc, space group $P\bar{1}$ (No. 2), a = 11.9380(5), b = 12.1701(5), c = 13.1018(7), σ = 67.444(4), β = 75.171(4), γ = 78.989(3), V = 1690.16(13) Å^3, Z = 1, D_c = 1.215 g/cm^3, F_{000} = 660, Xcalibur, Sapphire3, Gemini ultra, Mo Kα radiation, λ = 0.7107 Å, T = 120K, $2\theta_{max}$ = 55.0^o, 28252 reflections collected, 7743 unique (R_{int} = 0.0612). Final *GooF* = 1.023, *R1* = 0.0502, *wR2* = 0.1006, *R* indices based on 5539 reflections with I >2σ(I) (refinement on F^2), 422 parameters, 0 restraints. Lp and absorption corrections applied, μ = 0.091 mm^{-1}.

[Na_2(**5.1**)$_2$(μ-**5.1**)$_2$](BPh_4)$_2$ (**5.7**).

1-{2-[2-(2-oxo-pyrrolid-1-yl)-ethoxy]-ethyl}-pyrrolid-2-one (**5.1**) (0.1 g, 0.41 mmol) was added to $NaBPh_4$ (0.071 g, 0.20 mmol) dissolved in ethanol (1 mL). The resulting mixture was sonicated for 1 minute. Colourless crystals formed within 4 days at room temperature (Yield = 0.1339 g, 0.0814 mmol, 39.3%). Analysis calc. for $C_{96}H_{120}B_2N_8Na_2O_{12}$: C 70.07, H 7.35, N 6.81 %, found: C 69.87, H 7.26, N 6.89 %; IR (υ/ cm^{-1}): 1666, 1642 (C=O), 1116 (C-O, ether). Crystal data for $C_{96}H_{120}B_2N_8Na_2O_{12}$, M = 1645.60 , colourless block, 0.4125 x 0.2418 x 0.1581 mm^3, triclinic, space group $P\bar{1}$ (No. 2), a = 11.5127(6), b = 13.7549(9), c = 15.9209(7) Å, α = 71.514(5), β = 79.756(4), γ = 66.772(5) ^{o}, V = 2193.2(2) Å^3, Z = 1, D_c = 1.246 g/cm^3, F_{000} = 880, Xcalibur, Sapphire3, Gemini ultra, Mo Kα radiation, λ = 0.7107 Å, T = 120K, $2\theta_{max}$ = 54.0^o, 31465 reflections collected, 9579 unique (R_{int} = 0.0578). Final *GooF* = 1.032, *R1* = 0.0513, *wR2* = 0.1090, *R* indices based on 6919 reflections with I >2σ(I) (refinement on F^2), 541 parameters, 0 restraints. Lp and absorption corrections applied, μ = 0.090 mm^{-1}.

[K(**5.1**)$_2$]PF_6 (**5.8**).

1-{2-[2-(2-oxo-pyrrolid-1-yl)-ethoxy]-ethyl}-pyrrolid-2-one (**5.1**) (0.1000 g, 0.40 mmol) was added to KPF_6 (0.038 g, 0.2 mmol) dissolved in acetonitrile (1 mL). The resulting mixture was sonicated for 1 minute. Colourless crystals formed upon evaporation of the solvent at room temperature (Yield = 0.09 g, 0.135 mmol, 68 %). The crystals proved to absorb atmospheric moisture over time and elemental analysis on a fully dry material could not be obtained. Analysis calc. for $C_{24}H_{40}N_4O_6KPF_6$: C 43.37, H 6.07, N 8.43%, re-calc for $C_{24}H_{40}N_4O_6KPF_6{\cdot}2H_2O$: C41.14, H 6.34, N 7.99%, found: C 41.19, H 6.37, N 7.92%; IR (υ/ cm^{-1}): 1650 (C=O), 1121 (C-O, ether). Crystal data for $C_{24}H_{40}N_4O_6KPF_6$, M = 664.67, colourless block, 0.5484 × 0.4243 × 0.1448 mm^3, triclinic, space group $P\bar{1}$ (No. 2), a = 7.0028(2), b = 8.6199(3), c = 13.2814(4) Å, α = 79.410(3), β = 79.591(3), γ = 74.036(3)^o, V = 750.45(4) Å^3, Z = 1, D_c = 1.471 g/cm^3, F_{000} = 348, Xcalibur, Sapphire3, Gemini ultra, Mo Kα radiation, λ = 0.7107 Å, T = 120.0K, $2\theta_{max}$ = 55.0º,

19534 reflections collected, 3441 unique (R_{int} = 0.0431). Final *GooF* = 0.973, *R1* = 0.0365, *wR2* = 0.1162, *R* indices based on 2977 reflections with I >2σ(I) (refinement on F^2), 253 parameters, 0 restraints. Lp and absorption corrections applied, μ = 0.312 mm^{-1}.

[$K_4(\mu_4$-$H_2O)(\mu$-**5.1**$)_4](PF_6)_4$ (**5.9**)

1-{2-[2-(2-oxo-pyrrolid-1-yl)-ethoxy]-ethyl}-pyrrolid-2-one (**5.1**) (0.1318 g, 0.548 mmol) was added to KPF_6 (0.1007 g, 0.547 mmol) dissolved in acetonitrile (1 mL). The resulting mixture was sonicated for 1 minute. Colourless crystals formed upon evaporation of the solvent at room temperature (Yield = 0.20 g, 0.115 mmol, 21 %). Analysis calc. for $K_4P_4F_{24}C_{48}H_{84}N_8O_{14}$: C 38.19, H 5.61, N 7.42%, found C 38.11, H 5.62, N 7.51; IR (υ/ cm^{-1}): 1666 (C=O), 1121 (C-O, ether). Crystal data for $C_{48}H_{84}F_{24}K_4N_8O_{14}P_4$, *M* = 1733.51, colourless block, 0.941 x 0.6432 x 0.3017 mm^3, monoclinic, space group *C*2/c (No. 15), *a* = 28.4413(11), *b* = 12.8337(3), *c* = 23.8944(8) Å, α = 90.00, β = 120.757(5), γ = 90.00o, *V* = 7494.9(4) Å^3, *Z* = 4, *D*c = 1.536 g/cm^3, *F*000 = 3568, Xcalibur, Sapphire3, Gemini ultra, Mo Kα radiation, λ = 0.7107 Å, *T* = 120K, 2θ_{max} = 55.0º, 57703 reflections collected, 8606 unique (R_{int} = 0.0386). Final *GooF* = 1.046, *R1* = 0.0677, *wR2* = 0.1611, R indices based on 7330 reflections with I >2σ(I) (refinement on F^2), 561 parameters, 0 restraints. Lp and absorption corrections applied, μ= 0.443 mm^{-1}. The pyrrolidone rings of one ligand are disordered across two positions, occupancy refined to approximately 50 %.

A second polymorph was obtained as follows: 1-{2-[2-(2-oxo-pyrrolid-1-yl)-ethoxy]-ethyl}-pyrrolid-2-one (**5.1**) (0.050 g, 0.208 mmol) was added to KPF_6 (0.038 g, 0.206 mmol) dissolved in methanol (1 mL). The resulting mixture was sonicated for 1 minute. Colourless crystals formed upon evaporation of the solvent at room temperature (Yield = 0.04 g, 0.231 mmol, 11 %). Analysis calc. for $K_4P_4F_{24}C_{48}H_{84}N_8O_{14}$: C 33.26, H 4.89, N 6.46%, found C 33.37, H 4.71, N 6.61; IR (υ/ cm^{-1}): 1666 (C=O), 1122 (C-O, ether). Crystal data for $C_{48}H_{84}F_{24}K_4N_8O_{14}P_4$, *M* = 1733.49 g mol^{-1}, colourless prism, 0.6726 x 0.1765 x 0.0362 mm^3, monoclinic, space group *C*2/c (No. 15), *a* = 41.2572(13), *b* = 12.8318(4), *c* = 45.5789(17) Å, α = 90.00, β = 111.458(4), γ = 90.00º, *V* = 22457.2(13) Å^3, *Z* = 12, *D*c = 1.538 g/cm^3, F_{000} = 10704, Xcalibur, Sapphire3, Gemini ultra, Mo Kα radiation, λ = 0.7107 Å, *T* = 120K, 2θ_{max} = 55.0º, 118863 reflections collected, 25414 unique (R_{int} = 0.2077). Final *GooF* = 0.998, *R1* = 0.0973, *wR2* = 0.2059, R indices based on 10209 reflections with I >2σ(I) (refinement on F^2), 1387 parameters, 0 restraints. Lp and absorption corrections applied, μ = 0.443 mm^{-1}.

5.1·HPF_6 (**5.10**).

1-{2-[2-(2-oxo-pyrrolid-1-yl)-ethoxy]-ethyl}-pyrrolid-2-one (**5.1**) (0.1580 g, 0.657 mmol) was added to $LiPF_6$ (0.0998 g, 0.657 mmol) dissolved in methanol (2 mL). The resulting mixture was sonicated for 1 minute. Colourless crystals formed upon evaporation of the solvent at room temperature (Yield = 0.03 g, 0.078 mmol, 11.8 %). Analysis calc. for $C_{12}H_{21}N_2O_3PF_6$: C 37.31, H 5.48, N 7.25%, found: C 37.12, H 5.25, N 7.12%; IR (υ/ cm^{-1}): 1642 (C=O), 1116 (C-O, ether). Crystal data for $C_{12}H_{21}N_2O_3PF_6$, M = 386.28, colourless block, 0.6976 × 0.1279 × 0.1267 mm^3, orthorhombic, space group *Pbca* (No. 61), a = 11.6287(6), b = 13.8824(7), c = 20.0682(10) Å, α = 90.00, β = 90.00, γ = 90.00°, V = 3239.7(3) $Å^3$, Z = 8, D_c = 1.584 g/cm^3, F_{000} = 1600, Xcalibur, Sapphire3, Gemini ultra, Mo Kα radiation, λ = 0.7107 Å, T = 120.0K, $2\theta_{max}$ = 55.0°, 30797 reflections collected, 3708 unique (R_{int} = 0.1202). Final *GooF* = 1.060, *R1* = 0.0618, *wR2* = 0.1604, *R* indices based on 2595 reflections with I >2σ(I) (refinement on F^2), 221 parameters, 0 restraints. Lp and absorption corrections applied, μ = 0.249 mm^{-1}.

{[$ZnCl_2$(μ-**5.1**)]}$_n$ (**5.11**).

1-{2-[2-(2-oxo-pyrrolid-1-yl)-ethoxy]-ethyl}-pyrrolid-2-one (**5.1**) (0.1823 g, 0.786 mmol) was added to $ZnCl_2$ (0.0517 g, 0.379 mmol) dissolved in acetone (2 mL). The resulting mixture was sonicated for 1 minute. Colourless crystals formed upon evaporation of the solvent at room temperature (Yield = 0.0951 g, 0.253 mmol, 66.60 %). Analysis calc. for $C_{12}H_{20}N_2O_3ZnCl_2$: C 38.27, H 5.35, N 7.44%, found: C 38.25, H 5.26, N 7.47%; IR (υ/ cm^{-1}): 1611 (C=O), 1128 (C-O, ether). Crystal data for $C_{12}H_{20}N_2O_3ZnCl_2$, M = 376.57, colourless plate, 0.4654 × 0.197 × 0.0541 mm^3, monoclinic, space group $P2_1/n$ (No. 14), a = 11.3180(6), b = 8.6628(3), c = 16.7004(9) Å, α = 90.00, β = 107.888(6), γ = 90.00 °, V = 1558.26(13) $Å^3$, Z = 4, D_c = 1.605 g/cm^3, F_{000} = 776, Xcalibur, Sapphire3, Gemini ultra, Mo Kα radiation, λ = 0.7107 Å, T = 120.0K, $2\theta_{max}$ = 55.0°, 15272 reflections collected, 3543 unique (R_{int} = 0.0560). Final *GooF* = 1.042, *R1* = 0.0370, *wR2* = 0.0712, *R* indices based on 2795 reflections with I >2σ(I) (refinement on F^2), 181 parameters, 0 restraints. Lp and absorption corrections applied, μ = 1.926 mm^{-1}.

{[Na_2(μ-**2.3**)$_3$](PF_6)$_2$}$_n$ (**5.12**).

1,3-bis(pyrrolidin-2-on-1-yl)butane (**2.3**) (0.2672 g, 1.191 mmol) was added to $NaPF_6$ (0.1041 g, 0.6198 mmol) dissolved in methanol (1 mL). The resulting mixture was sonicated for 1 minute. Colourless crystals formed upon evaporation of the solvent at room temperature

(Yield = 0.2744 g, 0.544 mmol, 87.78 %). Analysis calc. for $C_{12}H_{20}N_2O_2NaPF_6$: C 42.86, H 5.99, N 8.33%, found: C 42.88, H 6.09, N 8.37%; IR (υ/ cm^{-1}): 1645 (C=O). Crystal data for $C_{18}H_{30}N_3O_3NaPF_6$, M = 504.41, colourless plate, 0.2116 × 0.1894 × 0.09 mm^3, trigonal, space group $P31c$ (No. 159), a = 23.9245(6), b = 23.9245(6), c = 13.3123(4) Å, α = 90.00, β = 90.00, γ = 120.00 °, V = 6598.9(3) $Å^3$, Z = 12, D_c = 1.523 g/cm^3, F_{000} = 3156, Xcalibur, Sapphire3, Gemini ultra, Mo Kα radiation, λ = 0.7107 Å, T = 120.0K, $2\theta_{max}$ = 55.0°, 104425 reflections collected, 10093 unique (R_{int} = 0.2215). Final *GooF* = 1.079, *R1* = 0.1126, *wR2* = 0.2853, *R* indices based on 5779 reflections with I >2σ(I) (refinement on F^2), 574 parameters, 7 restraints. Lp and absorption corrections applied, μ = 0.221 mm^{-1}.

$[Na_2(\mu$-**2.12**$)_2(H_2O)_3](BPh_4)_2$ (**5.13**).

1-(2-hydroxyethyl)-2-pyrrolidone (**2.12**) (0.019 g, 0.147 mmol) was added to $NaBPh_4$ (0.05 g, 0.146 mmol) dissolved in ethanol (2 mL). The resulting mixture was sonicated for 2 mintutes. Colourless crystals formed upon evaporation of the solvent at room temperature. (Yield = 0.049 g, 0.047 mmol, 32 %). The sample for analysis was dried *in vacuo* for 4 h at 110 °C resulting in loss of 3 molecules of coordinated water. Analysis calc for $C_{60}H_{62}B_2N_2Na_2O_4 \cdot 3H_2O$: C 72.3, H 6.88, N 2.81%, found: C 72.34, H 6.64, N 2.90%. IR (υ/ cm^{-1}): 1645 (C=O). Crystal data for $C_{60}H_{74}B_2N_2Na_2O_{10}$, M = 1050.81 g mol^{-1}, colourless plate, 0.4917 × 0.3219 × 0.196 mm^3, monoclinic, space group $P2_1/n$ (No. 14), a = 11.2982(5), b = 18.0303(7), c = 13.6061(7) Å, α = 90.00, β = 90.452(4), γ = 90.00 °, V = 2771.6(2) $Å^3$, Z = 2, D_c = 1.259 g/cm^3, F_{000} = 1120, Xcalibur, Sapphire3, Gemini ultra, Mo Kα radiation, λ = 0.71073 Å, T = 120.0K, $2\theta_{max}$ = 52.0°, 21859 reflections collected, 5445 unique (R_{int} = 0.0646). Final *GooF* = 1.033, *R1* = 0.0530, *wR2* = 0.1226, *R* indices based on 3911 reflections with I >2σ(I) (refinement on F^2), 349 parameters, 3 restraints. Lp and absorption corrections applied, μ = 0.097 mm^{-1}.

5.9 References

1. A. Perrin, O. M. Musa and J. W. Steed, *Chem. Soc. Rev.*, 2013, **42**, 1996-2015.
2. M. A. Kelland, *Energy Fuels*, 2006, **20**, 825-847.
3. F. Fischer and S. Bauer, *Chem. Unserer Zeit*, 2009, **43**, 376-383.
4. O. Clement, B. M. Rapko and B. P. Hay, *Coord. Chem. Rev.*, 1998, **170**, 203-243.
5. W. E. Bull, S. K. Madan and J. E. Willis, *Inorg. Chem.*, 1963, **2**, 303-306.
6. C. L. Rollinson and R. C. White, *Inorg. Chem.*, 1962, **1**, 281-285.
7. M. L. Good and T. H. Siddall, *J. Inorg. Nucl. Chem.*, 1968, **30**, 2679-2687.
8. T. H. Siddall and M. L. Good, *J. Inorg. Nucl. Chem.*, 1967, **29**, 149-158.
9. O.Musa and K.S.Narayanan, *US*20120148514 A1, 2012.

10. J. W. Steed and J. L. Atwood, *Supramolecular Chemistry*, 2nd Edition edn., Wiley-Blackwell, Chichester, 2009.
11. G. W. Gokel, W. M. Leevy and M. E. Weber, *Chem. Rev.*, 2004, **104**, 2723-2750.
12. J. S. Bradshaw and R. M. Izatt, *Acc. Chem. Res.*, 1997, **30**, 338-345.
13. S. S. Kukalenko, B. A. Bovykin, S. I. Shestakova and A. M. Omel'chenko, *Russ. Chem. Rev.*, 1985, **54**, 676.
14. S. K. Madan and H. H. Denk, *J. Inorg. Nucl. Chem.*, 1965, **27**, 1049-1058.
15. G. A. Doyle, D. M. L. Goodgame, S. P. W. Hill, S. Menzer, A. Sinden and D. J. Williams, *Inorg. Chem.*, 1995, **34**, 2850-2860.
16. G. A. Doyle, D. M. L. Goodgame, S. P. W. Hill and D. J. Williams, *J. Chem. Soc. Chem. Commun.*, 1993, 207-209.
17. D. M. L. Goodgame, S. P. W. Hill and D. J. Williams, *Polyhedron*, 1993, **12**, 2933-2939.
18. H. Valle, J. Sánchez and B. L. Rivas, *J. Appl. Polym. Sci.*, 2015, **132**, 41272.
19. A. Perrin, D. Myers, K. Fucke, O.M. Musa and J.W. Steed, *Dalton Trans.*, 2014, **43**, 3153 – 3161.
20. S. J. Borwick, J. A. K. Howard, C. W. Lehmann and D. Ohagan, *Acta Crystallogr. Sect. C-Cryst. Struct. Commun.*, 1997, **53**, 124-126.
21. W. J. Belcher, M. Fabre, T. Farhan and J. W. Steed, *Org. Biomol. Chem.*, 2006, **4**, 781-786.
22. F. H. Allen, J. A. K. Howard, V. J. Hoy, G. R. Desiraju, D. S. Reddy and C. C. Wilson, *J. Am. Chem. Soc.*, 1996, **118**, 4081-4084.
23. A. Bekaert, B. Viossat, D. Brion Jean and P. Lemoine, in *Zeitschrift für Kristallographie - New Crystal Structures*, 2009, vol. 224, p. 676.
24. R. W. Impey, M. Sprik and M. L. Klein, *J. Am. Chem. Soc.*, 1987, **109**, 5900-5904.
25. G. M. Sheldrick, *Acta Crystallogr. Sect. A*, 2008, **64**, 112-122.
26. O. V. Dolomanov, L. J. Bourhis, R. J. Gildea, J. A. K. Howard and H. Puschmann, *J. Appl. Crystallogr.*, 2009, **42**, 339-341.

6 Calcium complexes of lactam ligands

6.1 Introduction

Calcium chloride ($CaCl_2$) is hygroscopic and reacts exothermically with water; a property exploited by the cement industry in accelerating the drying process.[1] Addition of $CaCl_2$ at a 1-2 weight% dosage is known to significantly reduce cement setting time, and as such the metal salt has become one of the most widely used accelerators.[2-4] However, the performance of calcium chloride within dry mortar systems is limited as a result of its hygroscopicity.[5] In addition, the deliquescent nature of this material causes handling issues. In this project we postulate that complexation of calcium chloride may prolong the hydration process and thereby enhance performance. Suitable ligands for this purpose should form stable anhydrous coordination complexes with $CaCl_2$ with maximum water uptake potential that hydrate exothermically at a controlled rate.

We hypothesise that complexation of the hygroscopic metal salt with oxophilic lactam ligands may delay water uptake and hence prolong the activity of the species. The high polarity of the lactam amide carbonyl functionality enables metal complexation; a property previously exploited in the isolation of a series of alkali metal complexes, as described in Chapter 5.[6] Englert and coworkers analysed the calcium chloride complexes reported in the Cambridge Structural Database (CSD) and found a high proportion of Ca-O contacts in 6 coordinate complexes, and therein provided additional support for the oxophilic nature of the metal centre.[7]

Reports of calcium coordination complexes with DMF[8] and *N*-methylacetamide[9, 10] ligands provide support for the suitability of amide containing ligands for the development of calcium chloride complexes. Interestingly, the DMF-$CaCl_2$ complex contains two ligand molecules and two water molecules in the metal coordination sphere, therein highlighting the propensity of the metal salt for binding water despite the inert atmosphere used for reaction.[8] A CSD search confirmed the inclusion of very few reported cyclic lactam-calcium chloride complexes. Of most relevance to this work is the calcium chloride complex with ε-caprolactam, reported by Khrustalev in 2003.[11] The structure of the complex contains octahedral calcium with chloride ligands bound to the metal centre, in addition to two bound water molecules, as shown in Figure 6.1. The polarity of the amide moiety within caprolactam

is illustrated by the short carbonyl-calcium bond distances (2.25 Å) in contrast to the calcium-oxygen distances to the aqua ligand (2.34 Å).

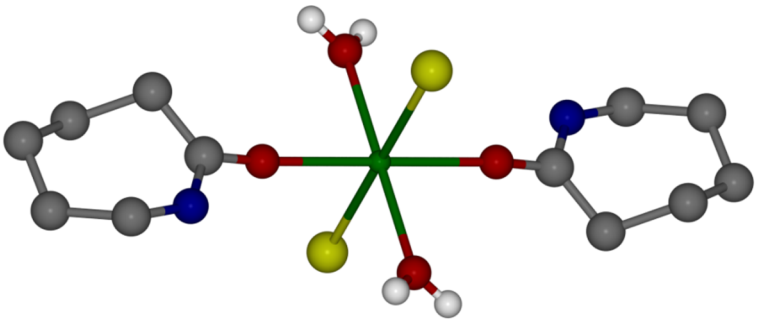

Figure 6.1: The molecular structure of dichloro-diaqua-bis(*ε*-caprolactam)-calcium(II) (CH and NH hydrogen atoms omitted for clarity).[11]

As part of work aimed at exploring the generation of slowly hydrating forms of calcium chloride we now report the synthesis, structures and hydration behaviour of a series of calcium chloride coordination complexes of 1-{2-[2-(2-oxo-pyrrolidin-1-yl)-ethoxy]-ethyl}-pyrrolidin-2-one (**5.1**) and 1-(2-hydroxyethyl)-2-pyrrolidone (**2.12**).[12]

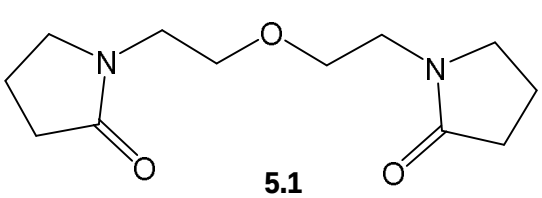

5.1

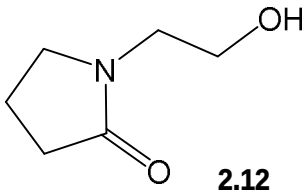

2.12

6.2 Results and discussion

Reaction of ligand **5.1** with anhydrous $CaCl_2$ in a 1:1 ratio, in ethanol, results in the crystallization of two coordination complexes following solvent evaporation at room temperature over 2-4 days. The X-ray crystal structures of both complexes were determined, showing them to be an aqua complex with a 1D coordination polymer structure $\{[Ca_2(\mathbf{5.1})_2(H_2O)_9]Cl_4]\}_n$ (**6.1**) and a related water containing coordination polymer incorporating additional lattice water of crystallization $\{[Ca(\mu\text{-}\mathbf{5.1})(H_2O)_5]Cl_2{\cdot}H_2O\}_n$ (**6.2**). Both complexes form under similar conditions from a stoichiometric solution but were not found to form concomitantly. In repeated experiments, crystals of complex **6.2** were isolated more frequently than complex **6.1**. Akin to calcium chloride itself, the coordination complexes were found to be hygroscopic, with absorption of atmospheric moisture resulting in the transformation to an oily residue. To prolong the crystallinity, samples were stored under a nitrogen atmosphere.

The asymmetric unit of complex **6.1** contains two ligand molecules bound to two calcium centres by the carbonyl oxygen atoms (Figure 6.2). Interestingly, the ether oxygen atoms of both ligands do not coordinate to the Ca^{2+} centres but instead the metal coordination sphere is completed by bound water molecules, illustrating the hygroscopicity of these species. This is in contrast to the previously reported alkali metal complexes (Chapter 5) in which the ether oxygen atoms do coordinate to the metal centres.[3] The pentagonal bipyramidal Ca(1) ion binds two oxygen atoms from ligand molecules in addition to five bound water molecules, giving an overall coordination number of seven. The geometry at the metal centre is slightly distorted in the axial direction with a O(1)-Ca(1)-O(6) angle of 171.98(7)°. In contrast, Ca(2) adopts a distorted octahedral geometry, binding two ligand oxygen atoms in addition to four water molecules. The carbonyl oxygen-metal bond distances are shorter for Ca(2) than Ca(1) at 2.2977(17) Å and 2.2962(18) Å compared to 2.3129(18) Å and 2.3134(18) Å for the seven coordinate ion. The carbonyl oxygen-calcium bond distances are considerably shorter than the calcium-aqua bond distances as a result of the high polarity of the amide moiety. The chloride anions are held within the structure through hydrogen bonding interactions with coordinated water molecules, with an average Cl···O distance of 3.18 Å.

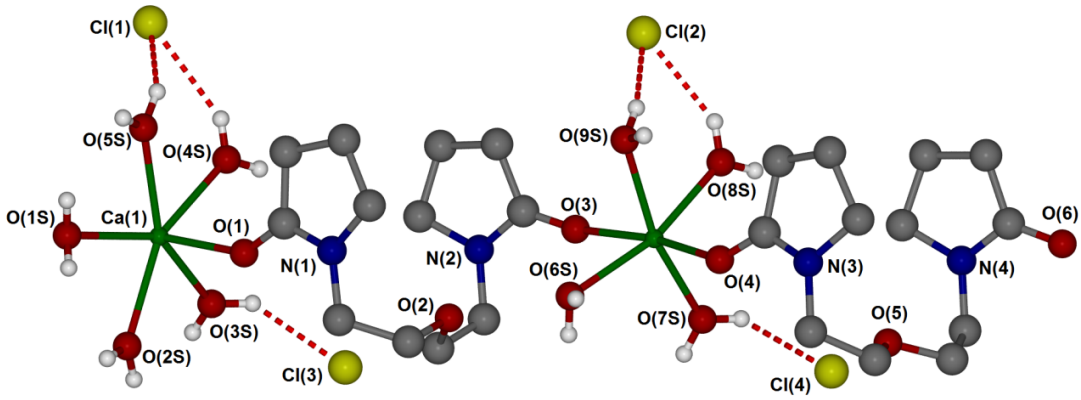

Figure 6.2: X-ray molecular structure of $\{[Ca_2(\mathbf{5.1})_2(H_2O)_9]Cl_4\}_n$ (**6.1**). CH hydrogen atoms omitted for clarity. Selected bond lengths (Å): Ca(1)-O(1) 2.3133(17), Ca(1)-O(1S) 2.4305(18), Ca(1)-O(2s) 2.4305(18), Ca(1)-O(3s) 2.4141(16), Ca(1)-O(4s) 2.4412(17), Ca(1)-O(5s) 2.44799(16), Ca(1)-O(6) 2.3134(18), Ca(2)-O(3) 2.2970(17), Ca(2)-O(4) 2.2962(17), Ca(2)-O(6s) 2.3303(17), Ca(2)-O(7s) 2.3458(17), Ca(2)-O(8s) 2.3595(17), Ca(2)-O(9s) 2.3615(17).

Hydrated complex **6.2** comprises a one dimensional coordination polymeric chain of calcium ions linked by bridging ligand **5.1** bound to the metal centres by the carbonyl oxygen atoms. A section of the polymer chain is shown in Figure 6.3. The metal-carbonyl bond distances are longer than those in complex **6.1** (Ca(1)-O(1) 2.3530(14) Å and Ca(1)-O(3)

2.3222(15) Å), and are considerably shorter than the calcium-aqua distances. The metal centres adopts a seven coordinate distorted pentagonal bipyramidal geometry, binding five water molecules in addition to the carbonyl oxygen atoms from two different lactam ligands. A further non-coordinated water molecule is held in the lattice *via* hydrogen bonding interactions to aqua ligands O(5s), with an O···O distance of 2.741(2) Å.

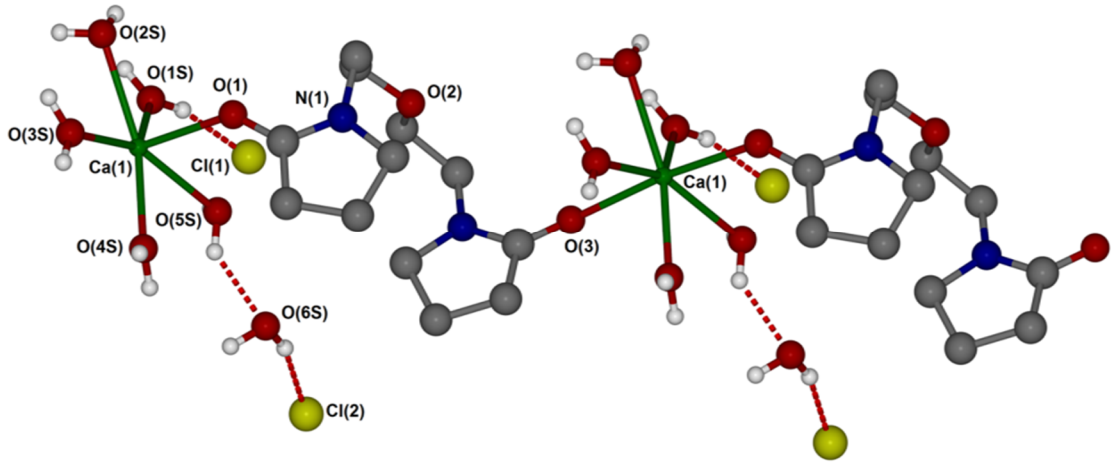

Figure 6.3: X-ray structure of {[Ca(μ-**5.1**)$(H_2O)_5$]$Cl_2 \cdot H_2O$}$_n$ (**6.2**). CH hydrogen atoms omitted for clarity. Selected bond distances (Å): Ca(1)-O(1) 2.3530(14), Ca(1)-O(3) 2.3222(15), Ca(1)-O(5s) 2.4237(15), Ca(1)-O(1s) 2.3888(15), Ca(1)-O(2s) 2.4444(15), Ca(1)-O(3s) 2.4111(16) and Ca(1)-O(4s) 2.4148(15).

The X-ray crystal structures show that ligand-metal coordination is achievable, in addition to confirming that the calcium centre retains the ability to bind water despite the presence of the ligand species. Such structural determinations may provide insight into the product post-application and hence post-hydration within the cement mixture. In the knowledge that water binding is possible, we therefore sought to prepare an anhydrous complex of $CaCl_2$ and ligand **5.1** with the potential to hydrate exothermically in a controlled fashion in order to produce products such as **6.1** and **6.2**.

Thermogravimetric analysis (TGA) confirms that dehydration of complex **6.1** occurs upon heating between 68 – 190 ^{o}C, as shown in Figure 6.4. There is an initial weight loss of 1.4% upon heating to 68 ^{o}C thought to arise from the loss of surface water, present as a result of the hygroscopicity of the complex. The main mass loss of 19 % occurs upon heating between 68 – 190 ^{o}C, corresponding to the loss of all nine water molecules in a two-stage process (calculated 18.75 %). Stage one (68 – 130 ^{o}C) corresponds to the loss of 1.5 water molecules, while stage two (130 – 190 ^{o}C) results in loss of the remaining 7.5 water molecules. The reasonably high temperature required for removal of the 9 water molecules

confirms complexation to the metal centre; surface and lattice water would be removed more readily at lower temperatures. Subsequent mass loss beyond 225 °C is assigned to decomposition. Hence there is a temperature window between 190 and 225 °C in which the complex is stable in a dehydrated state. Careful heating of the sample to within this temperature range may enable isolation of the desired anhydrous complex (*vide infra*).

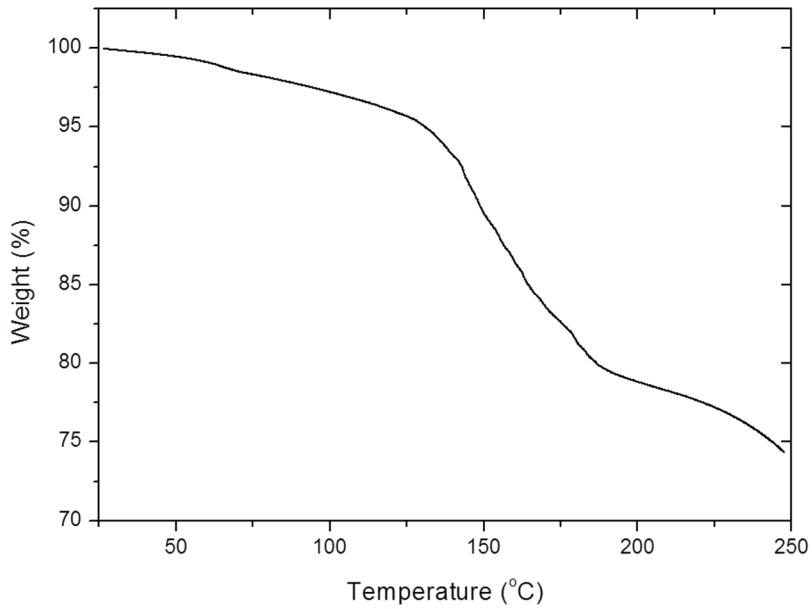

Figure 6.4: Thermogravimetric trace for {[Ca_2(**5.1**)$_2$(H_2O)$_9$]Cl_4}$_n$ (**6.1**). 19 % weight loss when heating 68 – 190 °C, attributed to the nine bound water molecules.

Similarly, TGA of complex **6.2** shows a three-step mass loss profile (Figure 6.5). The initial mass loss of 3.94 % upon heating to 111 °C is thought to arise from the loss of the unbound lattice water molecule (calculated 3.92 %). This is followed by a further mass loss of 19.18 % upon heating to 197 °C, attributed to the removal of the five metal bound water molecules (calculated 19.61 %). The mass loss upon further heating is thought to be a consequence of complex decomposition. The high temperatures required for dehydration shows the strong interactions between the water molecules and calcium ion. In both complexes **6.1** and **6.2** heating to approximately 200 °C is associated with complete dehydration and may enable isolation of the desired anhydrous calcium coordination complex.

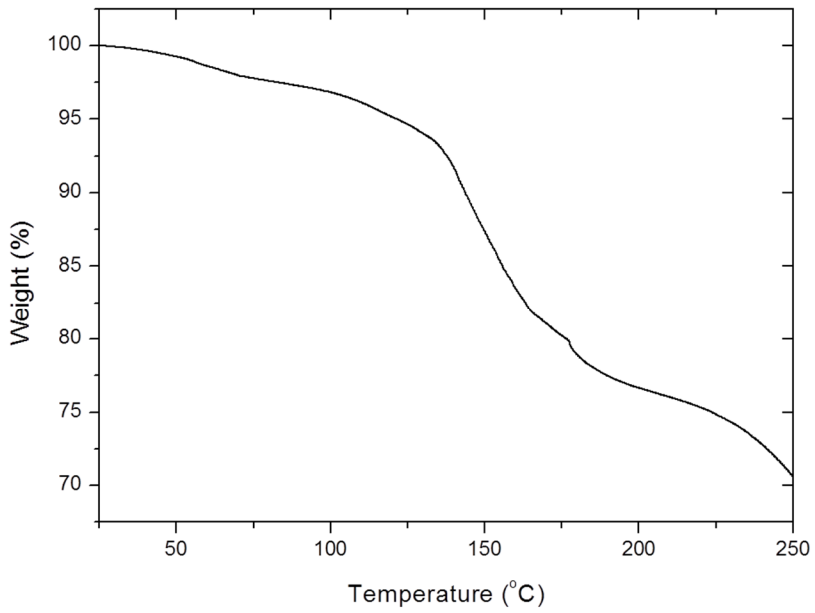

Figure 6.5: Thermogravimetric trace for {[Ca(μ-**5.1**)$(H_2O)_5$]Cl_2·H_2O}$_n$ (**6.2**).

While the isolation of single crystals has been beneficial for analysis, the product yields in this way are reasonably low (40 – 70%) which may limit the industrial viability. Solvent-free grinding of the two reactants (ligand **5.1** and $CaCl_2$) offers many advantages to conventional solution-phase processes for the synthesis of coordination complexes, most notably potentially higher yields, increased reaction efficiency and the elimination of organic solvent waste. In addition, the solventless approach eliminates the presence of excess solvent water and may enable the direct synthesis of an anhydrous complex. Mechanically mixing a stoichiometric ratio of ligand **5.1** and anhydrous $CaCl_2$, in a pestle and mortar for 5 minutes, results in the immediate formation of a tacky material, which upon oven-drying at 100 ^oC forms a cream crystalline powder.

The solid-state IR spectrum of the mechanically prepared powder confirms complexation of ligand **5.1**, identified by a shift in the C=O stretching mode to 1648 cm^{-1} in comparison to 1674 cm^{-1} in the "free" ligand. This wavenumber shift is similar to those observed in complexes **6.1** and **6.2**. In addition, the IR spectrum for the powder also contains a broad O-H stretch (3000 – 3500 cm^{-1}) confirming the hydrated state of the complex; this is unsurprising when considering the nature of **6.1** and **6.2**, however at this stage the precise composition of the powder is unknown.

A sample of the powder was dried in the oven at 70 ^oC for 3 hours and then submitted for thermal analysis. The TGA thermogram, shown in Figure 6.6, confirms a weight

loss of 12.87 % upon heating from room temperature to 170 °C, with the TGA-MS confirming loss of water. It is postulated that the lower temperature required for complete dehydration of this sample is resultant of the fine powdered nature of the material enabling more efficient heat transfer, as opposed to the block crystals examined previously. In addition, the lower water content in this sample is a consequence of partial drying. Confirmation of dehydration of the mechanochemically prepared sample indicates that it may be possible to isolate the anhydrous complex in quantitative yield.

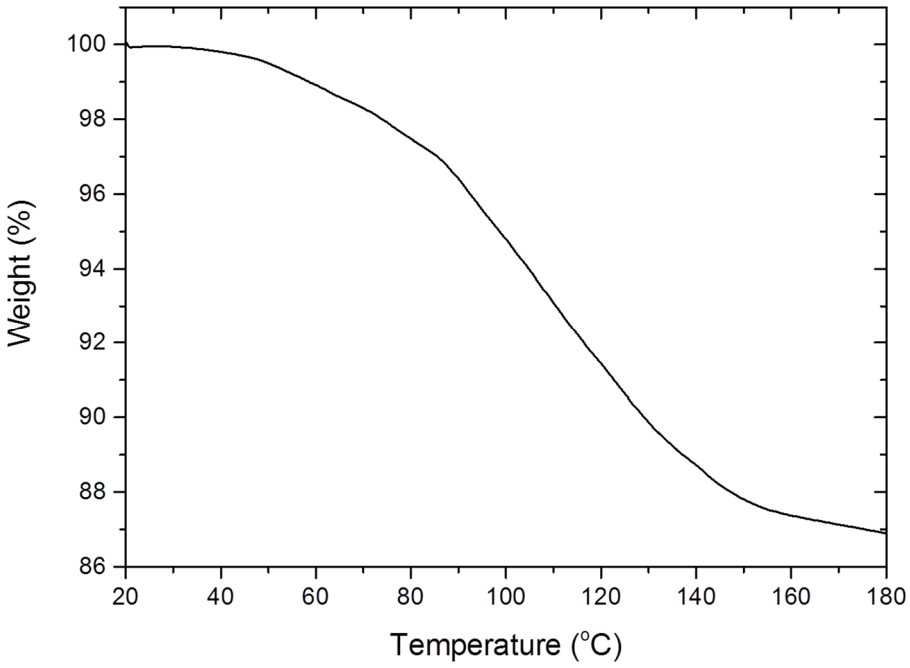

Figure 6.6: Thermogravimetric trace for the mechanochemically prepared product of reaction of $CaCl_2$ with ligand **5.1**. Product was previously dried at 70 °C for 3 hours.

Despite the thermogram indicating full sample dehydration upon heating to 170 °C, when visually monitoring the sample and following the IR spectra during the heating process it is believed that sample degradation occurs when heating above 130 °C, observed as a transition to an orange oily residue. Therefore, in an attempt to isolate the dehydrated species without consequential degradation, the material was heated at 110 °C for 36 hours, in the hope that the prolonged heating period would promote full removal of water while retaining the complex integrity.

IR spectroscopy was used to obtain a snapshot of the hydration state of the mechanically prepared sample prior to, and during, the drying process. Figure 6.7a shows the IR spectrum of the material immediately following synthesis; sample hydration is evident in

the occurrence of an O-H stretching band occurring between 3200 and 3400 cm^{-1}. Figure 6.7b shows the IR spectrum following heating of the sample in the oven at 110 ^{o}C for 36 hours; disappearance of the broad O-H band upon heating confirms dehydration and indicates formation of the desired anhydrous complex. During the heating process the powdered material becomes a viscous oil, which transforms back to a solid upon cooling to room temperature. The material rehydrates over a period of an hour when exposed to the atmosphere, observed by the reappearance of the O-H band in the IR spectrum.

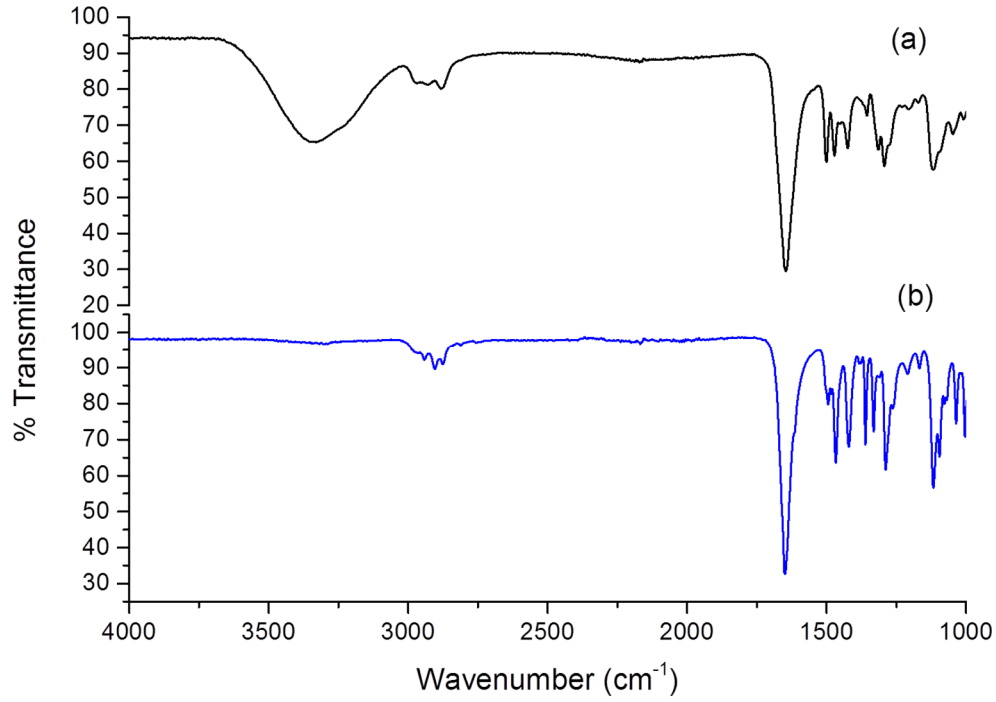

Figure 6.7: IR spectra for the mechanochemically prepared sample (a) immediately following synthesis and (b) after heating at 110 ^{o}C for 36 hours.

The composition of the mechanochemically prepared powder was explored using PXRD, as shown in Figure 6.8 along with the PXRD patterns for complexes **6.1** and **6.2** (calculated from the single crystal diffraction data)[13] and pure anhydrous $CaCl_2$. Figure 6.8a shows the experimental pattern following heating the mechanochemically prepared sample in an oven at 110 ^{o}C for 36 hours, while Figure 6.8b shows the same sample after standing at room temperature in a sealed vial for two weeks. The data indicate that after drying for 36 hours the resulting mechanochemically prepared sample, as shown in (a), is a mixture of complexes **6.1** and **6.2** ((c) and (d) respectively). It is worth noting that the PXRD analysis was performed on the sample once it had cooled (in a sealed vial), and it is therefore postulated that the rehydration process began during the time delay in heating the sample and recording the powder pattern; this highlights the instability of the complex to hydration. The

powder sample then transforms to pure complex **6.2** (the hydrate) upon standing for two weeks, as seen in (b); the additional water is thought to originate from exposure to the atmosphere. Transformation to the hydrated coordination complex is in agreement with the solvent evaporation experiments whereby complex **6.2** formed more frequently than **6.1**. Therefore, while the anhydrous complex can be identified using IR spectroscopy it has not been possible to obtain its PXRD pattern; further work involving *in situ* PXRD analysis while heating the sample may enable calculation of the anhydrous species, however this is outside of the scope of this work.

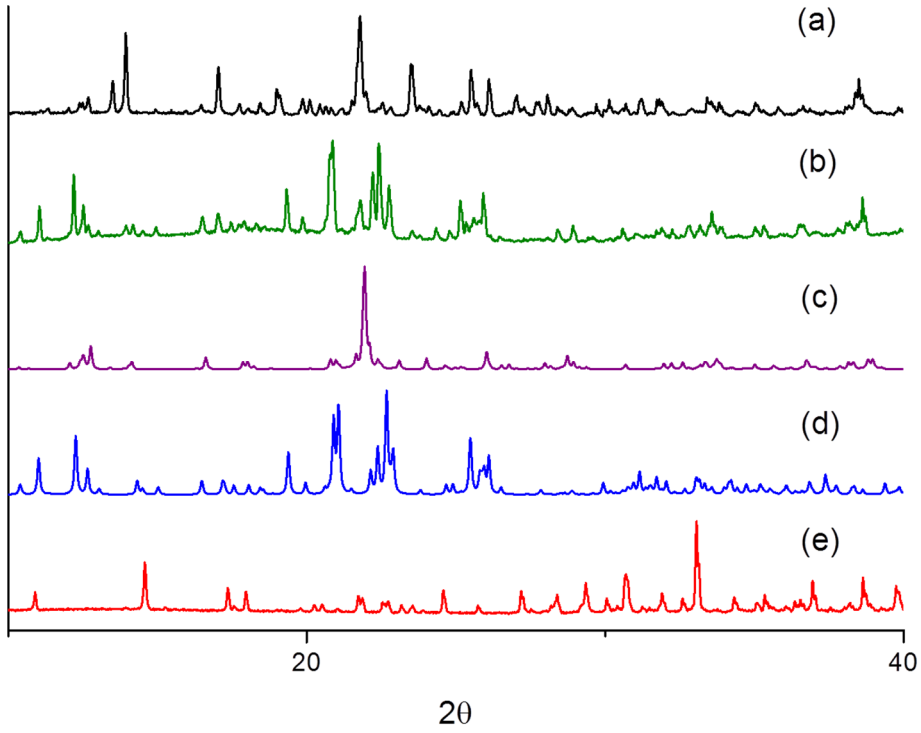

Figure 6.8: PXRD patterns for (a) mechanochemically prepared sample after heating for 36 hours at 110 °C; (b) mechanochemically prepared sample after being held at room temperature for two weeks; (c) calculated pattern for **6.1**; (d) calculated pattern for **6.2**; and (e) pure anhydrous $CaCl_2$

Figure 6.9 shows the rehydration of the dried mechanochemically prepared sample and anhydrous $CaCl_2$, highlighting the hygroscopicity of these species. Both samples were held in the oven at 110 °C for 36 hours prior to imaging. Images were taken over a 90 minute period following removal from the oven and exposure to ambient lab conditions (22 °C). Figure 6.9(a)-(d) shows hydration of the ligand **5.1** complex, with some transition from powder to liquid over the 90 minute study. For comparison, Figure 6.9(e)-(h) shows hydration of calcium chloride over time, with an appreciable transition from powder to liquid observed.

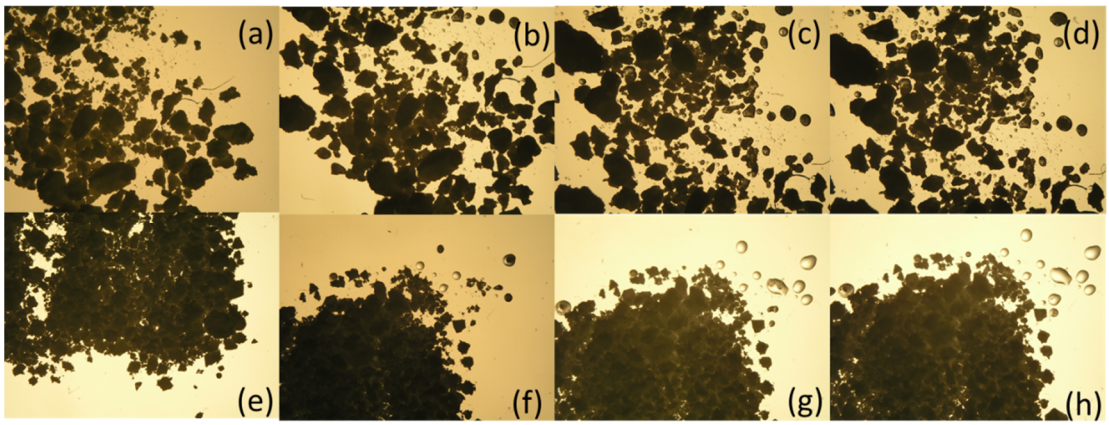

Figure 6.9 Time-elapsed microscopy images showing mechanochemically prepared $CaCl_2$ complex of **5.1** (a-d) and dried $CaCl_2$ (e-h) following removal from the oven (110 ^oC) after (a)(e) 0 minutes; (b)(f) 30 minutes; (c)(g) 60 minutes and (d)(h) 90 minutes.

Re-hydration of the dried mechanochemically prepared sample was monitored over a period of 4 days exposure to ambient lab conditions, during which time the mass of the powder increased to 137.5% of the original. In contrast, the mass of $CaCl_2$ increased to 287.5% of the original mass, corresponding to eleven water molecules per $CaCl_2$. However, if one assumes that metal-bound ligand **5.1** is non-hygroscopic and only considers the active content of calcium chloride (approximately 30%), the re-hydration behaviour is comparable in the coordination complex and free $CaCl_2$. Therefore, in this instance the synthesised coordination complex offers no improvement in performance than the pure metal salt.

Analogous metal-coordination with ligand **2.12** was investigated in the hope that the reduced ligand size may enable greater access to the metal centre and hence allow for improved water uptake in comparison to the bulky ligand **5.1** complexes. Reaction of **2.12** and $CaCl_2$, in a 1:1 ratio in ethanol, results in the crystallization of a 1D coordination polymer, namely $\{CaCl_2(\mathbf{2.12})_2\}_n$ (**6.3**), and an ethanol solvate $\{CaCl_2(\mathbf{2.12})(EtOH)\}_n$ (**6.4**). Complex **6.3** comprises a one–dimensional coordination polymeric chain of calcium ions linked by bridging ligand **2.12** bound to the metal centres *via* both the amide carbonyl and alcohol functionalities, Figure 6.10. Unlike complexes **6.1** and **6.2**, the chloride anions are bound to the metal centres and hydration does not occur. The chloride anions undergo hydrogen bonding interactions with the alcohol groups on the ligands, with an O(1)···Cl(1) distance of 3.1198(9) Å (DĤA 167(1) ^{o}). The metal centre is held in a distorted octahedral geometry, with a Cl(1)-Ca(1)-Cl(1) angle of 101.94(2)^o. In contrast, the angle subtended at the metal centre between the alcohol groups of two ligand molecules (O(1)-Ca(1)-O(1)) is relatively low, 81.53(4) ^{o}. As expected given the polarity of the lactam group, the carbonyl-calcium bond distance is considerably

shorter than the alcohol-calcium bond distance, with distances of 2.2832(9) Å and 2.3957(9) Å, respectively. Ligand **2.12** is considerably shorter than bis(lactam) ligand **5.1**, resulting in a significant reduction in the calcium-calcium distance (5.93 Å in **6.3** and 10.56 Å in **6.2**).

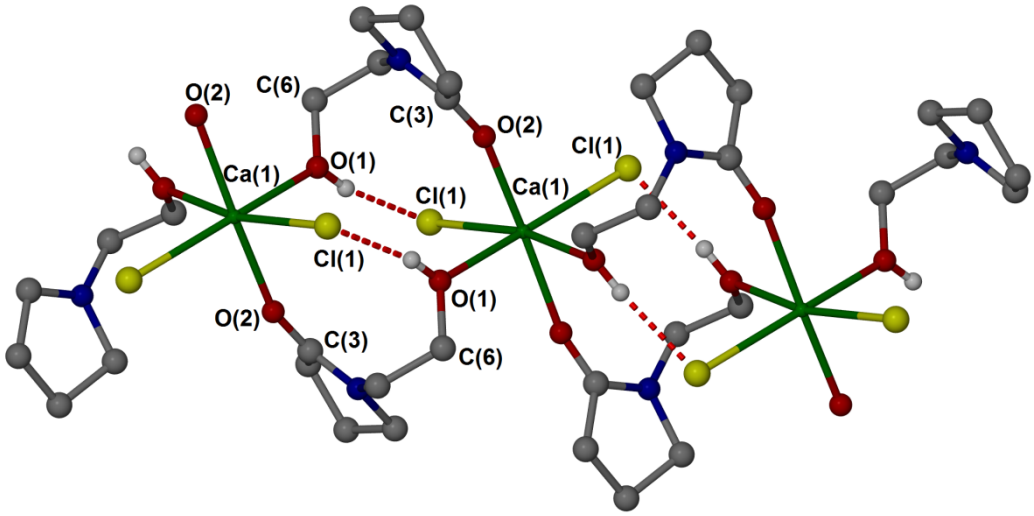

Figure 6.10: X-ray structure of $\{CaCl_2(\mathbf{2.12})_2\}_n$ (**6.3**). Selected hydrogen atoms have been omitted for clarity. Selected bond distances (Å): Ca(1)-O(1) 2.3957(9) and Ca(1)-O(2) 2.2832(9).

While it was not possible to characterise a hydrated calcium chloride complex of ligand **2.12** by X-ray crystallography, the determination of the ethanol solvate (**6.4**) is encouraging as this shows that the calcium centre retains the ability to bind solvent and should therein successfully coordinate water. The asymmetric unit of complex **6.4** contains two distinct calcium environments with chloride ligands bridging the metal centres, as seen in Figure 6.11. One calcium centre (Ca(1)) possesses three bridging chloride atoms in addition to a terminal chloride (Cl(1)). The terminal chloride ligand hydrogen bonds to the ethanol molecule (Cl(1)···O(5) distance 3.053(3) Å) in addition to the hydroxyl moiety of **2.12** (Cl(1)···O(2) distance 3.099(3) Å).

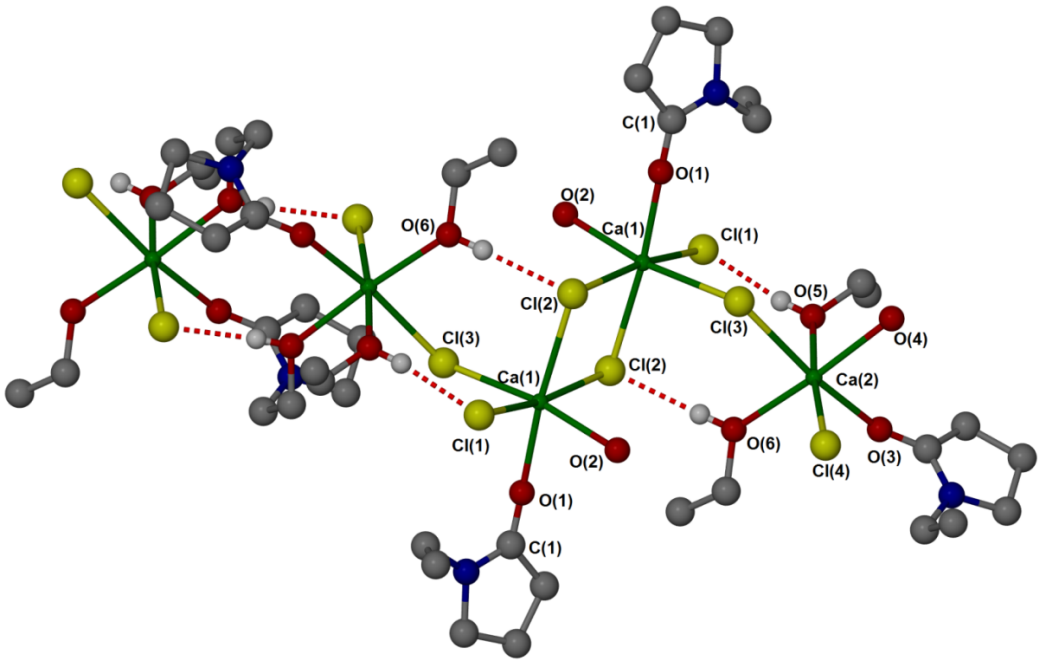

Figure 6.11: X-ray structure of $\{CaCl_2$(**2.12**)(EtOH)$\}_n$ (**6.4**). Selected hydrogen atoms have been omitted for clarity. Selected bond distances (Å): Ca(1)-O(1) 2.274(2), Ca(1)-O(2) 2.352(2), Ca(2)-O(3) 2.293(3), Ca(2)-O(4) 2.351(3), Ca(2)-O(5) 2.362(3) and Ca(2)-O(6) 2.381(2).

The carbonyl oxygen to metal bond distances are significantly shorter than the hydroxyl oxygen-calcium distances, with Ca(1)-O(1) 2.273(3) Å and Ca(2)-O(3) 2.293(3) Å, in contrast to Ca(1)-O(2) 2.350(3) Å and Ca(2)-O(4) 2.351(3) Å. The second calcium centre (Ca(2)) binds to two different molecules of ligand **2.12**, one *via* the hydroxyl moiety (O(4)) and the other by the carbonyl group (O(3)), in addition to binding two ethanol molecules. The TGA thermogram indicates that loss of the bound ethanol does not occur in a single process, as seen in Figure 6.12 where a steady mass loss is observed during the heating cycle from room temperature to 230 ^{o}C.

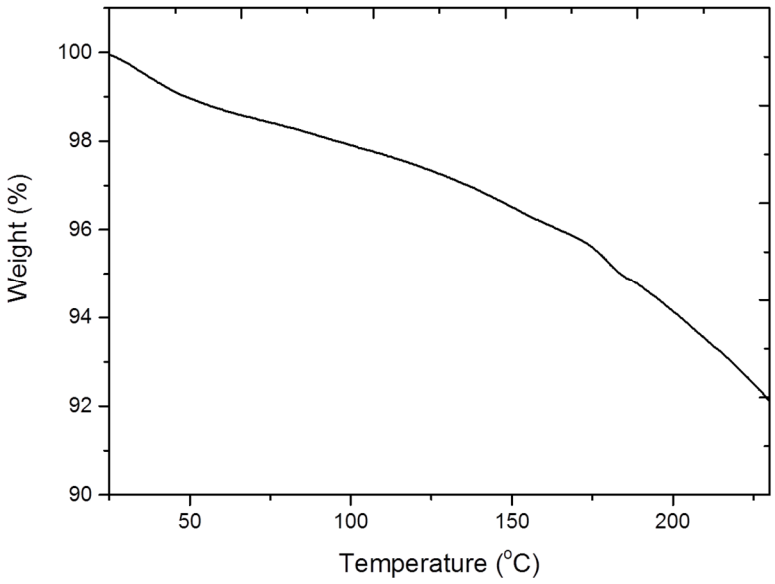

Figure 6.12: Thermogravimetric trace for the ethanol solvate $\{CaCl_2(\mathbf{2.12})(EtOH)\}_n$ (**6.4**).

Solvent-free grinding of a stoichiometric mixture of ligand **2.12** and $CaCl_2$ results in the formation of a cream powder. The experimental PXRD pattern could not be determined in this instance due to the transition to a liquid occurring too rapidly to allow for analysis. The solid-state IR spectrum for the mechanochemically prepared sample is in agreement with that for complex **6.3**, as seen in Figure 6.13. The absence of a broad O-H stretch in the spectra for complex **6.3** and the mechanochemical powder is consistent with the anhydrous nature of these complexes. The observed sharp band between 3200 – 3400 cm^{-1} is assigned to the O-H stretch of the alcohol functionality of the ligand. The O-H region is more complicated for complex **6.4** due to showing the O-H stretching mode of the ligand alcohol moiety in addition to the ethanol solvent.

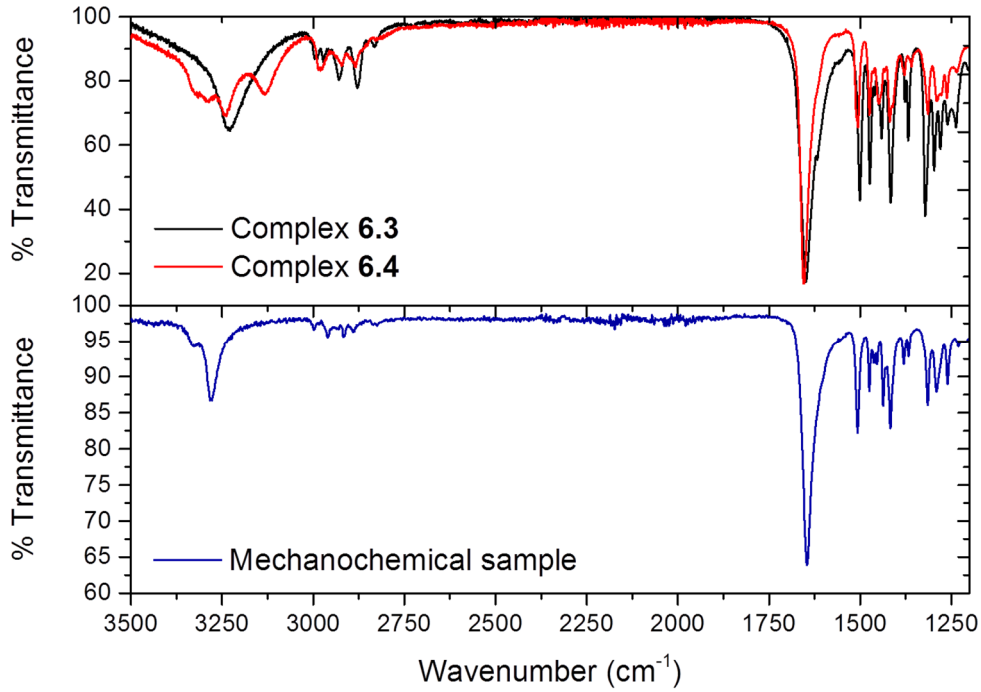

Figure 6.13: IR spectra for complexes **6.3** and **6.4** in comparison to the mechanochemically prepared sample.

A sample of the mechanochemically prepared powder was dried in the oven at 110 °C for 36 hours, and the IR spectrum quickly recorded on the hot material, as seen in Figure 6.14 (labelled anhydrous). The sample was then removed from the oven and allowed to return to room temperature in an open vial. IR spectra were recorded at intervals following removal from the oven, as seen in Figure 6.14, following a 10, 30 and 60 minute delay. A broad O-H stretch (3200 – 3600 cm^{-1}) appears and increases in intensity during this time period, indicating hydration of the material.

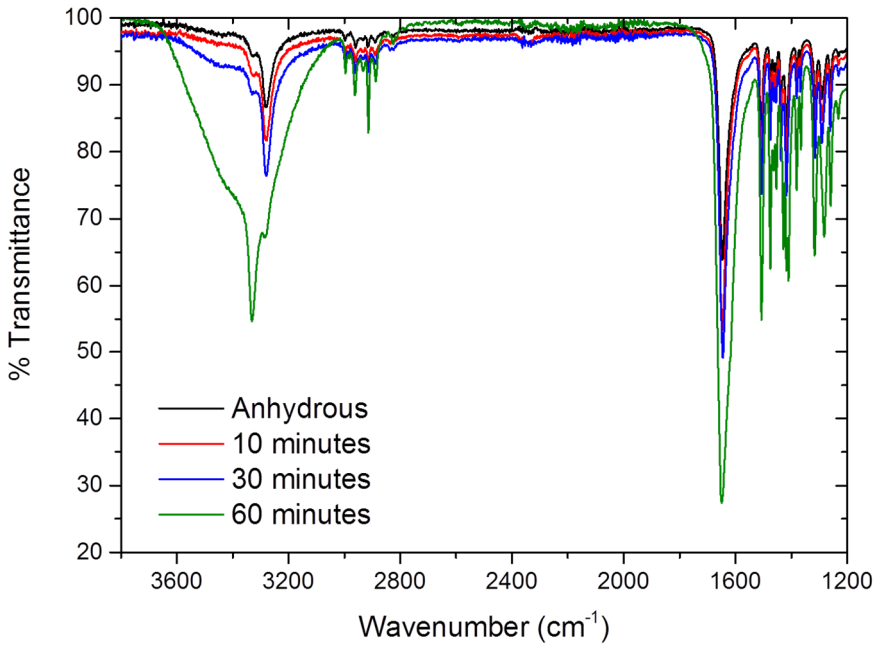

Figure 6.14: Overlaid IR spectra for the anhydrous mechanochemically prepared complex of $CaCl_2$ and ligand **2.12** following removal from the oven (110 ^{o}C).

Sample hydration is observable as a transition from crystalline material to a liquid as shown in the time elapsed images in Figure 6.15, with (a) showing the sample taken straight from the oven as a powder, to the mostly liquid sample (h) taken 2 hours post-removal from the oven.

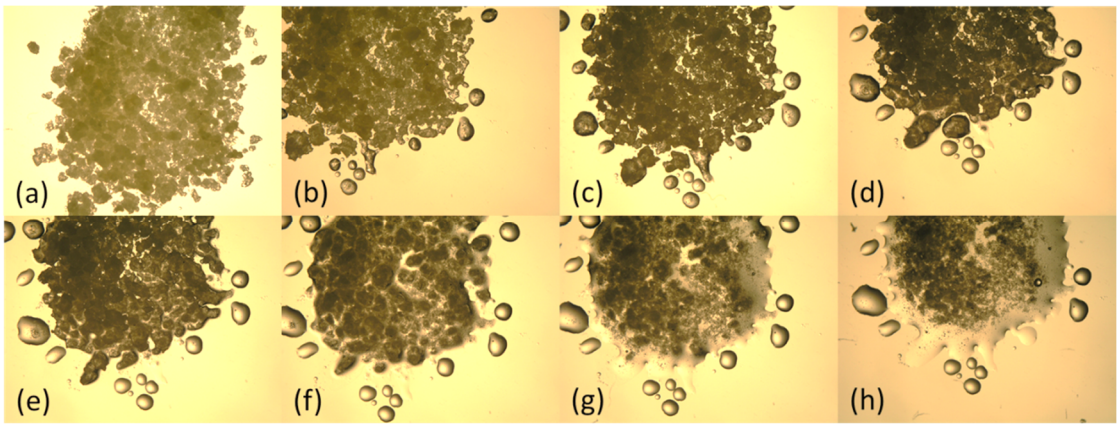

Figure 6.15: Time elapsed photographs following removal of the mechanochemically prepared complex of $CaCl_2$ and ligand **2.12** from the oven at the following times (minutes): (a) 0; (b) 10; (c) 20; (d) 30; (e) 45; (f) 60; (g) 90 and (h) 120.

Unfortunately the instability of the calcium chloride-ligand **2.12** complexes suggest that they are not viable for industrial application; the transition from solid to liquid state

occurs too readily, even in comparison to $CaCl_2$, and would cause significant handling issues within application.

6.3 Conclusions

The high basicity of the pyrrolidone carbonyl moiety enables effective calcium chelation for both ligands **5.1** and **2.12**. X-ray crystal structures of metal complexes with the bis(pyrrolidone) ether ligand are hydrated, whilst those containing ligand **2.12** are anhydrous. The ease of synthesis of the complexes has been proven through simple mechanical grinding of reactants, enabling product preparation in a quantitative yield. Re-hydration studies highlighted that non-complexed anhydrous $CaCl_2$ outperforms ligand **5.1** complexes in terms of hydration based on active content. Unfortunately, the mono(pyrrolidone) complexes proved too unstable to hydration, preventing ease of handling and therein limiting industrial viability.

While the novel complexes reported in this chapter do not meet the industrial demands as they show no improvement on anhydrous calcium chloride, they add further support to the high basicity of the pyrrolidone carbonyl moiety in the formation of metal-carbonyl bonds.

6.4 Experimental

6.4.1 General

1-{2-[2-(2-oxo-pyrrolidin-1-yl)-ethoxy]-ethyl}-pyrrolidin-2-one (**5.1**) and 1-(2-hydroxyethyl)-2-pyrrolidone (**2.12**) were supplied by Ashland Inc. and used without further purification. All other solvents and reagents were obtained from standard commercial sources and used without further purification. IR spectra were measured with a Perkin-Elmer 100 FT-IR spectrometer, using an ATR attachment. Thermogravimetric analysis was conducted using a Perkin Elmer Pyris 1 TGA with purge gas specified at 40 mls per minute. TGA temperature was increased at 10 ^{o}C per minute up to the temperature specified.

Crystals suitable for single crystal X-ray diffraction structure determination were selected, soaked in perfluoropolyether oil and mounted on a preformed tip. Single crystal X-ray data were collected at 120 K on an Agilent Gemini S-Ultra diffractometer equipped with the Cryostream (Oxford Cryosystems) open-flow nitrogen cryostats, using graphite monochromated MoKα-radiation (λ = 0.71073 Å). All structures were solved using direct

methods and refined by full-matrix least squares on F^2 for all data using SHELXL[14] and OLEX2[15]. All non-hydrogen atoms were refined with anisotropic displacement parameters. CH hydrogen atoms were placed in calculated positions, assigned an isotropic displacement factor that is a multiple of the parent carbon atom and allowed to ride. H-atoms attached to oxygen were located on the difference map when possible, or placed in calculated positions. Elemental analysis was performed using an Exeter Analytical inc. CE-400 Elemental Analyser. Powder diffraction was performed on glass slides using a Bruker AXS D8 Advance diffractometer, with a Lynxeye Soller PSD Detector, using CuKα radiation at a wavelength of 1.5406 Å (with assistance from Gary Oswald, Durham).

6.4.2 Synthesis of coordination complexes

{[Ca_2(**5.1**)$_2$(H_2O)$_9$]Cl_4}$_n$ (**6.1**)

1-{2-[2-(2-oxo-pyrrolidin-1-yl)-ethoxy]-ethyl}-pyrrolidin-2-one (**5.1**) (0.110 g, 0.459 mmol) was added to anhydrous calcium chloride (0.0461 g, 0.415 mmol) dissolved in ethanol (2 mL). The resulting mixture was sonicated for 1 minute and allowed to stand partially open to the atmosphere (crystals visible after 4 days). Colourless crystals formed upon slow evaporation of the solvent at room temperature (Yield = 0.143 g, 0.165 mmol, 40 %).

Analysis calc. for $C_{24}H_{58}N_4O_{15}Ca_2Cl_4$: C 33.33, H 6.77, N 6.48 %, found: C 33.45, H 6.81, N 6.52 %; IR (ν/cm^{-1}): 1641 (C=O) and 1126 (C-O). Crystal data for $C_{24}H_{58}N_4O_{15}Ca_2Cl_4$: M = 864.70, 0.5267 x 0.2548 x 0.1614 mm^3, triclinic, space group $P\bar{1}$ (No. 2), a = 8.9178(3) Å, b = 16.3074(7) Å, c = 16.3501(6) Å, α = 116.158(4)^o, β = 97.927(3)^o, γ = 99.693(4)^o, V = 2042.36(14) Å^3, Z = 2, D_c = 1.406 g/cm^3, F_{000} = 916, Mo Kα radiation, λ = 0.7107 Å, T = 120K, 2ϑmax = 55.0 ^{o}, 27871 reflections collected, 9386 unique (R_{int} = 0.0455). Final GooF = 1.035, R_1 = 0.0434, wR_2 = 0.1026, R indices based on 7195 reflections with $I > 2\sigma(I)$ (refinement on F^2), 451 parameters, 0 restraints. Lp and absorption corrections applied, μ = 0.604 mm^{-1}.

{[Ca(**5.1**)(H_2O)$_5$]Cl_2·H_2O}$_n$ (**6.2**)

1-{2-[2-(2-oxo-pyrrolidin-1-yl)-ethoxy]-ethyl}-pyrrolidin-2-one (**5.1**) (0.111 g, 0.46 mmol) was added to anhydrous calcium chloride (0.046 g, 0.414 mmol) dissolved in ethanol (2mL). The resulting mixture was sonicated for 1 minute. The vial was left loosely capped, and colourless crystals formed following slow evaporation of solvent at room temperature (visible after 2 days). (Yield = 0.139 g, 0.3015 mmol, 73 %). The crystals proved to absorb atmospheric moisture over time and elemental analysis on a fully dry material could not be obtained.

Crystals were held *in vacuo* for 6 h at 100 °C resulting in a di-hydrated complex. Analysis calc. for $C_{12}H_{20}N_2O_3CaCl_2{\cdot}6H_2O$: C 31.38, H 7.02, N 6.10%, re-calc for $C_{12}H_{20}N_2O_3CaCl_2{\cdot}2H_2O$: C 37.21, H 6.25, N 7.23%, found: C 37.74, H 6.37, N 7.01%; IR (υ/cm^{-1}) 1641 (C=O) and 1116 (C-O). Crystal data for $C_{12}H_{32}N_2O_9CaCl_2$: M = 459.38, colourless block, 0.4521 x 0.3035 x 0.1295 mm^3, triclinic, space group $P\bar{1}$ (No. 2), a = 8.8007(5) Å, b = 8.9311(5) Å, c = 14.7500(8) Å, α = 99.325(5)°, β = 95.103(4)°, γ = 104.163(5)°, V = 1099.18(11) Å^3, Z = 2, D_c = 1.388 g/cm^3, F_{000} = 488, Mo Kα radiation, λ = 0.7107 Å, T = 120K, $2\theta_{max}$ = 54.0°, 9198 reflections collected, 4793 unique (R_{int} = 0.0294). Final *GooF* = 1.039, *R1* = 0.0376, *wR2* = 0.0907, *R* indices based on 4128 reflections with I >2σ(I) (refinement on F^2), 243 parameters, 0 restraints. Lp and absorption corrections applied, μ = 0.571 mm^{-1}.

{$CaCl_2$(**2.12**)$_2$}$_n$ (**6.3**)

Anhydrous calcium chloride (0.086 g, 0.77 mmol) was dissolved in absolute ethanol and hydroxyethylpyrrolidone (**2.12**) (0.10 g, 0.77 mmol) was added. The reaction mixture was sonicated for 1 minute. The sample vial lid was left loosened and placed within an evacuated vacuum desiccator. Colourless crystals of the coordination complex were visible after 2 days (Yield = 0.20 g, 0.553 mmol, 72 %). The crystals proved to absorb atmospheric moisture over time and elemental analysis on a fully dry material could not be obtained. Analysis calc. for $C_{12}H_{22}N_2O_4CaCl_2$: C 39.03, H 6.00, N 7.59 %, re-calc for $C_{12}H_{26}N_2O_6CaCl_2$: C 35.56, H 6.47, N 6.91%, found C 35.50, H 6.75, N 6.86%; IR (υ/cm^{-1}) 1649 (C=O). Crystal data for $C_{12}H_{22}N_2O_4CaCl_2$: M = 369.30 g mol^{-1}, colourless irregular, 0.4869 x 0.3517 x 0.3486 mm^3, monoclinic, space group C_2/c (No. 15), a =12.9663(3) Å, b = 11.8541(3) Å, c = 11.4866(3) Å, α = 90.00°, β = 105.407(3)°, γ = 90.00°, V = 1702.08(7) Å^3, Z = 4, D_c = 1.441 g/cm^3, F_{000} = 776, MoKα radiation, λ = 0.71073 Å, T = 120K, $2\vartheta_{max}$ = 52.0°, 15388 reflections collected, 1675 unique (R_{int} = 0.0271). Final *GooF* = 1.080, *R1* = 0.0218, *wR2* = 0.0582, *R* indices based on 1603 reflections with I >2σ(*I*) (refinement on F^2), 99 parameters, 3 restraints. Lp and absorption corrections applied, μ= 0.697 mm^{-1}.

{$CaCl_2$(**2.12**)·EtOH}$_n$ (**6.4**)

Anhydrous calcium chloride (0.086 g, 0.77 mmol) was dissolved in absolute ethanol and hydoxyethylpyrrolidone (**2.12**) (0.1 g, 0.77 mmol) was added. The reaction mixture was sonicated for 1 minute to ensure thorough mixing. The sample vial was left open and placed within an evacuated vacuum desiccator. Colourless crystals of the coordination complex were visible after 2 days under a static vacuum (Yield = 0.1518 g, 0.133 mmol, 17.2 %). IR (υ/cm^{-1})

1655 (C=O). Crystal data for $C_{32}H_{64}N_4O_{12}Ca_4Cl_8$: M = 1140.79 g mol^{-1}, colourless trapezoid, 0.2903 x 0.2057 x 0.0683 mm^3, triclinic, space group $P\bar{1}$ (No. 2), a =9.2400(6) Å, b = 9.9217(7) Å, c = 15.7248(10) Å, α = 72.942(6)^o, β = 89.180(5)^o, γ = 74.421(6)^o, V = 1324.28(16) Å^3, Z = 1, D_c = 1.430 g/cm^3, F_{000} = 596, MoKα radiation, λ = 0.71073 Å, T = 120K, $2\vartheta_{max}$ = 52.0^o, 11341 reflections collected, 5215 unique (R_{int} = 0.0644). Final *GooF* = 0.985, *R1* = 0.0525, *wR2* = 0.1014, *R* indices based on 3562 reflections with I >2σ(*I*) (refinement on F^2), 279 parameters, 6 restraints. Lp and absorption corrections applied, μ= 0.865 mm^{-1}.

6.5 References

1. E. A. Kishar, D. A. Ahmed, M. R. Mohammed and R. Noury, *Beni-Suef University Journal of Basic and Applied Sciences*, 2013, **2**, 20-30.
2. X. Pang, P. Boul and W. Cuello Jimenez, *Construction and Building Materials*, 2015, **77**, 260-269.
3. M. C. G. Juenger, P. J. M. Monteiro, E. M. Gartner and G. P. Denbeaux, *Cement and Concrete Research*, 2005, **35**, 19-25.
4. E. A. Bortoluzzi, N. J. Broon, C. M. Bramante, W. T. Felippe, M. Tanomaru and R. M. Esberard, *J. Endod.*, 2009, **35**, 550-554.
5. Y.Simeonov and N. Djabarov, *US*4134773 A, 1979.
6. A. Perrin, D. Myers, K. Fucke, O. M. Musa and J. W. Steed, *Dalton Trans.*, 2014, **43**, 3153-3161.
7. K. Lamberts, S. Porsche, B. Hentschel, T. Kuhlen and U. Englert, *Crystengcomm*, 2014.
8. C. P. Rao, A. M. Rao and C. N. R. Rao, *Inorg. Chem.*, 1984, **23**, 2080-2085.
9. K. Lewinski and L. Lebioda, *J. Am. Chem. Soc.*, 1986, **108**, 3693-3696.
10. P. Chakrabarti, K. Venkatesan and C. N. R. Rao, *Proc. R. Soc. Lond. A Mat.* , 1981, **375**, 127-153.
11. V. A. Khrustalev, G. E. Vanina, N. U. Venskovskii, N. N. Lobanov, M. Y. Antipin, A. K. Molodkin and A. I. Ezhov, *Russ. J. Inorg. Chem.*, 2003, **48**, 1020-1023.
12. O.Musa and K.Narayanan, *US*20120148514 A1, 2012.
13. C. F. Macrae, I. J. Bruno, J. A. Chisholm, P. R. Edgington, P. McCabe, E. Pidcock, L. Rodriguez-Monge, R. Taylor, J. van de Streek and P. A. Wood, *J. Appl. Crystallogr.*, 2008, **41**, 466-470.
14. G. M. Sheldrick, *Acta Crystallogr. Sect. A*, 2008, **64**, 112-122.
15. O. V. Dolomanov, L. J. Bourhis, R. J. Gildea, J. A. K. Howard and H. Puschmann, *J. Appl. Crystallogr.*, 2009, **42**, 339-341.

7 Boric acid complexes of lactam derivatives

7.1 Introduction

Guar is a natural polysaccharide with the ability to form cross-linked gels and can therefore have interesting rheological properties.[1] As a result of these characteristics, Guar (and associated derivatives) finds use in a variety of applications including the food, textile and paper industries.[1, 2] One of the most common applications of Guar is within the oil and gas industries as hydraulic fracturing fluids.[3, 4] This water-soluble polysaccharide is comprised of a linear backbone of (1-4)-β-linked D-mannose units with (1-5)-α-linked D-galactose units randomly attached as side chains. The repeat unit of Guar and (hydroxypropyl)guar is shown in Figure 7.1.[3]

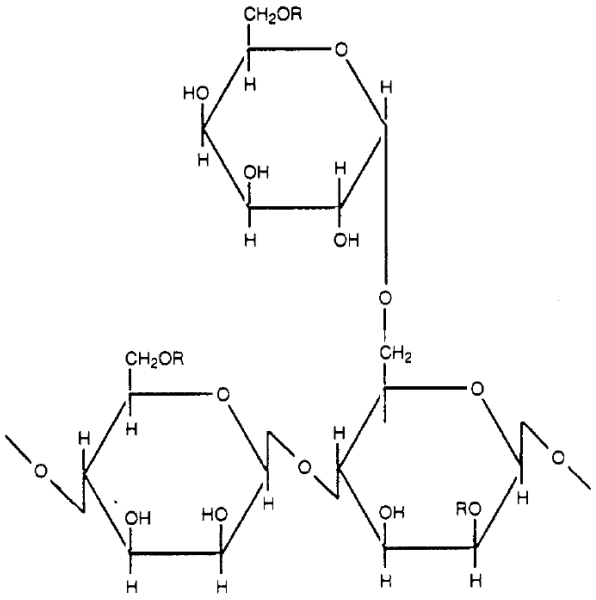

Figure 7.1: Repeat unit of Guar (R=H) and (hydroxypropyl)guar (R=$CH_2CH_2CH_2OH$).[3]

Sodium borate (borax) is commonly added in order to cross-link the system and increase the viscosity of the mixture.[3] Reaction of borax with water results in dissociation to boric acid and monoborate ions, as seen in equation 7.1. The generated boric acid can then react with additional water to form extra monoborate ions, according to equation 7.2.[3] It is believed that the monoborate ions react with the *cis*-hydroxyl groups in Guar, and therein promote the cross-linking process.[3]

$$B_4O_7^{2-} + 7H_2O \rightarrow 2B(OH)_3 + 2B(OH)_4^- \quad (7.1)$$

$$B(OH)_3 + H_2O \leftrightarrow B(OH)_4^- + H^+ \quad (7.2)$$

Temperature and pH play a major role in determining the physical properties of these materials; fluid-like behaviour is common at low pH (~7.0) while solid-like behaviour is prevalent at high pH (9.0-9.5). In addition, transition to solid-like behaviour is achieved upon lowering the temperature from 65°C to 15°C according to Kesavan *et al*.[3] A typical gel synthesis involves mixing the guar gum, water and boric acid in a 10:2000:1 wt/wt/wt ratio, and then adjusting the pH to 8.5-9.0.[4] At this ratio Bishop *et al.* calculated that there are approximately 2 boron centres per 3 monosaccharide repeat units.[4] The high boron-to-monosaccharide ratio required for increasing the fluid viscosity highlights the inefficiency of the process.[4]

In an attempt to develop novel commercial boron sources, this chapter explores complexes of simple boron cross link precursors. The aqueous reactivity of boric acid with diols and alcohols is well established,[4] alongside the ability of this small acidic molecule to form extensively hydrogen-bonded structures with urea, for example.[5] Based on previous work involving complexes with bis(lactam) ligands (Chapters 5 and 6),[6] this chapter examines the exploitation of the highly polar lactam carbonyl moiety in the formation of boric acid and boronic acid complexes.

7.2 Results and discussion

7.2.1 Bis(lactam)-boric acid complex

Reaction of the neutral bis(pyrrolidone) ether ligand used in Chapters 5 and 6, namely 1-{2-[2-(2-oxo-pyrrolid-1-yl)-ethoxy]-ethyl}-pyrrolid-2-one (**5.1**)[7] with boric acid ($B(OH)_3$) in a stoichiometric ratio in ethanol, results in the crystallization of a hydrogen-bonded complex of formula **5.1**·$(B(OH)_3)_2$ (**7.1**). The new complex was analysed using single crystal X-ray analysis and IR spectroscopy. The asymmetric unit, as shown in Figure 7.2, contains a single ligand species and two boric acid molecules, held by very short BOH···O=C interactions (O···O 2.6583(13) and 2.6045(13) Å). Such short interactions are indicative of strong hydrogen bonding as a result of the high polarity of the carbonyl moiety.

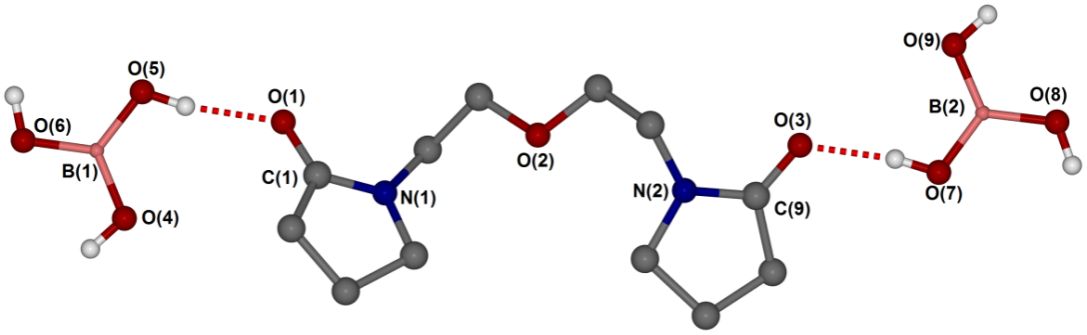

Figure 7.2: Asymmetric unit of **5.1**·$(B(OH)_3)_2$ (**7.1**). Hydrogen atoms are omitted for clarity with the exception of those of the boric acid molecules.

All three hydroxyl moieties of the boric acid molecule are involved in hydrogen bonding interactions; two OH groups interact with neighbouring boric acid molecules to form a tape arrangement, while the remaining OH group interacts with the carbonyl functionality of a ligand molecule. This results in the existence of hydrogen-bonded channels of boric acid, with ligand molecules bridging parallel channels, much like a ladder, as seen in Figure 7.3.

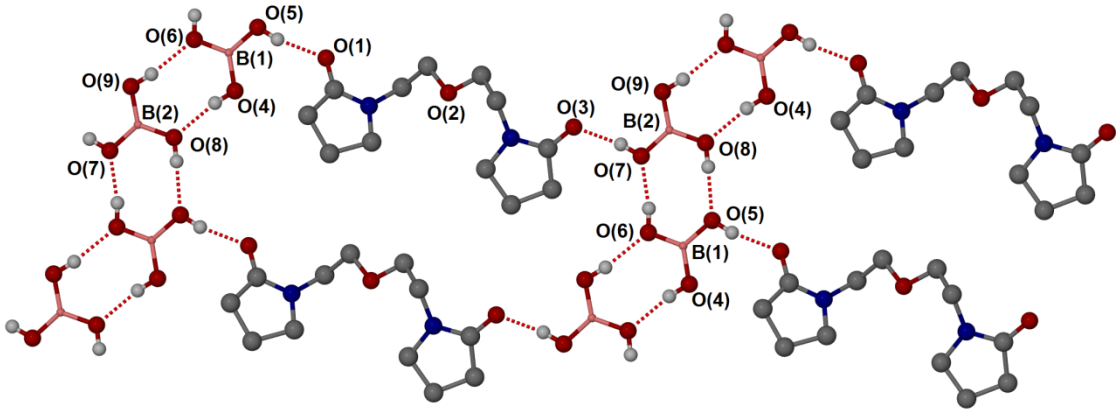

Figure 7.3: Crystallographic packing in **5.1**·$(B(OH)_3)_2$ (**7.1**). Hydrogen atoms are omitted for clarity with the exception of those of the boric acid molecules. Selected hydrogen bonding distances (Å): O(6)···O(7) 2.6860(14), O(7)···O(3) 2.6045(13), O(4)···O(8) 2.7000(14), O(9)···O(6) 2.7541(13), O(5)···O(1) 2.6583(13), O(8)···O(5) 2.7350(14).

The carbonyl stretching mode occurs at 1674 cm^{-1} in the solid-state IR spectrum of neat ligand **5.1**, shifting to 1641 cm^{-1} upon complexation with boric acid. This shift is similar to those seen in Chapters 5 and 6 for alkali metal complexes containing the bis(lactam) ligand[6] and is indicative of a shift to the enolate resonance form and hence strong hydrogen bonding interactions.

As outlined in Chapter 6, mechanochemical grinding of reactants offers many advantages to the conventional solvent-evaporation for the synthesis of coordination

complexes. Solvent-free mechanical grinding of ligand **5.1** and boric acid, in a 1:2 ratio (to match the stoichiometry of the crystal structure), using a pestle and mortar, results in the immediate formation of a white paste. The paste transforms to a white crystalline solid upon air drying over a period of 3 hours at room temperature. The IR spectrum for the crystalline solid is consistent with that for complex **7.1**, and hence suggests that the same co-crystalline product has formed, as seen in Figure 7.4.

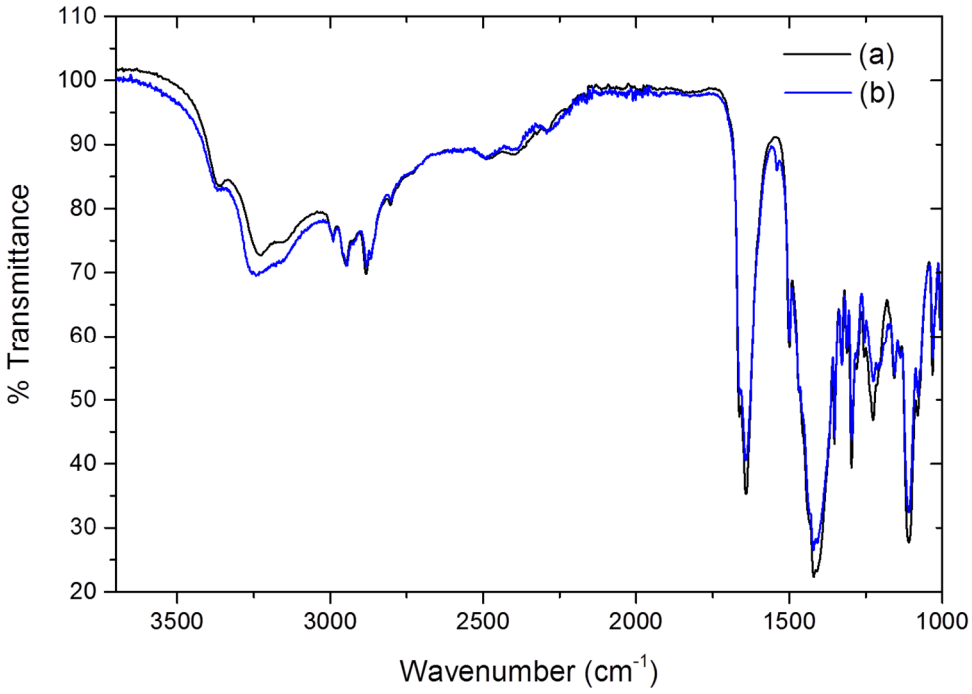

Figure 7.4: Solid-state IR spectra for (a) single crystals of complex **7.1** grown from ethanol and (b) mechanochemically prepared crystalline solid.

Unfortunately it was noted that the crystalline material transformed to an oily residue upon prolonged exposure to the atmosphere, with the elemental analysis results suggesting the uptake of 1.5 water molecules per asymmetric unit. This seems reasonable due to the hygroscopicity of both the ligand species and boric acid, although may prove problematic if used in industrial application. The hygroscopicity of the co-crystal limited the viability of obtaining an experimental PXRD pattern. Further work in this area would attempt attainment of the PXRD pattern by analysing the sample immediately post-drying or by storing the material in an inert atmosphere; however this is outside of the work published herein. Once the PXRD pattern for the mechanochemically prepared sample is obtained it would be possible to compare it to the pattern calculated based on the single crystal structure for complex **7.1** and therein confirm synthesis of the same co-crystalline species.

7.2.2 Guar cross-linking

As discussed in Section 7.1, addition of boric acid to an aqueous-Guar mixture results in the cross-linking of the polymer and causes an increase in the viscosity of the system. In order to establish whether co-crystallization affects the propensity for polymer cross-linking, the performance of the mechanically prepared sample was compared to that for free boric acid. In all cases the same procedure was followed, as detailed below:

1. Guar was weighed into a sample vial
2. Water was added and the sample mixed by sonication until homogeneous.
3. Complex **7.1** (or boric acid) was added.
4. The mixture was shaken for 1 minute to ensure complete dissolution.
5. NaOH (2M) was added dropwise, and the samples were shaken for 2 minutes.
6. Where stated the samples were heated with a heat gun for 30 seconds per cycle, for three cycles, allowing the sample to cool to room temperature between heating cycles.

A variety of conditions were studied, using the same mass of boric acid and complex **7.1** for comparison; an equivalent mass of **7.1** would equate to a lower boron content than for the free boric acid system. The systems studied are outlined in Table 7.1.

Complex	Complex (g)	NaOH (mL)	Temp	Sample
Boric Acid	0.01	0.1	Heated	**A**
5.1·$(B(OH)_3)_2$	0.01	0.1	Heated	**B**
Boric Acid	0.01	0.1	Room temp	**C**
5.1·$(B(OH)_3)_2$	0.01	0.1	Room temp	**D**

Table 7.1: Guar cross-linking systems studied using boric acid and complex **7.1**.

Initial testing of the samples was done by visual examination, observing the mixture viscosity upon upturning the sample vials. It was observed that strong gels typically hold their shape and do not fall upon sample inversion. The photographs in Figure 7.5 show the visual comparison between the various systems; the images on the right of the figure show the mixtures holding their shape upon vial inversion illustrating the similar mixture viscosity.

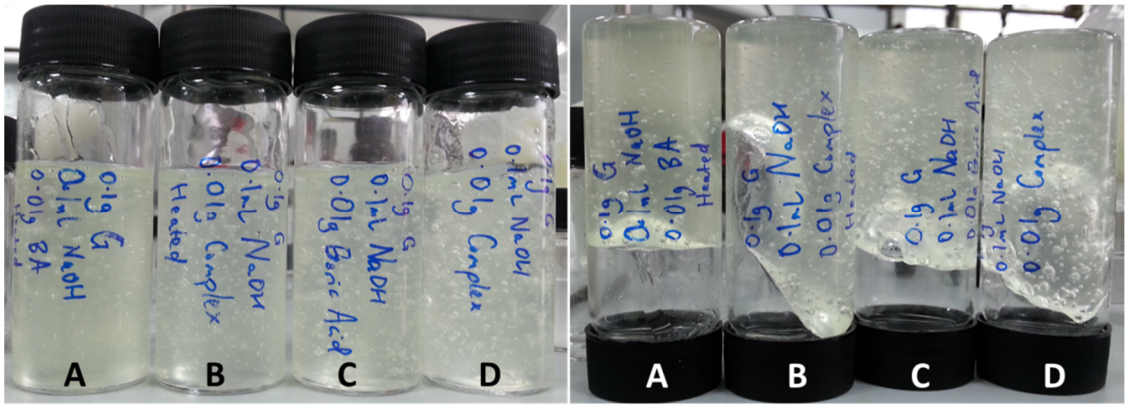

Figure 7.5: Photograph showing the different systems studied. Sample letters correspond to those in Table 7.2. Images on the right show the samples following vial inversion.

As anticipated, samples **A** and **C** (boric acid systems) form viscous gels almost immediately following addition of NaOH. The gels increase in viscosity when left undisturbed for 5 minutes. After 10 minutes, sample **C** is able to hold the shape of the vial and does not fall upon inversion. Heating of the mixture (as in **A**) results in increased homogeneity and a quicker transition to the gel state; the viscosity is enhanced upon cooling to room temperature.

In comparison, upon addition of NaOH to sample **D**, the mixture appears to thicken slightly but remains reasonably free-flowing; at this stage it is considerably less viscous than **C**. Again, the sample viscosity increases upon leaving undisturbed, and after 10 minutes the material holds the shape of the vial and does not fall upon upturning. Analogously, heating of the mixture results in a quicker transition to the gel state.

In both the heated and non-heated systems, the boric acid mixture forms a gel more quickly than the systems containing the co-crystalline solid. However, upon leaving undisturbed for approximately 10 minutes the resulting systems are of similar viscosity. The gels appear comparable for 5 days, after which point those containing the co-crystalline species appear to flow more readily.

In conclusion, complex **7.1** successfully increases the viscosity of an aqueous Guar system upon addition of NaOH. While the immediate gel is weaker than the analogous boric acid analogue, upon leaving to stand for a short time period the viscous materials are similar. It is interesting that the lower boron-to-polysaccharide ratio, in the case of complex **7.1**, still enables formation of a gel.

The same Guar thickening studies were conducted using boric acid and complex **7.1** on an equivalent boron basis. Use of an equivalent boron content of **7.1** resulted in the thickening of the Guar mixture, however the resulting gels were weaker than when using uncomplexed boric acid. It is believed that the presence of additional ligand **5.1** within the aqueous solution negatively affects the gel formation. In addition, over time the mixture containing **7.1** collapsed more readily than the boric acid equivalent. Upon close examination of the **7.1**-guar mixture upon leaving for 3 days it was noted that the sample had separated into a biphasic mixture with a liquid layer on top and a gel containing crystals in the lower layer, as seen in Figure 7.6. Whilst the formation of a collapsible gel may be desirable in some applications, the formation of crystalline species within the system would likely negate the potential use. Unfortunately, the crystals were of insufficient size and quality to be analysed by single crystal X-ray analysis, although are likely to be complex **7.1** or free boric acid.

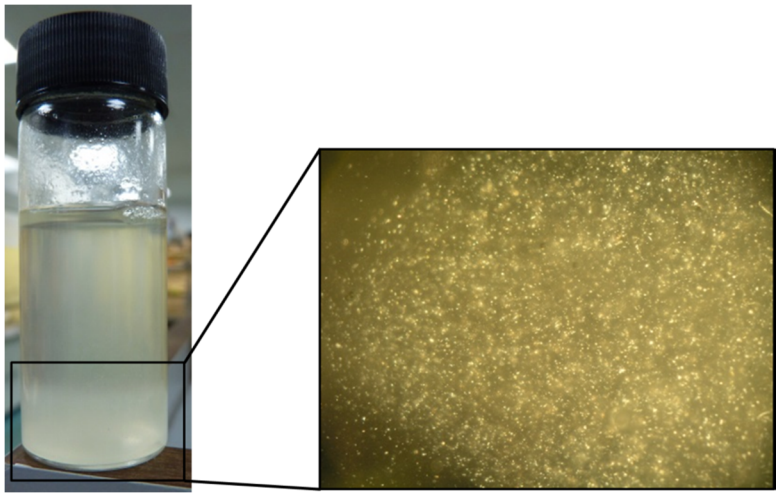

Figure 7.6: Sample vial showing biphasic **7.1**-guar mixture. Pop-out image shows the crystalline material of the lower layer viewed through the microscope using polarised light.

Investigations into the quantity of NaOH required to induce thickening of the guar-boric acid and guar-**7.1** mixtures suggested that there is an optimal quantity of base required for gel synthesis. It was found that addition of too much NaOH results in a colour change to a deep yellow with no thickening occurring, presumably due to decomposition of the system. Addition of too little NaOH also results in a liquid (*i.e.* no gelation). Therefore it was found that 0.1 mL of 2M NaOH was optimal for the systems using 0.01 g of boric acid or the coordination complex.

Due to time limitation, the detailed analysis of the resulting gels is outside of the scope of this work; however, in order to fully explore this area, completion of rheological studies

could form the focus of future work. It would be desirable to compare the stress-strain behaviour of the gels formed using boric acid and **7.1** in different conditions of temperature, pH and reactant ratio. Finally, it is unknown as to whether ligand **5.1** and boric acid remain as a complex during the gel synthesis, or whether addition of water to the system results in the dissociation into the individual components.

7.3 Mono(lactam)-boric acid

Solvent-free grinding of the mono(lactam) ligand 1-(2-hydroxyethyl)-2-pyrrolidone (**2.12,** HEP) and boric acid, in a 1:1 ratio, results in the immediate formation of a white paste. The IR spectrum of the resulting product shows no change in the frequency of the carbonyl stretching band following addition of boric acid, suggesting that carbonyl coordination does not occur, as seen in Figure 7.7. However, the OH mode in the 1:1 boric acid-**2.12** product is shifted to a lower wavenumber (3194 cm^{-1}) than that in the free ligand (3358 cm^{-1}), suggesting that this functionality experiences additional hydrogen bonding interactions.

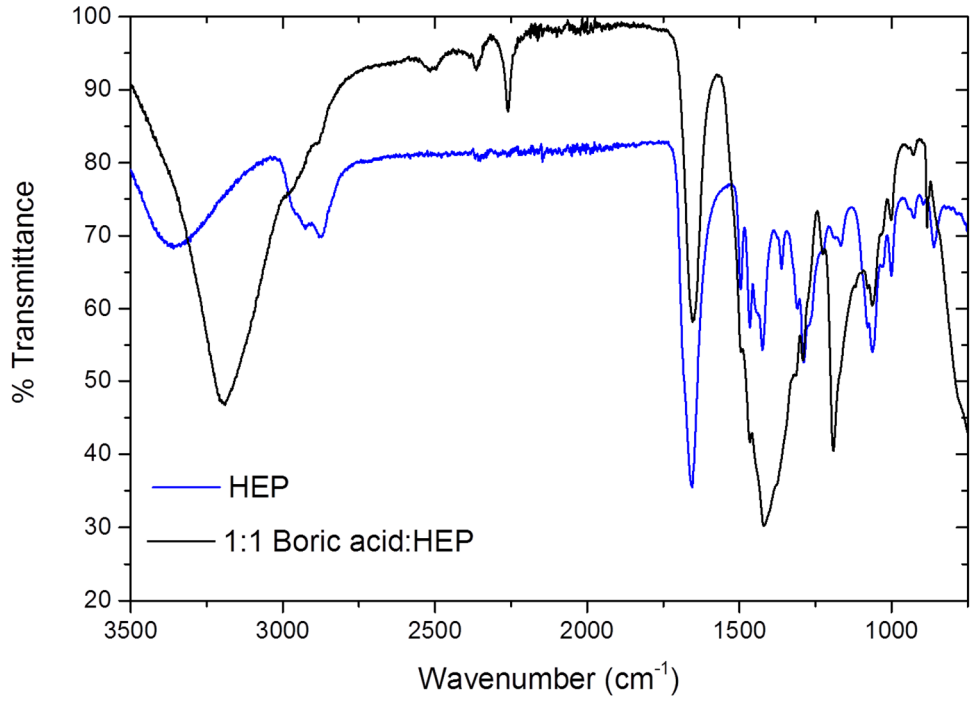

Figure 7.7: Solid-state IR spectra for ligand **2.12** and the paste formed by grinding a stoichiometric mixture of **2.12** and boric acid.

Unfortunately, it was not possible to unequivocally confirm the identity of the potential coordination complex of boric acid-**2.12** because a single crystal suitable for X-ray crystallographic work could not be isolated. Dissolution of the reactants in ethanol, in a 1:1

and 1:2 metal:ligand ratio, results in the formation of a viscous yellow oil following solvent evaporation. It is postulated that isolation of crystalline material is limited by the hygroscopicity of both reactants.

Complexation between 1-ethyl-2-pyrrolidone (**2.11**) and boric acid was also investigated. Mixtures of varying ratio were dissolved in a plethora of solvents but in all instances an oily residue was isolated. Analysis of the oil products did not show a shift in the carbonyl stretching mode upon addition of the acidic reactant.

7.4 Alternative boronic acids

Having established interaction between the lactam carbonyl moiety and the BOH groups in boric acid, complexation with a series of boronic acids was investigated. A wealth of literature exists into the use of boronic acids as potential co-crystal formers, particularly due to the different hydrogen bonding conformations for the key functionalities in such acids, as depicted in Figure 7.8.[8, 9]

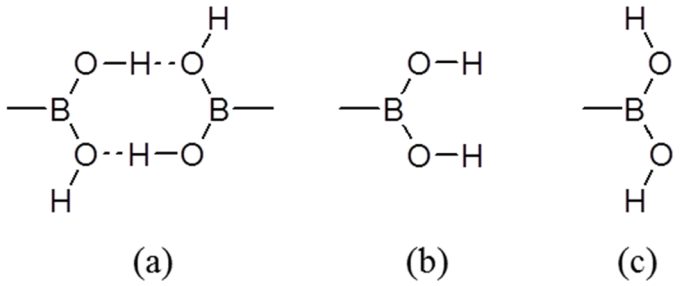

Figure 7.8: Hydrogen bonding conformations in boronic acid groups as follows (a) syn-anti, (b) syn-syn and (c) anti-anti.[8]

A variety of boronic acids are commercially available with a general formula *R*-B(OH)$_2$, in which *R* represents a range of functionalities. To this end, the complexation behaviours of phenylboronic acid, 4-hydroxyphenylboronic acid and 3-formylphenylboronic acid were investigated. These acids were chosen primarily due to their reasonable solubility in alcoholic solvents. A search of the Cambridge Structural Database (CSD)[10] showed that the structure of 4-hydroxyphenylboronic acid has not previously been reported. The commercial sample (purchased from TCI) contained good quality single crystals, and therefore the X-ray single crystal structural analysis is included herein. The asymmetric unit of this boronic acid contains two independent molecules with hydrogen bonding interactions between the hydroxyl moieties (O(3)···O(4) 2.836(2) Å), as seen in Figure 7.9.

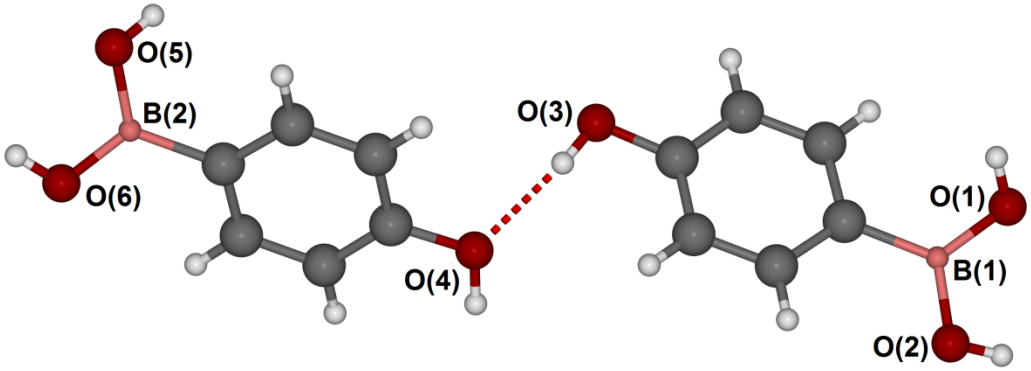

Figure 7.9: Asymmetric unit of 4-hydroxyphenylboronic acid.

The BOH groups of neighbouring molecules are held by hydrogen bonding interactions in a *syn-anti* conformation, resulting in an overall tape arrangement as seen in Figure 7.10. The Hirshfeld surface fingerprint plot is reported later in Figure 7.13, in comparison to that for other complexes, showing prominent spikes as a result of the strong hydrogen bonding interactions within this species.

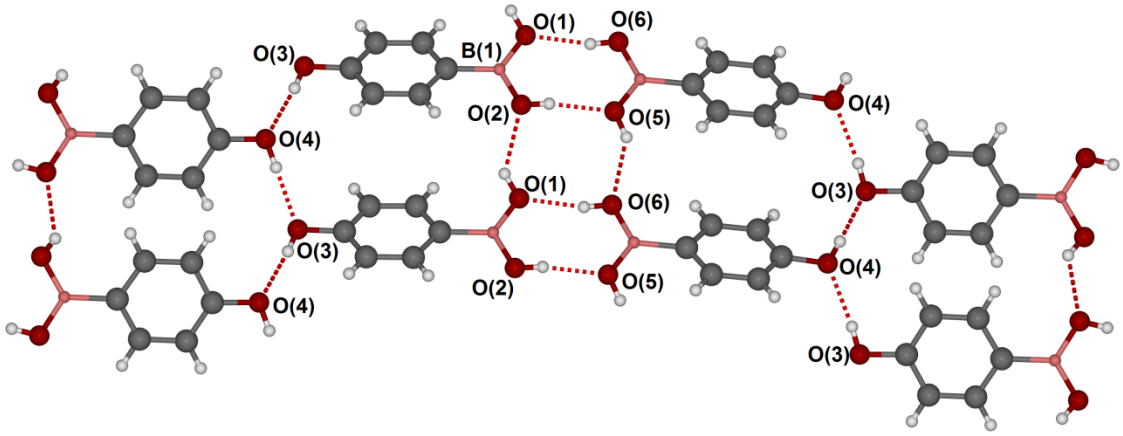

Figure 7.10: Crystallographic packing in 4-hydroxyphenylboronic acid. Hydrogen bonding distances (Å) (D···A): O(1)···O(2) 2.784(2), O(1)···O(6) 2.746(2), O(2)···O(5) 2.757(2), O(3)···O(4) 2.836(2), O(4)···O(3) 2.815(2), O(5)···O(6) 2.781(2) Å.

Anderson *et al.* report an increased propensity for the formation of co-crystalline analogues when the pure compound has a Z' greater than 1.[11] 4-hydroxyphenylboronic acid has a Z' of 2, and therefore it was postulated that co-crystalline species could be produced using this acid. Despite considerable efforts to isolate co-crystalline species with the lactam series from Chapter 2 (Figure 2.20), this proved unsuccessful, resulting in the formation of oily residues in all instances except with *N*-vinyl caprolactam. Lactam-boronic acid complexation was investigated using a process of slow solvent evaporation, at room

temperature, using a plethora of solvent systems and different ligand-acid stoichiometries. IR spectroscopic analysis of the oily products suggested a lack of coordination to the acidic reactant as identified by an absence in a shift of the carbonyl stretching mode. It is postulated that once again the lactam hygroscopicity, which may be crucial to the species industrial application as KHIs, prevents the isolation of crystalline material. In an attempt to remove any water from the oily residues, in the hope of isolating a crystalline powder, the products were held in an Abderhalden drying pistol for 8 hours; however, this did not result in powder formation but instead resulted in a colour-change in most instances, presumably due to some degree of thermal decomposition.

In contrast, reaction of *N*-vinyl caprolactam with 4-hydroxyphenylboronic acid in a 1:1 ratio in methanol results in the isolation of the co-crystalline species (ε-caprolactam)$_2$·4-hydroxyphenylboronic acid (**7.2**). It was surprising that the *N*-vinyl caprolactam had lost the alkene functionality, resulting in the incorporation of ε-caprolactam within the co-crystal. The exact reason for this decomposition is unknown, although may be as a result of the presence of residual anhydride in the supplied sample of 4-hydroxyphenylboronic acid. The X-ray structure of this co-crystal is shown in Figure 7.11, highlighting the interesting hydrogen bonding interactions between the lactam and BOH functionalities.

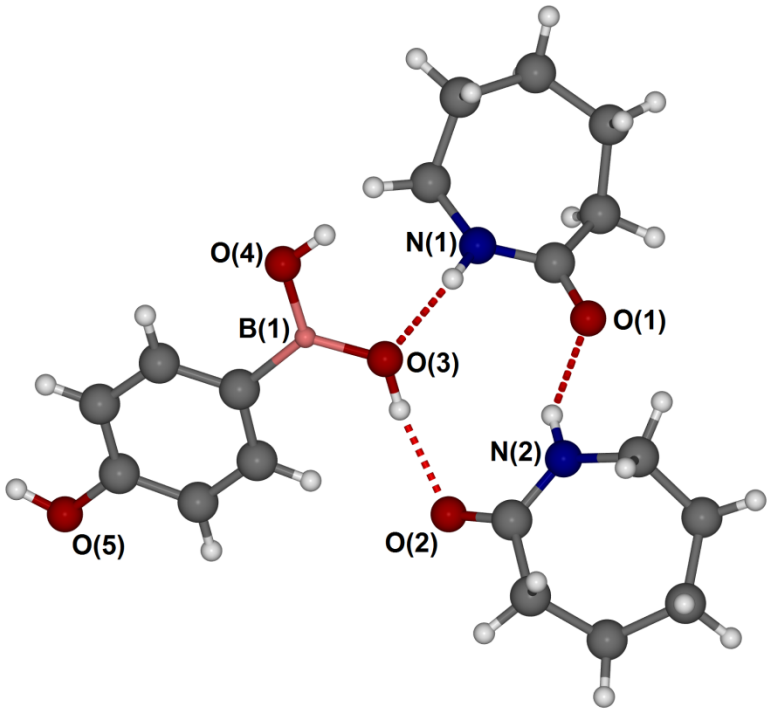

Figure 7.11: Asymmetric unit of (ε-caprolactam)$_2$·4-hydroxyphenylboronic acid (**7.2**). Selected bond distances (Å): N(1)···O(3) 2.969(3), N(2) ···O(1) 2.914(3), O(3) ···O(2) 2.803(3), O(4) ···O(2) 2.733(3), O(5)-O(1) 2.664(3) Å.

The ε-caprolactam molecules interact with each other through a C=O···HN interaction, with an O(1) ···N(2) distance of 2.914(3) Å. Both ε-caprolactam molecules hydrogen bond to the BOH groups of 4-hydroxyphenylboronic acid, one *via* the NH functionality (N1···O(3)) and the other *via* the carbonyl moiety (O(2) ···O(3)). In addition, one carbonyl group interacts with the hydroxyl moiety of 4-hydroxphenylboronic acid, as seen in Figure 7.12.

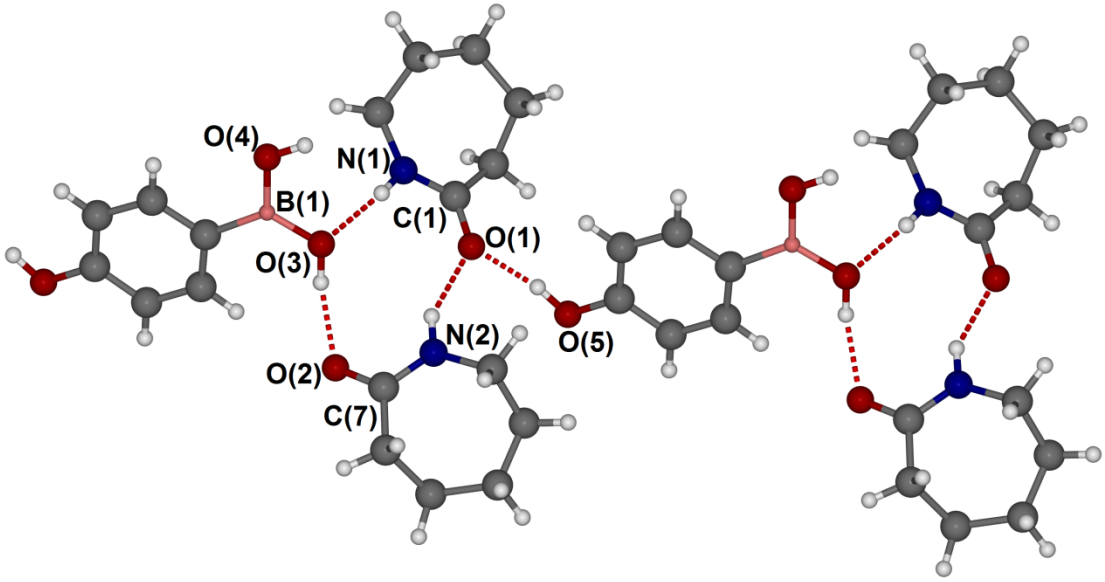

Figure 7.12: Crystallographic packing in complex (ε-caprolactam)$_2$·4-hydroxyphenylboronic acid (**7.2**).

Slow evaporation of solvent from mixtures of ε-caprolactam and 4-hydroxyphenylboronic acid did not result in crystalline material, with IR spectroscopy on the oily products showing no shift in the carbonyl stretching mode upon addition of the boronic acid reactant. Therefore it is suggested that reaction between the residual anhydride from the supplied boronic acid sample with the alkene functionality is critical to complexation. The inability of the 5-membered *N*-vinyl pyrrolidone analogue to complex 4-hydroxyphenylboronic acid may be due to the reduced polarity of the carbonyl functionality as a result of increased ring strain reducing the contribution to the enolate resonance form.

For completeness, it is interesting to compare the Hirshfeld surface fingerprint plots[12] for 4-hydroxyphenylboronic acid, **7.2** and **7.1**, as seen in Figure 7.13. In all instances there are two prominent spikes, attributed to the strong O···O hydrogen bonding interactions. In addition, the "wings" in (a) and (b) represent the CH···π interactions in the hydroxyphenylboronic acid complexes.

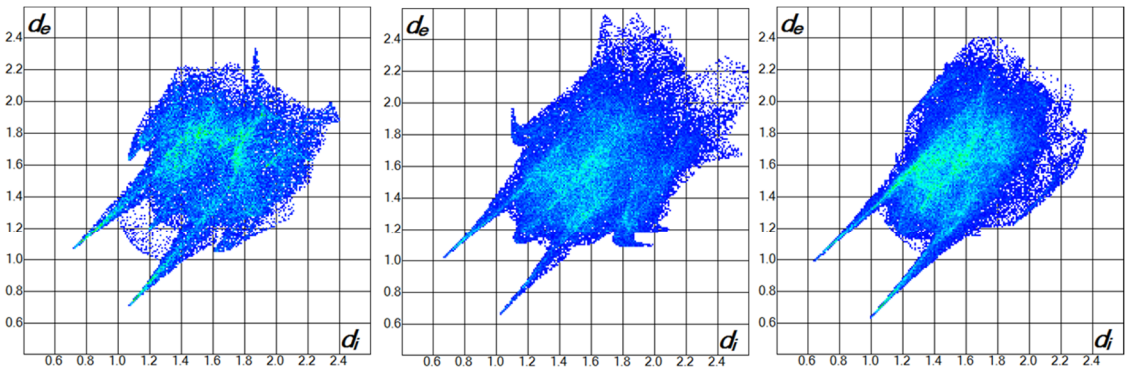

Figure 7.13: Hirshfeld surface fingerprint plots for (a) 4-hydroxyphenylboronic acid, (b) (ε-caprolactam)$_2$·4-hydroxyphenylboronic acid (**7.2**) and (c) **5.1**·(B(OH)$_3$)$_2$ (**7.1**).

Complexation of the lactam series with phenylboronic acid and 3-formylphenylboronic acid proved less fruitful. Slow evaporation of a variety of solvents from a plethora of mixtures of differing ligand:acid stoichiometry resulted in the formation of oily residues. The resulting oily products were analysed using IR spectroscopy; however, this showed no change in the carbonyl stretching mode upon addition of the acidic reactant, indicating that complexation does not occur.

7.5 Conclusions

The high polarity of the amide carbonyl functionality enables formation of co-crystalline species with boric acid. The short hydrogen bond distances between the bis(pyrrolidone) ether ligand and boric acid confirm the strong interactions. Interestingly, the co-crystalline material successfully increases the viscosity of an aqueous Guar system upon addition of NaOH. While the immediate resulting gel is weaker than the analogous boric acid analogue, upon leaving to stand for a short time period the materials are comparable. While further work is necessary to quantify the strengths of the gels formed by these species, it is interesting that the lower boron-to-polysaccharide ratio, in the case of the complex, still enables formation of a gel.

Further, the crystal structure of 4-hydroxyphenylboronic acid is included in conjunction with that of the co-crystalline species formed following addition of *n*-vinyl caprolactam. This confirms that the amide carbonyl moiety within the 7-membered caprolactam ring is also highly polar, and is therein able to form interesting interactions with the acidic molecule.

7.6 Experimental

7.6.1 General

Ligands **5.1** and **2.12** were supplied by Ashland Inc. and used without further purification. 4-hydroxyphenylboronic acid was purchased from TCI and used without further purification. All other solvents and reagents were obtained from standard commercial sources and used without further purification. IR spectra were measured with a Perkin-Elmer 100 FT-IR spectrometer, using an ATR attachment. Thermogravimetric analysis was conducted using a Perkin Elmer Pyris 1 TGA with purge gas specified at 40 mls per minute; temperature was increased at 10 ^{o}C per minute up to the temperature specified.

Crystals suitable for single crystal X-ray diffraction structure determination were selected, soaked in perfluoropolyether oil and mounted on a preformed tip. Single crystal X-ray data were collected at 120 K on an Agilent Gemini S-Ultra diffractometer equipped with the Cryostream (Oxford Cryosystems) open-flow nitrogen cryostats, using graphite monochromated MoKα-radiation (λ = 0.71073 Å). All structures were solved using direct methods and refined by full-matrix least squares on F^2 for all data using SHELXL[13] and OLEX2[14]. All non-hydrogen atoms were refined with anisotropic displacement parameters. CH hydrogen atoms were placed in calculated positions, assigned an isotropic displacement factor that is a multiple of the parent carbon atom and allowed to ride. H-atoms attached to oxygen were located on the difference map when possible, or placed in calculated positions. In some cases disordered H atoms could not be included in the model. Elemental analysis was performed using an Exeter Analytical inc. CE-400 Elemental Analyser. Powder diffraction was performed on glass slides using a Bruker AXS D8 Advance diffractometer, with a Lynxeye Soller PSD Detector, using CuKα radiation at a wavelength of 1.5406 Å (with assistance from Gary Oswald, Durham).

7.6.2 Synthesis of coordination complexes

5.1·$(B(OH)_3)_2$ (**7.1**).

1-{2-[2-(2-oxo-pyrrolid-1-yl)-ethoxy]-ethyl}-pyrrolid-2-one (**5.1**) (0.1 g, 0.416 mmol) was added to a solution of boric acid (0.0257 g, 0.416 mmol) in ethanol. The mixture was sonicated to ensure thorough mixing. Slow evaporation at room temperature resulted in single crystals of **5.1**·$(B(OH)_3)_2$ (**7.1**). (Yield = 0.056 g, 0.154 mmol, 37%); IR (ν/cm^{-1}) 1641

(C=O) and 1110 (C-O). Crystal data for complex **7.1**: *M* = 363.97, colourless block, 0.507 x 0.3695 x 0.1711 mm^3, triclinic, space group $P\bar{1}$ (No. 2), *a* = 7.0629(4) Å, *b* = 7.9863(4) Å, *c* = 17.6846(9) Å, α = 79.301(5)°, β = 80.217(5) °, γ = 68.622(5) °, *V* = 907.03(8) $Å^3$, *Z* = 2, D_c = 1.333 g/cm^3, F_{000} = 388, Xcalibur, Sapphire3, Gemini ultra, Mo Kα radiation, λ = 0.7107 Å, *T* = 120K, $2\theta_{max}$ = 54.0°, 10266 reflections collected, 3945 unique (R_{int} = 0.0357). Final *GooF* = 1.029, *R1* = 0.0397, *wR2* = 0.0884, *R* indices based on 3067 reflections with I >2σ(I) (refinement on F^2), 235 parameters, 0 restraints. Lp and absorption corrections applied, μ = 0.110 mm^{-1}.

4-hydroxyphenylboronic acid

Crystal data for 4-hydroxyphenylboronic acid, *M* = 137.93, colourless trapezoid, 0.4094 × 0.1855 × 0.1143 mm^3, monoclinic, space group $P2_1/c$ (No. 14), *a* = 14.3765(4) Å, *b* = 5.04525(19) Å, *c* = 17.3563(7) Å, α = 90 °, β = 90.695(3) °, γ = 90 °, *V* = 1258.81(8) $Å^3$, *Z* = 8, D_c = 1.457 g/cm^3, F_{000} = 574.000, Xcalibur, Sapphire3, MoKα radiation, λ = 0.71073 Å, *T* = 120K, $2\theta_{max}$ = 52.0°, 15899 reflections collected, 2475 unique (R_{int} = 0.0445). Final *GooF* = 1.088, *R1* = 0.0438, *wR2* = 0.1088, *R* indices based on 2036 reflections with I >2σ(I) (refinement on F^2), 193 parameters, 0 restraints. Lp and absorption corrections applied, μ = 0.113 mm^{-1}.

(ε-caprolactam)$_2$·4-hydroxyphenylboronic acid (**7.2**)

VCap (0.0300 g, 0.216 mmol) was added to a solution of 4-hydroxyphenylboronic acid (0.0300 g, 0.216 mmol) dissolved in MeOH. The mixture was sonicated to ensure thorough mixing. Slow evaporation at room temperature resulted in single crystals after 5 days. (Yield = 0.048 g, 61 %); IR (ν/cm^{-1}) 1647 (C=O). Crystal data for complex **7.2**, *M* = 364.24, colourless block, 0.3181 × 0.1605 × 0.1042 mm^3, monoclinic, space group $P2_1/n$ (No. 14), *a* = 6.4207(3) Å, *b* = 26.1612(11) Å, *c* = 11.4892(4) Å, α = 90 °, β = 93.522(4) °, γ = 90 °, *V* = 1926.22(14) $Å^3$, *Z* = 4, D_c = 1.256 g/cm^3, F_{000} = 784, Xcalibur, Sapphire3, MoKα radiation, λ = 0.71073 Å, *T* = 120K, $2\theta_{max}$ = 52.0°, 28141 reflections collected, 3771 unique (R_{int} = 0.1271). Final *GooF* = 0.906, *R1* = 0.0594, *wR2* = 0.1473, *R* indices based on 2422 reflections with I >2σ(I) (refinement on F^2), 255 parameters, 0 restraints. Lp and absorption corrections applied, μ = 0.090 mm^{-1}.

7.7 References

1. R. Chudziko, *J. Soc. Cosmet. Chem.*, 1971, **22**, 43-60.
2. D. Mudgil, S. Barak and B. S. Khatkar, *J. Food Sci. Tech. Mys.*, 2014, **51**, 409-418.
3. S. Kesavan and R. K. Prud'homme, *Macromolecules*, 1992, **25**, 2026-2032.
4. M. Bishop, N. Shahid, J. Yang and A. R. Barron, *Dalton Trans.*, 2004, 2621-2634.
5. M. S. Mashuta, L. Cheruzel and R. M. Buchanan, *Acta Crystallogr. Sect. C-Cryst. Struct. Commun.*, 2002, **58**, O629-O631.
6. A. Perrin, D. Myers, K. Fucke, O. M. Musa and J. W. Steed, *Dalton Trans.*, 2014, **43**, 3153-3161.
7. O. Musa and K.Narayanan, *US*20120148514 A1, 2012.
8. M. Talwelkar and V. R. Pedireddi, *Tetrahedron Lett.*, 2010, **51**, 6901-6905.
9. S. Varughese, S. B. Sinha and G. R. Desiraju, *Sci. China-Chem.*, 2011, **54**, 1909-1919.
10. C. F. Macrae, I. J. Bruno, J. A. Chisholm, P. R. Edgington, P. McCabe, E. Pidcock, L. Rodriguez-Monge, R. Taylor, J. van de Streek and P. A. Wood, *J. Appl. Crystallogr.*, 2008, **41**, 466-470.
11. K. M. Anderson, M. R. Probert, C. N. Whiteley, A. M. Rowland, A. E. Goeta and J. W. Steed, *Cryst. Growth Des.*, 2008, **9**, 1082-1087.
12. M. A. Spackman and D. Jayatilaka, *Crystengcomm*, 2009, **11**, 19-32.
13. G. M. Sheldrick, *Acta Crystallogr. Sect. A*, 2008, **64**, 112-122.
14. O. V. Dolomanov, L. J. Bourhis, R. J. Gildea, J. A. K. Howard and H. Puschmann, *J. Appl. Crystallogr.*, 2009, **42**, 339-341

Conclusion

The initial aim of this work was to gain insight into the behaviours of poly(lactam) hydrate inhibitors, in the hope of furthering inhibition mechanistic understanding. The systematic study using commercially available polymers confirms hydration at the amide carbonyl moiety, and in all instances multiple hydrated environments are experienced. This work indicates analogous hydration behaviour in all species irrespective of the inclusion of additional functionalities upon the methylene backbone. This is encouraging from an inhibition perspective, if one assumes that hydration at the carbonyl group is crucial to performance, as this would allow different groups to be added in order to fine-tune properties without compromising inhibition behaviours.

Model compounds have been developed and the solution and solid-state properties examined using a plethora of analytical techniques. Hydration behaviours of the small models were found to be representative of the parent polymers. Analysis of small molecule model compounds provides novel insight into the properties of lactam species, particularly highlighting the polarity of the carbonyl group and it's propensity for water complexation. Comparison between the monomeric and dimeric analogues suggests that the hydration behaviour of the small monomer species is less representative of the parent polymer, and therefore that some degree of binding complementarity may occur in the KHI.

Neutron scattering experiments are outlined for aqueous-THF and aqueous-2butoxyethanol systems. This research has highlighted the benefits of combining neutron studies with computational modelling, using EPSR, and the consequential elucidation of atomistic information. Combining these techniques may provide unique insight into the liquid structures of complex systems. In addition, the initial neutron scattering studies are reported for two aqueous-lactam systems. While it was not possible to gain the desired atomistic insight into these hydrated systems, this work provides a starting point for further investigation.

Finally, this research has exploited the polarity of the amide carbonyl moiety in the development of novel lactam coordination complexes. This key property of the C=O group enables complexation to sodium, potassium, zinc and calcium cation centres. The high solubility of the bis(pyrrolidone) ether ligand and the relative ease of synthesis of

coordination complexes suggests that there may be potential for industrial application; with one such example noted in the development of a Guar-thickening agent.

Future Work

In the quest to explore the behaviour of KHIs and model compounds in ever-more realistic systems, further work could explore the effects of lower temperatures and increased salinity. It may be useful to undertake the solution IR spectroscopic titrations as a function of temperature, in order to probe resulting behavioural effects, particularly in the knowledge that the polymers are effective and used at low temperatures. The water present in oil and gas pipelines is known to be saline, and as such it may be interesting to examine the effects of introducing salt to the model compound systems. Having established that the carbonyl group can bind to sodium cations (chapter 5), it would be interesting to explore whether the introduction of salt to the system reduces the hydration propensity of the lactam species.

In an ideal world this research would then examine the effect of water containing gas molecules; however gaining quantitative insight is likely to present a significant challenge. This research has confirmed that studying dimeric model compounds provides a more realistic insight into the behaviour of KHIs than previously used monomers, and therefore it may be useful to synthesise and analyse longer chain lactam oligomers. Trimeric and tetrameric chains would allow the closer examination of the potential complementarity effects.

This research reports the first step in the utilisation of neutron scattering studies to gain atomistic insight into clathrate hydrate systems of interest. In order to optimise, and finalise, the aqueous-2butoxyethanol system it may be worth exploring the possibilities of using EPSR to model molecule aggregation. In addition, SANS experiments could be conducted for the 2-butoxyethanol systems with and without PVCap as a function of temperature. Such SANS studies, and associated analysis, would hopefully provide information regarding the shape of the 2–butoxyethanol aggregates in addition to the effect of including the inhibitor. While the solution IR spectroscopy studies in Chapter 2 suggest that PVCap does not bind to the alcohol solvent, it may be worth exploring whether the polymer disrupts the formation of aggregates. Further work is necessary into the optimisation of the aqueous-lactam computational models; initially it may be useful to computationally probe and verify the Lennard-Jones parameters included within the simulation. Development of a

consistent and reliable simulated model would enable the extraction of the atomic pair site distribution functions; this would be the ideal outcome, particularly for the carbonyl-water functions.

While chapters 5 – 7 focus primarily on the complexation behaviour of a bis(pyrrolidone) ether ligand, it may be interesting to synthesise and study the behaviour of the 7-memebered ring analogue. Isolation of the caprolactam based metal complexes would allow comparison between the C=O properties as a result of the different ring sizes. Finally, chapter 7 reports the initial studies into the application of the bis(pyrrolidone) ether ligand-boric acid complex as a Guar thickening agent; further work would probe the rheological behaviours of the Guar mixtures in an attempt to elucidate the effect of incorporating the lactam ligand.

Appendix

^{1}H NMR Spectroscopic Titration Isotherms

Data from ^{1}H NMR spectroscopic titrations were fitted using non-linear least squares regression using HypNMR2006[1]. The titration isotherms are included below, and the following colours apply:

- Spheres – show experimental data points
- Black line – overall fit of the model
- Red line – Free host
- Brown line – Host:Guest (1:1)
- Blue line – Host:Guest (1:2)

1. C. Frassineti, S. Ghelli, P. Gans, A. Sabatini, M. S. Moruzzi and A. Vacca, *Anal. Biochem.*, 1995, **231**, 374-382.

Compound 2.1 (VCap Saturated dimer)

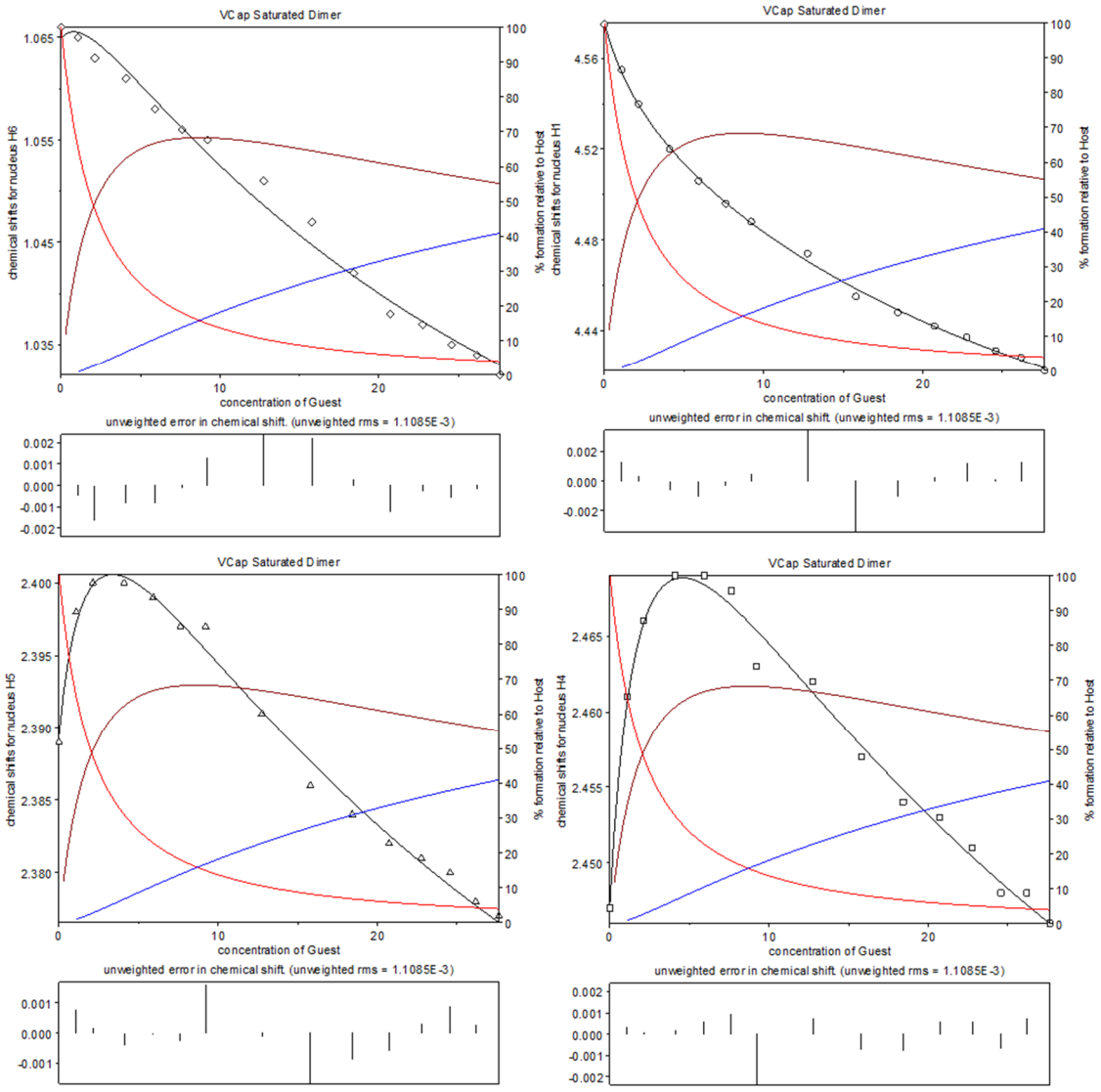

Compound 2.3 (VP Saturated dimer)

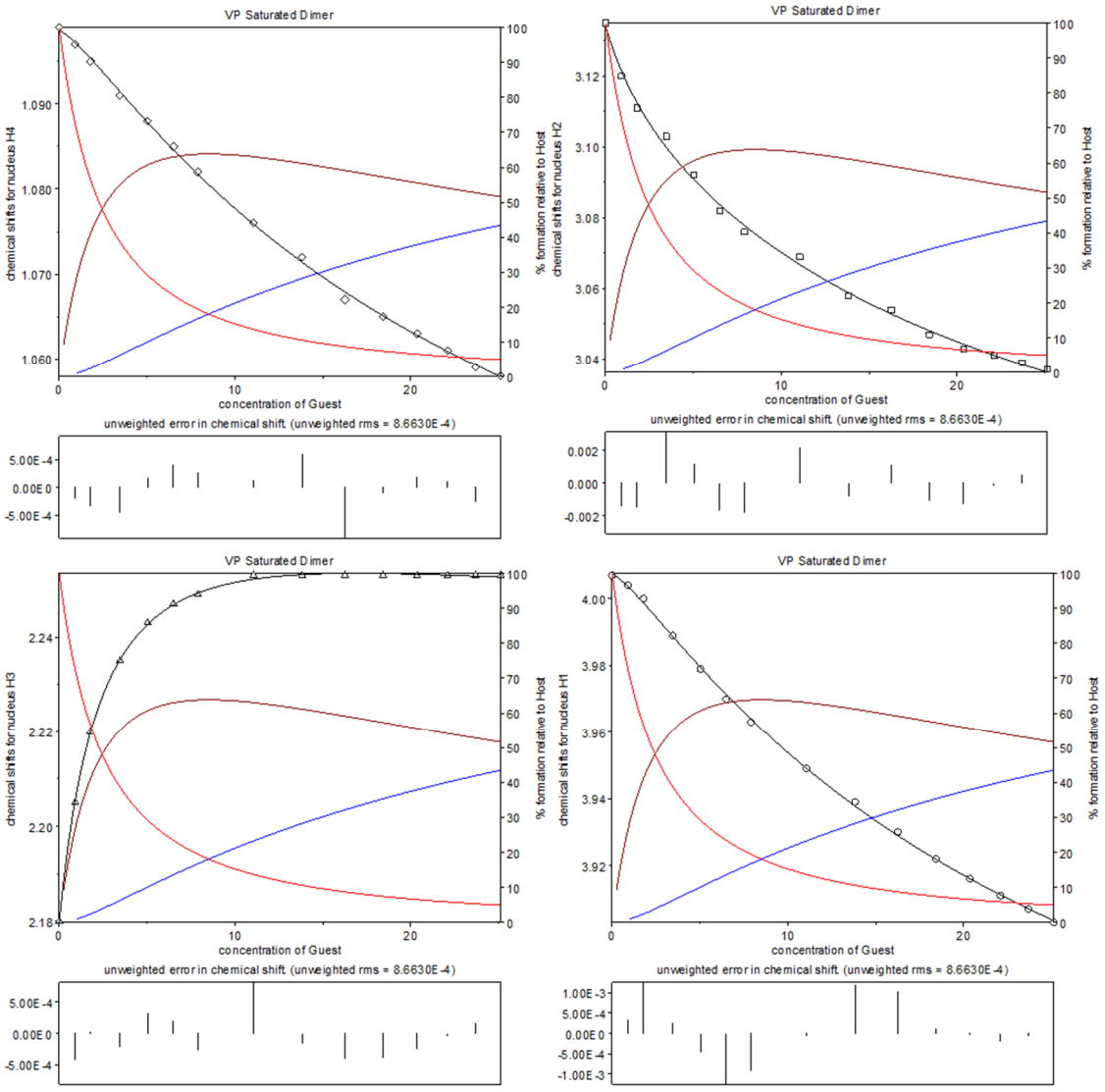

Compound 2.4 (VP Unsaturated dimer)

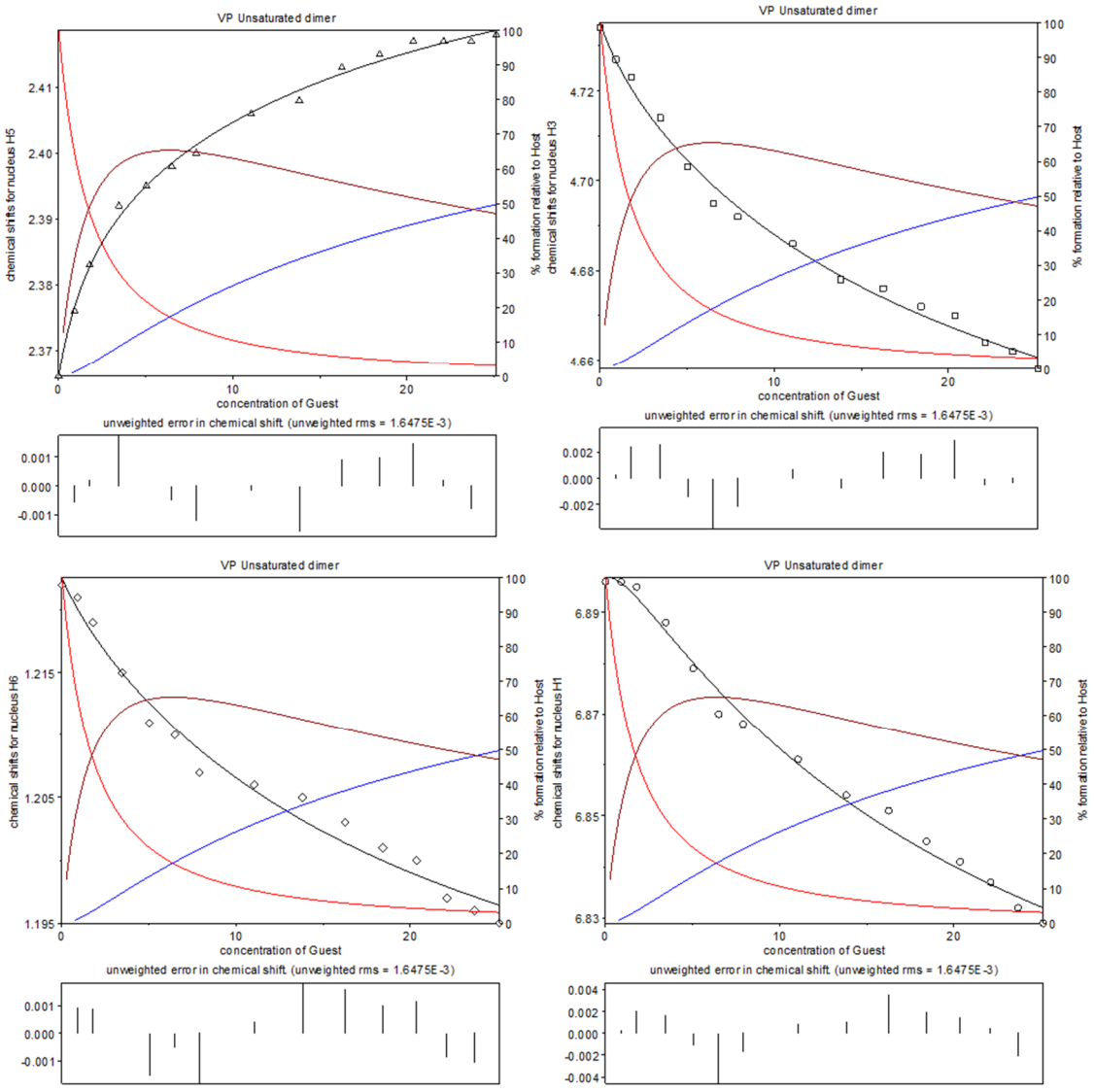

Compound 2.7 (VOH/VCap Model compound)

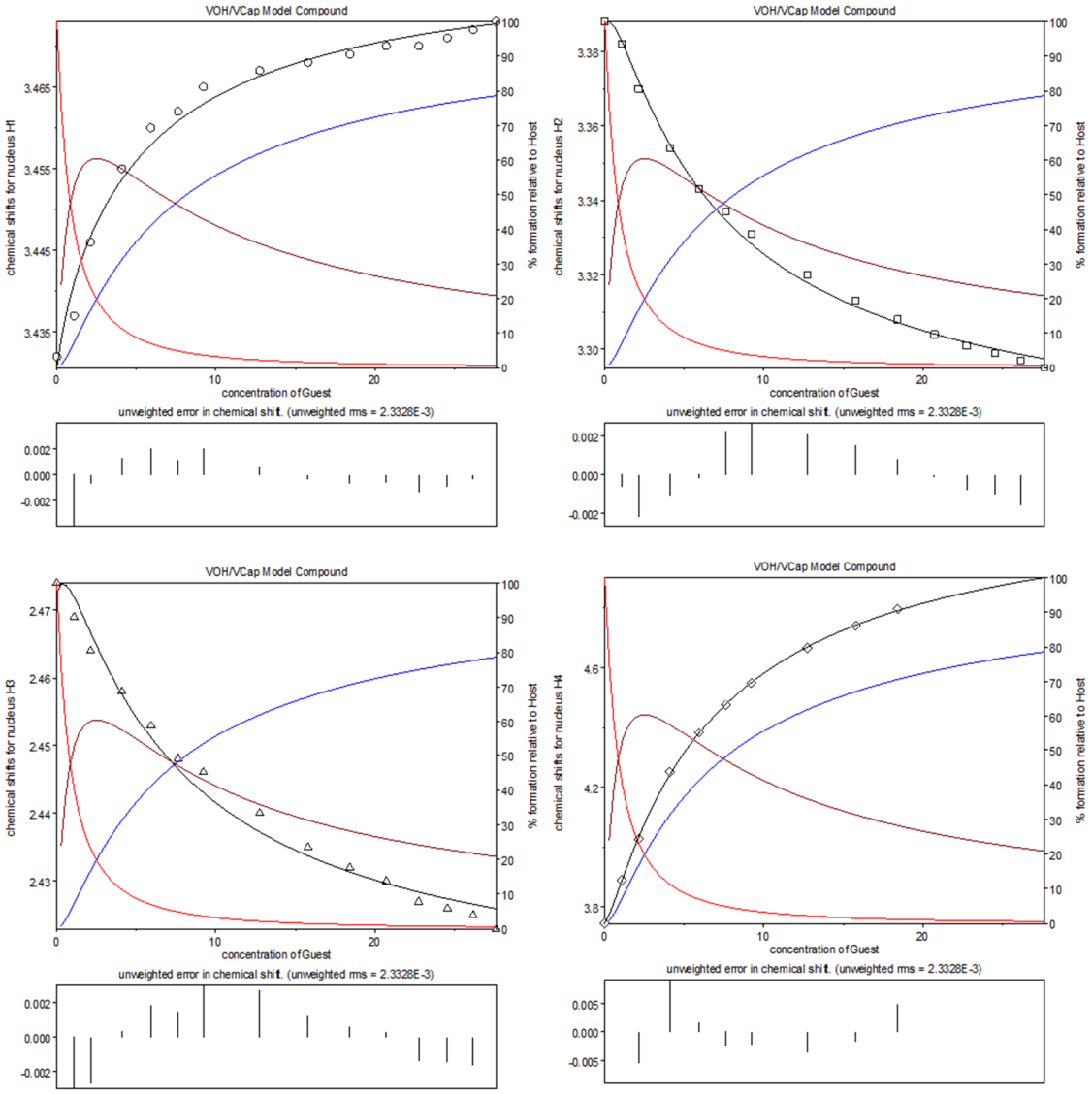

Compound 2.9 (VCap)

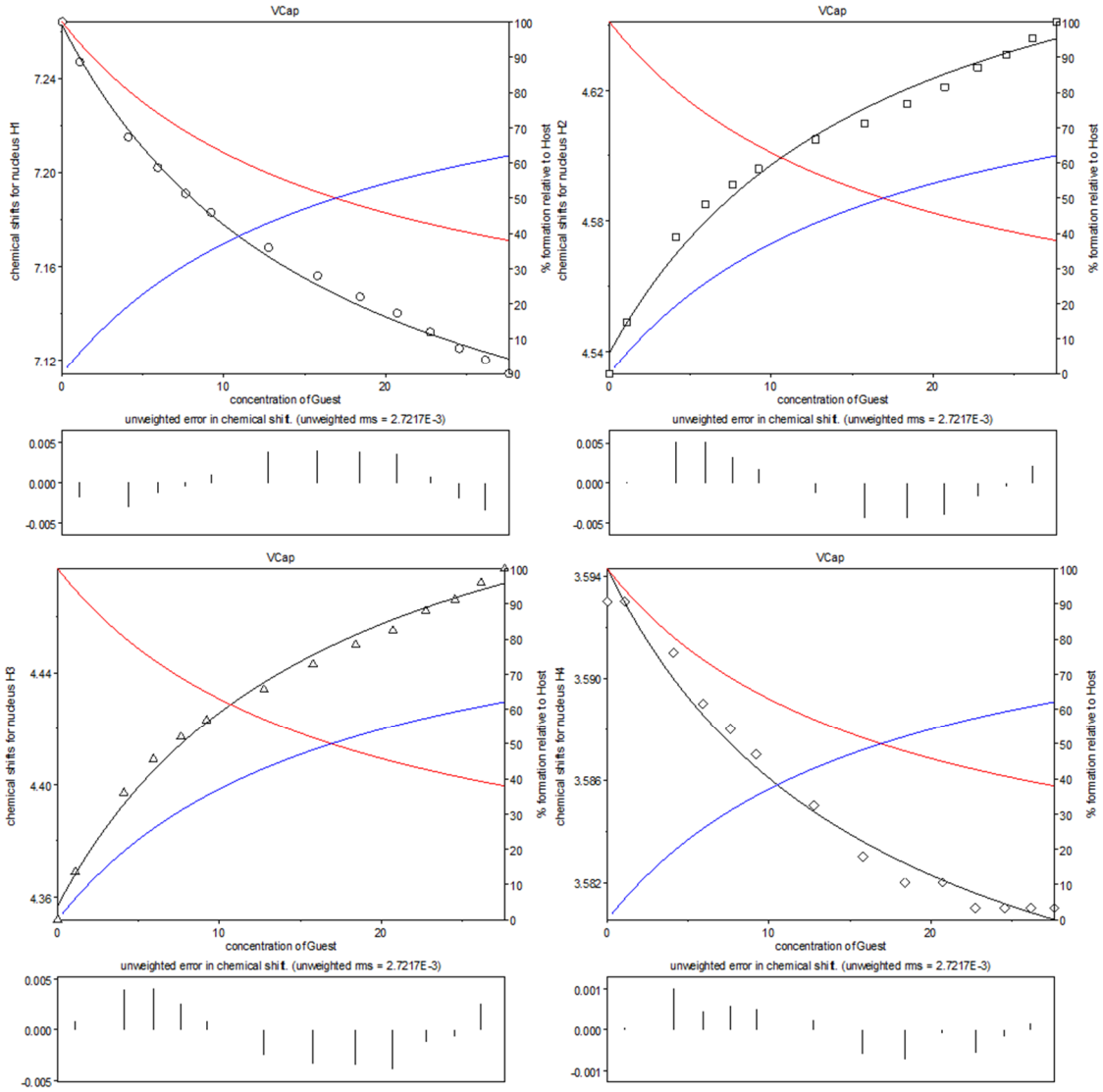

Compound 2.10 (VP)

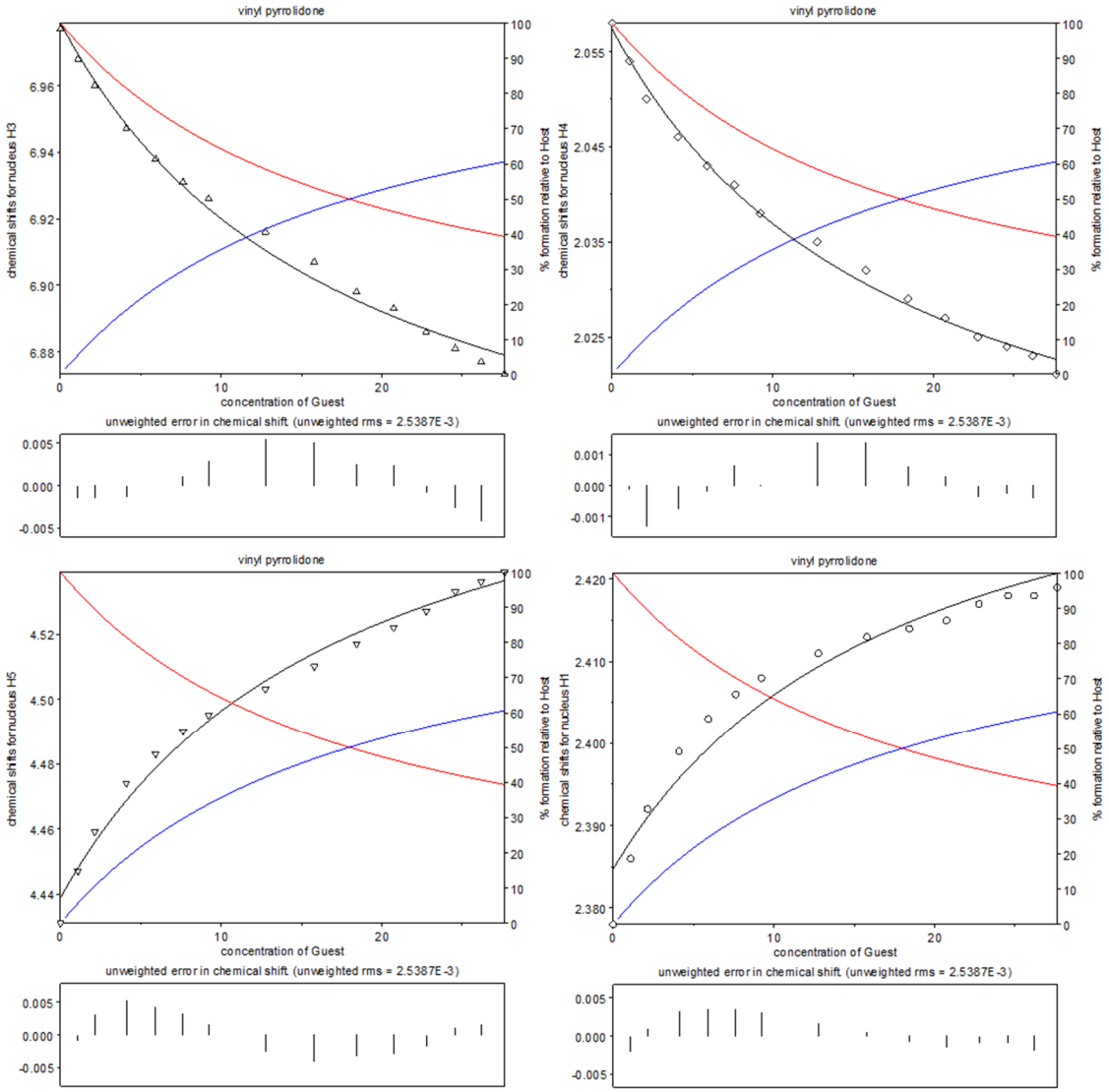

Compound 2.11 (EP)

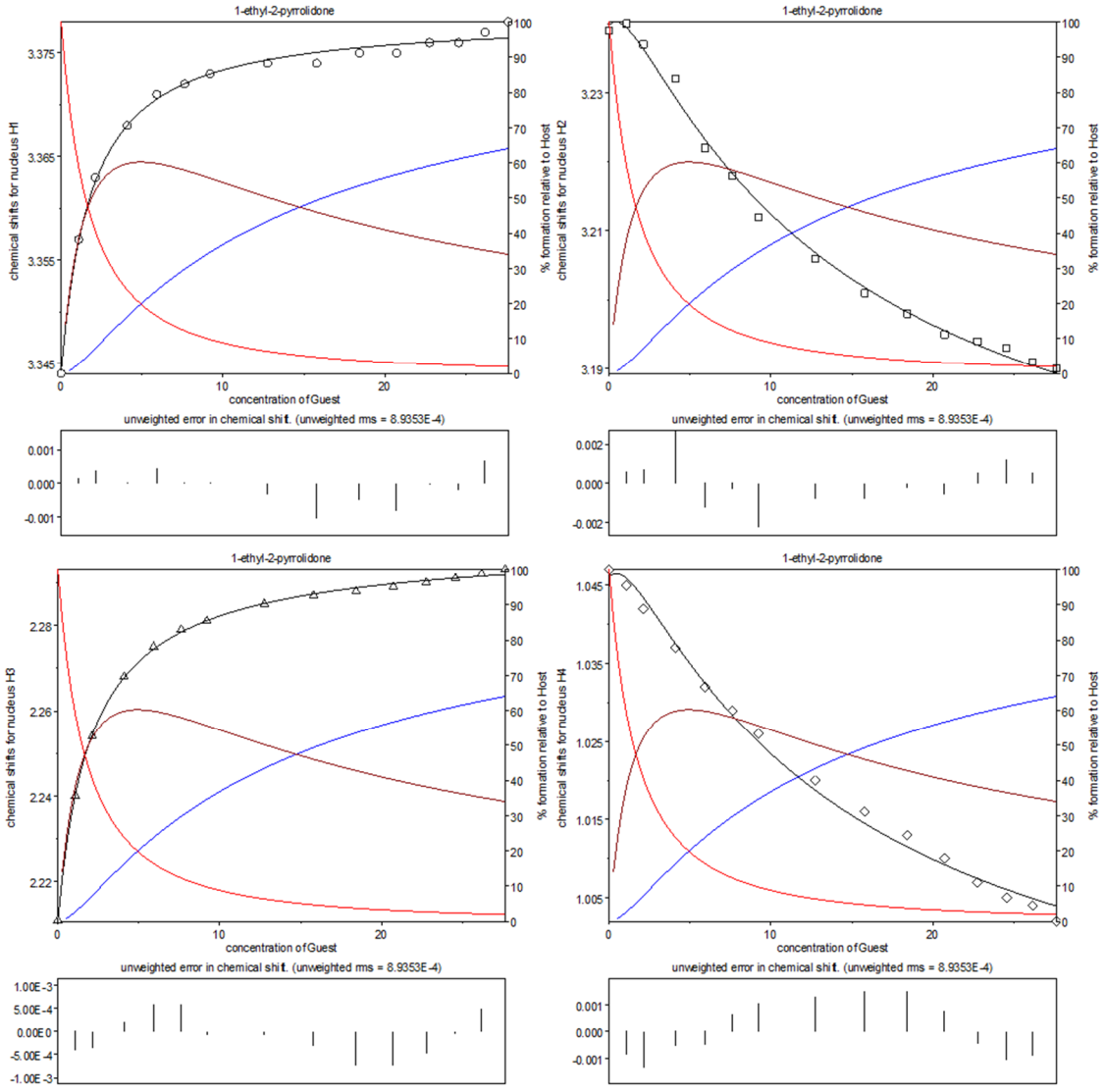

Neutron scattering data

Outlined below are plots of the raw neutron data obtained using NIMROD and SANDALS at the Rutherford Appleton Laboratory. Plots of DSCS *vs* Q show the extracted differential scattering cross section for several detector groups as a function of Q prior to any data processing. There are many detectors within the instruments which allow scattering at many angles to be detected. The data processing was completed using GudrunN, whereby the raw DSCS files were merged and the backgrounds subtracted as appropriate. The MDSCS *vs* Q plots below show the data following merging of the DSCS files and after removal of all necessary backgrounds.

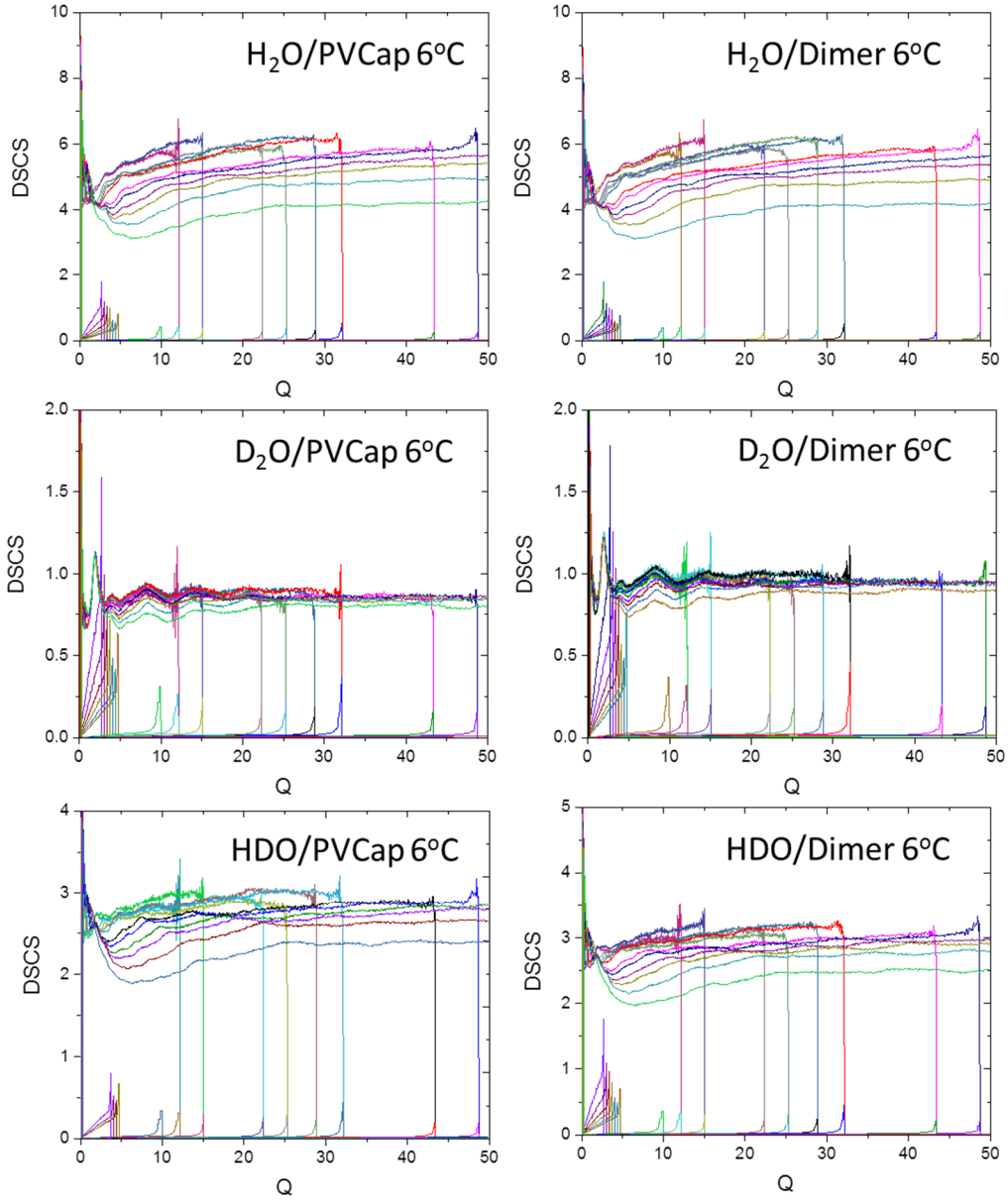

Figure A.1: Extracted differential scattering cross section data plotted as a function of *Q*. These plots show the lactam solutions of aqueous-PVCap and aqueous-dimer (**2.1**) at 6°C. HDO = 1:1 mixture of H_2O/D_2O.

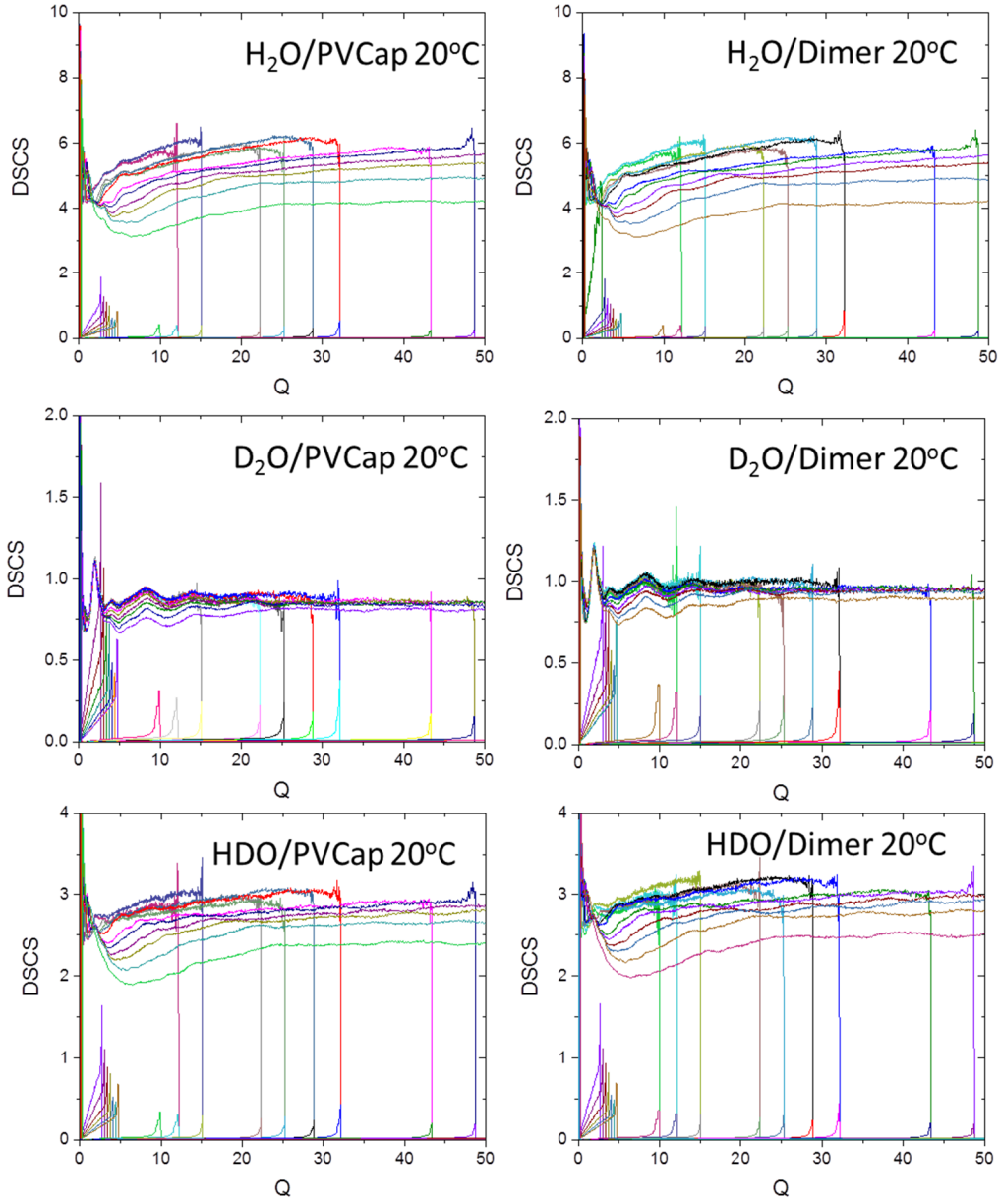

Figure A.2: Extracted differential scattering cross section data plotted as a function of *Q*. These plots show the lactam solutions of aqueous-PVCap and aqueous-dimer (**2.1**) at 20°C.

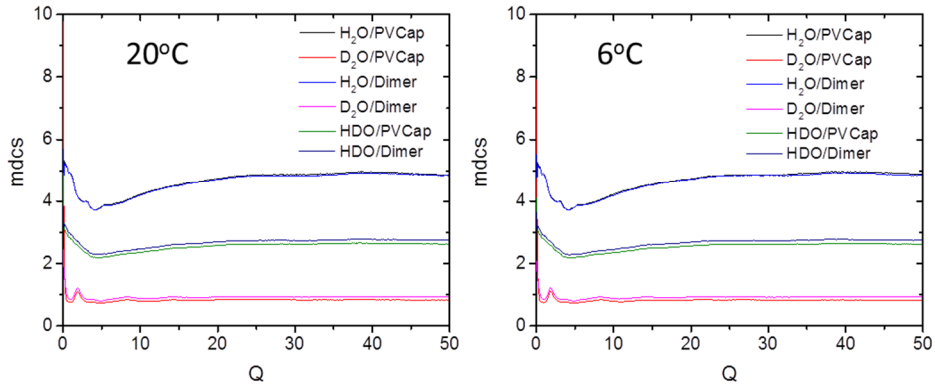

Figure A.3: Merged DSCS files as a function of Q for the aqueous-lactam systems at 20°C and 6°C.

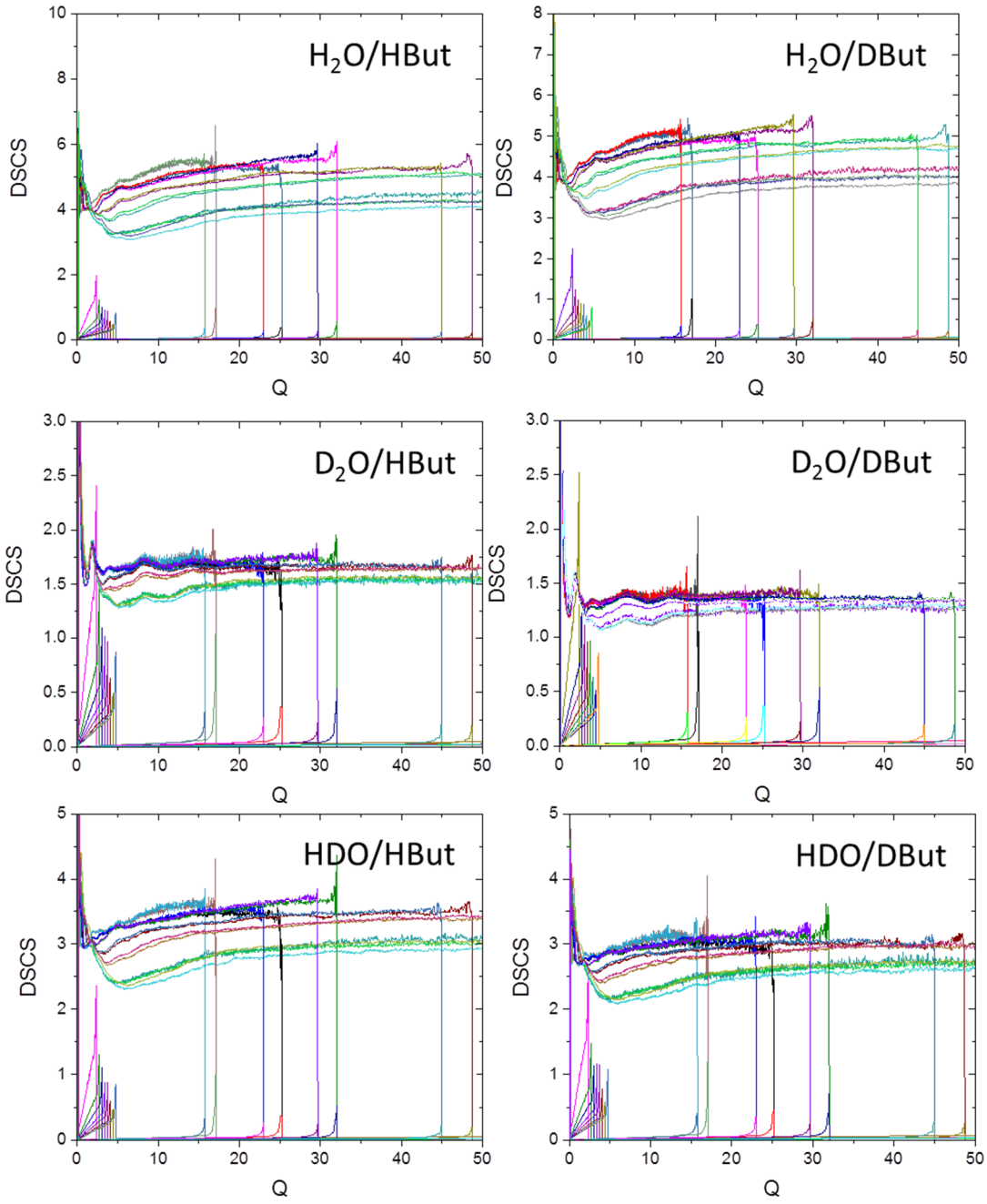

Figure A.4: Plots of the extracted differential scattering cross sections as a function of Q for aqueous-butoxyethanol systems. Plot labels show the isotopic substitutions used. HBut = protic butoxyethanol; DBut = (partially) deuterated butoxyethanol; HDO = A 1:1 mixture of H_2O/D_2O.

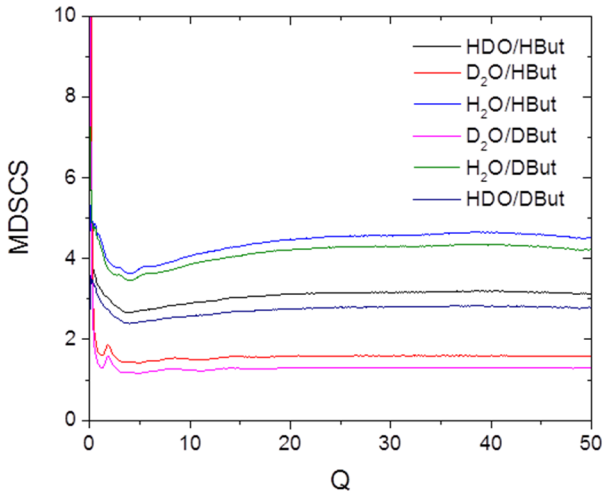

Figure A.5: Merged DSCS files as a function of Q for the aqueous-butoxyethanol systems.

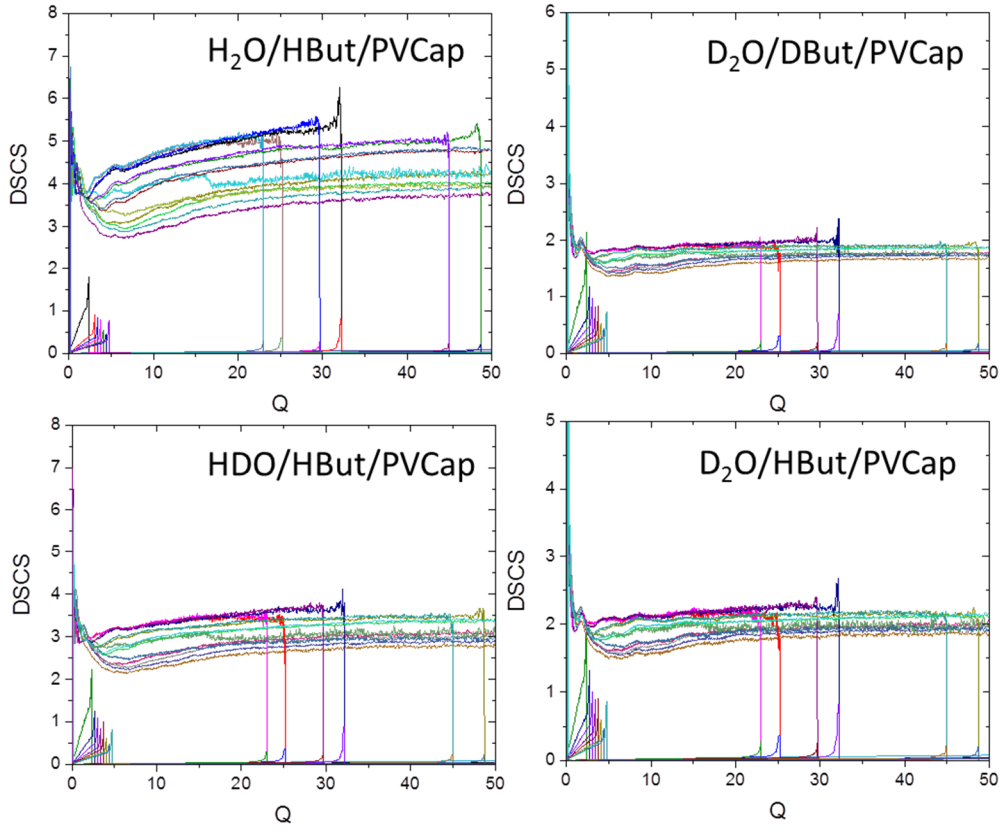

Figure A.6: Plots of the extracted differential scattering cross sections as a function of Q for the ternary aqueous-butoxyethanol-PVCap systems.

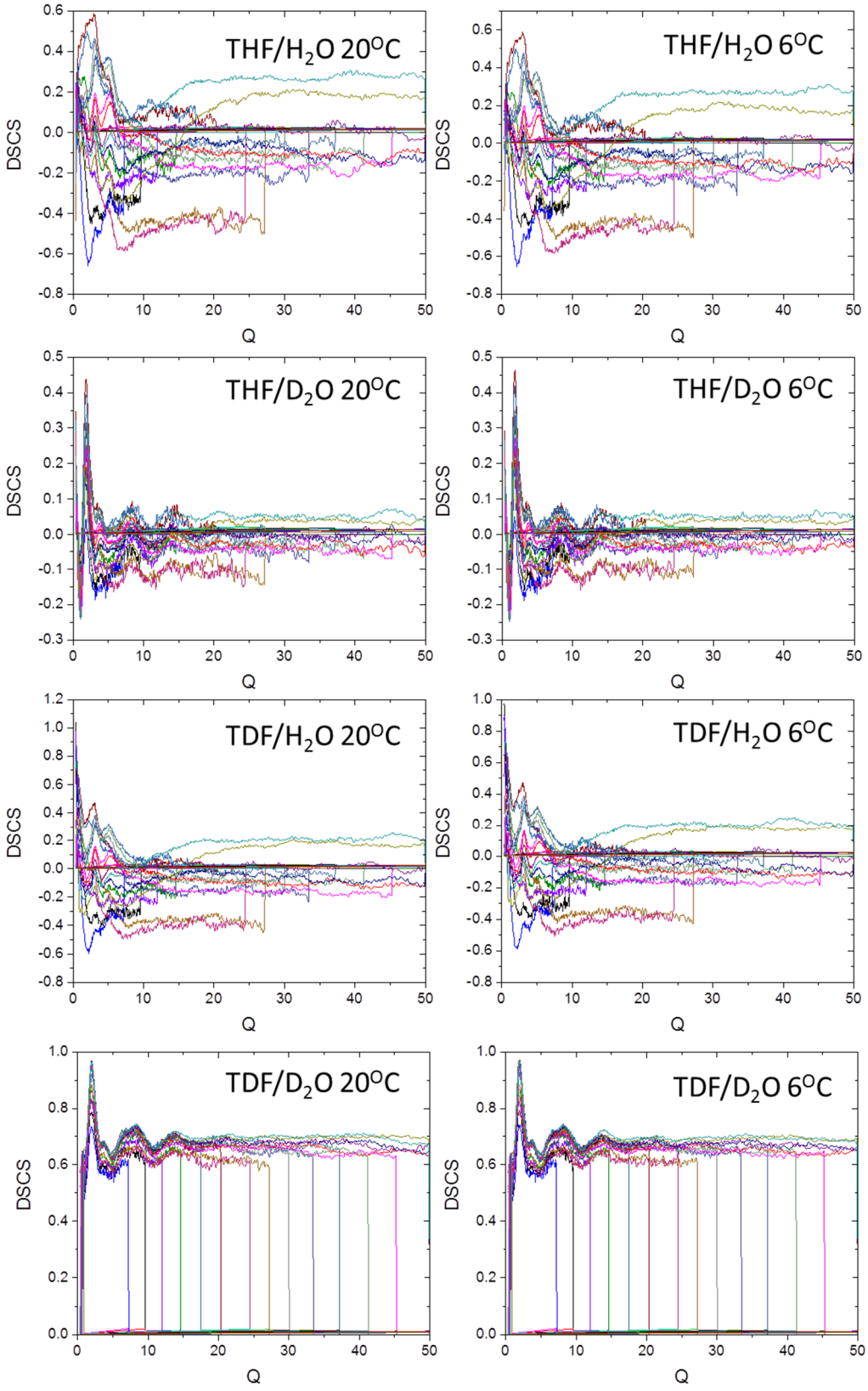

Figure A.7: Plots of the extracted differential scattering cross sections as a function of Q for aqueous-THF systems at 20 °C and 6 °C.